UNIVERSITAT POLITÈCNICA DE CATALUNYA BARCELONATECH

Deriving vertical total electron ontent maps from SMOS full polarimetric data to compensate the Faraday rotation effects

Roselena Rubino

ADVERTIMENT La consulta d'aquesta tesi queda condicionada a l'acceptació de les següents condicions d'ús: La difusió d'aquesta tesi per mitjà del repositori institucional UPCommons (http://upcommons.upc.edu/tesis) i el repositori cooperatiu TDX (http://www.tdx.cat/) ha estat autoritzada pels titulars dels drets de propietat intel·lectual **únicament per a usos privats** emmarcats en activitats d'investigació i docència. No s'autoritza la seva reproducció amb finalitats de lucre ni la seva difusió i posada a disposició des d'un lloc aliè al servei UPCommons o TDX. No s'autoritza la presentació del seu contingut en una finestra o marc aliè a UPCommons (*framing*). Aquesta reserva de drets afecta tant al resum de presentació de la tesi com als seus continguts. En la utilització o cita de parts de la tesi és obligat indicar el nom de la persona autora.

ADVERTENCIA La consulta de esta tesis queda condicionada a la aceptación de las siguientes condiciones de uso: La difusión de esta tesis por medio del repositorio institucional UPCommons (http://upcommons.upc.edu/tesis) y el repositorio cooperativo TDR (http://www.tdx.cat/?locale-attribute=es) ha sido autorizada por los titulares de los derechos de propiedad intelectual **únicamente para usos privados enmarcados** en actividades de investigación y docencia. No se autoriza su reproducción con finalidades de lucro ni su difusión y puesta a disposición desde un sitio ajeno al servicio UPCommons No se autoriza la presentación de su contenido en una ventana o marco ajeno a UPCommons (*framing*). Esta reserva de derechos afecta tanto al resumen de presentación de la tesis como a sus contenidos. En la utilización o cita de partes de la tesis es obligado indicar el nombre de la persona autora.

WARNING On having consulted this thesis you're accepting the following use conditions: Spreading this thesis by the institutional repository UPCommons (http://upcommons.upc.edu/tesis) and the cooperative repository TDX (http://www.tdx.cat/?locale- attribute=en) has been authorized by the titular of the intellectual property rights **only for private uses** placed in investigation and teaching activities. Reproduction with lucrative aims is not authorized neither its spreading nor availability from a site foreign to the UPCommons service. Introducing its content in a window or frame foreign to the UPCommons service is not authorized (framing). These rights affect to the presentation summary of the thesis as well as to its contents. In the using or citation of parts of the thesis it's obliged to indicate the name of the author.

UNIVERSITAT POLITÈCNICA
DE CATALUNYA
BARCELONATECH

Ph.D. Program in Signal Theory and Communications

Deriving Vertical Total Electron Content Maps from SMOS Full Polarimetric Data to Compensate the Faraday Rotation Effect

Doctoral thesis by:

Roselena Rubino

Thesis advisors:

Nuria Duffo Ubeda

Verónica González-Gambau

Signal Theory and Communications

Barcelona, July 2022

El Señor ha estado grande con nosotros y estamos alegres (Sl 126, 3)

The Lord has done great things for us, and we are filled with joy (Sl 126, 3)

Abstract

The Faraday rotation is a geophysical effect that causes a rotation of the electromagnetic field components emitted by the Earth when it propagates through the ionosphere. It depends on the vertical total electron content (VTEC) of the ionosphere, the geomagnetic field, and the frequency. For satellite measurements at the L band, this effect is not negligible and must be compensated for. This is the case of the Soil Moisture and Ocean Salinity (SMOS) mission, where the measured polarimetric brightness temperature must be corrected from the Faraday rotation effect before the retrieval of the geophysical parameters.

The Faraday rotation angle (FRA) can be estimated using a theoretical formulation that makes use of external sources for the VTEC and the geomagnetic field. Alternatively, it can be continuously retrieved from the SMOS full-polarimetric data. However, this is not straightforward due to the relatively poor radiometric sensitivity (thermal noise) and accuracy (spatial bias) of its payload MIRAS (Microwave Interferometer Radiometer by Aperture Synthesis).

In this thesis, a methodology for estimating the total electron content of the ionosphere by using an inversion procedure from the measured rotation angle has been developed. These SMOS VTEC maps are derived from SMOS measurements in the Extended Alias-Free Field of View (EAF-FoV) by applying spatio-temporal filtering techniques to mitigate the radiometric errors present in the full-polarimetric measured brightness temperatures. Systematic error patterns found in the Faraday rotation angle retrieval have been characterized along the mission and corrected. The methodology is independent, not only of external databases and forward models, but also of the target that is being measured.

Eventually, these SMOS-derived VTEC maps can then be used in the SMOS level 2 processors to improve the geophysical retrievals. The impact of using these SMOS VTEC maps to correct the FRA in the SMOS mission instead of the commonly used VTEC data from GPS has also been assessed, particularly over ocean, where the ionospheric effect is stronger. This assessment has demonstrated improvements in the spatial biases, in the stability of the brightness temperatures (especially in the third Stokes parameter), and in the reduction of the latitudinal gradient present in the third Stokes parameters. All these quality indicators point to a better quality of the geophysical retrievals.

Resumen

La rotación de Faraday es un efecto geofísico que causa un giro en las componentes del campo electromagnético emitido por la Tierra cuando éste se propaga a través de la ionosfera. Ésta depende del contenido vertical total de electrones (VTEC) en la ionosfera, el campo geomagnético y la frecuencia. En las medidas de los satélites que operan en banda L, este efecto no es despreciable y se debe compensar. Este es el caso de la misión SMOS (*Soil Moisture and Ocean Salinity*), por lo que el efecto de Faraday se tiene que corregir en las medidas polarimétricas captadas por el instrumento antes de obtener parámetros geofísicos.

El ángulo de rotación de Faraday (FRA) se puede estimar con una fórmula teórica que usa bases de datos externas para el VTEC y el campo geomagnético. Alternativamente, se puede obtener de una manera continua a partir de los datos polarimétricos de SMOS. Sin embargo, esto no se logra con un cálculo directo debido a la pobre sensibilidad radiométrica (ruido térmico) y a la baja precisión (sesgos espaciales) que presenta el instrumento MIRAS (*Microwave Interferometer Radiometer by apertura Synthesis*), que se encuentra a bordo del satélite.

En esta tesis, se desarrolla una metodología para estimar el VTEC de la ionosfera usando un proceso inverso a partir del ángulo de rotación medido. Estos mapas de VTEC se derivan de medidas en todo el campo de visión extendido en donde no hay *aliasing*. Para mitigar los errores radiométricos en las temperaturas de brillo polarimétricas, se aplican técnicas de filtrados temporales y espaciales. En el ángulo de rotación de Faraday recuperado se detectaron errores sistemáticos. Estos se caracterizaron a lo largo de la misión y se corrigieron. La metodología es independiente, no solo de bases de datos externas y modelos de océano, sino también de la superficie medida.

Estos mapas de VTEC derivados de los datos SMOS se pueden usar en el procesador de nivel 2 para mejorar las recuperaciones geofísicas. Se ha evaluado el impacto de usar estos mapas para corregir el FRA en la misión, en vez de los datos de VTEC que comúnmente se emplean (mapas provenientes de datos de GPS), particularmente sobre océano, en donde los efectos de la ionosfera son más críticos. Esta verificación ha demostrado mejoras en el sesgo espacial, en la estabilidad de las temperaturas de brillo (especialmente en el tercer parámetro de Stokes) y en la reducción del gradiente latitudinal presente en el tercer parámetro de Stokes. Todos estos indicadores de calidad apuntan a la obtención de parámetros geofísicos de mejor calidad.

Acknowledgement

I would like to thank the *Ministerio de Economía y Competitividad* and the *Universidad Politécnica de Cataluña* for giving me this great opportunity to grow up professionally and as a whole person, and moreover, to my tutors, Nuria and Verónica, and Ignasi that have helped me, taught me so much, led me, and helped me in my path to sanctification. To all my collages in the office, but in particular to My Boys that have made me enjoy every moment of the thesis especially the last year. To all the people that have supported me and prayed for me in the toughest moments, that have made me laugh, and that had made this a great journey… Without you, this hasn't been possible! To Montse, that has been always there to help me and being like a mom. I know one day we'll share all these experiences! Also, to the three musketeers that God has put me in my way this last year to live all these ducktales, to share amazing moments, but most importantly, to live all for one and one for all in Christ… especially to Bea, for putting me up with the hardest moments of the thesis, encouraging to face my fears, and making me grow up. A special thankful to my Spanish family, every member of the Ibarra family, that has giving me so much love and affection, support, companion, and making me feel part of the family, for better or worse, since the beginning. You've been always there for me, and that is priceless! To my family, especially my parents and sister, that has been always there giving me support in everything I have needed, especially in the trips where we've been all gathered. A big thanks to Saint Joseph, who's intercession conceived this amazing adventure that has given me incalculable graces, experiences, and opportunities to both grow up and help redeeming the world, and also to the Virgen Mary that has taken me by her hand in all this journey… but most importantly, to God, who gave me life, kept me alive and gives me life in every instant, holding me up and giving me exactly what I need in every second, allowing me to enjoy every moment of life.

Table of Contents

Chapter 1 – Introduction 1

1.1. Motivation 1

1.2. Context of the Thesis 2

1.3. Objectives 3

1.4. Thesis Outline 4

Chapter 2 – Theoretical Framework 6

2.1. Microwave Radiometry Fundamentals 6

2.1.1. Thermal Microwave Radiation 6

2.1.2. Power Collected by an Antenna 10

2.2. Microwave Radiometry for Earth Observation 10

2.2.1. Power Collected by an Antenna Pointing to the Earth 10

2.2.2. Microwave Radiometers 12

2.3. The SMOS Mission 14

2.4. MIRAS, the SMOS Payload 16

2.5. MIRAS Operating Fundamentals 17

2.5.1. The Stokes Parameters 23

2.5.2. The SMOS Field of View 24

2.5.3. MIRAS Measurement Modes 26

2.5.4. Radiometric Sensitivity 28

2.5.5. Stokes Parameters at Antenna and Ground Frames 30

2.5.6. Geolocation of the Brightness Temperatures 32

2.5.7. Radio Frequency Interference 33

Chapter 3 – Faraday Rotation Angle and Vertical Total Electron Content Fundamentals 36

3.1. FRA Variability 38

3.2. VTEC and FRA Data Sources 42

3.2.1. Models 42

3.2.2. Datasets Coming from Satellite's Data 43

3.3. Implementation of SMOS FRA End-to-End Simulator 54

3.3.1. Modeled TB 55

3.3.2. FRA Retrieval 57

Chapter 4 – Faraday Rotation Angle and Vertical Electron Content from SMOS Radiometric Data 59

4.1. Recovery with SMOS Simulated Data 59

4.1.1. FRA and VTEC Computation 60

4.1.2. Geolocation 61

4.1.3. Avoiding the Indetermination when Retrieving the FRA using the SMOS Radiometric Data 65

4.1.4. Avoiding the Indetermination when Calculating the VTEC from the Retrieved FRA 67

4.1.5. Spatio-temporal Filtering Techniques 69

4.1.6. FRA Recovery from the SMOS-derived VTEC Maps Using the First Approach 74

4.1.7. Analysis for Ascending Orbits 75

4.2. Recovery with SMOS Radiometric Data Using the First Approach 78

4.2.1. Improving the Recovered Systematic Pattern in the Laterals of the Swath.... 82

4.3. Conclusions 100

Chapter 5 – Characterization and Correction of Systematic Error Patterns in the Faraday Rotation Angle 102

5.1. Characterization of the FRA Systematic Error Pattern 103

5.2. Recovering VTEC Maps Using the Third Approach 105

5.3. VTEC Maps Using the Third Approach 107

5.3.1. FRA Recovery from the Retrieved VTEC Maps from SMOS Radiometric Data 111

5.3.2. Comparison of the Retrieved VTEC using the third approach from SMOS with other VTEC Sources 115

5.4. Conclusions 128

Chapter 6 – Assessment of the Recovered Vertical Electron Content 130

6.1. Hovmöller Diagrams of VTEC 130

6.2. Monthly VTEC Global Maps 135

6.3. Spatial Bias on Brightness Temperatures 142

6.4. Assessment on Brightness Temperature Stability 146

6.5. Ocean Anomaly Global Maps 165

6.6. Conclusions 173

Chapter 7 – Conclusions and Future Lines 175

7.1. Main Conclusions 175

7.2. Thesis Outcomes 177

7.3. Future Research Lines 179

Appendix A 181

Appendix B 192

References 203

Table of Figures

Figure 2.1. Spectral power density from an observation point. 7

Figure 2.2. Planck's radiation law and its approximation for microwave frequencies (Rayleigh-Jeans law), considering physical temperature T=300 K. 8

Figure 2.3. Emissivity (left axis) and reflectivity (right axis) for flat surfaces with different dielectric constants in the horizontal (solid line) and vertical (dashed line) polarization (figure 4.21 from Ulaby et al., 1981). 9

Figure 2.4. Relationship between the antenna temperature, the apparent temperature and the brightness temperature (Figure 4.8 from Ulaby et al., 1981). 11

Figure 2.5. Real aperture radiometer 13

Figure 2.6. Scanning configurations (figure 4.69 from Emery & Camps, 2017): (a) conical scan, (b) cross-track scan, and (c) push-broom schemes. 13

Figure 2.7. Interferometric radiometer 14

Figure 2.8. Earth's water cycle (credits: ESA Centre National d'Etúdes Spatiales, CNES) 15

Figure 2.9. MIRAS at Maxwell anechoic chamber during Image Validation Tests at ESTEC facilities. 17

Figure 2.10. MIRAS operating principle 18

Figure 2.11. Position of an antenna with respect to a distant source point 18

Figure 2.12. MIRAS block diagram 21

Figure 2.13. Antenna positions in the MIRAS arms (Corbella et al., 2019) 24

Figure 2.14. Planes: (a) u-v plane (visibility), (b) ξ-η plane (brightness temperature). 25

Figure 2.15. Replicas of the fundamental hexagon in: (a) the u-v plane, (b) the $\xi - \eta$ plane. 25

Figure 2.16. Field of view: (a) EAF-FoV and AF-FoV, (b) incidence angles in SMOS FoV. 26

Figure 2.17. Pair of antennas measuring in dual-pol. Image from (Martin-Neira et al., 2002). 27

Figure 2.18. Switching of a pair of receivers in the four different instants of the sequence (Martin-Neira et al., 2002). 27

Figure 2.19. Equi-radiometric sensitivity contours, where the ration $\Delta TB \Delta TB boresight$ is annotated in pink. 29

Figure 2.20. MIRAS boresight radiometric sensitivity with respect the integration time. 30

Figure 2.21. Coordinate rotation in the antenna frame $(x - y)$ and ground frame $(h - v)$. 31

Figure 2.22. Ludwig's third definition 32

Figure 2.23. Snapshot projected to ground coordinates: (a) swath, (b) constant incidence angle contours. 33

Figure 2.24. Spatial resolution: (a) in antenna frame, (b) projected to ground coordinates. 33

Figure 2.25. RFI probability worldwide map: (a) 16-31 of January, 2010, (b) 4-17 of May, 2017 (Uranga et al., 2018). 35

Figure 3.1. Solar activity (SILSO, s. f.): (a) of the 15th solar cycle to the 24th, (b) of the SMOS mission. 37

Figure 3.2. Local Time variation of TEC averaged for different seasons from different sources vs LT: (a) Summer (May, June, July, August), (b) Winter (November, December, January, February), (c) Spring (March, April), (d) Fall (September, October) (Kakoti et al., 2017). 37

Figure 3.3. FRA at SMOS boresight coordinates of three consecutive days in different periods. Top: Descending orbits in (a) March 2014 (high solar activity), (b) January 2011 (low solar activity), Bottom: Ascending orbits in (c) March 2014 (high solar activity), and (d) January 2011 (low solar activity). 38

Figure 3.4. Hövmoller of the FRA at boresight through the mission for: (a) descending orbits and (b) ascending orbits. 39

Figure 3.5. FRA with the SMOS boresight coordinates in: (a) March 18, 2011, (b) March 21, 2011, and (c) both dates. 40

Figure 3.6. Global distribution of the error in the TB (H-pol) as a function of incidence angle due to neglecting the FRA at 6 a. m. (left) and noon (right). The data are for high solar activity (June 1989; Rz = 158) and for a sensor at altitude of 675 km and looking perpendicular to the satellite heading to the right. The surface is ocean with Salinity = 35 PSU and T = 20 C. Figure from (Le Vine & Abraham, 2002). 41

Figure 3.7. Simulated afternoon ionosphere electronic content contribution (Floury, 2007). 45

Figure 3.8. VTEC Hövmollers of orbits for the period 2014-2016: (a) L1 VTEC descending-orbit, (b) IGS VTEC descending-orbit, (c) L1 VTEC ascending-orbit, (d) IGS VTEC ascending-orbit, (e) difference between L1 VTEC and the IGS VTEC of descending orbits, (f) difference between L1 VTEC and the IGS VTEC of ascending orbits. 47

Figure 3.9. VTEC vs latitude of the middle pixel of a descending orbit (left: IGS in blue, L1 in red, and corrected IGS in dotted IGS; right: IGS VTEC - L1 VTEC). Top: March, 2014; middle: November, 2015; bottom: July, 2016..... 49

Figure 3.10. Correlation of the difference of the L1 VTEC and the IGS VTEC with respect to: (a) the L1 VTEC and (b) the solar activity. 50

Figure 3.11. VTEC sensitivity with respect to the A3 (figure 1 from Vergely et al., 2014): (a) magnitude, and (b) zone of the FoV with highest sensitivity. 51

Figure 3.12. FRA over a snapshot: (a) total angle and reference area, (b) FRA from VTEC and the IGRF , and (c) error between using the averaged FRA in the reference area assigned to the boresight with respect to the FRA of every pixel. 54

Figure 3.13. Typical open ocean Fresnel brightness temperature snapshots per polarization (left: X-pol, middle: Y-pol, right: third Stokes parameter). Top: Fresnel modeled brightness temperature, middle: considering the FRA, bottom: adding the effect of noise in addition to the FRA..... 56

Figure 3.14. Radiometric sensitivity per polarization: (a) X-pol, (b) Y-pol, (c) mixed polarization. 56

Figure 3.15. Brightness temperature snapshots emphasizing where it tends to zero: (a) T3, and (b) Tx-Ty..... 57

Figure 3.16. FRA snapshot: (a) L1 FRA, (b) recovered FRA, and (c) difference between the recovered FRA and the L1 FRA. 58

Figure 3.17. Noisy FRA snapshot: (a) recovered FRA, (b) difference between the recovered FRA and the L1 FRA. 58

Figure 4.1. FRA snapshots of a descending orbit simulated with the realistic SMOS measurement scenario: (a) L1 FRA, (b) retrieved FRA, (c) difference between the retrieved FRA and the L1 FRA. 60

Figure 4.2. VTEC snapshots of a descending orbit simulated with the realistic SMOS measurement scenario: (a) L1 VTEC, (b) recovered VTEC, and (c) difference between the recovered VTEC and the L1 VTEC. 60

Figure 4.3. FRA and VTEC single snapshot of the descending orbit simulated with the realistic SMOS measurement scenario considering the effect of noise: (a) recovered FRA, (b) difference between the recovered FRA and the L1 FRA, (c) recovered VTEC, (d) difference between the recovered VTEC and the L1 VTEC. 61

Figure 4.4. VTEC maps of a descending orbit over the Pacific simulated without taking into account the effect of noise: (a) L1 VTEC, (b) recovered VTEC, and (c) VTEC error. 62

Figure 4.5. Number of averages done per pixel in the generation of the VTEC map. 63

Figure 4.6. VTEC maps of the descending orbit simulated considering the effect of noise: (a) recovered VTEC and (b) VTEC error. 63

Figure 4.7. Recovery errors of the descending orbit when assuming the brightness temperatures measured at the same instant despite the polarization within each block (not taking into account the effect of noise): (a) FRA snapshot error, (b) VTEC snapshot error, and (c) VTEC map error. 64

Figure 4.8. FRA snapshots of the descending orbit avoiding indetermination when retrieving the FRA (taking into account the effect of noise): (a) recovered FRA and (b) FRA error. 65

Figure 4.9. VTEC maps of the descending orbit avoiding the indetermination when retrieving the FRA (taking into account the effect of noise): (a) recovered VTEC and (b) VTEC error. 65

Figure 4.10. Number of averages done per pixel in the geolocation when avoiding the indetermination in Eq. (4.1). 66

Figure 4.11. FRA snapshots of the ascending orbit avoiding the indetermination when retrieving the FRA (considering the effect of noise): (a) recovered FRA and (b) FRA error. 66

Figure 4.12. Filtered brightness temperature snapshots affected by the indetermination in Eq. (4.2) in the X polarization (left column), Y polarization (middle column), and T3 (right column): (top) snapshot less affected, (bottom) snapshot in the worst scenario. 67

Figure 4.13. Recovered VTEC map of the descending orbit avoiding both indeterminations (considering the effect of noise): (a) recovered VTEC map, and (b) VTEC error map. 68

Figure 4.14. Number of averages when avoiding indeterminations in the equations needed in the retrieval. 68

Figure 4.15. Optimization of the temporal filter with a coarse binning (4 snapshots): root mean square error (recovered VTEC - L1 VTEC) vs size of the temporal filter. 69

Figure 4.16. Optimization of the spatial filter fixing the temporal filter to 43 snapshots: RMSE vs size of the spatial filter. 70

Figure 4.17. Optimization of the temporal filter fixing the spatial filter to 0.1969: RMSE vs size of the temporal filter. 70

Figure 4.18. Optimization of the spatial filter fixing the temporal filter to 43 snapshots: RMSE error vs size of the spatial filter. 71

Figure 4.19. FRA snapshots of the descending orbit analyzing the application of the temporal filter: (a) L1 FRA, (b) recovery when not applying the temporal filter, (c) FRA error when not applying the temporal filter, (d) recovery when applying the temporal filter, (e) FRA error when applying the temporal filter. 72

Figure 4.20. VTEC snapshots of the descending orbit analyzing the application of spatio-temporal filtering techniques: (a) L1 VTEC, (b) recovered VTEC before applying the spatial filter, (c) VTEC error before applying the spatial filter, (d) number of averages when applying the spatial filter, (e) recovered VTEC after applying the spatial filter, and (f) VTEC error after applying the spatial filter. 72

Figure 4.21. VTEC maps of the descending orbit applying filtering techniques (once the indeterminations are avoided) using the first approach: (a) recovered VTEC and (b) VTEC error. 73

Figure 4.22. Number of averages after applying the filtering techniques. 74

Figure 4.23. FRA versus latitude of a pixel in the center of the swath along the descending orbit: (a) L1 FRA (red) and retrieved FRA from simulated data using the first approach (green), (b) error of the retrieved FRA with respect to the L1 FRA. 75

Figure 4.24. FRA snapshots of the ascending orbit analyzing the application of the temporal filter: (a) L1 FRA, (b) recovery when the temporal filter is not applied, (c) FRA error when not applying the temporal filter, (d) recovery when applying the temporal filter, (e) FRA error when applying the temporal filter..... 76

Figure 4.25. VTEC snapshots of the ascending orbit analyzing the application of spatio-temporal filtering techniques: (a) L1 VTEC, (b) recovered VTEC before applying the spatial filter, (c) VTEC error before applying the spatial filter, (d) number of averages before applying the spatial filter, (e) recovered VTEC after applying the spatial filter, (f) VTEC error after applying the spatial filter. 76

Figure 4.26. VTEC maps of the ascending orbit: (a) L1 VTEC (b) recovered VTEC using the first approach, and (c) VTEC error. 77

Figure 4.27. FRA vs latitude of a pixel along the ascending orbit: (a) L1 FRA (red) and retrieved FRA with simulated data (green), (b) error of the retrieved FRA with respect to the L1 one. 78

Figure 4.28. FRA snapshots from SMOS radiometric data in the descending orbit: (a) recovered FRA, (b) difference between the recovered and the L1 FRA. 79

Figure 4.29. VTEC snapshots retrieved from SMOS radiometric data in the descending orbit: (a) the SMOS-derived VTEC before applying the spatial filter, (b) the difference between the SMOS-derived (before applying the spatial filter) and the L1 VTEC, (c) the SMOS-derived VTEC after applying the spatial filter, (b) the difference between the SMOS-derived (after applying the spatial filter) and the L1 VTEC. 80

Figure 4.30. VTEC maps of the descending-orbit SMOS radiometric data: (a) recovery using the first approach, and difference between the retrieval and the L1 VTEC (b) over ocean and (c) over land..... 81

Figure 4.31. VTEC snapshots analyzing the approach application in the EAF-FoV: (a) recovered VTEC when not extending to the EAF-FoV, (b) VTEC difference between the recovery when extending to the EAF-FoV and the L1 VTEC, (c) retrieval when extending to the EAF-FoV, and (d) VTEC difference between the retrieval when extending to the EAF-FoV and the L1 VTEC. 83

Figure 4.32. VTEC maps of the descending orbit when using the second approach: (a) recovered VTEC, (b) difference between the recovery and the L1 VTEC over ocean, (c) difference between the recovery and the L1 VTEC over land, and difference between the recovery when using the second approach and the first one (d) over ocean and (e) over land. 84

Figure 4.33. Recovered VTEC maps of the ascending orbit: (a) recovered VTEC using the first approach, (b) recovery using the second approach..... 85

Figure 4.34. Difference between the recovery Top: recovering in the EAF-FoV and the L1 VTEC over ocean, (a) using the first approach and (b) using the second approach; middle: recovering in the EAF-FoV and the L1 VTEC over land (c) using the first approach and (d) using the second approach; bottom: difference between applying the second and first approach over (e) ocean and (f) land. 86

Figure 4.35. FRA vs latitude of a pixel along the descending orbit: (a) L1 FRA (red) and retrieved FRA with SMOS radiometric data when using the second approach (green), (b) difference between the retrieved FRA with respect to the L1 one. 87

Figure 4.36. FRA vs latitude of a pixel along the ascending orbit: (a) L1 FRA (red) and retrieved FRA with SMOS radiometric data when using the second approach (green), (b) difference between the retrieved FRA with respect to the L1 one. 88

Figure 4.37. Comparison of the descending-orbit VTEC coming from different sources. 89

Figure 4.38. Comparison of the ascending-orbit VTEC coming from different sources.. 90

Figure 4.39. VTEC maps of the descending orbits of March 21st, 2011: (a) L1 VTEC and (b) recovered VTEC using the second approach. 91

Figure 4.40. Difference between the recovered VTEC maps using the second approach and the L1 VTEC of the descending orbits of March 21st, 2011: (a) over ocean and (b) over land. 92

Figure 4.41. Zoomed recovered VTEC of descending orbits (using the second approach) over: a) the Bering Sea on March 21st, 2011 (RFI contaminated), b) the Bering Sea on March 20th, 2012 (RFI not contaminated), c) the Barents Sea on March 21st, 2011 (RFI contaminated), d) Barents Sea on March 20th, 2014 (RFI not contaminated). 93

Figure 4.42. VTEC maps of the descending orbits on March 20th, 2014: (a) L1 VTEC and (b) recovered VTEC using the second approach..... 94

Figure 4.43. Difference between the recovered VTEC maps using the second approach and the L1 VTEC of the descending orbits on March 20th, 2014: (a) over ocean and (b) over land. 95

Figure 4.44. 9-day TB maps: (a) difference between $TBxx$ and $TByy$ in March 2011, (b) T3 in March 2011, (c) difference between $TBxx$ and $TByy$ in March 2014, and (d) T3 in March 2014. 96

Figure 4.45. VTEC maps of the ascending orbits of March 21st, 2011: (a) L1 VTEC and (b) recovered VTEC using the second approach. 97

Figure 4.46. Difference between the recovered VTEC maps using the second approach and the L1 VTEC of the ascending orbits on March 21st, 2011: (a) over ocean and (b) over land. 98

Figure 4.47. VTEC maps of the ascending orbits on March 20th, 2014: (a) L1 VTEC and (b) recovered VTEC using the second approach. 99

Figure 4.48. Difference between the recovered VTEC maps using the second approach and the L1 VTEC of the ascending orbits on March 20th, 2014: (a) over ocean and (b) over land. 100

Figure 5.1. Recovered VTEC map when using the second approach (descending orbit of March 20th, 2014). 102

Figure 5.2. FRA systematic error pattern computed using data in 2017. 104

Figure 5.3. Δ three consecutive days of: (a) December 2018, (b) July 2014, and (c) July 2010-2019. 104

Figure 5.4. FRA snapshots of date: (a) L1 FRA, (b) recovered FRA when the Δ is not corrected and (b) recovered FRA once Δ is subtracted. 106

Figure 5.5. VTEC snapshot: (a) L1 VTEC, (b) recovery when the Δ is not corrected, (c) the difference between (b) and the L1 VTEC, (d) recovery once Δ is subtracted, (e) the difference between (d) and the L1 VTEC. 106

Figure 5.6. VTEC maps of the descending orbit: (a) using the second approach, (b) using the third approach, (c) difference between the recovery when using the third approach and the L1 VTEC over ocean, (d) the same but using the third approach, (e) difference between the recovery when using the second approach and the L1 VTEC over land, (f) the same but using the third approach. 108

Figure 5.7. Difference between the recovery when using the third approach and the second one in the descending orbit: (a) over ocean and (b) over land. 109

Figure 5.8. VTEC maps of the ascending orbit: (a) using the second approach, (b) using the third approach, (c) difference between the recovery when using the second approach and the L1 VTEC over ocean, (d) the same but when using the third approach, (e) difference between the recovery when using the second approach and the L1 VTEC over land, (f) the same but when using the third approach. 110

Figure 5.9. Difference between the recovery when using the second approach and using the second one in the ascending orbit: (a) over ocean and (b) over land. 111

Figure 5.10. FRA vs latitude of a pixel along the descending orbit comparing when using different VTEC sources: (left plots) using the L1 VTEC in red, using the third approach in green, using the second approach in blue; (right plots) difference between the recovered FRA using the third approach and the L1 FRA in green, and the recovered FRA using the second approach and the L1 FRA in blue: (a) and (b) of a pixel in the center of the swath, (c) and (d) of a pixel in the right part of the swath, and (e) and (f) of a pixel in the left part of the swath..... 112

Figure 5.11. FRA vs latitude of a pixel along the ascending orbit comparing when using different VTEC sources: (left plots) using the L1 VTEC in red, using the third approach in green, using the second approach in blue; (right plots) difference between the recovered FRA using the third approach and the L1 FRA in green, and the recovered FRA using the second approach and the L1 FRA in blue: (a) and (b) of a pixel in the center of the swath, (c) and (d) of a pixel in the right part of the swath, and (e) and (f) of a pixel in the left part of the swath..... 114

Figure 5.12. Comparison of the descending-orbit VTEC coming from different sources when correcting Δ..... 115

Figure 5.13. Comparison of the ascending-orbit VTEC coming from different sources when correcting Δ..... 116

Figure 5.14. VTEC maps of the descending orbits of March 21st, 2011: (a) L1 VTEC and (b) recovered VTEC using the third approach. 117

Figure 5.15. Difference between the recovered VTEC maps using the third approach and the L1 VTEC of the descending orbits of March 21st, 2011: (a) over ocean and (b) over land. 118

Figure 5.16. Difference between the recovered VTEC maps when using the third approach and when using the second one of the descending orbits of March 21st, 2011: (a) over ocean and (b) over land. 119

Figure 5.17. VTEC maps of the descending orbits of March 20th, 2014: (a) L1 VTEC and (b) recovered VTEC using the third approach. 120

Figure 5.18. Difference between the recovered VTEC maps using the third approach and the L1 VTEC of the descending orbits of March 20th, 2014: (a) over ocean and (b) over land. 121

Figure 5.19. Difference between the recovered VTEC maps when using the third approach and when using the second one of the descending orbits of March 20th, 2014: (a) over ocean and (b) over land. 122

Figure 5.20. VTEC maps of the ascending orbits of March 21st, 2011 correcting the FRA systematic error: (a) L1 VTEC and (b) recovered VTEC using the third approach. 123

Figure 5.21. Difference between the recovered VTEC maps using the third approach and the L1 VTEC of the ascending orbits of March 21st, 2011: (a) over ocean and (b) over land. 124

Figure 5.22. Difference between the recovered VTEC maps when using the third approach and when using the second one of the ascending orbits of March 21st, 2011: (a) over ocean and (b) over land. 125

Figure 5.23. VTEC maps of the ascending orbits of March 20th, 2014: (a) L1 VTEC, (b) recovered VTEC using the third approach. 126

Figure 5.24. Difference between the recovered VTEC maps using the third approach and the L1 VTEC of the ascending orbits of March 20th, 2014: (a) over ocean and (b) over land. 127

Figure 5.25. Difference between the recovered VTEC when using the third approach and when using the second one of the descending orbits of March 20th, 2014: (a) over ocean and (b) over land. 128

Figure 6.1. Descending orbits selected for the VTEC Hovmöller. 131

Figure 6.2. VTEC Hovmöllers of the descending orbits: (a) L1 VTEC, (b) SMOS-derived VTEC, and (c) difference between the SMOS-derived VTEC and the L1 VTEC. 132

Figure 6.3. Ascending orbits selected for the VTEC Hovmöller. 133

Figure 6.4. VTEC Hovmöllers for ascending orbits: (a) L1 VTEC, (b) SMOS-derived VTEC, and (c) difference between the SMOS-derived VTEC and the L1 VTEC..... 134

Figure 6.5. VTEC global maps of January 2014 (descending orbits): (a) L1 VTEC, (b) SMOS-derived VTEC, and (c) difference between the SMOS-derived VTEC and the L1 VTEC. 136

Figure 6.6. VTEC global maps of March 2014 (descending orbits): (a) L1 VTEC, (b) SMOS-derived VTEC, and (c) difference between the SMOS-derived VTEC and the L1 VTEC. . 137

Figure 6.7. The world's forests (Food and Agriculture Organitation, FAO, n.d.)..... 139

Figure 6.8. VTEC global maps of January 2014 (ascending orbits): (a) L1 VTEC, (b) SMOS-derived VTEC, and (c) difference between the SMOS-derived VTEC and the L1 VTEC. . 140

Figure 6.9. VTEC global maps of March 2014 (ascending orbits): (a) L1 VTEC, (b) SMOS-derived VTEC, and (c) difference between the SMOS-derived VTEC and the L1 VTEC. . 141

Figure 6.10. Standard deviation of the difference between SMOS and modeled TB normalized by the radiometric accuracy for the X polarization (descending orbits of April 27th to May 6th, 2012): (a) when the L1 VTEC is used to transform modeled TB at ocean surface to antenna frame, and (b) when the SMOS VTEC is used. 143

Figure 6.11. Standard deviation of the difference between SMOS and modeled TB normalized by the radiometric accuracy for the Y polarization (descending orbits of April 27th to May 6th, 2012): (a) when the L1 VTEC is used to transform modeled TB at ocean surface to antenna frame, and (b) when the SMOS VTEC is used. 143

Figure 6.12. Standard deviation of the difference between SMOS and modeled TB normalized by the radiometric accuracy for T3 (descending orbits of April 27th to May 6th, 2012): (a) when the L1 VTEC is used to transform modeled TB at ocean surface to antenna frame, and (b) when the SMOS VTEC is used. 144

Figure 6.13. Standard deviation of the difference between SMOS and modeled TB normalized by the radiometric accuracy for the X polarization (descending orbits of May 26th to June 5th, 2014): (a) when the L1 VTEC is used to transform modeled TB at ocean surface to antenna frame, and (b) when the SMOS VTEC is used. 144

Figure 6.14. Standard deviation of the difference between SMOS and modeled TB normalized by the radiometric accuracy for the Y polarization (descending orbits of May 26th to June 5th, 2014): (a) when the L1 VTEC is used to transform modeled TB at ocean surface to antenna frame, and (b) when the SMOS VTEC is used. 145

Figure 6.15. Standard deviation of the difference between SMOS and modeled TB normalized by the radiometric accuracy for T3 (descending orbits of May 26th to June 5th, 2014): (a) when the L1 VTEC is used to transform modeled TB at ocean surface to antenna frame, and (b) when the SMOS VTEC is used 145

Figure 6.16. Hovmöller diagram of the difference between the SMOS TB and the modeled TB (averaged in the AF-FoV) for the X polarization at antenna reference for descending orbits: (a) the L1 VTEC product has been used to correct for the FR in the modeled TB, and (b) SMOS-derived VTEC maps have been used for the FR correction. 147

Figure 6.17. Hovmöller diagram of the difference between the SMOS TB and the modeled TB (averaged in the AF-FoV) for the Y polarization at antenna reference for descending orbits: (a) the L1 VTEC product has been used to correct for the FR in the modeled TB, and (b) SMOS-derived VTEC maps have been used for the FR correction. 148

Figure 6.18. X-polarization TB bias vs latitude of different descending orbits along 2014: (a) January 3rd, (b) February 27th, (c) March 15th, (d) May 15th, (e) September 6th, and (f) November 11th. 149

Figure 6.19. X-polarization TB bias vs latitude of different descending orbits along 2015: (a) January 13th, (b) March 10th, (c) May, 13th, (d) August 16th, (e) October 20th, and (f) November 17th. 151

Figure 6.20. Figure 6.20 shows the X-polarization TB bias with respect to the latitude of different descending orbits along 2016. 152

Figure 6.21. Y-polarization TB bias vs latitude of different descending orbits along 2014: (a) January 3rd, (b) February 27th, (c) March 15th, (d) May 15th, (e) September 6th, and (f) November 11th. 153

Figure 6.22. Y-polarization TB bias vs latitude of different descending orbits along 2015: (a) January 13th, (b) March 10th, (c) May, 13th, (d) August 16th, (e) October 20th, and (f) November 17th. 154

Figure 6.23. Y-polarization TB bias vs latitude of different descending orbits along 2016: (a) January 29th, (b) February 20th, (c) March 16th, (d) September 5th, (e) November 11th, and (f) December 22nd. 155

Figure 6.24. Hovmöller diagram of the difference between the SMOS TB and the modeled TB (averaged in the AF-FoV) for the third Stokes parameter at antenna reference for descending orbits: (a) the L1 VTEC product has been used to correct for the FR in the modeled TB, and (b) SMOS-derived VTEC maps have been used for the FR correction. . 156

Figure 6.25. T3 bias vs latitude of different descending orbits along 2014: (a) January 3rd, (b) February 27th, (c) March 15th, (d) May 15th, (e) September 6th, and (f) November 11th. . 157

Figure 6.26. T3 bias vs latitude of different descending orbits along 2015: (a) January 13th, (b) March 10th, (c) May, 13th, (d) August 16th, (e) October 20th, and (f) November 17th. 158

Figure 6.27. T3 bias vs latitude of different descending orbits along 2016 (a) January 29th, (b) February 20th, (c) March 16th, (d) September 5th, (e) November 11th, and (f) December 22nd. 159

Figure 6.28. Hovmöller diagram of the difference between the SMOS TB and the modeled TB (averaged in the AF-FoV) for the X polarization at antenna reference for ascending orbits: (a) the L1 VTEC product has been used to correct for the FR in the modeled TB, and (b) SMOS-derived VTEC maps have been used for the FR correction. 160

Figure 6.29. Hovmöller diagram of the difference between the SMOS TB and the modeled TB (averaged in the AF-FoV) for the Y polarization at antenna reference for ascending orbits: (a) the L1 VTEC product has been used to correct for the FR in the modeled TB, and (b) SMOS-derived VTEC maps have been used for the FR correction. 161

Figure 6.30. Hovmöller diagram of the difference between the SMOS TB and the modeled TB (averaged in the AF-FoV) for the third Stokes parameter at antenna reference for ascending orbits: (a) the L1 VTEC product has been used to correct for the FR in the modeled TB, and (b) SMOS-derived VTEC maps have been used for the FR correction..... 162

Figure 6.31. Bias of different ascending orbits: Left: X polarization of (a) June 9th, 2014; (b) February 12th, 2015; (c) October 14th, 2016, Right: Y polarization of (d) June 9th, 2014; (e) February 12th, 2015; (f) October 14th, 2016. 163

Figure 6.32. T3 Bias of different ascending orbits: (a) June 9th, 2014; (b) February 12th, 2015; and (c) October 14th, 2016. 164

Figure 6.33. Zone of the South Pacific where the OTT is computed: (a) for descending orbits and (b) for ascending orbits (figure 1 of Yin et al., 2013). 165

Figure 6.34. X-polarization ocean TB anomaly of a descending orbit on May 30th, 2014 when using: (a) the L1 VTEC, (b) the SMOS-derived VTEC, and (c) difference between (a) and (b). 166

Figure 6.35. Y-polarization ocean TB anomaly of a descending orbit on May 30th, 2014 when using: (a) the L1 VTEC, (b) the SMOS-derived VTEC, and (c) difference between when using the SMOS-derived VTEC and the L1 VTEC. 167

Figure 6.36. X-polarization ocean TB anomaly of a descending orbit on June 3th, 2014 when using: (a) the L1 VTEC, (b) the SMOS-derived VTEC, and (c) difference between (a) and (b). 168

Figure 6.37. Y-polarization ocean TB anomaly of a descending orbit on June 3th, 2014 when using: (a) the L1 VTEC, (b) the SMOS-derived VTEC, and (c) difference between (a) and (b). 169

Figure 6.38. X-polarization ocean TB anomaly of all descending orbits on June 5th, 2014 over the Pacific Ocean, when using (a) the L1 VTEC and (b) the SMOS-derived VTEC; over the Indian Ocean, when using (c) the L1 VTEC and (d) the SMOS-derived VTEC. 170

Figure 6.39. Difference of the X-polarization ocean TB anomaly when using the SMOS-based VTEC and the L1 VTEC of all descending orbits on June 5th, 2014 over (a) the Pacific Ocean and (b) the Indian Ocean. 171

Figure 6.40. Y-polarization ocean TB anomaly of all descending orbits on June 5th, 2014 over the Pacific Ocean, when using (a) the L1 VTEC and (b) the SMOS-derived VTEC; over the Indian Ocean, when using (c) the L1 VTEC and (d) the SMOS-derived VTEC. 172

Figure 6.41. Difference of the Y-polarization ocean TB anomaly when using the SMOS-based VTEC and the L1 VTEC of all descending orbits on June 5th, 2014 over (a) the Pacific Ocean and (b) the Indian Ocean. 173

List of Tables

Table 2.1. Switching sequence of the MIRAS arms 28

Table 3.1. Coefficients for the translation of the IGS from 20000 km to 800 km of altitude 46

Table 3.2. Average antenna temperature (TA) and average noise receiver temperature (TR) at the antenna plane (typical values for open ocean). 56

List of Acronyms

A3TEC	**T**otal **E**lectron **C**ontent from third Stokes parameter at **A**ntenna level
AF-FoV	**A**lias **F**ree-**F**ield **o**f **V**iew
BEC	**B**arcelona **E**xpert **C**enter
CESBIO	**C**entre d'**E**tudes **S**patiales de la **BIO**sphère
CIMR	**C**opernicus **I**maging **M**icrowave **R**adiometer
CCU	**C**orrelation and **C**ontrol **U**nit
CMN	**C**ontrol and **M**onitoring **N**ode
CNES	**C**entre **N**ational d'**E**túdes **S**patiales
CODE	**C**enter of **O**rbit **D**etermination in **E**urope
CommSensLab	**Comm**unications and Remote **S**ensing **L**aboratory
CONAE	**C**omisión **N**acional de **A**ctividades **E**spaciales
CSIC	**C**onsejo **S**uperior de **I**nvestigaciones **C**ientíficas
DPGS	SMOS **D**ata **P**rocessing **G**round **S**egment
EAF	**E**xtended **A**lias **F**ree
EAF-FoV	**E**xtended **A**lias **F**ree-**F**ield **o**f **V**iew
EASE	**E**qual-**A**rea **S**calable **E**arth
ECMWF	**E**uropean **C**enter for **M**edium-Range **W**eather **F**orecasts
ESA	**E**uropean **S**pace **A**gency
ETOPO-5	**E**arth **TOPO**graphy-**5** minute

FAO	**F**ood and **A**griculture **O**rganization
FPI	**F**ormación de **P**ersonal **I**nvestigador
FR	**F**araday **R**otation
FRA	**F**araday **R**otation **A**ngle
FoV	**F**ield **o**f **V**iew
GMF	**G**eophysical **M**odel **F**unction
GNSS	**G**lobal **N**avigation **S**atellite **S**ystems
GPS	**G**lobal **P**ositioning **S**ystem
GTIM	**G**lobal **T**heoretical **I**onospheric **M**odel
***h*-pol**	**H**orizontal **p**olarization
IAGA	**I**nternational **A**ssociation of **G**eomagnetism and **A**eronomy
ICM	**I**nstitute of **M**arine **S**ciences
IGRF	**I**nternational **G**eomagnetic **R**eference **F**ield
IGS	**I**nternational **G**NSS **S**ervice
IONEX	**ION**osphere **EX**change format
IRI	**I**nternational **R**eference **I**onosphere
ISEA	**I**cosahedral **S**nyder **E**qual **A**rea
ISO	**I**nternational **O**rganization for **S**tandardization
ITU	**I**nternational **T**elecommunication **U**nion
JJA	**J**une, **J**uly, and **A**ugust
JPL	**J**et **P**ropulsion **L**aboratory
L1	SMOS **L**evel **1** data product

L1A	SMOS **L**evel **1A** data product
L1B	SMOS **L**evel **1B** data product
L1C	SMOS **L**evel **1C** data product
L1OP	**L1 O**perational **P**rocessor
lat	**Lat**itude
LICEF	**Li**ghtweight **C**ost-**E**ffective **F**ront-End
lon	**Lon**gitude
LT	**L**ocal **T**ime
MIRAS	**M**icrowave **I**maging **R**adiometer using **A**perture **S**ynthesis
MTS	**M**IRAS **T**esting **S**oftware
NASA	**N**ational **A**eronautics and **S**pace **A**dministration
NeQuick	**Ne**w **Quick**-run Ionospheric Electric
NH	**N**orthern **H**emisphere
NIR	**N**oise **I**njector **R**adiometer
OS	**O**cean **S**alinity
OTT	**O**cean **T**arget **T**ransformation
PIM	**P**arameterized **I**onospheric **M**odel
PMS	**P**ower **M**easurement **S**ystem
PSU	**P**ractical **S**alinity **U**nits
RFI	**R**adio **F**requency **I**nterference
RMSE	**R**oot **M**ean **S**quare **E**rror
SAC-D	**S**atélite de **A**plicaciones **C**ientíficas - **D**

SH	**S**outhern **H**emisphere
SM	**S**oil **M**oisture
SMAP	**S**oil **M**oisture **A**ctive **P**assive
SMOS	**S**oil **M**oisture and **O**cean **S**alinity
SMOS ESL	**S**oil **M**oisture and **O**cean **S**alinity **E**xpert **S**upport **L**aboratory
SSS	**S**ea **S**urface **S**alinity
SST	**S**ea **S**urface **T**emperature
STD	**ST**andard **D**eviation
TB	**B**rightness **T**emperature
TDIM	**T**ime **D**ependent **I**onospheric **M**odel
TEC	**T**otal **E**lectron **C**ontent
TECU	**TEC U**nit
UPC	**U**niversitat **P**olitècnica de **C**atalunya
UT	**U**niversal **T**ime
UTC	**U**niversal **T**ime **C**oordinated
***v*-pol**	**V**ertical **p**olarization
VTEC	**V**ertical **T**otal **E**lectron **C**ontent
WCOM	**W**ater **C**ycle **O**bservation **M**ission

List of Symbols

Latin Symbols

A_{eff}	Antenna Effective Area $[m^2]$
A_t	Effective Transmitted Area $[m^2]$
$A3$	T_3 over the Antenna Frame [Kelvin]
$\overline{\lvert b(f)\rvert^2}$	Spectral Power of a Signal Collected by an Antenna $[W/Hz]$
B	Brightness of a Gray Body $[W \cdot sr^{-1} \cdot m^{-2}]$
B_f	Spectral Brightness Density $[W \cdot sr^{-1} \cdot m^{-2} \cdot Hz^{-1}]$
B_k	Receiver Noise Equivalent Bandwidth of Receiver K [Hz]
B_0	Magnitude of the Geomagnetic Field [Teslas]
c	Speed of Light $[m \cdot s^{-1}]$
C_{hk}	Cross Polar Pattern of antenna k at Horizontal Polarization
C_{vk}	Cross Polar Pattern of antenna k at Vertical Polarization
d_1	Antenna Location [m]
d	Distance between Antennas [m]
e	Emissivity
E_v	Vertical Component of the Electric Field of the Electromagnetic Wave $[N \cdot C^{-1}]$
E_h	Horizontal Component of the Elect. Field of the Electromagnetic Wave $[N \cdot C^{-1}]$
f_0	Central Frequency [Hz]

f	Frequency [Hz]
F_n	Complex Normalized Field Antenna Pattern
F_t	Directional Distribution Function of the Source $[W \cdot sr^{-1}]$
G	G Matrix
G^+	Moore-Penrose Pseudo-inverse of G
G_k	Available Power Gain of Receiver k
G_S	Average Gain System of a Superheterodyne Receiver
h	Planck's Constant $(6.63 * 10^{-34}\ J \cdot s)$
H_k	Frequency Response of the Receiver k
I	First Stokes Parameter [Kelvin]
k	Boltzmann's Constant $(1.38 * 10^{-23}\ J/K)$
$\hat{L}_x$	Unitary Vector in X direction (Ludwing Definition)
$\hat{L}_y$	Unitary Vector in Y direction (Ludwing Definition)
N_v	Number of None Redundant Visibility Samples
OTT	Ocean Target Transformation [Kelvin]
P_r	Measured Power by the Receiving Antenna $[W]$
Q	Second Stokes Parameter [Kelvin]
Q_A	Second Stokes Parameter Measured by the Satellite Antenna [Kelvin]
R	Distance between Two Antennas [m]
R_{hk}	Reference Pattern of antenna k at Horizontal Polarization
R_{vk}	Reference Pattern of antenna k at Vertical Polarization
r_1	Distance from the source to an antenna [m]

$\tilde{r}_{kj}$ Fringe Washing Function

t Normalized Power Pattern

T Absolute Temperature [Kelvin]

T_A Antenna Temperature [Kelvin]

T_{AP} Apparent Temperature [Kelvin]

T_B Brightness Temperature [Kelvin]

T_B' Modified Brightness Temperature [Kelvin]

T_R Receiver Equivalent Noise Temperature [Kelvin]

T_{SC} Atmospheric Downward Radiation Reflected by the Earth's Surface [Kelvin]

T_{sys} System Output Temperature [Kelvin]

T_{UP} Atmospheric Upward Radiation [Kelvin]

T_h Brightness Temperature in the Horizontal Polarization [Kelvin]

T_v Brightness Temperature in the Vertical Polarization [Kelvin]

T_3 Third Stokes Parameter [Kelvin]

T_4 Four Stokes Parameter [Kelvin]

$Ta3$ Third Stokes Parameter measured at antenna frame [Kelvin]

Tav Brightness Temperature in the Vertical Polarization at Antenna Frame [Kelvin]

Tah Brightness Temperature in the Horizontal Pol. at Antenna Frame [Kelvin]

T_B^{hh} Brightness Temperature at Horizontal Polarization [Kelvin]

T_B^{vv} Brightness Temperature at Vertical Polarization [Kelvin]

T_B^{hv} Complex Brightness Temperature at Horizontal-Vertical Polarization [Kelvin]

T_B^{vh} Complex Brightness Temperature at Vertical-Horizontal Polarization [Kelvin]

T_B^{xx}	Brightness Temperature at X Polarization (Antenna Frame) [Kelvin]
T_B^{yy}	Brightness Temperature at Y Polarization (Antenna Frame) [Kelvin]
T_B^{xy}	Complex Brightness Temperature at X-Y Polarization (Antenna Frame) [Kelvin]
T_B^{yx}	Complex Brightness Temperature at Y-X Polarization (Antenna Frame) [Kelvin]
u	Antenna Spacing normalized to the Wavelength in x Direction
U	Third Stokes Parameter [Kelvin]
U_A	Third Stokes Parameter measured by the Satellite Antenna [Kelvin]
v	Antenna Spacing normalized to the Wavelength in y Direction
V	Four Stokes Parameter [Kelvin]
V_{12}	Visibility [Kelvin]
V_{kj}	Frequency Domain System Visibility [Kelvin]
V_{kj}^{hh}	Visibility between 2 Antennas both Receiving in h Polarization [Kelvin]
V_{kj}^{vv}	Visibility between 2 Antennas both Receiving in v Polarization [Kelvin]
V_{kj}^{vh}	Visibility between 2 Antennas Receiving in v and h Polarizations [Kelvin]
V_{kj}^{hv}	Visibility between 2 Antennas Receiving in h and v Polarizations [Kelvin]
VTEC	Vertical Total Electron Content [TECU]

Greek Symbols

α_w	Windowing Factor
Γ	Reflectivity
Δ	FRA Systematic Error Pattern [°]

Δf	Bandwidth of the Receiving System [Hz]
Δr	Distance between Antennas [m]
Δs	Elementary Area [m^2]
$\Delta \xi$	Minimum Distance in the Cosine Plane
$\Delta \Omega$	Solid Angle [sr]
$\Delta \Omega_r$	Solid Angle subtended by the Receiving Antenna [sr]
$\Delta \Omega_t$	Solid Angle of the Radiating Body [sr]
η	Director Cosine
θ	Incident Angle referred to Nadir [°]
Θ_B	Angle between the Magnetic Field and the Wave Propagation Direction [°]
λ	Wavelenght [m]
ξ	Director Cosine
σ	Standard Deviation
τ	Integration Time [s]
φ	Geometrical Rotation [°]
ϕ	Azimut Angle referred to Nadir [°]
Ψ	Rotation Angle including both the Geometric and Faraday Rotation Angles [°]
Ω	Rotation Angle including both the Geometric and Faraday Rotation Angles [°]
Ω_a	Antenna Equivalent Solid Angle [sr]
Ω_f	Faraday Rotation Angle [°]
Ω_f^m	Measured Faraday Rotation Angle [°]

Chapter 1

Introduction

1.1. Motivation

In the last decade, a new generation of L-band satellites was launched to measure frequently and globally geophysical variables that allow improving the knowledge of the water cycle and the meteorological modeling. The first one was launched in November 2009, the ESA (European Space Agency) Soil Moisture and Ocean Salinity (SMOS) mission devoted to observing soil moisture over the Earth's landmasses and salinity over the oceans on a global and frequent scale. Its payload MIRAS (Microwave Imaging Radiometer) has been orbiting for more than twelve years, measuring the Earth's brightness temperature in the L-band, and it is still doing it with great quality. A variety of applications have been developed using its measurements such as a better meteorological modelling, hydrological modelling, plant growth monitoring, modelling forest decline, prediction of meteorology disasters and fires, the thermohaline circulation, estimation of the absorption of CO_2, measurements of the thin ice floating, and so on (ESA, 2019), (Mecklenburg et al., 2016).

In radiometric measurements from space, as microwave radiation from the Earth propagates through the ionosphere, the electromagnetic field components are rotated an angle that is called Faraday rotation. It depends on different variables: the Total ionospheric Electron Content (TEC), the geomagnetic field, the frequency, and the viewing angle. At L-band or lower bands, Faraday rotation is not negligible and must be corrected for obtaining accurate geophysical retrievals from these satellite measurements. The FRA can be calculated using a classical formulation (Le Vine & Abraham, 2002) that makes use of the Vertical Total Electron Content (VTEC) and geomagnetic field data provided by external sources.

Alternatively, Faraday rotation can be continuously retrieved from SMOS radiometric data. This is possible by using the full-polarization mode of MIRAS and thanks to the improvements done in the image reconstruction in the last years, particularly in the third and fourth Stokes parameters (Lin, 2014). However, estimating Faraday rotation from SMOS measurements is not a straightforward process due to the presence of spatial errors in the SMOS images, image reconstruction artifacts, and antenna uncertainties (Corbella et al., 2013), which makes it difficult to do it with the appropriate accuracy (Corbella et al., 2015).

The possibility of measuring the Faraday rotation from radiometric data opens the door to estimating the total electron content of the ionosphere by using an inversion procedure from this measured Faraday rotation angle. Besides, this leads to the possibility of creating a TEC product derived from SMOS radiometric data. Eventually, this product could then be re-used in the SMOS level 2 processors to improve the geophysical retrievals.

In this context, this research is focused on the proposal of a novel methodology that can derive VTEC maps from the SMOS radiometric data over its entire Field of View (FoV), which could be used to correct the Faraday rotation in the polarization of the electromagnetic field radiated by the Earth. The rationale is that the methodology does not depend on any external VTEC databases or models, and that works independently on the target measured by the instrument. The main challenges to deal with are to get accurate TEC data over land zones, especially those strongly contaminated by Radio-Frequency Interferences (RFI) since the quality of the brightness temperatures is degraded. Also, regions covered by dense forests are challenging, since the electric field at horizontal and vertical polarizations have similar strength, making the TEC retrieval highly ill-conditioned. Also, since Faraday rotation vanishes when the geomagnetic field is aligned with the signal path, there are some areas of the Earth where TEC retrieval will simply not be possible.

1.2. Context of the Thesis

The research of this Ph.D. thesis has been carried out as part of the Passive Microwave Remote Sensing Antennas Group, which belongs to the Specific Center for Research in Communications and Remote Sensing Laboratory (CommSensLab) of the *Universitat Politècnica de Catalunya (UPC)*. This group has been involved in the SMOS mission since its proposal in 1993, mainly proving theoretical support to the conception and construction of its payload MIRAS. This research group has also participated in SMOS/MIRAS payload ground characterization tests that took place in Maxwell anechoic chamber (Corbella et al., 2009), at ESA premises on spring 2007, and in the SMOS in orbit commissioning phase after launch in November 2009 (Corbella et al., 2011). An important contribution that this research group has done is the development of a software tool to analyze SMOS data in near real time, called MTS (MIRAS Testing Software), which reads the raw data sent by the MIRAS X-band transmitter and automatically computes a number of data products including levels 1A (calibrated visibilities) and 1B (brightness temperature maps at antenna plane) (Corbella et al., 2008). Moreover, the UPC has also worked in development and improvements of calibration and image reconstruction algorithms such as the mitigation of both the land-sea contamination and spatial bias, the improvements in full-polarization image reconstruction, the enhancement of the stability and absolute accuracy, among others.

The research of this thesis has also been done jointly with the Barcelona Expert Center (BEC), which was founded in 20007, in the Institute of Marine Sciences (ICM) of the Spanish Research Council (*Consejo Superior de Actividades Científicas*, CSIC). Its main purpose has

been to provide assessment to ESA as a Level 2 Ocean Salinity Expert Support Laboratory, to contribute to SMOS radiometric calibration and validation activities, to develop algorithms for the generation of added-value products at Level 3 and 4. In this context, the outcomes and VTEC products obtained in this thesis have been proved in the usual metrics over the ocean (Oliva & ESA team, 2015).

Most of the research of this thesis has been carried out in the framework of the following projects and contracts:

- 2016-2017: "SMOS enhanced performance and future missions". Programa estatal de investigación, desarrollo e innovación orientada a los retos de la sociedad, TEC2014-58582-R, with an FPI grant (*Formación de Personal Investigador*).
- 2018-2021: "SMOS and follow-on missions improved Level 1 performance". Programa estatal de investigación, desarrollo e innovación orientada a los retos de la sociedad, TEC2017-88850-R
- 2020-2024: "SMOS Expert Support Laboratory for SMOS Level 1 and Level 2 over Land, Ocean and Ice", SMOS ESL (c-11806) European Space Agency, subcontractor of DEIMOS ENGENHARIA, SA

In the context of the last contract, all the research and main outcomes have been presented at the regular SMOS Payload Calibration meetings, as part of the contribution of the UPC and BEC as Expert Support Laboratories of Level 1, particularly related to Task 1.6 "Development of new SMOS products: Ionospheric Total Electron Content".

1.3. Objectives

The main objectives of this Ph.D. thesis, as already outlined, are the following:

- To develop a methodology capable of retrieving VTEC maps directly from SMOS radiometric data.
- To demonstrate the feasibility of reingesting these SMOS-derived VTEC maps by the SMOS Level 2 processors to correct the Faraday Rotation (FR) effect in the SMOS mission when retrieving geophysical variables.
- To analyze the impact of this correction in the geophysical retrievals, mainly focused over the ocean, where the impact of ionospheric corrections is stronger.

These main objectives have led to the following more specific activities:

- To analyze the Faraday rotation effect and its temporal and geographical variability within the years of the SMOS mission.
- To study the existing VTEC datasets, especially the ones that have been used in the mission. This gives the possibility to compare the obtained results of the

novel methodology presented in this thesis with other sources and to perform an analysis of its added value and limitations.

- To develop a simulator to trim and assess the performance of several Faraday Rotation Angle (FRA) retrieval approaches to derive SMOS VTEC maps and to correct the FRA.
- To analyze systematic error patterns that could emerge in the retrieval of both the FRA and the VTEC and to develop their corrections to obtain the most accurate results in the recovered maps.
- To assess the VTEC performance in terms of temporal and geophysical variability throughout the mission and the main added value and limitations of this product.
- To analyze the impact of using the SMOS-derived VTEC maps when correcting the Faraday rotation angle in the brightness temperature quality along the mission.

1.4. Thesis Outline

This Ph.D. thesis is organized in seven chapters as follows:

Chapter 1 describes the motivation of the research, justifies its scientific and technological interest within the SMOS mission as well as the context in which the thesis has been developed.

Chapter 2 defines the theoretical framework needed to understand the concepts that have been researched. It is divided into different parts: microwave radiometry fundamentals, microwave radiometry for Earth observation, description of the SMOS mission, and finally a deep explanation of the SMOS payload called MIRAS.

Chapter 3 is devoted to explaining in detail the Faraday rotation angle and the total electron content fundamentals, including an analysis of their temporal and geographical variability. The state-of-the-art of VTEC datasets and models are explained. Finally, the SMOS FRA End-to-end simulator that has been developed to assess the different approaches for the retrieval is presented.

Chapter 4 explains the methodology developed to retrieve VTEC maps from SMOS radiometric data over any kind of surfaces (ocean, land and ice) and how they are used to correct Faraday rotation. Results are shown, first, using simulated data, and then, with SMOS radiometric data.

Chapter 5 studies the presence of an FRA systematic error and proposes a correction of it. Final results of the VTEC and FRA retrievals over any kind of surfaces (ocean, land, and ice) using SMOS radiometric data are shown.

Chapter 6 shows the assessments of the SMOS-derived VTEC maps with its geophysical and temporal variation. Subsequently, the impact of using the SMOS-derived VTEC maps in the mission over ocean is studied. It is done in two analyses in the brightness temperature –its bias and stability–, and also the impact in the global maps of ocean anomaly (the magnitude from which the salinity is retrieved).

Chapter 7 summarizes the main conclusions as well as the original contributions of this work. Future lines of research are also outlined.

Chapter 2

Theoretical Framework

A blackbody is an ideal body that entirely absorbs and radiates all the power impinging on it regardless of its frequency, direction, or polarization. However, real bodies do not radiate it all. Microwave radiometry is the science of the electromagnetic radiation measurement emitted by the bodies at a physical temperature.

2.1. Microwave Radiometry Fundamentals

2.1.1. Thermal Microwave Radiation

The power emitted by a body in a given direction (θ, ϕ) at a solid angle per unit area $[W \cdot sr^{-1} \cdot m^{-2}]$ is called Brightness $B(\theta, \phi)$. The definition of Brightness for an extended source of incoherent radiation with a determined pattern is (Ulaby et al., 1981):

$$B(\theta, \phi) = \frac{F_t(\theta, \phi)}{A_t} \tag{2.1}$$

where $F_t(\theta, \phi)$ is the directional distribution function $[W \cdot sr^{-1}]$ of the source and A_t $[m^2]$ is the effective radiating area. Considering the case of two lossless antennas separated a distance R, oriented in the direction of maximum directivity with an effective area A_t $[m^2]$ for the transmitting antenna and A_r $[m^2]$ for the receiving antenna, being R large enough to be considered a constant power over a solid angle $\Delta\Omega(sr)$, then the measured power by the receiving antenna is described by:

$$P_r = B \cdot A_t \cdot \Delta\Omega_r \tag{2.2}$$

where P_r is the power measured by the receiving antenna. The solid angle subtended by the receiving antenna $\Delta\Omega_r$ when observed by the transmitting antenna is:

$$\Delta\Omega_r = \frac{A_r}{R^2} \tag{2.3}$$

The solid angle of the radiating body (transmitter) as seen from the receiving antenna can also be expressed as:

$$\Delta\Omega_t = \frac{A_t}{R^2} \tag{2.4}$$

Then the power measured by the receiver antenna is usually expressed as:

$$P_r = B \cdot A_r \cdot \Delta\Omega_t \tag{2.5}$$

And the spectral power density S $[W \cdot m^{-2} \cdot Hz^{-1}]$ is defined as:

$$S = \frac{P_r}{A_r} = B \cdot \Delta\Omega \tag{2.6}$$

as shown in Fig. 2.1.

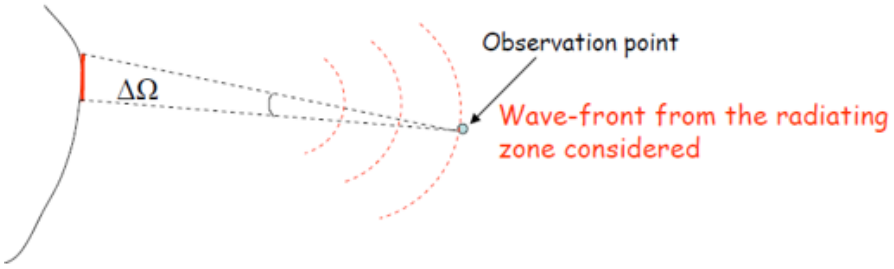

Figure 2.1. Spectral power density from an observation point.

Now, in general the brightness seen by the receiving antenna is written as $B(\theta, \phi)$ since it is not constant in the different directions (θ, ϕ) defined in the receiving antenna frame. Moreover, if the brightness is not constant with frequency, it is defined as the spectral brightness density $B_f(\theta, \phi)$ $[W \cdot sr^{-1} \cdot m^{-2} \cdot Hz^{-1}]$. Therefore, the total power measured by the receiving antenna can be obtained by integrating the expression in bandwidth and space as:

$$P = \frac{1}{2} A_r \int_f^{f+\Delta f} \iint_{4\pi} B_f(\theta, \phi) \cdot |F_n(\theta, \phi)|^2 d\Omega \mathrm{df} \tag{2.7}$$

where $F_n(\theta, \phi)$ is the complex normalized field antenna pattern. The term ½ takes into account that the antenna presents a determined polarization and only half of the thermal emitted power is measured if the source emission is randomly polarized. The bandwidth of the receiving system is given by Δf.

A blackbody absorbs all incoming radiation; there is no reflection. In thermal equilibrium, the absorbed incident power is re-emitted. Its radiation is defined by Planck's radiation law (Planck, 1901) as a function of the frequency (f) in Hertz and the absolute temperature (T) in Kelvin expressed in Eq. (2.8):

$$B_f(f,T) = \frac{2hf^3}{c^2}\left(\frac{1}{e^{hf/kT} - 1}\right) \tag{2.8}$$

In the previous expression h corresponds to the Planck's constant ($6.63 * 10^{-34}\ J \cdot s$); c, to the speed of light and k, to the Boltzmann's constant ($1.38 * 10^{-23}\ J/K$).

At microwave frequencies ($f \leq 117\ GHz$), the term $hf/kT \ll 1$ and then Eq. (2.8) can be approximated to Eq. (2.9) which is called the Rayleigh-Jeans law:

$$B_f(f,T) \approx \frac{2kf^2T}{c^2} = \frac{2kT}{\lambda^2} \tag{2.9}$$

Figure 2.2 shows in blue Planck's radiation law and in red, the Rayleigh-Jeans law of the spectral brightness density at 300 K versus frequency.

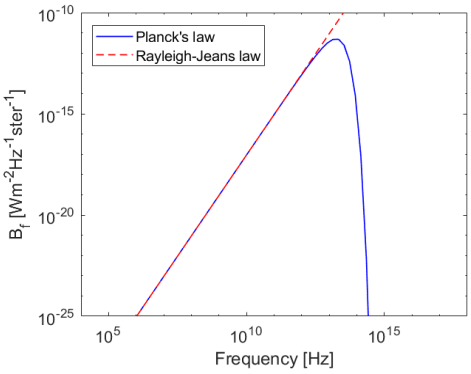

Figure 2.2. Planck's radiation law and its approximation for microwave frequencies (Rayleigh-Jeans law), considering physical temperature T=300 K.

Real bodies radiate less power than blackbodies. They do not absorb all the incident power; a part is reflected, the other part is absorbed and then, re-emitted. Its brightness at a certain direction (θ, ϕ) is described by:

$$B_f(\theta,\phi) = \frac{2k}{\lambda^2} T_B(\theta,\phi) \tag{2.10}$$

where T_B corresponds to the so-called brightness temperature (units of Kelvin) which is the temperature that a blackbody should have to emit that brightness.

The brightness of a material relative to the brightness of a blackbody at the same physical temperature T is defined as the emissivity (Emery & Camps, 2017):

$$e(\theta,\phi) = \frac{B_f(\theta,\phi)}{B_{f\ blackbody}} = \frac{T_B(\theta,\phi)}{T} \tag{2.11}$$

The emissivity is always $0 \leq e \leq 1$. For a perfect reflecting material, i.e. a lossless conductor, the emissivity is zero; for a perfect absorber, i.e. a blackbody, the emissivity is equal to one. The relationship between a body emissivity coefficient e at a certain direction (θ,ϕ) and its reflectivity Γ is $e(\theta,\phi) = 1 - \Gamma(\theta,\phi)$.

The emissivity depends on the electrical properties of the body. When measured, two other parameters affect its value: the angle of observation and the polarization of the measurement. *Figure 2.3* shows the emissivity and reflectivity with respect to the incidence angles of flat surfaces with different electrical properties However, natural surfaces do not have that specific behavior; they are much more complex.

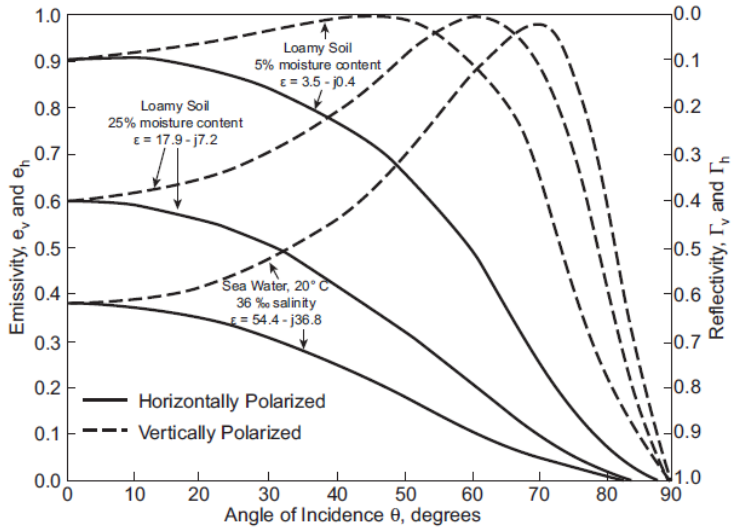

Figure 2.3. Emissivity (left axis) and reflectivity (right axis) for flat surfaces with different dielectric constants in the horizontal (solid line) and vertical (dashed line) polarization (figure 4.21 from Ulaby et al., 1981).

2.1.2. Power Collected by an Antenna

The spectral power $\overline{|b(f)|^2}$ $[W/Hz]$ of a signal collected by an antenna can be computed as:

$$\overline{|b(f)|^2} = \frac{1}{2}\iint_{4\pi} B_f(\theta,\phi)\cdot A_{eff}(\theta,\phi)\, d\Omega = k\iint_{4\pi} T_{AP}(\theta,\phi)\cdot\frac{A_{eff}(\theta,\phi)}{\lambda^2}\, d\Omega \tag{2.12}$$

It depends on parameters of the antenna such as its effective area A_{eff}, the apparent temperature $T_{AP}(\theta,\phi)$, which is equivalent to the addition of all the contributions from the elementary emitters and the wavelength at which the antenna is measuring (λ).

The antenna effective area A_{eff} is the ratio of the collected power in reception to the incoming power density:

$$A_{eff} = \lambda^2/\Omega_a \tag{2.13}$$

where Ω_a is the antenna equivalent solid angle and can be computed as the integral of the power pattern in the whole space:

$$\Omega_a = \iint_{4\pi} t(\theta,\phi)d\Omega \tag{2.14}$$

and $t(\theta,\phi)$, corresponds to the normalized power pattern, i.e. the power radiated in a given direction relative to the maximum.

2.2. Microwave Radiometry for Earth Observation

When the Earth's surface or the atmosphere wants to be explored, the microwave frequency range (1 GHz to 100 GHz) is frequently used with an antenna pointing to Earth onboard a satellite. Different variables can be retrieved from microwave radiometry measurements, such as the soil moisture and ocean salinity. By studying them, many applications can be onboard developed: better weather predictions, modeling the seasonal climate to benefit the climate-sensitive activities, including water management, agriculture, detection of risk of fires and floods, among others.

2.2.1. Power Collected by an Antenna Pointing to the Earth

When pointing to the Earth, the contributions of different sources are measured by the antenna. They are shown in Figure 2.4. It can be said that the apparent temperature T_{AP} is

the addition of three terms: the terrain emission (land or sea) attenuated by the atmosphere (T_B) which is the major contribution, the atmospheric downward radiation reflected by the Earth's surface (T_{SC}), and the atmospheric upward radiation (T_{UP}).

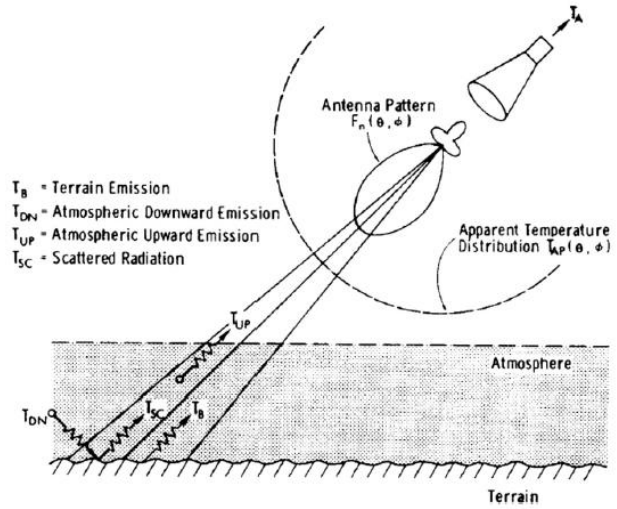

Figure 2.4. Relationship between the antenna temperature, the apparent temperature and the brightness temperature (Figure 4.8 from Ulaby et al., 1981).

Radiometers measure the Earth brightness temperature at different frequencies and polarizations. The range of frequencies to use depends on the sensitivity of the geophysical parameter with respect to the frequency and the atmosphere opacity. In the case of the low microwave frequency range (1 to 10 GHz), the atmosphere can be considered lossless and therefore, the main contribution is the emission from the terrain. For this reason, Eq. (2.12) can be approximated to:

$$\overline{|b(f)|^2} = k \iint_{4\pi} T_B(\theta,\phi) \cdot \frac{A_{eff}(\theta,\phi)}{\lambda^2}\, d\Omega = k \cdot T_A \tag{2.15}$$

where T_A is called antenna temperature (in Kelvin), i.e. the brightness temperature captured by the antenna, and it is expressed as follows:

$$T_A = \frac{1}{\Omega_a} \iint_{4\pi} T_B(\theta,\phi) \cdot t(\theta,\phi)\; d\Omega \approx T_B(\theta_0,\phi_0) \tag{2.16}$$

Eq. (2.16) assumes the fundamental relation:

$$\frac{A_{eff}(\theta,\phi)}{\lambda^2} = \frac{t(\theta,\phi)}{\Omega_a} \tag{2.17}$$

When an extended source –in this case, the Earth– is pointed by a narrow beam-width antenna, the antenna temperature (T_A) equals the brightness temperature of the pointed spot ($T_B(\theta_0, \phi_0)$) by the antenna boresight. It is independent of the distance antenna-source. (Gonzalez-Gambau, 2012).

2.2.2. Microwave Radiometers

Microwave radiometers are very sensitive instruments working in the microwave frequency range that measure the brightness temperature emitted by the Earth. The different types of radiometers are described in this section.

2.2.2.1. Real Aperture Radiometer

The simplest real aperture radiometer is the total power radiometer. It measures at the particular pixel being pointed by the antenna beam (Fig. 2.5). The antenna footprint determines the spatial resolution (pixel size), which is given by the antenna size. The resolution in x and y are defined as follows, where $\Delta\theta_{-3db}$ corresponds to the antenna half-power beam width ($\Delta\theta_{-3db} \approx \lambda/\emptyset$; being $\emptyset$ the maximum antenna size); r, to the distance from the radiometer to the target; and θ_i, to the incidence angle.

$$\Delta x = r \cdot \Delta\theta_{-3db} \tag{2.18}$$

$$\Delta x = r \cdot \frac{\Delta\theta_{-3db}}{\cos\theta_i} \tag{2.19}$$

The system consists on an antenna connected to a superheterodyne receiver, followed by a power detector and a low-pass filter. Eq. (2.20) gives the average output voltage of the system, where G_S corresponds to the average gain system; T_A, to the antenna temperature; T_R, to the receiver equivalent noise temperature; and T_{sys}, to the system output.

$$V = G_S \cdot (T_A + T_R) = G_S \cdot T_{sys} \tag{2.20}$$

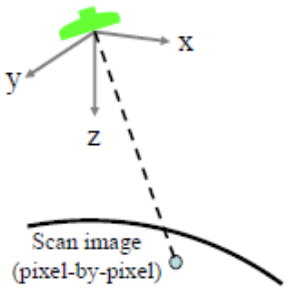

Figure 2.5. Real aperture radiometer

Maps of brightness temperature are obtained by either using multiple beams or scanning configurations such as conical scan, across-track scan, or bush-broom schemes as shown in Figure 2.6.

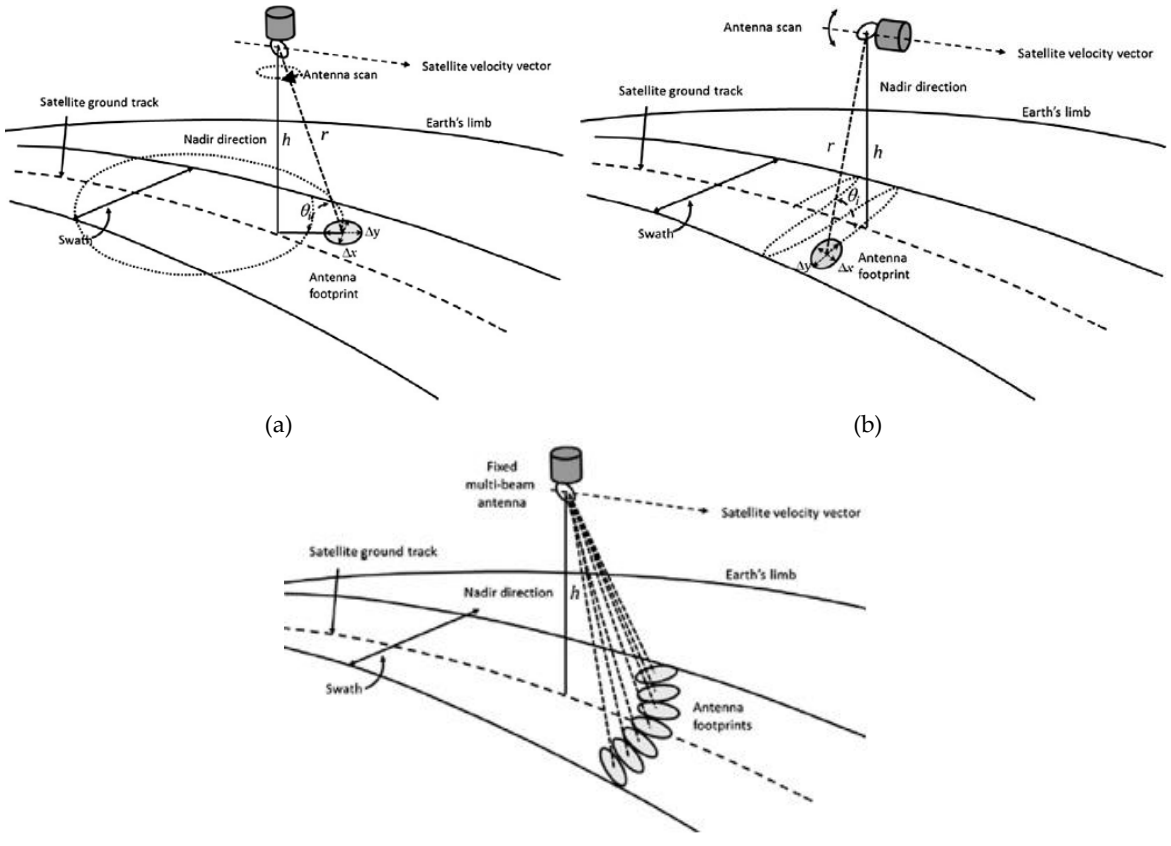

Figure 2.6. Scanning configurations (figure 4.69 from Emery & Camps, 2017): (a) conical scan, (b) cross-track scan, and (c) push-broom schemes.

2.2.2.2. Interferometric Radiometer with Aperture Synthesis

This type of radiometer is composed of an array of antennas (Fig. 2.7). Unlike real aperture radiometers, synthetic aperture radiometers do not measure directly the brightness temperature image but the visibility samples, that is, the cross-correlation between the signals collected by many pairs of antennas located at different relative distances (explained more deeply in section 2.5.). Using image inversion algorithms, the image per scene is reconstructed to obtain brightness temperature worldwide maps. No antenna motion is required but much more data processing is needed. Its spatial resolution depends on the distance between antennas.

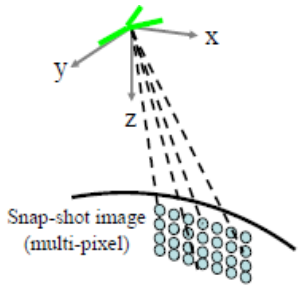

Figure 2.7. Interferometric radiometer

2.3. The SMOS Mission

The SMOS mission launched on November 2, 2009, is the second Earth Explorer mission in the ESA's Living Planet Program. It was designed with an extended lifetime of 5 years with the main objective of improving our understanding of the Earth's water cycle, proving much-needed data for the weather and climate modelling and predictions; and also, providing information on root zone soil moisture, vegetation, and biomass, and to contribute in the research on the cryosphere (Drinkwater et al., 2009). All this is possible because it observes two key geophysical variables for our planet: Soil Moisture (SM) over land and Ocean Salinity (OS) –hence its name, SMOS–, being the first satellite up to its launching to provide maps of both variables at a global scale and with the adequate accuracy, sensitivity, spatial resolution and temporal coverage for global climate applications (Silvestrin et al., 2001).

SM and OS are key parameters related to the Earth's water cycle (Fig. 2.8). SM and its spatio-temporal variations are key variables in the hydrological cycle and vegetation monitoring. The water and energy fluxes at the Earth's surface-atmospheric boundary are strongly dependent on it. It drives the evaporation, infiltration, percentage of rainfall running on the surface (runoff), and the vegetation uptake water. On the other hand, the OS is a key variable for ocean circulation characterization and an important tracer of water masses circulation. Therefore, the characterization of the Sea Surface Salinity (SSS) and its

seasonal and interannual variability constraints the water cycle on the coupled ocean-atmosphere models (Barre et al., 2008). SSS varies with the evaporation/precipitation and the freezing/melting in ice polar regions affecting the ocean circulation.

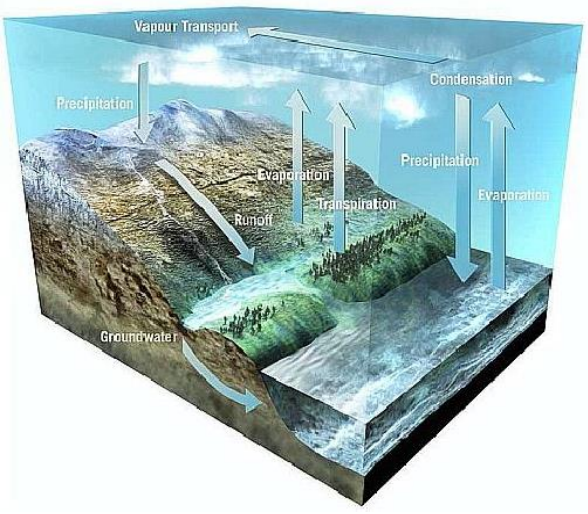

Figure 2.8. Earth's water cycle (credits: ESA Centre National d'Etúdes Spatiales, CNES)

At microwave frequencies, the emissivity of land and oceans are strong functions of the soil moisture and sea surface salinity, respectively. Consequently, by measuring the Earth's surface brightness temperature, which in this case would equal the effective emitting temperature of the surface modified by the emissivity (Y. H. Kerr et al., 2010), the main objective of the SMOS mission can be achieved: producing SM and SSS global maps.

In the low microwave frequency range, L-band, the measurements are not much affected by the atmosphere and clouds, i.e. low attenuation. The soil emission at that band is from typically top 5 cm, taking into account that vegetation is transparent up to a density typically of 5 kg/m^2. Additionally, this band is protected for Earth exploration and research, avoiding unwanted man-made emissions and radio frequency interferences (RFI), even if it is not fully respected. However, there is an important drawback in this band though; the antenna diameter is proportional to the spatial resolution, and to accomplish the SMOS requirements, 50 km of spatial resolution, and an antenna with a diameter of several meters is needed, which implies a significant technical challenge. Additionally, to accomplish the global coverage of the earth within three days for the SM requirements, a large instrument swath is required (1000 km).

To overcome this drawback and to fulfill the desired scientific requirements, MIRAS, the unique SMOS's payload, is a two-dimensional synthetic aperture radiometer operating at the L-band (1.4135 GHz). The satellite is in a low-Earth polar Sun-synchronous orbit with local solar times of 6.00 a.m. and 6.00 p.m. at the equator crossing (dawn-dusk orbit) –orbit

characterizations that improves the mission performance, principally due to stable thermal conditions– at a mean altitude of 758 km (Silvestrin et al., 2001). The instrument has a constant forward tilt angle of 32.5° between the instrument boresight and the local nadir in the flight direction giving it multiangular capabilities with an angular coverage up to 65° depending on the position within the field of view (FoV).

SMOS scientific requirements for soil moisture imply providing global maps within 3 days with a spatial resolution of 50 km and an accuracy of 4% volumetric humidity ($0.04\ m^3/m^3$); and for SSS, a spatial resolution of 100 km and an accuracy of 0.1 psu (practical salinity units) every 30 days. The system was designed with a life-time of five years (Kerr et al., 2010), but it has been able to operate successfully for more than twelve years today.

ESA distributes to the scientific community the SMOS products through the SMOS Data Processing Ground Segment (DPGS). They are in charge of data acquisition, processing and storing the SMOS scientific data up to level 2 and associated data generated in-orbit. The different products are:

- Raw data: observation data and telemetry as received from the satellite
- Level 0: unprocessed data containing the Earth Explored headers
- Level 1: there are the level 1A (L1A), the level 1B (L1B), and the level 1C (L1C). The first one corresponds to the calibrated visibilities, i.e., the output of the correlations between the different pairs of antennas; the second one, to the Fourier components of brightness temperature at the antenna polarization reference frame in the measured instants; and the last one, to the brightness temperatures geolocated at the top of the atmosphere in an Icosahedral Snyder Equal Area projection grid system ISEA 4H9.
- Level 2: Soil Moisture and Ocean Salinity swath-based maps.

After so many years of operation, more applications have been developed. Some of them are: daily sea ice thickness estimations, severe wind speeds/storm tracking, drought index, forest height and biomass, the freeze and thaw state of soil, vegetation phenology, river discharge predictions, among others (Kerr et al., 2016) (Mecklenburg et al., 2016).

2.4. MIRAS, the SMOS Payload

As mentioned earlier, MIRAS is a two-dimensional synthetic aperture radiometer operating at the L band. It has a Y shape, i.e. three arms of 8 m diameter equally spaced with an angular separation of 120° which are connected to a central structure called hub. Every arm is composed of three segments, each one having six equally spaced receivers, which are known as Lightweight Cost-Effective Front-Ends (LICEFs). The arms are complemented with four other LICEFs in the central hub, where there are also three Noise Injection

Radiometers (NIRs) that are included for calibration purposes. Each NIR consists of two receivers coupled to a single antenna. Therefore, MIRAS (Fig. 2.9) comprises 69 antennas – for the 66 LICEFs and 3 NIRs– but 72 receivers – 66 LICEFs and 6 for the NIRs– (McMullan et al., 2008).

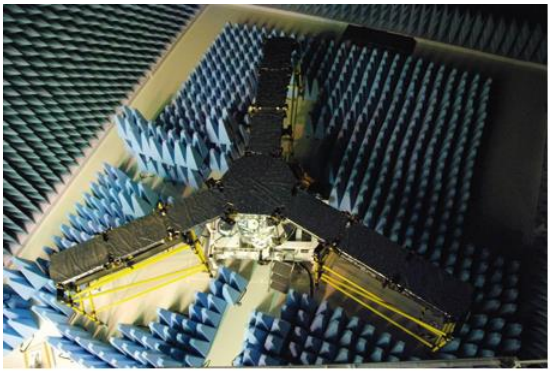

Figure 2.9. MIRAS at Maxwell anechoic chamber during Image Validation Tests at ESTEC facilities.

LICEFs and NIRs measure the antenna radiometric temperature. This represents the radiation noise power delivered by the antenna to the receivers, which corresponds to the brightness temperature of the scene. A LICEF unit consists of a radiometric receiver integrated with a dual polarization antenna that allows full polarimetric capabilities. They generate 1-bit digital signals corresponding to the sign of the in-phase and quadrature components of the received noise signal. This information per LICEF is transmitted to the Correlation and Control Unit (CCU) that is in the central structure. On the other hand, every LICEF has a Power Measurement System (PMS) that provides the amplitude of the measured noise signal to the Control and Monitoring Node (CMN), where the information is digitalized and then passed to the CCU. The CCU is in charge of generating and storing source packets (telemetry) with information coming from the LICEF units, NIRs and CMNs every integration time. This content is downloaded through an X-band channel when a ground contact is established. In order to support the calibration procedure, the NIRs provide an accurate measurement of the average brightness temperature scene and also act as reference radiometers to calibrate the PMS of each receiver (Colliander et al., 2007).

2.5. MIRAS Operating Fundamentals

As it was previously mentioned, MIRAS operating principle is based on 2D interferometric aperture synthesis. This consists of cross-correlating the power density, i.e. antenna temperature, collected by every pair of antennas $b_1(f)$ and $b_2(f)$:

$$\overline{|b_1(f)|^2} = kT_{A_1} \quad \overline{|b_2(f)|^2} = kT_{A_2} \tag{2.21}$$

as it is shown in Figure 2.10.

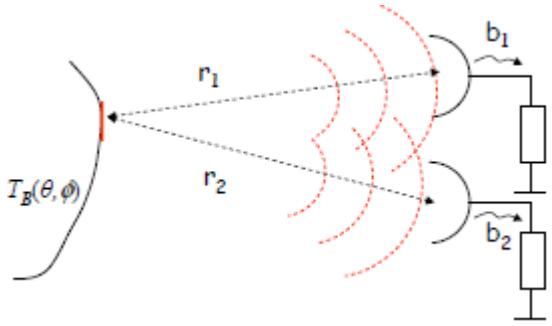

Figure 2.10. MIRAS operating principle

By doing so, the cross-power spectral density, or the so-called visibility (unit of Kelvin), is obtained:

$$\overline{b_1(f)b_2^*(f)} = kV_{12} \tag{2.22}$$

In terms of the antenna parameters, the visibility can be expressed as:

$$V_{12} = \frac{1}{\sqrt{\Omega_1\Omega_2}} \iint_{4\pi} T_B(\theta,\phi)F_{n1}(\theta,\phi)F_{n2}^*(\theta,\phi)e^{-jk(r_1-r_2)}\,d\Omega \tag{2.23}$$

where Ω corresponds to the solid angle; $F_{n1}(\theta,\phi)$ and $F_{n2}(\theta,\phi)$, to the normalized field patterns; and the term $k(r_1 - r_2)$, to the phase difference between the measured signals. Normally, Eq. (2.23) is expressed in terms of both (u,v), which is the antenna spacing normalized to the wavelength; and (ξ,η), which corresponds to the director cosines. Figure 2.11 illustrates the position of an antenna with respect to a distant source point.

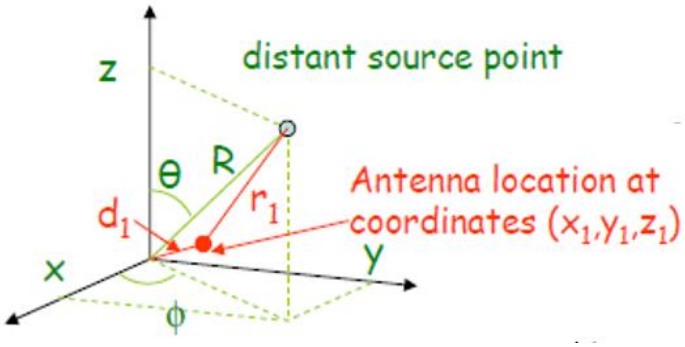

Figure 2.11. Position of an antenna with respect to a distant source point

In the case of the Earth observation, R is much larger than d_1, so r_1 can be expressed as:

$$r_1 \approx R + \frac{d_1^2}{2R} - \left(\frac{x}{R}x_1 + \frac{y}{R}y_1 + \frac{z}{R}z_1\right) \tag{2.24}$$

The director cosines are defined as:

$$\xi = \frac{x}{R} = \sin\theta\cos\phi \qquad \eta = \frac{y}{R} = \sin\theta\sin\phi \tag{2.25}$$

For two close antennas in the $x-y$ plane:

$$r_2 - r_1 \approx -[\xi(x_2 - x_1) + \eta(y_2 - y_1)] \tag{2.26}$$

with a phase difference of:

$$-k(r_2 - r_1) \approx -2\pi(\xi u + \eta v) \tag{2.27}$$

and the antenna normalized spacing is defined as:

$$u = \frac{x_2 - x_1}{\lambda} \qquad v = \frac{y_2 - y_1}{\lambda} \tag{2.28}$$

By using these terms, the visibility from Eq. (2.23) can be expressed as:

$$V_{12}(u,v) = \frac{1}{\sqrt{\Omega_1\Omega_2}} \iint\limits_{\xi^2+\eta^2\leq 1} \frac{T_B(\xi,\eta)}{\sqrt{1-\xi^2-\eta^2}} F_{n1}(\xi,\eta)F_{n2}^*(\xi,\eta)e^{-j2\pi(u\xi+v\eta)}\,d\xi\,d\eta \tag{2.29}$$

where $d\Omega = \sin\theta\,d\theta\,d\phi = \frac{d\xi\,d\eta}{\sqrt{1-\xi^2-\eta^2}}$.

A new term is defined for simplicity, which is called the modified brightness temperature T_B':

$$T_B'(\xi,\eta) = \frac{T_B(\xi,\eta)F_{n1}(\xi,\eta)F_{n2}^*(\xi,\eta)}{\sqrt{\Omega_1\Omega_2}\sqrt{1-\xi^2-\eta^2}} \tag{2.30}$$

For identical antennas and using Eq. (2.29)–this time in terms of the director cosines, $t(\xi,\eta) = |F_n(\xi,\eta)|^2$–, the visibility can also be expressed as follows:

$$V(u,v) = \iint\limits_{\xi^2+\eta^2\leq 1} \frac{T_B(\xi,\eta)t(\xi,\eta)}{\Omega_a\sqrt{1-\xi^2-\eta^2}} e^{-j2\pi(u\xi+v\eta)}\, d\xi\, d\eta \tag{2.31}$$

where $t(\theta,\phi)$ is the normalized power pattern of an antenna:

$$t(\theta,\phi) = |F_n(\theta,\phi)|^2 \tag{2.32}$$

Then the modified brightness temperature T_B' is expressed as:

$$T_B'(\xi,\eta) = \frac{T_B(\xi,\eta)t(\xi,\eta)}{\Omega_a\sqrt{1-\xi^2-\eta^2}} \tag{2.33}$$

and Eq. (2.31) yields:

$$V(u,v) = \iint\limits_{\xi^2+\eta^2\leq 1} T_B'(\xi,\eta)\cdot e^{-j2\pi(u\xi+v\eta)}\, d\xi\, d\eta \tag{2.34}$$

According with Eq. (2.22) and Eq. (2.23), the cross power spectral density of a pair of antennas inside an anechoic chamber at constant temperature T is:

$$\overline{b_1(f)b_2^*(f)} = kV_{12} = \frac{kT}{\sqrt{\Omega_1\Omega_2}} \iint\limits_{4\pi} F_{n1}(\theta,\phi)F_{n2}^*(\theta,\phi)e^{-jk(r_1-r_2)}\, d\Omega \tag{2.35}$$

V_{12} is apparently non-zero and antenna dependent but it should be zero by Bosma Theorem and experiments also confirm it. The solution is found when all noise contributors are taken into account. Then the system visibility –Corbella's equation (Corbella et al., 2004)–becomes:

$$V_{12}(u,v) = \frac{1}{\sqrt{\Omega_1\Omega_2}} \iint\limits_{\xi^2+\eta^2\leq 1} \frac{T_B(\xi,\eta)-T_r}{\sqrt{1-\xi^2-\eta^2}} F_{n1}(\xi,\eta)F_{n2}^*(\xi,\eta)e^{-j2\pi(u\xi+v\eta)}\, d\xi\, d\eta \tag{2.36}$$

where T_r is the equivalent temperature of the noise produced by the receivers and entering to the antennas. This noise is coupled from one antenna to the other. If the receivers have input isolators, T_r is simply their physical temperature.

So, the modified brightness temperature T_B' expressed in Eq. (2.30) is actually:

$$T_B'(\xi,\eta) = \frac{T_B(\xi,\eta) - T_r}{\sqrt{\Omega_1\Omega_2}\sqrt{1-\xi^2-\eta^2}} F_{n1}(\xi,\eta)F_{n2}^*(\xi,\eta) \tag{2.37}$$

The basic measurement of the instrument are the time domain visibility samples V_{kj}^t obtained from the time domain complex correlation of the analytical signals $b_k(t)$ and $b_j^*(t)$ for any pair of antennas k, j $(k \neq j)$:

$$V_{kj}^t = \frac{1}{k\sqrt{\mathrm{B}_k\mathrm{B}_j}\sqrt{\mathrm{G}_k\mathrm{G}_j}} \frac{1}{2}\langle b_k b_j^* \rangle \tag{2.38}$$

where $\mathrm{G}_k, \mathrm{G}_j$ are the available power gains of each receiver chain and $\mathrm{B}_k, \mathrm{B}_j$ correspond to the receiver noise equivalent bandwidths and it is shown with a block diagram shown in Figure 2.12.

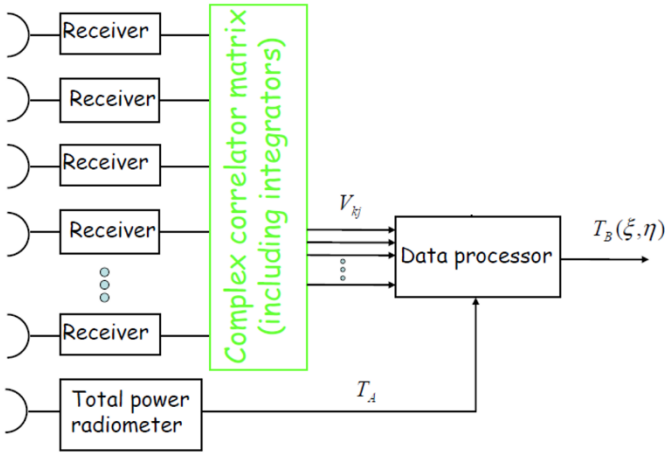

Figure 2.12. MIRAS block diagram

The cross-correlation of the signals at the output of the receivers can also be expressed assuming infinite integration time, as a function of the signals at the input b_{sk}, b_{sj} and the frequency response of the receivers H_k and H_j:

$$\frac{1}{2}\langle b_k(t)b_j^*(t)\rangle = \int_0^\infty \overline{b_{sk}(f)b_{sj}^*(f)} H_k(f)H_j^*(f)df = \int_0^\infty kV_{kj}H_k(f)H_j^*(f)df \tag{2.39}$$

where V_{kj} is the frequency domain system visibility.

Substituting Eq. (2.39) in Eq. (2.38) and expressing V_{kj} as $\iint_{4\pi} T_B' \cdot e^{-jk(r_k - r_j)} d\Omega$:

$$V_{kj}^t = \iint_{4\pi} T_B' \frac{1}{\sqrt{\mathrm{B}_k \mathrm{B}_j}\sqrt{\mathrm{G}_k \mathrm{G}_j}} \int_0^\infty H_k(f) H_j^*(f) \cdot e^{-jk(r_k - r_j)} df \, d\Omega \tag{2.40}$$

Considering the fringe washing function definition, which considers spatial decorrelation effects:

$$\tilde{r}_{kj}(t) = \frac{1}{\sqrt{\mathrm{B}_k \mathrm{B}_j}\sqrt{\mathrm{G}_k \mathrm{G}_j}} \cdot e^{-j2\pi f_0 t} \int_0^\infty H_k(f) H_j^*(f) \cdot e^{j2\pi f t} df \tag{2.41}$$

It gives the system visibility measured using time-domain cross-correlation:

$$\begin{aligned} V_{kj}(u_{kj}, v_{kj}) = \frac{1}{\sqrt{\Omega_k \Omega_j}} \iint_{4\pi} & \frac{T_B(\xi,\eta) - T_r}{\sqrt{1 - \xi^2 - \eta^2}} F_{nk}(\xi,\eta) F_{nj}^*(\xi,\eta) \\ & \cdot \tilde{r}_{kj}\left(-\frac{u_{kj}\xi + v_{kj}\eta}{f_0}\right) e^{-j2\pi(u_{kj}\xi + v_{kj}\eta)} \, d\xi \, d\eta \end{aligned} \tag{2.42}$$

being $(u_{kj}, v_{kj}) = (x_j - x_k, y_j - y_k)/\lambda_0$ the set of spatial frequencies where the visibility function V_{kj} is sampled and f_0 is the central frequency of the receivers. Note that the superscript "t" to indicate temporal cross-correlation has been omitted and will be omitted from now for simplicity.

In the ideal case all the antenna patterns are equal ($F_{nk}(\xi,\eta) = F_{nj}^*(\xi,\eta)$ and $\Omega_k = \Omega_j$) and the decorrelation effects are considered negligible ($\tilde{r}_{kj} \approx 1$). Then, the modified brightness temperature map is retrieved directly from calibrated visibilities by applying an inverse Fourier Transform:

$$T_B'(\xi,\eta) = \Im^{-1}[V(u,v)] \tag{2.43}$$

In a real case such as SMOS, antenna patterns present non-negligible differences, which are measured on ground. The Fourier transformation cannot be applied; instead, the so called G-matrix technique is required that turns the recovery as:

$$V = G \cdot T_B' \tag{2.44}$$

If the G-matrix. G is known, the modified brightness temperature can be estimated using the following equation:

$$T_B' = G^+ \cdot V \tag{2.45}$$

where $G^+ = G^*(GG^*)^{-1}$ is called the Moore-Penrose pseudo-inverse of G.

In summary, MIRAS measures the visibility function $V(u,v)$ by cross-correlating the signals of all pairs of antennas –or so called baselines–. These visibilities are then processed in the data processor –inherent and fundamental component in interferometric radiometers– to obtain the modified brightness temperature (called from now on T_B) that makes possible the reconstruction of a brightness temperature snapshot.

2.5.1. The Stokes Parameters

The Earth's surface radiates in two polarizations, vertical and horizontal, that are orthogonal between them. To capture the contributions of both electromagnetic waves (E_v and E_h), antennas have to measure in both polarizations. To describe an electromagnetic wave, four parameters are defined, so-called Stokes parameters:

$$I_s = \begin{bmatrix} I \\ Q \\ U \\ V \end{bmatrix} = \begin{bmatrix} T_v + T_h \\ T_v - T_h \\ T_3 \\ T_4 \end{bmatrix} \propto \begin{bmatrix} \langle E_h E_h^* \rangle + \langle E_v E_v^* \rangle \\ \langle E_h E_h^* \rangle - \langle E_v E_v^* \rangle \\ 2\Re e\langle E_v E_h^* \rangle \\ 2\Im m\langle E_v E_h^* \rangle \end{bmatrix} \tag{2.46}$$

The first Stokes parameter (I) represents the total radiated power density and the second Stokes parameter (Q) refers to the difference between the power density in the vertical and horizontal polarizations. The third and fourth parameters, also known as T_3 and T_4, characterize the correlation between both h and v polarizations (Randa et al., 2008).

As the antennas are no ideal, i.e. finite cross-polar patterns and not perfectly isolated, there is, per polarization, the reference pattern (R) and the cross-polar pattern (C), where $C \ll R$. The four possible visibilities (in terms of the solid angle) are expressed as follows (Corbella et al., 2004):

$$V_{kj}^{hh} = \frac{1}{\sqrt{\Omega_k \Omega_j}} \iint_{4\pi} \left[R_{hk} R_{hj}^* \left(T_B^{hh} - T_r \right) + R_{hk} C_{hj}^* T_B^{hv} + C_{hk} R_{hj}^* T_B^{vh} + C_{hk} C_{hj}^* (T_B^{vv} - T_r) \right] e^{jk\Delta r} \, d\Omega \tag{2.47}$$

$$V_{kj}^{vv} = \frac{1}{\sqrt{\Omega_k \Omega_j}} \iint_{4\pi} \left[C_{vk} C_{vj}^* \left(T_B^{hh} - T_r \right) + C_{vk} R_{vj}^* T_B^{hv} + R_{vk} C_{vj}^* T_B^{vh} + R_{vk} R_{vj}^* (T_B^{vv} - T_r) \right] e^{jk\Delta r} \, d\Omega \tag{2.48}$$

$$V_{kj}^{hv} = \frac{1}{\sqrt{\Omega_k \Omega_j}} \iint_{4\pi} \left[R_{hk} C_{vj}^* \left(T_B^{hh} - T_r \right) + R_{hk} R_{vj}^* T_B^{hv} + C_{hk} C_{vj}^* T_B^{vh} + C_{h1} R_{v2}^* (T_B^{vv} - T_r) \right] e^{jk\Delta r} \, d\Omega \tag{2.49}$$

$$V_{kj}^{vh} = \frac{1}{\sqrt{\Omega_k \Omega_j}} \iint_{4\pi} \left[C_{vk} R_{hj}^* \left(T_B^{hh} - T_r \right) + C_{vk} C_{hj}^* T_B^{hv} + R_{vk} R_{hj}^* T_B^{vh} + R_{vk} C_{hj}^* (T_B^{vv} - T_r) \right] e^{jk\Delta r} \, d\Omega \tag{2.50}$$

In both Eq. (2.47) and Eq. (2.48), the terms that multiply the reference antenna pattern of both antennas in the measured polarization, $R_{hk} R_{hj}^* \left(T_B^{hh} - T_r \right)$ and $R_{vk} R_{vj}^* (T_B^{vv} - T_r)$, respectively, are the ones that make the main contribution in the pertinent visibility samples because the other terms are much lower and can be neglected. On the other hand, in Eq. (2.49) and Eq. (2.50), the terms $R_{hk} R_{vj}^* T_B^{hv}$ and $R_{vk} R_{hj}^* T_B^{vh}$ are the ones that contribute the most, respectively. In Eq. (2.49) and Eq. (2.50), the terms of the reference antenna patterns also make a contribution that cannot be negligible.

2.5.2. The SMOS Field of View

As aforementioned, MIRAS antennas are equally spaced. It was decided that the space between antennas is $d = 0.875\lambda$ (Fig. 2.13) due to the size of the antennas –which is compromised by the desired radiometric sensitivity– and the limited space in the structure.

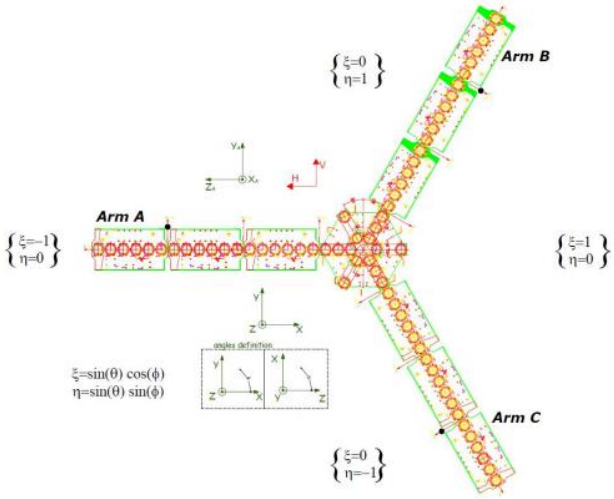

Figure 2.13. Antenna positions in the MIRAS arms (Corbella et al., 2019)

In the frequency domain, the visibility sample positions form the (u, v) plane (Fig. 2.14a) with coordinates $(\Delta x, \Delta y)/\lambda$, which corresponds to a hexagonal grid. In the figure, it is shown in magenta the non-redundant baselines –visibility samples of antennas with

different values of (u, v)–, and in cyan, the redundant baselines –visibility samples of antennas with equal values of (u, v), including the zero baselines ($u = v = 0$), i.e. antennas in the same arm and reciprocal ones, e. g. arm A-B and B-A– assuming that all antenna patterns are equal. In order to obtain a smoother spectrum's shape without adding extra information, zero padding is performed in the rest of the points of the hexagon (gray points in Fig. 2.14a). In the image inversion, the choice of the (ξ, η) grid Figure 2.14b must be reciprocal to the (u, v) grid in order to apply the standard rectangular FFT to the hexagonal (u, v) coverage (Camps et al., 1997).

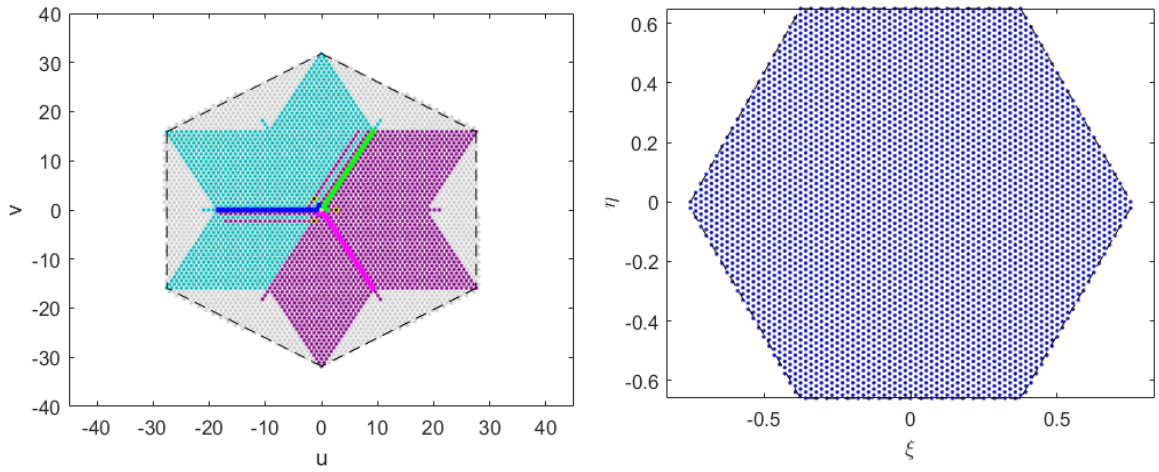

(a) (b)

Figure 2.14. Planes: (a) u-v plane (visibility), (b) ξ-η plane (brightness temperature).

The chosen distance between antennas ($d = 0.875\lambda$) does not fulfill the Nyquist criteria, because it should be $d \leq \lambda/\sqrt{3} = 0.577\lambda$. As a result, there is aliasing in the FoV in the brightness temperature snapshot. The replicas in both the $u - v$ and the $\xi - \eta$ planes of the fundamental period (in blue) can be seen in Fig. 2.14a and 2.14b, respectively.

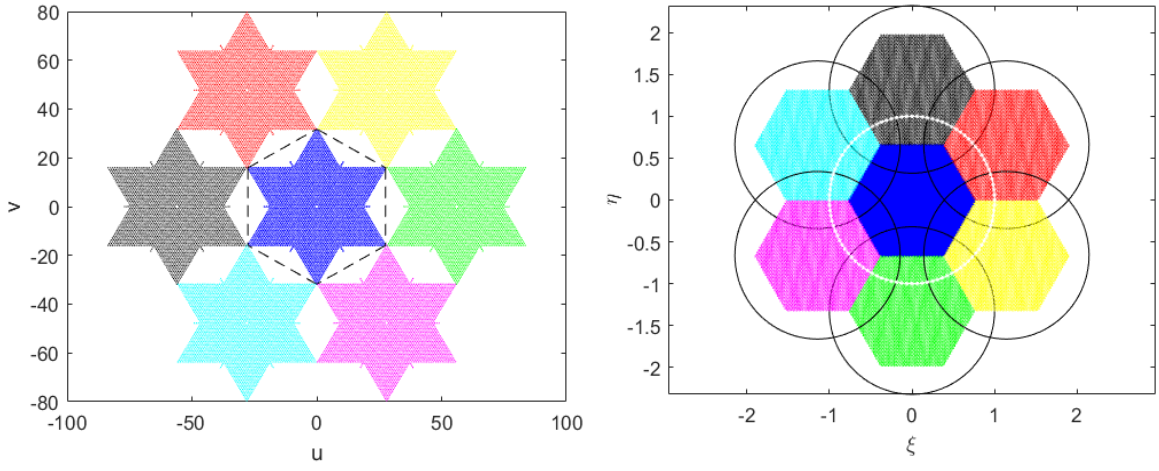

(a) (b)

Figure 2.15. Replicas of the fundamental hexagon in: (a) the u-v plane, (b) the $\xi - \eta$ plane.

In the right image, it is also shown the unit circle of the fundamental period (white dotted line) and the ones of the other replicas (solid black lines). The unit circle represents the visible space projected onto the plane of the instrument and it is characterized by $\xi^2 + \eta^2 = 1$.

The region where there is no overlapping of the unit circles is defined as the Alias-Free Field of View (AF-FoV), as seen in Figure 2.16a (zone delimited by the green line). In this image, the Earth contour (Earth-sky horizon) of the fundamental period (dotted magenta line) and the ones of the replicas (blue dotted lines) are also shown. The region between the Earth contour and the unit circle corresponds to the sky, which also includes the galaxy. Because it is well known and much colder than the Earth brightness temperature, the AF-FoV can be enlarged in a zone limited by the Earth-sky horizon. This zone is called the Extended Alias-Free Field of View (EAF-FoV) and corresponds to the zone delimited by the gold line in Fig. 2.16a.

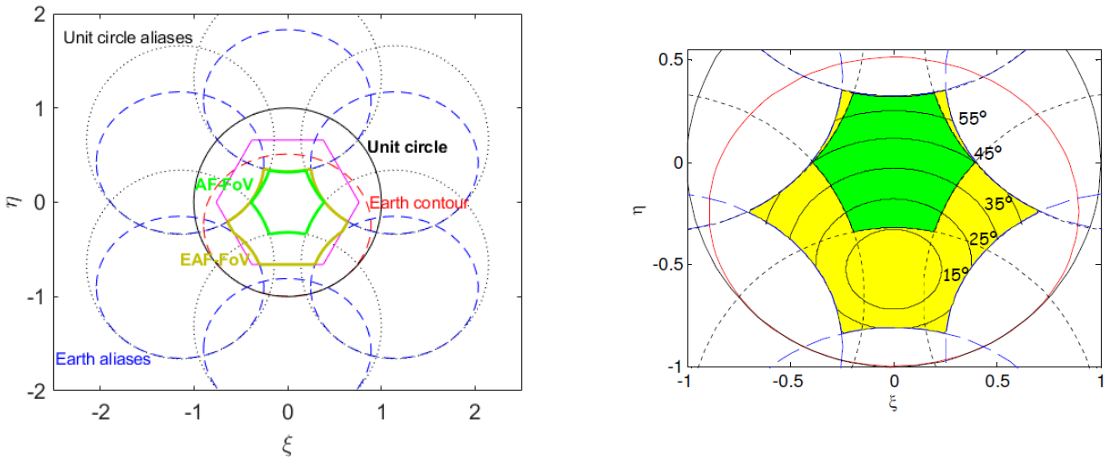

(a) (b)

Figure 2.16. Field of view: (a) EAF-FoV and AF-FoV, (b) incidence angles in SMOS FoV.

As mentioned in section 2.3. , because of its interferometric capabilities, MIRAS is able to measure at different incidence angles in its FoV. Constant incidence angle circles centered at nadir are shown in (Fig. 2.16b). During every measured instant, an image corresponding to the (E)AF-FoV is processed. As each snapshot overlaps with the preceding and successive one, each ground position is viewed from a range of incidence angles.

2.5.3. MIRAS Measurement Modes

To be able to measure in both the horizontal (h-pol) and vertical (v-pol) polarizations, LICEFs have a single-channel receiver but a dual polarization antenna. A switch per antenna allows to select between the two observation modes (h or v), which makes possible the measurement in a unique polarization at a time.

2.5.3.1. Dual Polarization Mode

When working in this mode, all receivers select sequentially the horizontal and vertical polarization port of the antennas with an integration time of 1.2 s each to obtain Brightness Temperature snapshots (TB) in the pertinent polarization. The case of the configuration of two receivers in Horizontal Polarization (H-pol) and in Vertical Polarization (V-pol) is shown in Fig. 2.17.

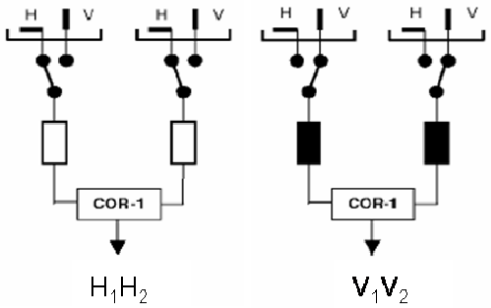

Figure 2.17. Pair of antennas measuring in dual-pol. Image from (Martin-Neira et al., 2002).

2.5.3.2. Full Polarization Mode

MIRAS is also able to measure in full polarimetric mode. This means that it measures not only in the *h* and *v* polarizations, but also in the cross-correlations *vh* and *hv* polarizations. To do so, a four-step sequence is needed where every receiver has to select twice each polarization, but in different orders. When the cross-correlation is done in the different instances of the sequence, the four correlations that are obtained are *hh*, *hv*, *vh*, and *vv*. An example is shown in Figure 2.18.

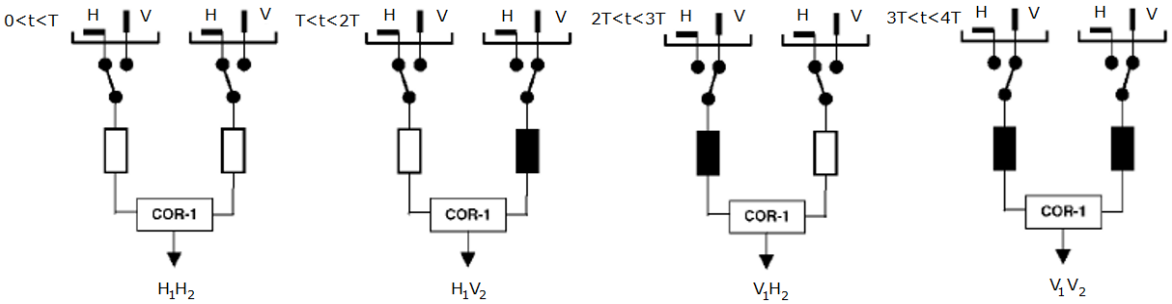

Figure 2.18. Switching of a pair of receivers in the four different instants of the sequence (Martin-Neira et al., 2002).

To implement this in MIRAS, all antennas of an arm have to measure in the same polarization but in different switching sequences. There has to be four integration periods lasting 1.2 s each as shown in Table 2.1 referred to Figure 2.13.

Table 2.1. Switching sequence of the MIRAS arms

Integration period	Arm A	Arm B	Arm C	Integration time (s)
1st	H	H	H	1.2
2nd	V	H	H	0.4
	H	V	H	0.4
	H	H	V	0.4
3rd	V	V	V	1.2
4th	H	V	V	0.4
	V	H	V	0.4
	V	V	H	0.4

During the first integration period, as all receivers are measuring in the horizontal polarization, the hh-baseline samples of the star (Fig. 2.14a) are obtained. In the following integration period, only one arm is in one polarization, let's say the v-pol, and the rest, in the other polarization (h-pol). This means that the baselines of the vv, vh, and hv-visibility samples of the star are generated with a shorter integration time. As a result, the radiometric sensitivity for these three visibility samples is poorer, but an entire full-polarimetric block of TB is obtained after 2.4 s (Martin-Neira et al., 2002).

By setting all receivers in the v-pol in the third integration period, it is possible the measurement of all vv-baseline samples of the star with the same radiometric sensitivity as the hh ones of the first integration period. Repeating the sequence of the second integration period but with the h-pol per arm in the fourth integration period, the hh, hv, and vh-visibility samples of the stars are also generated with the same radiometric sensitivity as the second integration period.

2.5.4. Radiometric Sensitivity

Radiometric sensitivity is the smallest variation in brightness temperature that can be measured by the instrument. This parameter is inversely proportional to both the bandwidth (B) and the integration time (τ) of the antennas, and for interferometric radiometers, it is also limited by the discretization and the finite coverage in the $u - v$ plane since the image is composed of the measurements of many antennas and their cross-correlation.

Radiometric sensitivity is defined as (Camps et al., 1998):

$$\Delta T_B(\xi,\eta) = \Delta s \frac{T_{sys}}{\sqrt{B\tau}} \frac{\Omega_a}{t(\xi,\eta)} \sqrt{1-\xi^2-\eta^2}\alpha_w\sqrt{N_v} \tag{2.51}$$

where ΔS corresponds to the elementary area in (ξ,η), T_{sys} to the system temperature, α_w to the windowing factor (Rectangular =1, Blackmann=0.45), N_v to the number of non-redundant visibility samples in the $u-v$ plane and Ω_a is the antenna equivalent solid angle. The equi-radiometric sensitivity contours around the boresight within the snapshots are shown in Fig. 2.19.

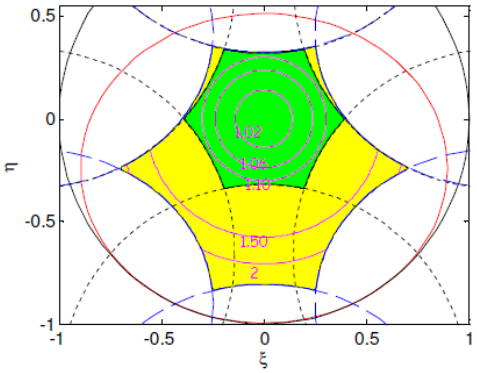

Figure 2.19. Equi-radiometric sensitivity contours, where the ration $\frac{\Delta T_B}{\Delta T_{B_{boresight}}}$ is annotated in pink.

For the MIRAS boresight ($\xi = 0, \eta = 0$), the radiometric sensitivity remains equal to:

$$\Delta T_B = \Delta S \frac{T_{sys}}{\sqrt{B\tau}} \Omega_a \alpha_w \sqrt{N_v} \tag{2.52}$$

In Figure 2.20, the theoretical boresight radiometric sensitivity with respect to the integration time is compared with measurements with good agreement.

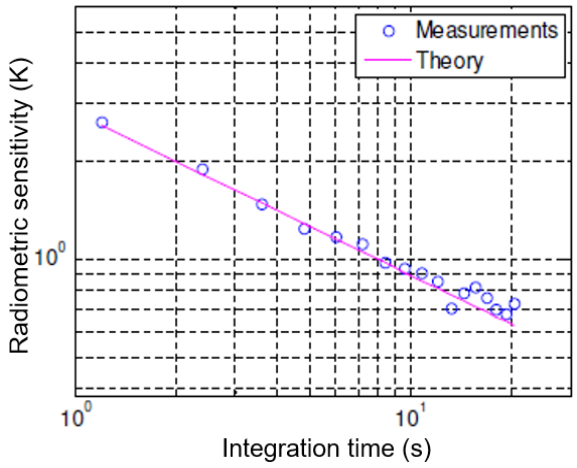

Figure 2.20. MIRAS boresight radiometric sensitivity with respect the integration time.

By analyzing Eq. (2.51), it is clear that the mixed-pol (hv-pol) has much worse radiometric sensitivity –in the range of 3 to 8 K– than the pure-pols (hh and vv-pol) –in the range of 1.5 to 4.5 K– because it has a shorter integration time as shown in Table 2.1.

2.5.5. Stokes Parameters at Antenna and Ground Frames

Due to the altitude and tilt angle of the platform, there is a relative alignment between the Earth's surface frame (h and v polarizations) and the antenna reference frame of the instrument (referred as x and y polarizations from now on). As a result, at each spatial direction from the instrument to the Earth's surface, there is a geometric rotation φ that must be applied to T_B^{xx} and T_B^{yy} to obtain the brightness temperature in the ground frame. The brightness temperature in the antenna frame can be expressed as a linear combination of the brightness temperature in the ground frame (Martin-Neira et al., 2002), referred to Figure 2.21:

$$\begin{bmatrix} T_B^{xx} \\ T_B^{xy} \\ T_B^{yx} \\ T_B^{yy} \end{bmatrix} = \begin{bmatrix} A^2 & AB & AB & B^2 \\ -AB & A^2 & -B^2 & AB \\ -AB & -B^2 & A^2 & AB \\ B^2 & -AB & -AB & A^2 \end{bmatrix} \begin{bmatrix} T_B^{hh} \\ T_B^{hv} \\ T_B^{vh} \\ T_B^{vv} \end{bmatrix} \tag{2.53}$$

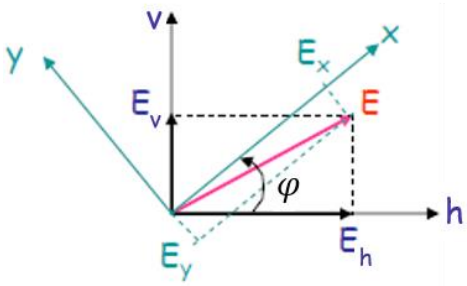

Figure 2.21. Coordinate rotation in the antenna frame $(x - y)$ and ground frame $(h - v)$.

Additionally, due to the electromagnetic wave propagation through the ionosphere, the propagation axes rotate an angle equal to the Faraday rotation (FR). Therefore, the total angle of the rotation at any spatial direction φ_T is the sum of φ and the Faraday rotation angle Ω_f.

$$\varphi_T = \varphi + \Omega_f \tag{2.54}$$

That means that A and B of Eq. (2.53) are actually $A = \cos\varphi_T$, $B = \sin\varphi_T$.

Assuming that the horizontal and vertical polarization of the ground emission are uncorrelated ($T_B^{hv} = T_B^{vh} = 0$) and that T_B^{xy} and T_B^{yx} are the complex cross-polarization brightness temperatures in the antenna frame –which are hermitic of each other–, the instrument full polarimetric measurement at each snapshot is related to the ground emission by:

$$\begin{bmatrix} T_B^{xx} \\ 2\Re e\left(T_B^{xy}\right) \\ T_B^{yy} \end{bmatrix} = \begin{bmatrix} \cos^2(\varphi + \Omega_f) & \sin^2(\varphi + \Omega_f) \\ -\sin 2(\varphi + \Omega_f) & \sin 2(\varphi + \Omega_f) \\ \sin^2(\varphi + \Omega_f) & \cos^2(\varphi + \Omega_f) \end{bmatrix} \begin{bmatrix} T_B^{hh} \\ T_B^{vv} \end{bmatrix} \tag{2.55}$$

Therefore, the brightness temperatures at $(h - v)$ can be obtained from the measured $(x - y)$ ones.

If no polarimetric measurements are available, T_B^{hh} and T_B^{vv} can be expressed in terms of A and B as:

$$T_B^{hh} = \frac{A^2 T_B^{xx} - B^2 T_B^{yy}}{A^4 - B^4} \tag{2.56}$$

$$T_B^{vv} = \frac{A^2 T_B^{yy} - B^2 T_B^{xx}}{A^4 - B^4} \tag{2.57}$$

It is important to mention that, at the particular $\varphi_T = 45°$, there is a singularity that does not make possible the extraction of the brightness temperatures at the ground frame from the antenna frame.

All this formulation is consistent with the Ludwig's third definition of polarization defined as (Ludwig, 1973) related to Fig. 2.22:

$$\hat{L}_x = \cos\phi\,\hat{\theta} - \sin\phi\,\hat{\phi} \tag{2.58}$$

$$\hat{L}_y = \sin\phi\,\hat{\theta} + \cos\phi\,\hat{\phi} \tag{2.59}$$

where $\hat{L}_x$ and $\hat{L}_y$ correspond to the unitary vectors in the direction of the two orthogonal polarizations. This definition is consistent with $\hat{L}_x \times \hat{L}_y = \hat{r}$.

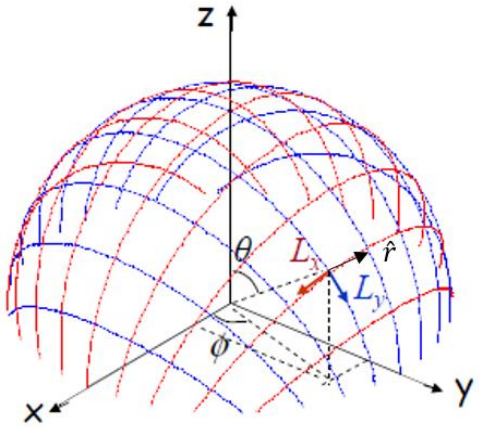

Figure 2.22. Ludwig's third definition

2.5.6. Geolocation of the Brightness Temperatures

The brightness temperatures have to be geolocated from the antenna frame $(x - y)$ to the ground frame $(h - v)$ considering not only the geometric rotation and the correction of the Faraday rotation angle introduced by the ionosphere (section 2.5.5.) but also, the fact that SMOS has multiangular information (Fig. 2.23b). When the snapshot is projected to ground coordinates (Fig. 2.23a), the constant incidence angle contours stay as circles on ground centered at nadir (Fig. 2.23b), mentioned in section 2.5.2.

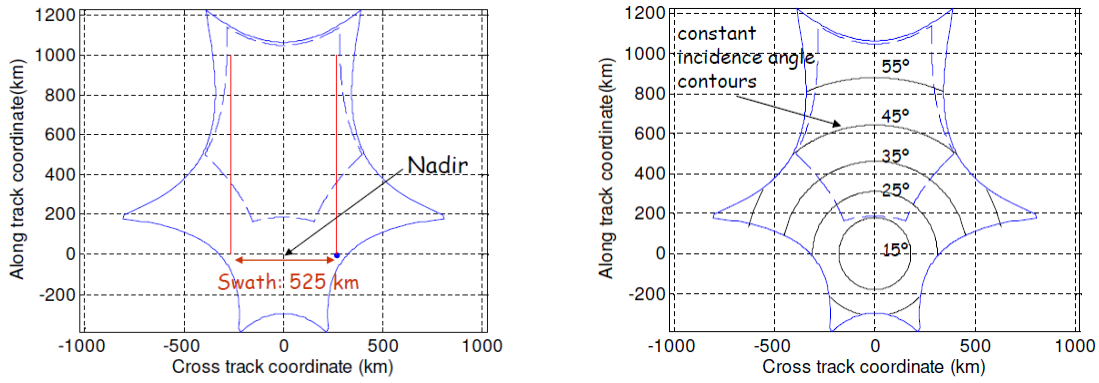

(a) (b)

Figure 2.23. Snapshot projected to ground coordinates: (a) swath, (b) constant incidence angle contours.

On the other hand, with the spatial resolution, it does not happen the same. At the antenna frame, pixels represent circles of radius 2.43° (Fig 2.24a, black circles), while at the ground frame, pixels are converted to ellipses with different orientations and sizes (Fig 2.24b, black ellipses).

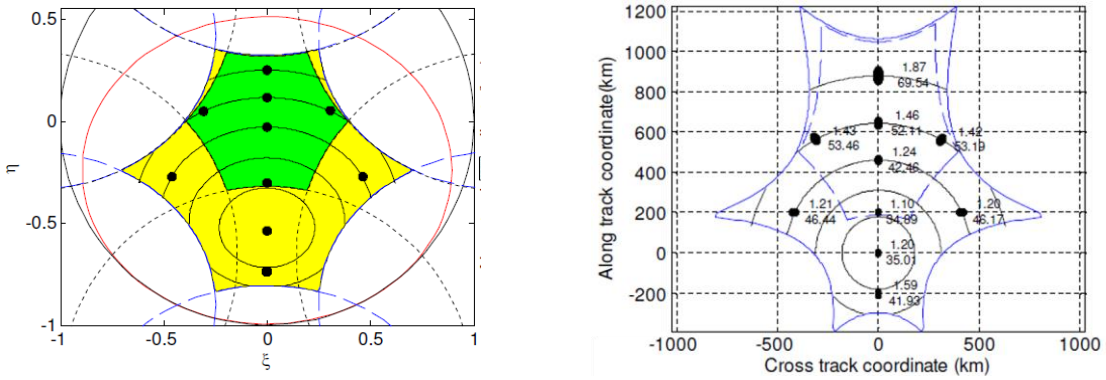

(a) (b)

Figure 2.24. Spatial resolution: (a) in antenna frame, (b) projected to ground coordinates.

Several projection grids can be used in the geolocation. There is the Equal-Area Scalable Earth (EASE) grid which utilizes an equal-area projection (square-based of 3,244,518 points at 12 km), minimizing the amount of distortion over the poles; the Earth Topography-5 minute (ETOPO-5) grid, which corresponds to a square-based of 9,331,200 points (grid of 8.33 km); the Icosahedral Snyder Equal Area (ISEA) grid, that in its hexagonal projection at an aperture 4 and resolution 9 (15-km grid) is made up 2,621,442 points; among others. The last one provides the smallest average error and the greatest angular resolution possessing a uniform adjacency with its neighbors, reasons to be chosen for ESA for all their products.

2.5.7. Radio Frequency Interference

The Radio Frequency Interference (RFI) is defined by the ITU Radio Regulations (RR1.166 to RR1.169) as "the effect of unwanted energy due to one or a combination of emissions,

radiations, or inductions upon reception in a radio-communication system, manifested by any performance degradation, misinterpretation, or loss of information which could be extracted in the absence of such unwanted energy". When the interference "seriously degrades, obstructs, or repeatedly interrupts a radiocommunication-service operating in accordance with a Radio Regulation", it becomes harmful.

The 1400-1427 MHz frequency range (L-band) was selected for SMOS because it corresponds to the protected band for passive Satellite Earth Exploration, passive Space Research Service, and Radio-astronomy Service. Any other type of emissions on that band is prohibited. Despite this, there are a high number of RFI observed worldwide causing problems in the SMOS retrieval. This does not represent only a problem for SMOS but for other L-band sensors as well.

SMOS is mostly affected either by illegal man-made emissions or active service stations in the adjacent bands with out-of-band and spurious emissions, the last one spilling over the protected passive band. These sources are mainly distributed over large parts of Europe, Asia, and the Middle East.

SMOS is mainly affected by the following considerations (Oliva et al., 2016):

- The interference sources are either radar systems with excessive out-of-band emissions or radio-links, surveillance cameras or local terrestrial broadcast systems operating without authorization.
- The RFI sources correspond to antennas located on continental territory, although some (a smaller number) have been found over boats. Even though the sources are over land, their effects spread to surrounding surfaces, including ocean.
- Active systems generally provide service to in-ground receivers, which involves the usage of high directivity antennas pointing either the horizon or low elevation angles.

The presence of RFI was evident as soon as SMOS obtained its first images (Daganzo et al., 2012). Unfortunately, SMOS does not have on-board RFI protection as other satellites (Piepmeier et al., 2014). Instead, the SMOS team put together a successful strategy to clean the RFI in its operating band that consists of monitoring and reporting illegal transmissions (Oliva et al., 2019). Even though it is a time consuming and not always a successful procedure, it has proved to be effective, allowing to improve the interference scenario over extensive areas (Daganzo et al., 2012).

To show the results of this strategy, Figure 2.25 shows the RFI probability worldwide map over land surface in both 16-31 of January 2010 (top) and 4-17 of May 2017 (bottom) (Uranga et al, 2018).

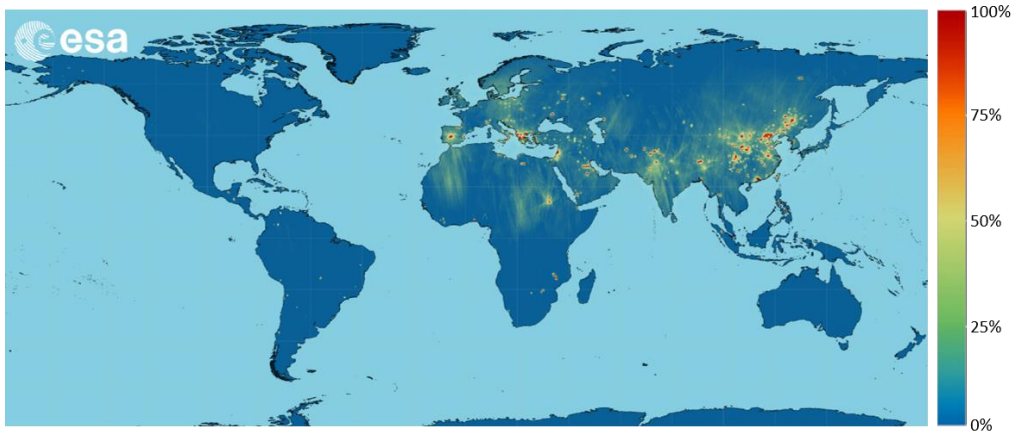

(a)

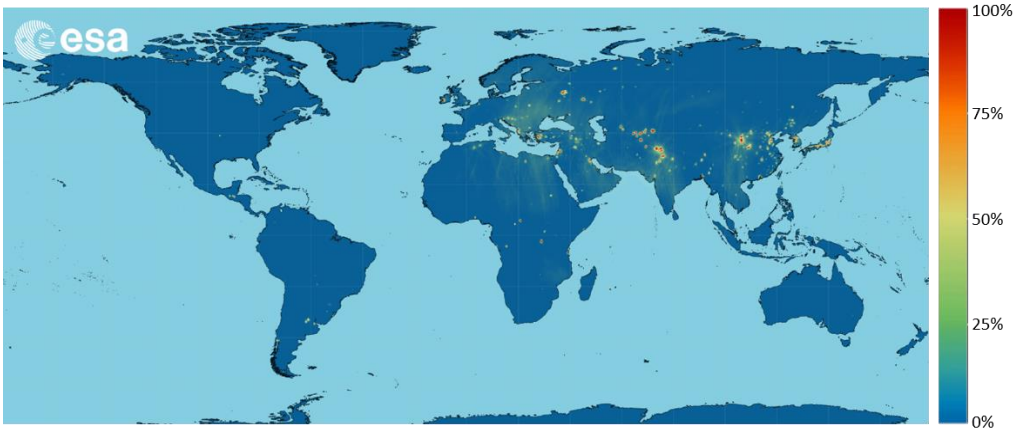

(b)

Figure 2.25. RFI probability worldwide map: (a) 16-31 of January, 2010, (b) 4-17 of May, 2017 (Uranga et al., 2018).

Chapter 3

Faraday Rotation Angle and Vertical Total Electron Content Fundamentals

As mentioned in the previous chapter (section 2.5.5.), the FRA is a rotation in the electromagnetic field components due to its propagation through the ionosphere. The ionosphere corresponds to the region in the uppermost portion of the Earth's atmosphere that extends from ~50 km altitude to more than ~600 km where there are ionized particles and electrons due to the interaction of the solar wind with the very thin air particles that have escaped the Earth's gravity. The Sun is the source of energy that ionizes these particles (Emery & Camps, 2017). Therefore, this effect is mainly determined by the solar activity and its sunspot number within the 11-year cycle (Fig. 3.1a). SMOS mission lifetime is within the 24th solar cycle (Fig. 3.1b), which has not been the highest one.

The solar activity within a solar cycle reaches its peak of magnitude around the half of its duration. As it can be seen in Fig. 3.1b, this has happened in the SMOS lifetime in 2014. Another peak of magnitude is expected to occur around the year 2025. On the other hand, in the figure it can also be seen that the minimum solar activity occurred in 2022.

The FRA can be theoretically defined as (Yueh, 2000), (Le Vine & Abraham, 2002):

$$\Omega_f = 1.355 \times 10^4 f^{-2} B_0 \cos\Theta_B \sec\theta \ \text{VTEC} \tag{3.1}$$

where Ω_f represents the FRA in degrees, f corresponds to the frequency in GHz; B_0, to the magnitude of the geomagnetic field in Teslas; Θ_B, to the angle between the magnetic field and the wave propagation direction; θ, to the polar angle between the nadir and the line of sight to the surface, i.e. incidence angle; and VTEC, to the Vertical Total Electron content, which is the content of electrons in a vertical column of 1 m² expressed in TEC units (TEC unit $\approx 10^{16}\ electrons/m^2$). Both the geomagnetic field and the VTEC are given at a geodetic altitude of 450 km.

There is a directly proportional relationship between the FRA and the VTEC. Thus, this Faraday rotation is also determined by the VTEC diurnal and seasonal variation at Local Time (LT) (Fig. 3.2).

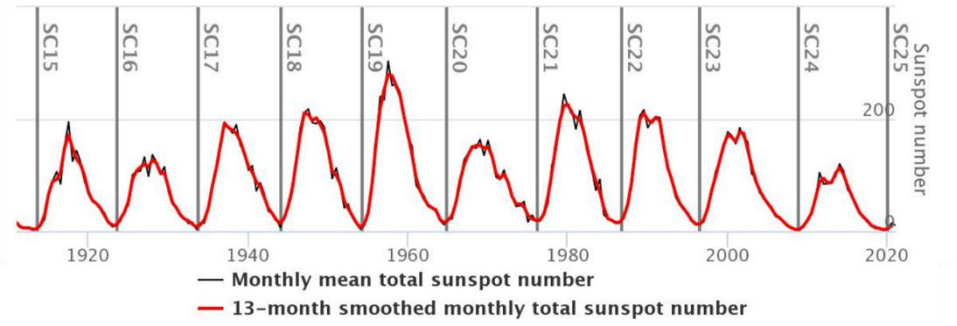

(a)

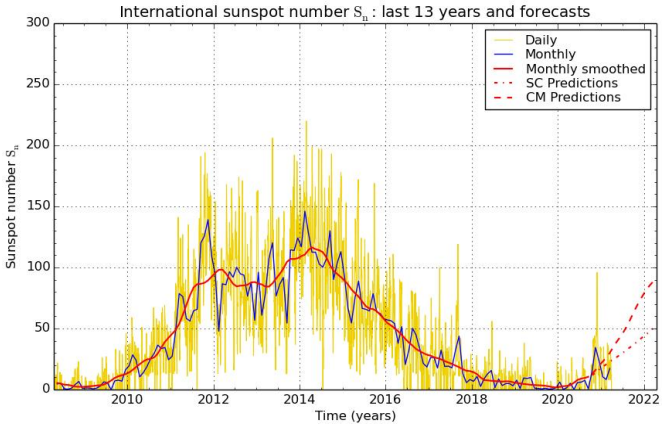

(b)

Figure 3.1. Solar activity (SILSO, s. f.): (a) of the 15th solar cycle to the 24th, (b) of the SMOS mission.

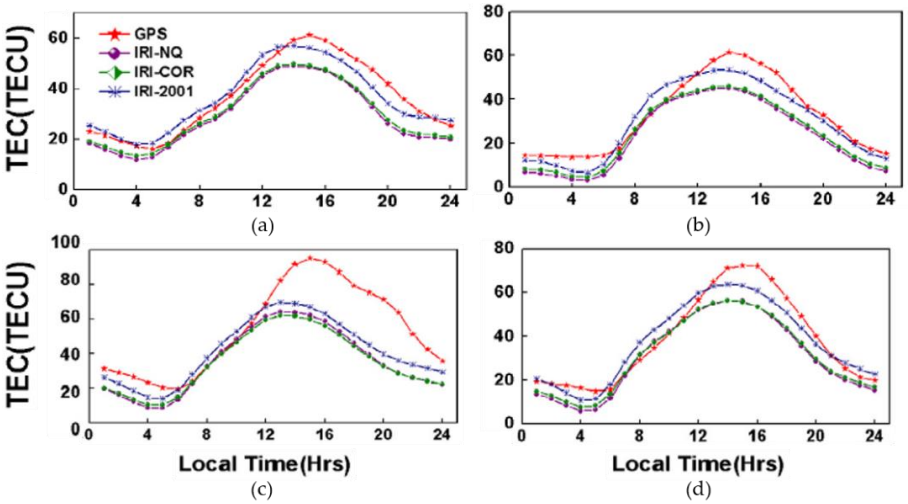

Figure 3.2. Local Time variation of TEC averaged for different seasons from different sources vs LT: (a) Summer (May, June, July, August), (b) Winter (November, December, January, February), (c) Spring (March, April), (d) Fall (September, October) (Kakoti et al., 2017).

In the afternoon LT, the surviving amount of VTEC generated by the sunlight during the preceding hours is higher than in the morning LT.

3.1. FRA Variability

The FRA has an important geophysical and temporal variability. Figure 3.3 shows the FRA in the SMOS boresight coordinates of three consecutive days for two different solar activity periods (see Fig. 3.1b): high solar activity (March 2014) and low solar activity (January 2011). In Fig. 3.3a and 3.3c, it can be seen the descending and ascending orbits of the first period; and in Fig. 3.3b and 3.3d, of the second one. It is noticeable that there is a big difference between the magnitude of the FRA in descending orbits with respect to ascending ones (be aware of the scale).

As shown in Fig. 3.2, at evening LT the solar activity is higher than in the morning, and since SMOS is in a 6 a.m.-6 p.m. sun-synchronous orbit, i.e. descending orbits occur at evening LT, descending orbits always have a much higher FRA and higher dynamic ranges than for ascending ones.

On the other hand, there is an important difference between the FRA magnitude in 2014 and in 2011, due to the different solar activities in the two years (Fig. 3.1b); 2014 has the highest solar activity throughout the entire period of the SMOS mission. Finally, it is also worth mentioning that the geophysical FRA variability does not have a defined pattern, except for a change of sign that occurs at the equatorial crossing due to the corresponding sign change of the magnetic field dip angle (see Eq. (3.1)).

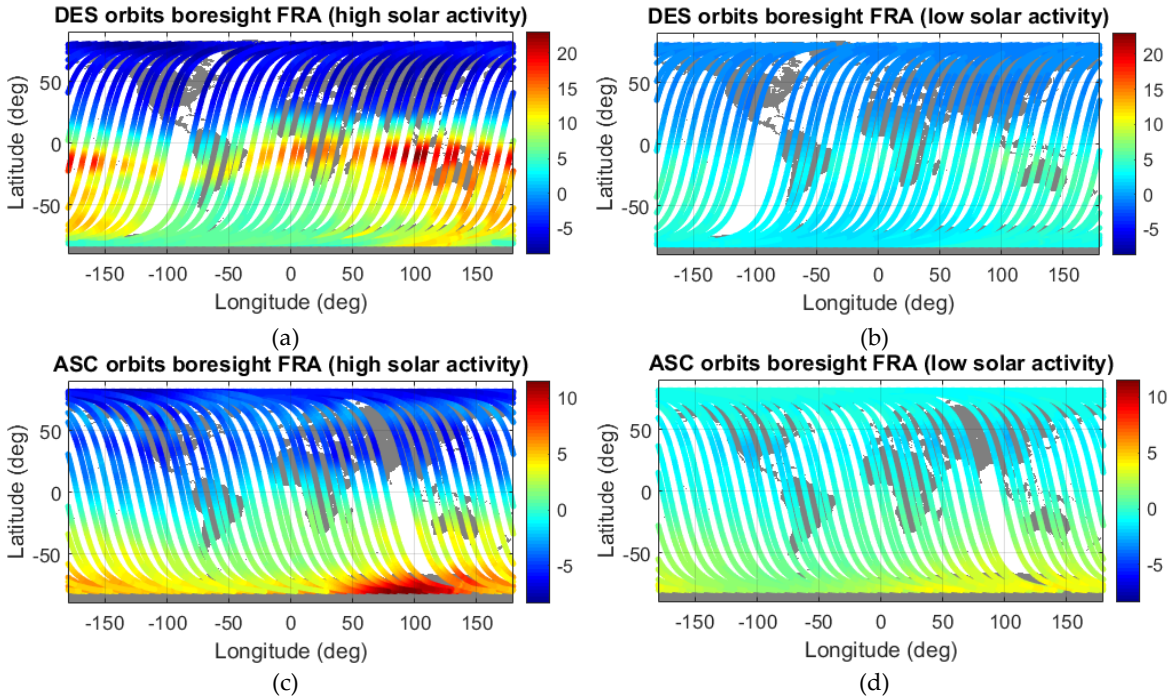

Figure 3.3. FRA at SMOS boresight coordinates of three consecutive days in different periods. Top: Descending orbits in (a) March 2014 (high solar activity), (b) January 2011 (low solar activity), Bottom: Ascending orbits in (c) March 2014 (high solar activity), and (d) January 2011 (low solar activity).

To analyze how the FRA temporally changes, Figure 3.4 shows the latitudinal-temporal FRA variation. This plot is called Hovmöller diagram and constitutes a powerful tool to analyze any seasonal and latitudinal variations. The longitudinal for descending (Fig. 3.4a) and ascending (Fig. 3.4b) orbits for the entire mission. Once again, the differences between descending and ascending orbits caused by the VTEC depending on the LT are evident. It is also visible, taking as a reference Figure 3.1b, that, the higher the solar activity, the higher the FRA. The orbits were chosen over the eastern Pacific Ocean in order to avoid the presence of RFI and maximize the coverage of measurements over ocean.

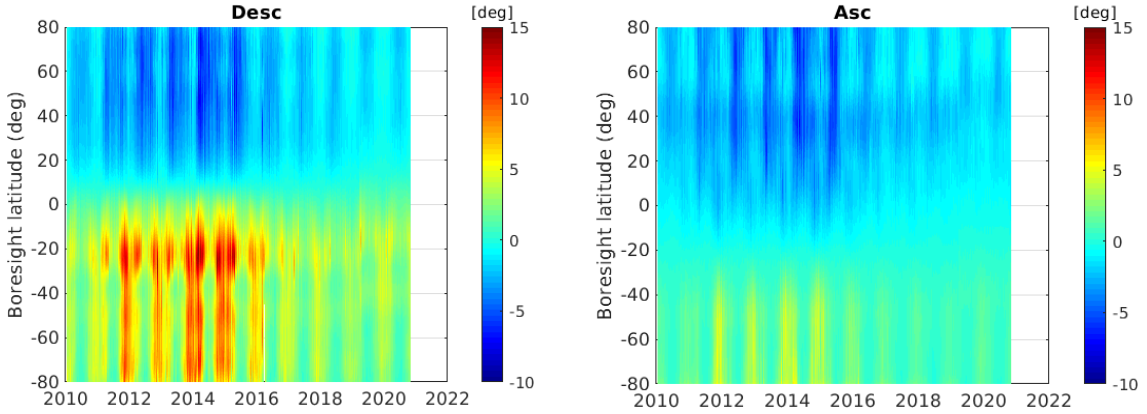

Figure 3.4. Hövmoller of the FRA at boresight through the mission for: (a) descending orbits and (b) ascending orbits.

The FRA variation between close dates cannot be appreciated in Figure 3.4. In order to perceive it more carefully, Figure 3.5 shows the FRA using the SMOS boresight coordinates of a date (March 18, 2011) and three days later (March 21, 2011), which corresponds to the number of days to have global coverage, as it was mentioned in section 2.3. Fig. 3.5a and 3.5b show the FRA of every date separately with their own scales, and Fig. 3.5c shows the FRA of both days together where it is noticeable the important differences between them.

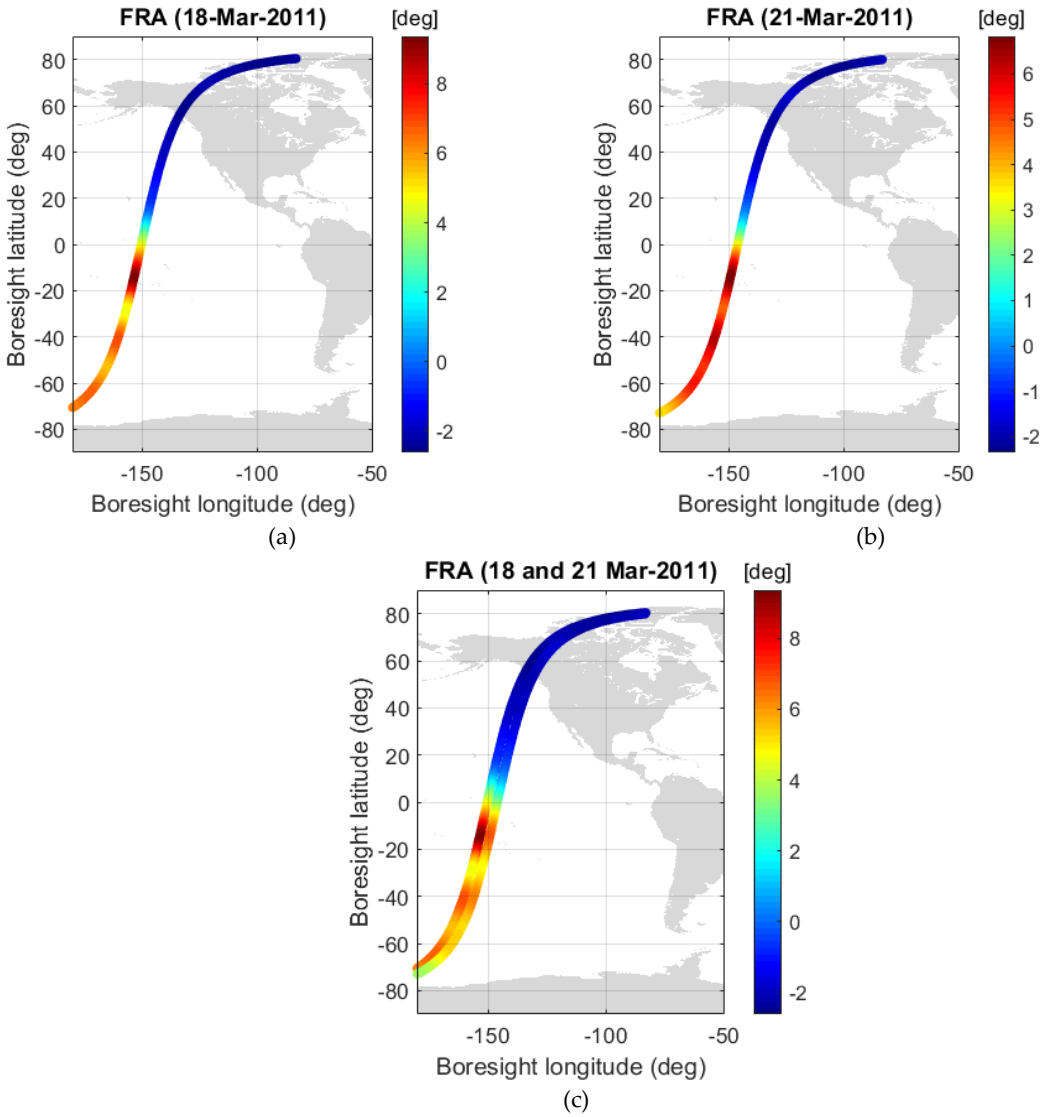

Figure 3.5. FRA with the SMOS boresight coordinates in: (a) March 18, 2011, (b) March 21, 2011, and (c) both dates.

The Faraday Rotation introduces an important rotation of several degrees in the electromagnetic field polarization (in the order of -10 to 20°). If neglected, the measured TB is affected. Figure 3.6 shows the global distribution of the error in the TB over the ocean when the Faraday rotation is not corrected. For the calculus, it was assumed an ocean salinity of 35 PSU and a sea surface temperature of 20° C for a period of high solar activity (June 1989). The plot shows the error for different incidence angles (20°, 30°, 40°, and 50°) and for 6 a.m. (Fig 3.6 left) and noon (Fig 3.6 right) LT. For higher incidence angles, the error increases, as expected, due to its linear relationship with the FRA (Eq. (3.1)). It is also worth mentioning that at mid-latitudes, the error is less than 0.3 K for all the incident angles, in contrast with the rest of latitudes where it is much larger (much higher than 1 K at higher incidence angles) (Le Vine & Abraham, 2002).

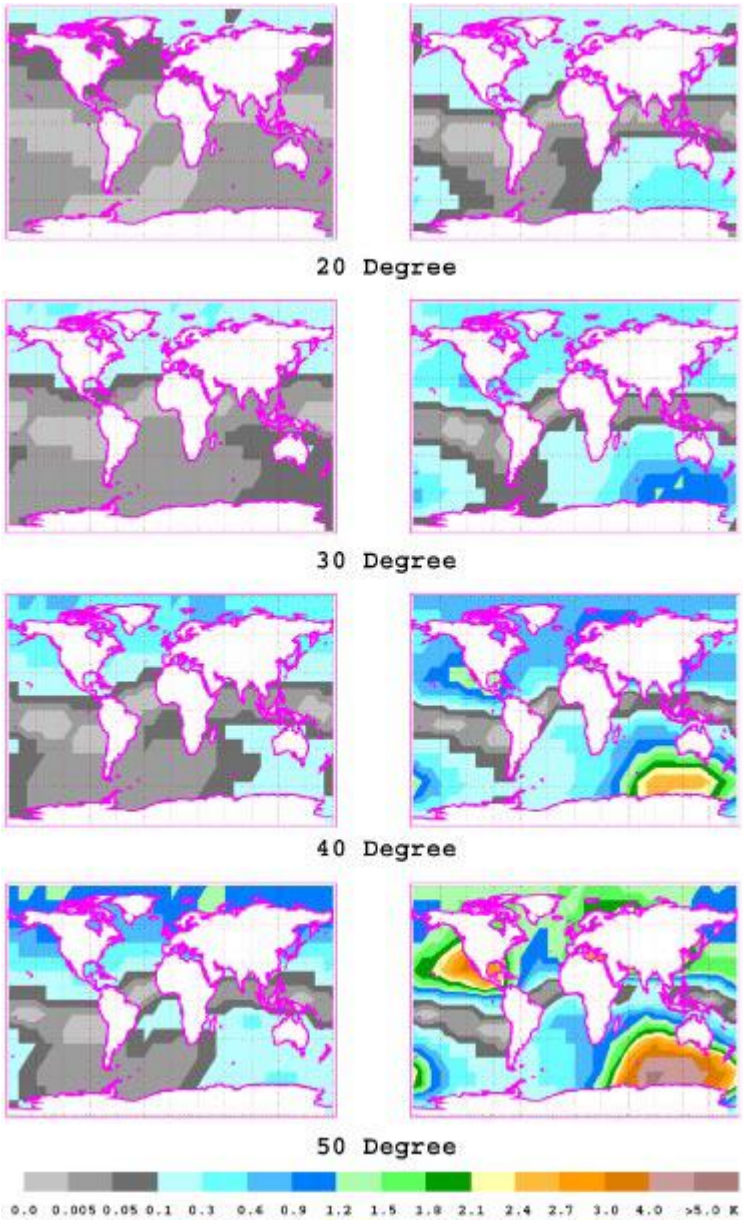

Figure 3.6. Global distribution of the error in the TB (H-pol) as a function of incidence angle due to neglecting the FRA at 6 a. m. (left) and noon (right). The data are for high solar activity (June 1989; Rz = 158) and for a sensor at altitude of 675 km and looking perpendicular to the satellite heading to the right. The surface is ocean with Salinity = 35 PSU and T = 20 C. Figure from (Le Vine & Abraham, 2002).

In terms of sensitivity, a variation on the SSS of 0.1 K can represent an error up to 0.2 psu, which is paramount; and in SM, 3 K corresponds to an error of 0.04 $^{m^3}/_{m^3}$. For this reason, it is crucial to compensate the FRA in order to obtain more accurate SSS and SM retrievals. To do so, either FRA external data sources or VTEC datasets, and Eq. (3.1) can be used.

3.2. VTEC and FRA Data Sources

There are different types of data sources that can be used to compute the FRA: models or datasets coming from satellites.

3.2.1. Models

There are a variety of VTEC models available (Radicella, 2009). Only the most relevant climatological ones of the ionosphere are going to be commented in this section. They correspond to the ones studied for the SMOS mission (Floury, 2007).

3.2.1.1. International Reference Ionosphere (IRI)

With its latest release in 2018, IRI (International Reference Ionosphere) project goal has been developing an international standard for the specification of plasma parameters in the Earth's ionosphere. It consists of a data-based model that uses most of the available and reliable observations of the ionospheric plasma from the ground and space to represent monthly averages of electron and ion densities and temperatures in the altitude range of 50 km to 2000 km as well as the VTEC from lower boundary (60-80 km). It is able to avoid the uncertainty of theory-based models that comes from the lack of theoretical understanding. The project started in 1968 and it has become the International Organization for Standardization ISO for the ionosphere in 2014 (Bilitza et al., 2017).

3.2.1.2. Parameterized Ionosphere Model (PIM)

The Parameterized Ionospheric Model (PIM) consists of a theoretical global model built by combining three models: the Global Theoretical Ionospheric Model (GTIM) for low and middle latitudes, the Time Dependent Ionospheric Model (TDIM) for high latitudes, and the empirical Gallagher's model (Gallagher et al., 1988) for plasmaspheric altitudes. The output data corresponds to electron density and ion composition profiles as well as profile parameters such as the total electron content among others on a global or regional grid (Daniell et al., 1995).

3.2.1.3. New Quick-run Model (NeQuick)

It is a Quick-run model that describes the electron density of the ionosphere up to the peak of the F2 layer (2000 km). It uses a profile formulation that includes the model of five layers empirically determined with height-dependent thickness parameters. The model depends on the solar activity (given by the sunspot number R12 or 10.7 cm solar radio flux F10.7), the season (month), and the Universal Time (UT). The data is provided in terms of the ionosphere height and geocentric coordinates using routines that evaluate the electron

density along any ground-to-satellite straight line ray-path and its corresponding Total electron Content (Hochegger et al., 2000), (Nava et al., 2008).

3.2.2. Datasets Coming from Satellite's Data

There are FRA or VTEC datasets coming from different satellites. Some of them are:

3.2.2.1. Aquarius/SAC-D Mission

This mission was developed as a partnership between NASA (National Aeronautics and Space Administration) and CONAE (*Comisión Nacional de Actividades Espaciales, Argentina*) consisting of the combination of an active and a passive instruments that worked in the L-band. Aquarius was able to provide global SSS maps from August 2011 to June 2015. Its primary instrument, composed of three real aperture radiometers with a total wide swath of 390 km, was used to retrieve the salinity; and the active one, to provide information for the correction of major errors, such as the roughness. The radiometers had different incidence angles (29.2°, 38.4°, and 46.3°) and were used to measure both the vertical and horizontal polarizations. In addition, the instrument included a polarimetric radiometer channel that enabled the measurement of the sum and difference of both polarizations (i.e., $V \pm H$), making possible to obtain the third Stokes parameter in order to correct the FRA in its data (Lagerloef et al., 2008), (Le Vine et al., 2014).

The second Q_A and third U_A Stokes parameters measured by the satellite antenna are related to those emitted from de surface by:

$$Q_A = Q\cos(2\Psi) \tag{3.2}$$

$$U_A = -Q\sin(2\Psi) \tag{3.3}$$

where the subscription A denotes the satellites measurements, Ψ corresponds to the rotation angle including both the geometric and Faraday Rotation angles defined in the antenna reference, and the contribution of U is neglected. Then the total angle is calculated as:

$$\Psi = -\frac{1}{2}\tan^{-1}\left(\frac{U_A}{Q_A}\right) \tag{3.4}$$

Based on the retrieved Faraday rotation, the Aquarius polarimetric channels appear to be performing well. The retrieved rotation angles are consistent with values predicted using TEC values from the IGS and also with measurements obtained from the Jason-II altimeter that are made at closely coincident points (Le Vine et al., 2013).

3.2.2.2. Soil Moisture Active Passive (SMAP) Mission

NASA developed the Soil Moisture Active Passive (SMAP) mission with the main purpose of providing soil moisture global maps distinguishing frozen from thawed land surfaces. SMAP was launched in January 2015 and consists of an L-band radar and radiometer. Its active part ceased operating in early 2015, but the passive one (radiometer) is still operating flawlessly. It uses a 6-m reflector that produces a conical scanning antenna beam with an incidence angle of approximately 40° and a swath of 1000 km. The radiometer is fully polarimetric producing the third and fourth Stokes parameters (T3 and T4) via complex correlation of the signals at vertical and horizontal polarizations (Entekhabi et al., 2010).

To calculate the Faraday rotation, the ratio of the third and second Stokes parameters is used:

$$\Omega = -\frac{1}{2}\arctan\left(\frac{Ta3}{(Tav - Tah)}\right) \tag{3.5}$$

where the a refers to the measurement at antenna frame, i.e. the output of the antenna, as in Aquarius (Le Vine & Abraham, 2016a) and Ω to the total rotation angle.

Since the antenna is not ideal, a cross-pol coupling introduces a bias in the retrieved Faraday rotation. In order to improve this effect, a correction to the radiometer output to account for imperfections in the antenna pattern is applied. On the other hand, to mitigate the effect of noise, they apply a sliding 20-sample window, giving results in agreement when comparing with the FRA calculus using the theoretical formulation (3.1) (Le Vine & Abraham, 2016b). The retrieval of FRA has been shown to work well over homogeneous scenes over ocean. However, the retrieval over land can be noisy and unreliable.

3.2.2.3. International GNSS Service (IGS) VTEC

Since June 1998, the Ionosphere Working Group from the International GNSS (Global Navigation Satellite Systems) Service (IGS), has worked to provide a product with ionosphere vertical total electron content maps with a 2-hour time resolution and 5° x 2.5° spatial resolution (longitude x latitude) in the IONosphere map EXchange format (IONEX). The product comes from the combination of independently calculated VTEC global maps by four different analysis centers: Center for Orbit Determination in Europe (CODE), ESA, Jet Propulsion Laboratory (JPL), and *Universitat Politècnica de Catalunya* (UPC); all of them derived from the dual-frequency Global Navigation Satellite Systems (GNSS) measurements of 384 stations. The VTEC is calculated at the Global Positioning System (GPS) altitude, which is 20000 km.

This working group provides three products: the predicted solution, the rapid one, and final product. The first one is available both one and two days prior; the second one with a latency of less than 24 hours; and the third one, of approximately 11 days later (Hernández-Pajares et al., 2009), (Roma-Dollase et al., 2018). All of them are available in https://cddis.nasa.gov/archive/gnss/products/ionex/.

3.2.2.4. SMOS

Since the beginning of the mission, the compensation of this effect has been considered. In order to correct it, the theoretical formulation (3.1) has been used to calculate the FRA with external sources: the International Geomagnetic Reference Field (IGRF) (Thébault et al., 2015) for the geomagnetic field and the L1 VTEC. The first one corresponds to a series of mathematical models that has been able to describe the large-scale internal part of the Earth's magnetic field between epochs 1900 and the present by the International Association of Geomagnetism and Aeronomy (IAGA). They provide daily global maps with a 5° x 2.5° spatial resolution (longitude x latitude) of both a 5-year prediction and a final product. The second one is explained with more detail as follows.

3.2.2.4.1. L1 VTEC

Even though this VTEC data comes from the IGS VTEC, it is used in the SMOS mission. As mentioned in 3.2.2.3. , the IGS VTEC is given with the total electron content below the GPS altitude (20000 km).

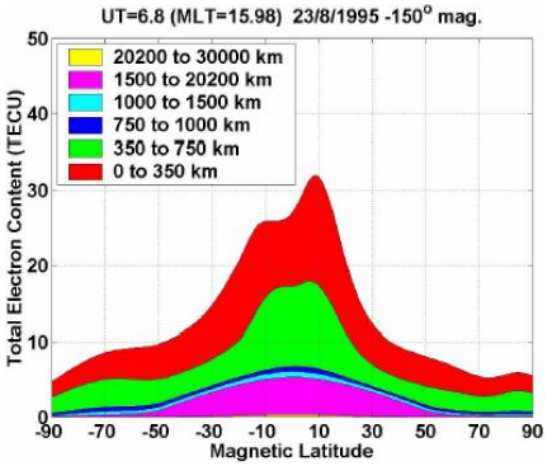

Figure 3.7. Simulated afternoon ionosphere electronic content contribution (Floury, 2007).

Despite the fact that most of the contribution to the ionosphere electronic content lies below the SMOS orbit, there is a non-negligible amount between the SMOS altitude (~800 km) and the GPS one (~20.000 km) as shown in Figure 3.7 for an afternoon simulation. For

this reason, a correction is performed to eliminate the residual TEC that is above the SMOS altitude.

This residual TEC is calculated by the SMOS DPGS using the ratio of NeQuick model at 800 km and 20000 km as follows (Floury, 2007):

$$VTEC_{IGS}^{corrected}(800\ km) = VTEC_{IGS}(20000\ km)\frac{NeQuick(800\ km)}{NeQuick(20000\ km)} \tag{3.6}$$

As it may not be possible to run the NeQuick model for every measurement point, an estimation based on a polynomial fit in terms of the latitude, the longitude, and the solar flux is used:

$$\begin{aligned} VTEC_{IGS}^{corrected,800\ km}(lat, lon) \\ = VTEC_{IGS}(lat, lon) \\ * \left[(A * Solar\ flux + B) + C * \cos\left(D * lat * \frac{\pi}{180}\right)\right] \end{aligned} \tag{3.7}$$

It has to be considered that the VTEC varies considerably between the morning and evening LT. That is why two different set of coefficients have to be applied depending on the LT (see Table 3.1).

Table 3.1. Coefficients for the translation of the IGS from 20000 km to 800 km of altitude

	A	B	C	D
Morning (6 a. m.)	$-1.43 * 10^{-4}$	$8.66 * 10^{-1}$	$3.75 * 10^{-3}$	3.70
Evening (6 p. m.)	$-9.67 * 10^{-5}$	$8.76 * 10^{-1}$	$8.98 * 10^{-3}$	2.03

The morning coefficients are applied for longitudes around +/- 90° centered on the longitude of LT 6 a. m., i.e. between LT 00:00 and 11:59; the evening ones, for longitude of LT 6 p. m., i.e. between LT 12:00 and 23:59 (Crapolicchio, 2008). The information regarding the solar flux is derived from the Penticton solar radio flux, available in https://lasp.colorado.edu/lisird/data/penticton_radio_flux/.

The L1 VTEC has a 2-hour temporal resolution and a 5° x 2.5° spatial resolution and it is available in the SMOS dissemination website (https://smos-diss.eo.esa.int/oads/access/) in the IONEX format with the AUX_VTEC_ name. There are three products per orbit: the prediction (AUX_VTEC_P), the rapid one (AUX_VTEC_R), and the so called "consolidated VTEC" (AUX_VTEC_C). All information related to the VTEC_AUX_ products can be found in (Barbosa, 2021).

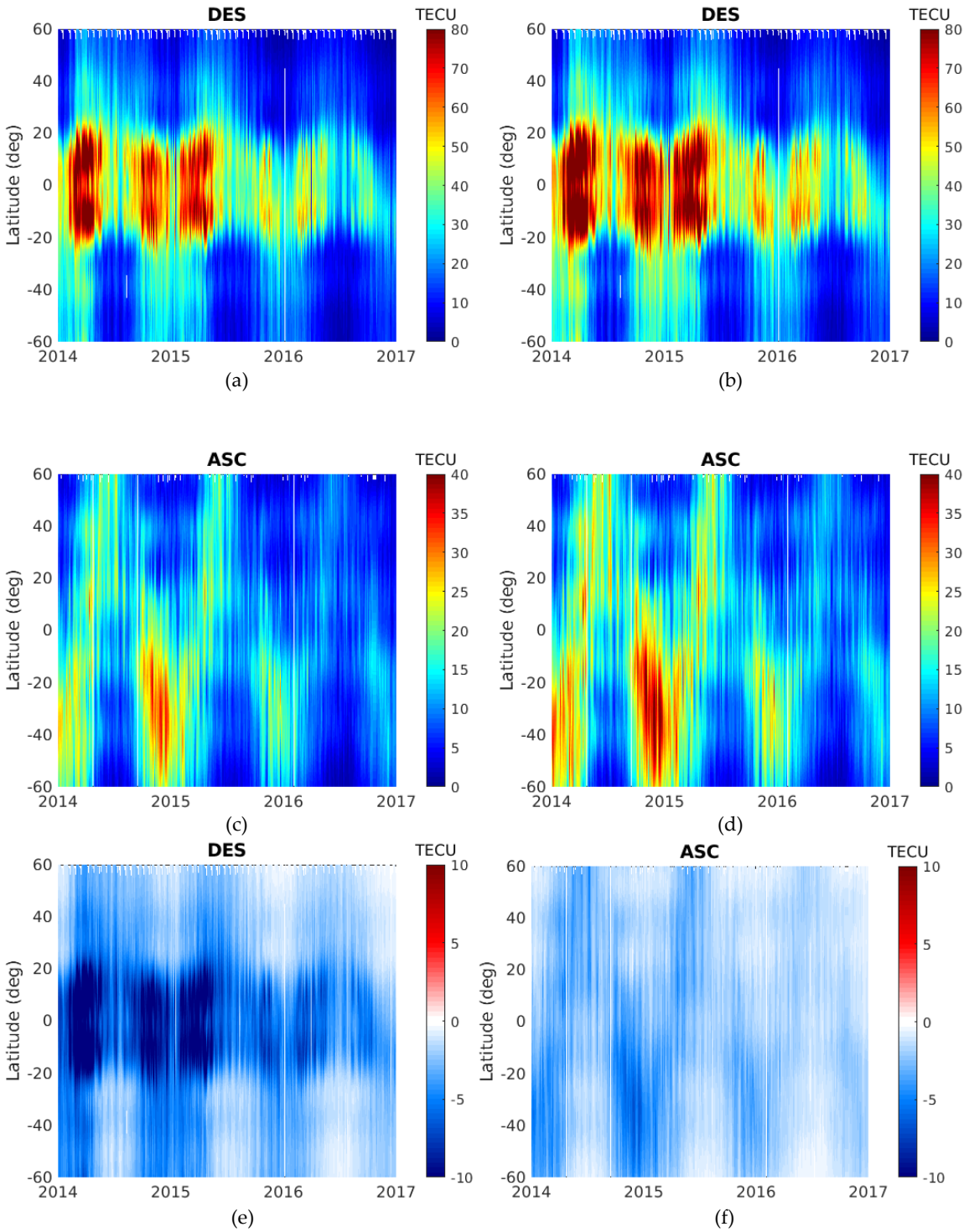

Figure 3.8. VTEC Hövmollers of orbits for the period 2014-2016: (a) L1 VTEC descending-orbit, (b) IGS VTEC descending-orbit, (c) L1 VTEC ascending-orbit, (d) IGS VTEC ascending-orbit, (e) difference between L1 VTEC and the IGS VTEC of descending orbits, (f) difference between L1 VTEC and the IGS VTEC of ascending orbits.

To assess the calculus of the L1 VTEC over the mission, three VTEC Hovmöllers were calculated for three years (2014-2016) and are shown in Figure 3.8: the L1 VTEC, the IGS VTEC and the difference between them (L1 VTEC - IGS VTEC) for descending orbits (Fig. 3.8a, b, and e, respectively), and for ascending orbits (Fig. 3.8c, d, and f, respectively)

As it is expected, the L1 VTEC is always below the IGS VTEC because it considers the vertical electron content of less layers of the atmosphere.

To evaluate the precision of its calculus with the mentioned equation (Eq. (3.7) with Table 3.1), the computation of the corrected IGS VTEC to an altitude of 800 km was done and it is shown in Figure 3.9 in a plot of the VTEC with respect to the latitude of the swath middle pixel of descending orbits. In the left column, the VTEC of three different datasets can be seen: the IGS VTEC in blue, the L1 VTEC in red, and the corrected IGS in black dotted line; and in the right column, the difference between the IGS VTEC and the L1 VTEC. One orbit per year was chosen: March 26, 2014 (Fig. 3.9, top row); November 21, 2015 (Fig. 3.9, middle row); and July 5, 2016 (Fig. 3.9, bottom row).

Different conclusions can be taken. The first one is that the calculus of the L1 VTEC through the mission has been done in the same way despite the years. In addition, it is probable that there might be a linear relationship between the difference of the L1 VTEC and the IGS VTEC with respect to the L1 VTEC and also with respect to the solar flux. This is realized when analyzing the difference between the IGS VTEC and the L1 VTEC in Fig 3.9 (right column) for the different years. In these plots, it is important to be aware of the different scales.

To analyze if there is an existing relationship between these variables, the correlation of both variables was calculated for descending orbits. In Figure 3.10, it is shown, the correlation between the difference of the L1 VTEC and the IGS VTEC with respect to both the L1 VTEC (in the left); and with respect to the solar activity (in the right) in the latitude range [20S, 20N], which corresponds to the region with more VTEC variability.

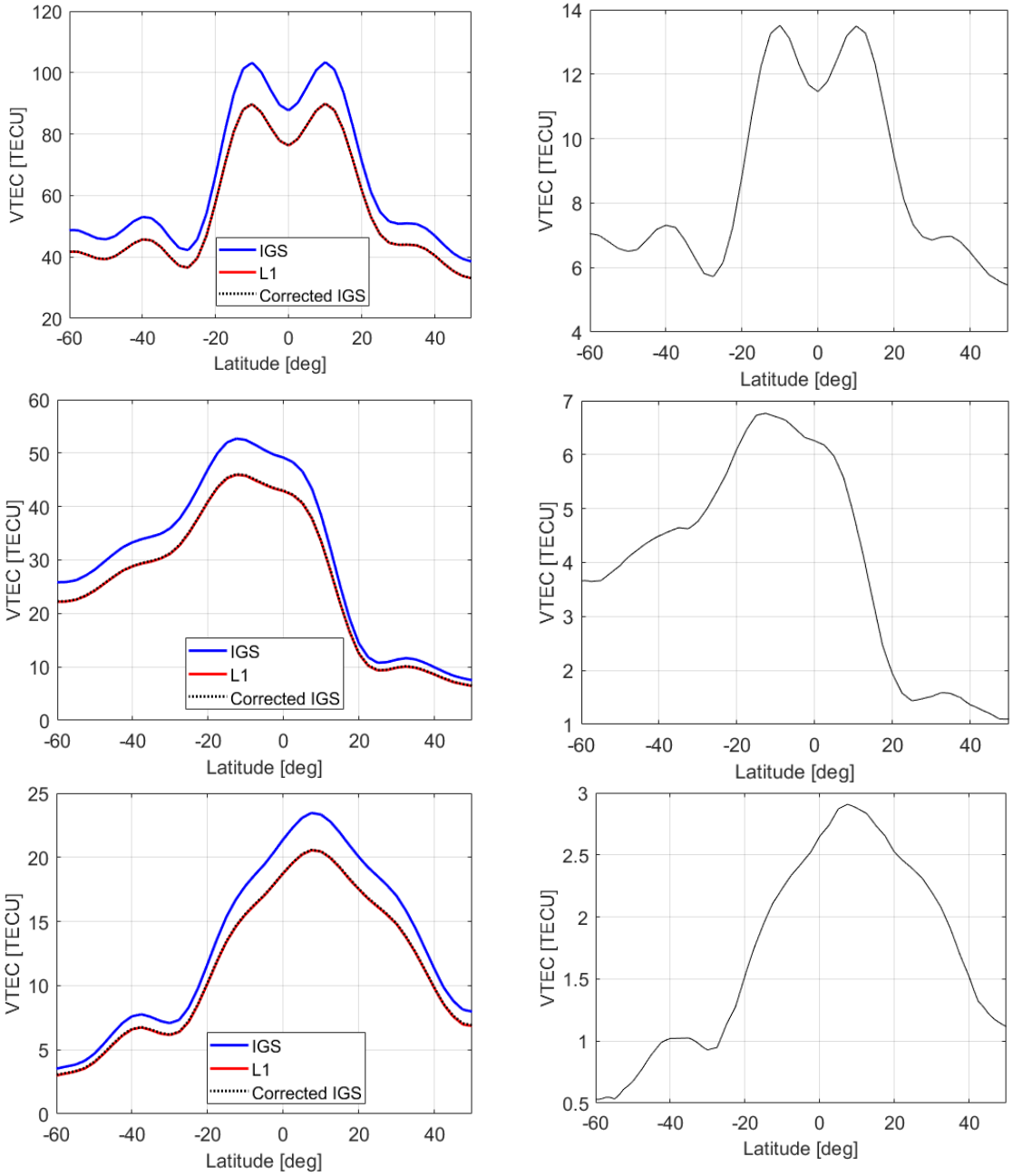

Figure 3.9. VTEC vs latitude of the middle pixel of a descending orbit (left: IGS in blue, L1 in red, and corrected IGS in dotted IGS; right: IGS VTEC - L1 VTEC). Top: March, 2014; middle: November, 2015; bottom: July, 2016.

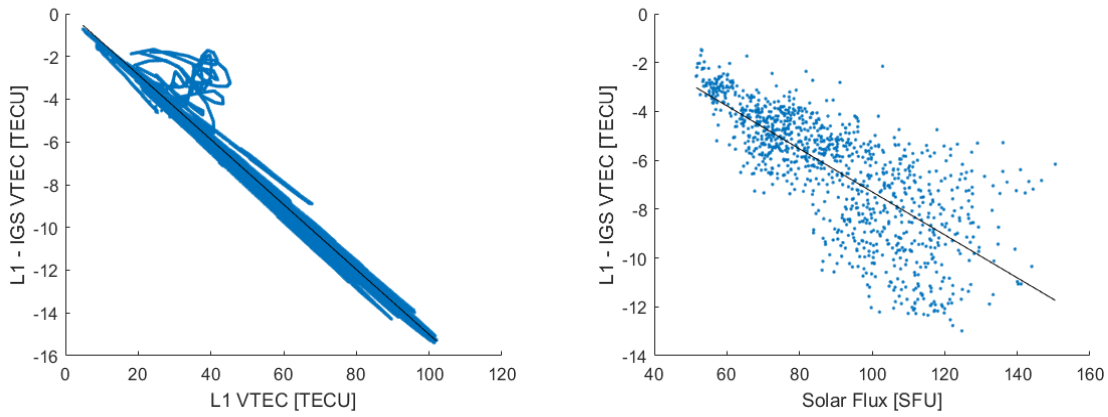

Figure 3.10. Correlation of the difference of the L1 VTEC and the IGS VTEC with respect to: (a) the L1 VTEC and (b) the solar activity.

The correlation of the variables in Fig. 3.10a is -0.996. This shows the good correspondence that there is between both variables. It catches the attention the important variation that there is between 20 and 40 TECU (Total Electron Content Unit) in the L1 VTEC, which shows that at that range of values, the difference between the L1 VTEC and the IGS VTEC is less stable. Furthermore, there is also a good correlation between the difference of the L1 VTEC and the IGS VTEC and the solar flux, which corresponds to -0.75.

3.2.2.4.2. SMOS Radiometric Data

Several efforts have been made in order to extract the FRA/VTEC from SMOS radiometric data.

3.2.2.4.2.1. A3TEC (Total Electron Content from Third Stokes Parameter at Antenna Level)

The L2 salinity team developed a methodology to calculate the VTEC from the SMOS radiometric data. It consists on applying a first order Taylor approximation starting with the use of the L1 VTEC (Vergely et al., 2014):

$$TEC_{A3} = TEC_{L1} + \frac{dTEC}{dA3}[A3 - A3_M(TEC_{L1}) - OTT] \tag{3.8}$$

where $A3$ corresponds to the T3 over the antenna frame. The term TEC_{L1} corresponds to the L1 TEC, $A3_M(TEC_{L1})$ to the radiative model (Zine et al., 2008) where the L1 TEC is used, $\frac{dTEC}{dA3}$ to the sensitivity of TEC to A3 measurements and the OTT to the Ocean Target Transformation (OTT). The OTT compensates the systematic biases present in SMOS caused

by the imperfections in the instrument calibrations, image reconstruction, TB forward model, and external sources such as the Sun and galaxy (Yin et al., 2013).

This computation is done in the zone of the FoV that has the highest VTEC sensitivity with respect to the A3 (Fig. 3.11a). That zone corresponds to the 60° incidence angle circle, specifically circle [$\xi = 0, \eta = 0.2$] as shown in Fig. 3.11b (cyan square).

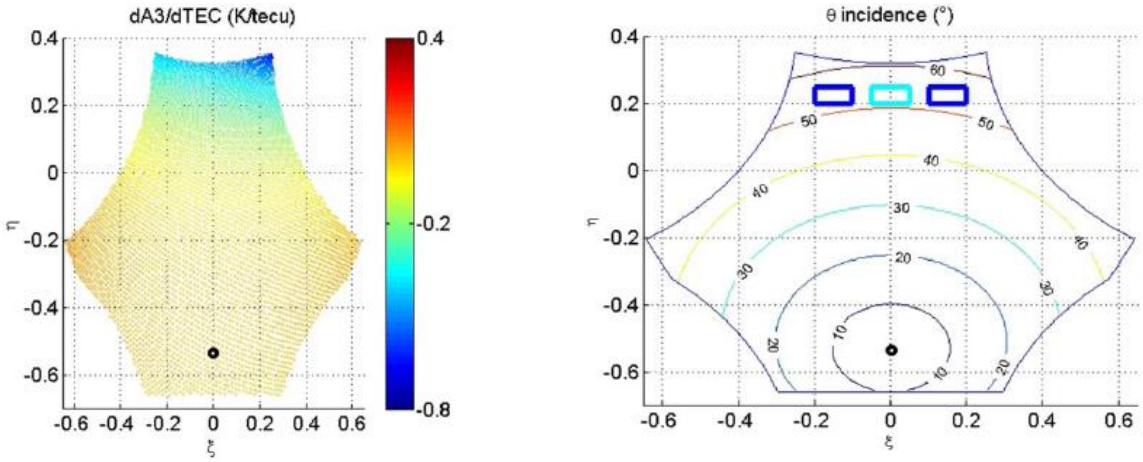

(a) (b)

Figure 3.11. VTEC sensitivity with respect to the A3 (figure 1 from Vergely et al., 2014): (a) magnitude, and (b) zone of the FoV with highest sensitivity.

This product can also be downloaded from the SMOS dissemination website with the name AUX_DTBXY_ <*instance_ID*>. The description of the product is detailed in (Bengoa, 2020). It is noteworthy mentioning that it provides only one VTEC value per snapshot.

SMOS-derived TEC were compared to TEC maps based on GPS measurements. Overall satisfactory agreement is found; the well-known equatorial anomaly is present and emphasized in the SMOS-derived TEC, owing most probably to the better spatial resolution. Discrepancies for high latitudes, especially on the Southern Hemisphere where TECA3 values are found close to zero have been found. Only the FOV region with the highest sensitivity to TEC has been considered and also the study is focused on SMOS data collected over the oceans.

3.2.2.4.2.2. FRA from TB

Corbella et al. (2015) developed a methodology that is able to retrieve the FRA from SMOS radiometric data. It comes from Eq. (2.55) that is repeated here for better understanding:

$$\begin{bmatrix} T_B^{xx} \\ 2\Re e\left[T_B^{xy}\right] \\ T_B^{yy} \end{bmatrix} = \begin{bmatrix} \cos^2(\varphi+\Omega_f) & \sin^2(\varphi+\Omega_f) \\ -\sin 2(\varphi+\Omega_f) & \sin 2(\varphi+\Omega_f) \\ \sin^2(\varphi+\Omega_f) & \cos^2(\varphi+\Omega_f) \end{bmatrix} \begin{bmatrix} T_B^{hh} \\ T_B^{vv} \end{bmatrix} \quad (3.9)$$

By dividing the second row of the system over the sum of the first and third ones then:

$$\Omega_f = -\varphi - \frac{1}{2} arctan\left(\frac{2\Re e\left(T_B^{xy}\right)}{T_B^{xx} - T_B^{yy}}\right) \quad (3.10)$$

This equation is equivalent to (22) of (Yueh et al., 1999) but it is written in terms of the SMOS level 1 products. The equation is used to calculate an instantaneous value of the FRA for the entire FoV, to then, being able to obtain the rotated T_B^{hh} and T_B^{vv} over ground. However, there are some singularities that arises from Eq. (3.10). There are two different cases:

1. When $T_B^{hh} = T_B^{vv}$ and $2\Re e\left[T_B^{xy}\right] = 0$. Rewriting equations from Eq. (3.9),

$$T_B^{xx} = T_B^{hh} * \left[\cos^2(\varphi+\Omega_f) + \sin^2(\varphi+\Omega_f)\right] \quad (3.11)$$

$$T_B^{yy} = T_B^{vv} * \left[\sin^2(\varphi+\Omega_f) + \cos^2(\varphi+\Omega_f)\right] \quad (3.12)$$

$$2\Re e\left[T_B^{xy}\right] = 0 \quad (3.13)$$

   This makes $T_B^{xx} = T_B^{yy}$, so the arctangent argument of Eq. (3.10) would be $\frac{0}{0}$ and the Faraday rotation angle cannot be recovered. That does not mean that T_B^{hh} and T_B^{vv} cannot be retrieved. It means that $T_B^{xx} = T_B^{hh}$ and $T_B^{yy} = T_B^{vv}$ despite the value of the Ω_f.

2. When $T_B^{xx} = T_B^{yy}$. By equalizing equation 1 and 3 of Eq. (3.9) and working it out, Eq. (3.14) is obtained.

$$T_B^{hh} * \left[\cos^2(\varphi+\Omega_f) - \sin^2(\varphi+\Omega_f)\right] = T_B^{vv} * \left[\cos^2(\varphi+\Omega_f) - \sin^2(\varphi+\Omega_f)\right] \quad (3.14)$$

   There are two possible solutions:

   a. If $\cos^2(\varphi+\Omega_f) - \sin^2(\varphi+\Omega_f) \neq 0$, the term in the expression cancels out, and case 1 applies.

b. If $\cos^2(\varphi + \Omega_f) - \sin^2(\varphi + \Omega_f) = 0$, the term cannot be canceled out. $\cos^2(\varphi + \Omega_f) = \sin^2(\varphi + \Omega_f)$, which means that $\varphi + \Omega_f = \pm\frac{\pi}{4}$. Working out equations 1, 2, and 3 from Eq. (3.9), it is obtained:

$$T_B^{xx} = \frac{1}{2} * \left(T_B^{hh} + T_B^{vv}\right) \tag{3.15}$$

$$T_B^{yy} = \frac{1}{2} * \left(T_B^{hh} + T_B^{vv}\right) \tag{3.16}$$

$$2\Re e\left[T_B^{xy}\right] = \left(T_B^{hh} - T_B^{vv}\right) * \sin 2\left(\varphi + \Omega_f\right) = T_B^{hh} - T_B^{vv} \tag{3.17}$$

Multiplying by 2 Eq. (3.15) and adding to it Eq. (3.17), and the same for (3.16),

$$T_B^{vv} = T_B^{xx} + \frac{1}{2} 2\Re e\left[T_B^{xy}\right] \tag{3.18}$$

$$T_B^{hh} = T_B^{yy} - \frac{1}{2} 2\Re e\left[T_B^{xy}\right] \tag{3.19}$$

Therefore, both T_B^{hh} and T_B^{vv} can be calculated from T_B^{xx} and T_B^{yy}.

SMOS images present spatial errors due to calibration inaccuracy, image reconstruction artifacts, and antenna pattern uncertainty (Corbella et al., 2013). They are degraded by thermal noise as well. All these cause limitations in the quality of the retrieval not making possible the usage of the methodology to get instantaneous values of FRA at each pixel of the FoV.

Applying temporal and spatial filtering techniques reduce these effects. Therefore, the retrieval is done only in a reference area of the FoV where there is lowest thermal noise and minimum image reconstruction artifacts (Corbella et al., 2011). The chosen area corresponds to a circle of radius 0.3 around the boresight as depicted in white in Fig. 3.12a. That figure shows the typical total rotation angle of a snapshot (φ_T) and the black dot, the position of the boresight. It can be seen that the chosen area includes only part of the AF-FoV, avoiding pixels with 45° rotation. Once the FRA is calculated in the chosen area, it is averaged and assigned to the boresight.

Even though this methodology is able to reproduce the natural variation of the Faraday rotation, it was realized that the assignment of just one FRA value for the entire FoV is not representative due to the important variation of the FRA in the SMOS FoV. To perceive this, Fig. 3.12b and 3.12c are shown. The FRA is computed in this case using Eq. (3.1) with the L1 VTEC and the IGRF. In the first one, it can be seen the FRA of a snapshot from a descending

orbit over the Pacific on March 20, 2014 (high solar activity) at 2.75° of latitude. Both the standard deviation (bottom left) and averaged FRA value (bottom right) are shown for the circle of 0.3. In the second figure, the error within the snapshot when using the calculated FRA assigned to the boresight for all the pixels in the FoV with respect to the value computed for every pixel is shown.

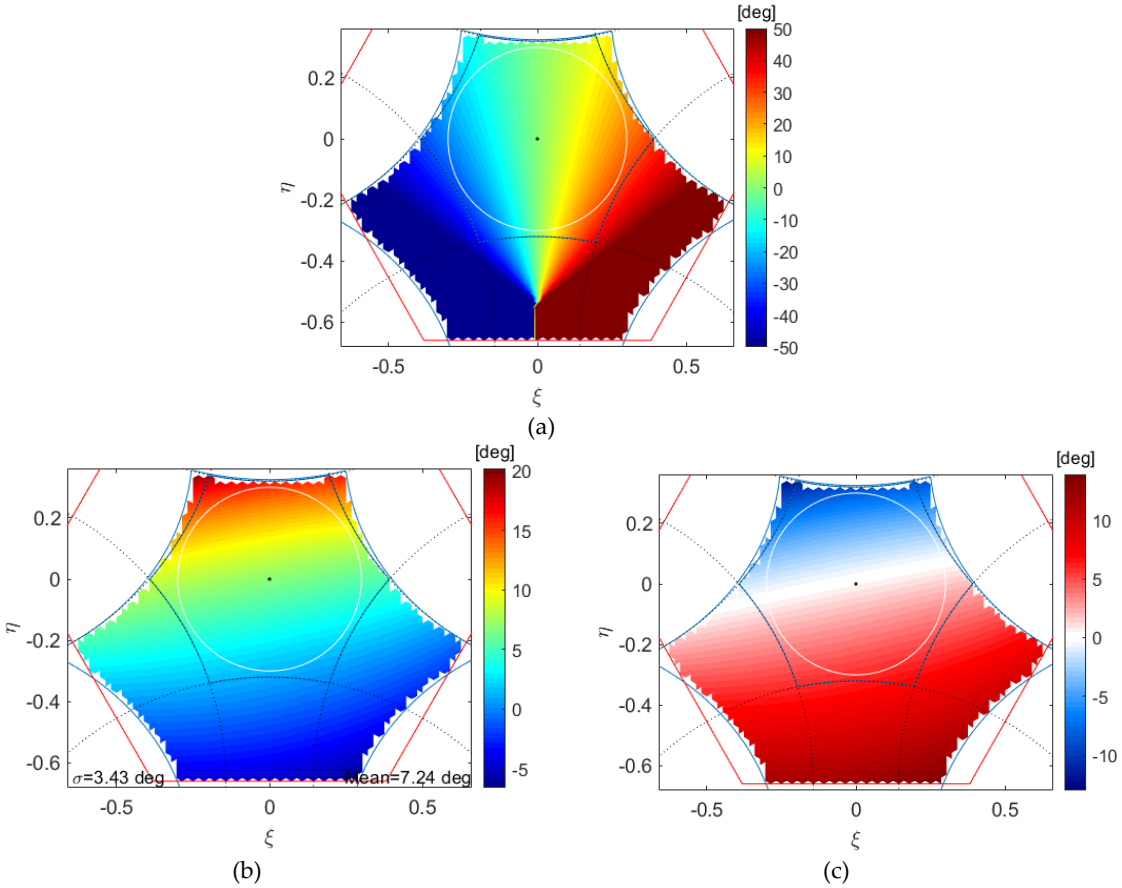

Figure 3.12. FRA over a snapshot: (a) total angle and reference area, (b) FRA from VTEC and the IGRF , and (c) error between using the averaged FRA in the reference area assigned to the boresight with respect to the FRA of every pixel.

3.3. Implementation of SMOS FRA End-to-End Simulator

In order to evaluate different approaches and find the best one to retrieve the FRA from SMOS radiometric data, a FRA end-to-end simulator was developed (Rubino et al., 2017) at the beginning of this thesis. It consists of emulating the TB at the antenna frame, to then extract the FRA from them.

3.3.1. Modeled TB

For each snapshot, the ξ and η coordinates defined in the antenna frame (director cosine plane) at 450 km of altitude are translated to Earth's surface coordinates. The incidence angle θ and the geometric rotation angle φ are computed using standard geometry.

Then, a simple geophysical model is used to simulate the emission of the Earth. Ocean TB are built by assuming a Fresnel model with a typical salinity value of 35 PSU and a typical sea surface temperature of 294 K. For land TB, a constant brightness temperature value of 258 K for the h-pol and 285 K for the v-pol are assumed. Typical open ocean TB images per polarization are shown in the top row of Figure 3.13 (left: X-pol, middle: Y-pol, right: third Stokes parameter).

In order to add the Faraday rotation for each pixel, Eq. (3.1) is used together with both the L1 VTEC and the geomagnetic field databases. This Faraday rotation angle derived from external datasets shall be referred to as "L1 FRA" from now on. Once calculated, it is added to the geometrical angle φ to obtain the total rotation φ_T per pixel as defined in Eq. (2.54*)*:

$$\varphi_T = \varphi + \Omega_f \tag{3.20}$$

when simulating the emission of the Earth. Open ocean TB images considering the FRA are shown in Figure 3.13 (middle row).

Then, the effect of noise is also included in the simulator. To do so, first, the radiometric sensitivity per polarization is calculated with Eq. (2.51):

$$\Delta T_B = \Delta S \frac{T_{sys}}{\sqrt{B\tau}} \Omega_a \alpha_w \sqrt{N_v} \tag{3.21}$$

where, for SMOS, $\Delta S = \sqrt{3}d^2/2$; $T_{sys} = T_A + T_R$ –as mentioned in section 2.2.2.1. –, which are different per polarization (see typical values for the open ocean in Table 3.2); $B = 19$ MHz; $\tau = \tau_i * Q$, where τ_i corresponds to the integration time that is 1.2 s for the pure epochs and 0.4 s for the mixed epochs, and $Q = 0.552$ for 1 bit/23 level digital correlator (Corbella et al., 2000); $\Omega_a = 1.4$; $\alpha_w = 0.45$, for a Blackman window; and $N_v = 2791$. The simulated SMOS radiometric sensitivities per polarization and per pixel are shown in Figure 3.14. Accordingly, with the magnitude of T_A and T_R, the radiometric sensitivity in the Y-pol is higher than in the X-pol. On the other hand, because of the shorter integration that the mixed polarization has with respect to the pure ones (0.4 s vs 1.2 s), its radiometric sensitivity is the highest with respect to the pure polarizations (be aware of the scale of Fig. 3.14c with respect to Fig. 3.14a and Fig 3.14b).

Table 3.2. Average antenna temperature (T_A) and average noise receiver temperature (T_R) at the antenna plane (typical values for open ocean).

Polarization	T_A [K]	T_R [K]
X	76.8	203
Y	95.5	206

The noise is added to the TB with a normal distribution of zero mean and a standard deviation equal to the radiometric sensitivity of each pixel. Figure 3.13 (bottom row) shows typical open ocean TB images with FRA including the effect of noise calculated depending on the position of the pixel within the FoV (Camps et al., 1998).

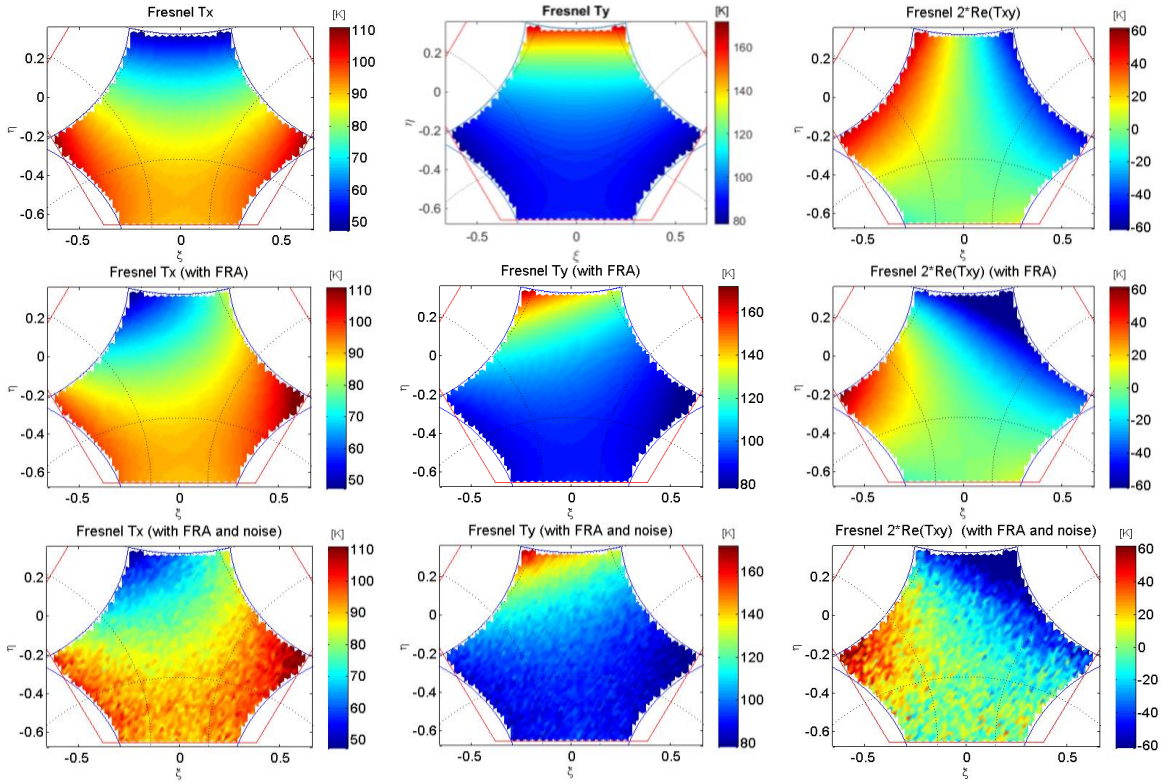

Figure 3.13. Typical open ocean Fresnel brightness temperature snapshots per polarization (left: X-pol, middle: Y-pol, right: third Stokes parameter). Top: Fresnel modeled brightness temperature, middle: considering the FRA, bottom: adding the effect of noise in addition to the FRA.

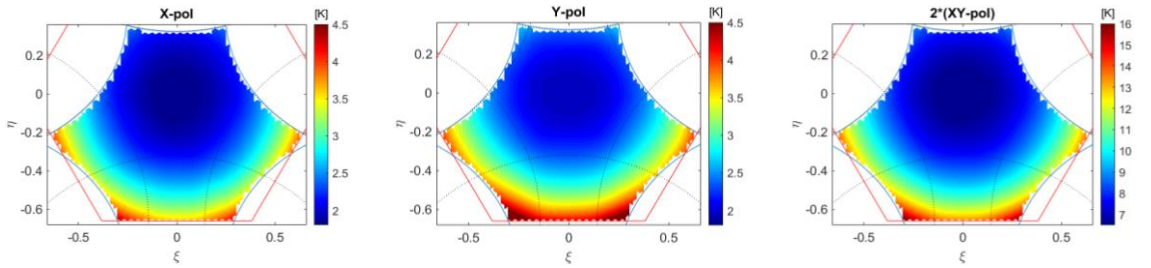

(a) (b) (c)

Figure 3.14. Radiometric sensitivity per polarization: (a) X-pol, (b) Y-pol, (c) mixed polarization.

3.3.2. FRA Retrieval

By using Eq. (3.10) ($\Omega_f = -\varphi - \frac{1}{2}\arctan\left(\frac{2\Re e(T_B^{xy})}{T_B^{xx}-T_B^{yy}}\right)$), the FRA can be retrieved from the TB snapshots. The geometric rotation, φ, is a parameter that, as already mentioned, is specific to the platform attitude and instrument orientation. It is calculated at an altitude of 450 km since the FRA is defined for SMOS at that altitude (Eq. (3.1)).

As it was mentioned in 3.2.2.4.2.2. , a singularity arises from the Eq. (3.10) when both the numerator ($2\Re e(T_B^{xy})$) and the denominator ($T_B^{xx} - T_B^{yy}$) of the expression tend to zero. Figure 3.15 shows two Fresnel TB snapshots emphasizing the zone where they tend to zero (bottom part of the snapshot). It is noticeable that the impossibility of the recovery occurs in the bottom part of the snapshot, a zone that corresponds to low incidence angles.

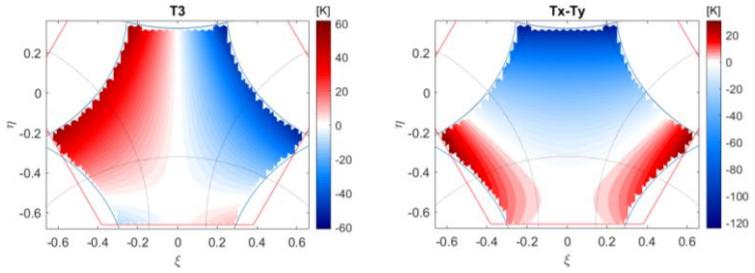

(a) (b)

Figure 3.15. Brightness temperature snapshots emphasizing where it tends to zero: (a) T3, and (b) Tx-Ty.

On the other hand, the calculus of the term $\arctan\left(\frac{2\Re e(T_B^{xy})}{T_B^{xx}-T_B^{yy}}\right)$ is not as simple as it seems. Given that the value of $\arctan\alpha$ is positive, it cannot distinguish whether the angle α is from the first or third quadrant and if it is negative, it could come from the second or fourth quadrant. In order to get back the full information, it must not use the result of the division in Eq. (3.10) but it has to look at the values of numerator and denominator. Thus, in order to retrieve the FRA in the entire snapshot, an assumption has to be made: the lower value is the one chosen, because it is known that the FRA is not higher than 90°.

Figure 3.16 shows a FRA snapshot from a descending orbit over the Pacific from March 20, 2014: in the left, the one calculated using Eq. (3.1) and the L1 VTEC –or so called, L1 FRA snapshot–; in the middle, the recovered FRA one from the TB using Eq. (3.9); and in the right, the difference between the database and the recovered FRA. It is important to remark that Fig 3.16b is calculated assuming that the TB are simulated as if all polarizations are measured in the same instant (ideal case), but this does not happen in SMOS as it was mentioned earlier. This scenario is used to show only how the indetermination affects the recovery.

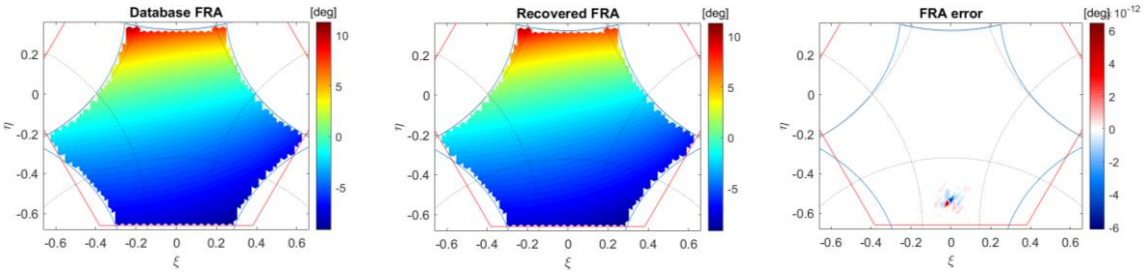

(a) (b) (c)

Figure 3.16. FRA snapshot: (a) L1 FRA, (b) recovered FRA, and (c) difference between the recovered FRA and the L1 FRA.

Even though the TB are ideally simulated, it can be seen in Fig. 3.16c that the FRA is able to be retrieved in the entire snapshot but in the zone where there is the indetermination, that corresponds to low incidence angles. Although it is a small area, when the effect of noise is considered, the error in the retrieval exacerbates, and the mentioned assumption is even more necessary. Any of the solutions of the FRA equation could be the possible value, and so, the aforementioned assumption is even more necessary to calculate the retrieval without affecting its mean.

Figure 3.17 shows the FRA of the same snapshot as in Fig. 3.16 but when considering the effect of noise: in the left, the recovery; and in the right, the error with respect to the L1 FRA. The statistics of the error in the EAF-FoV are also shown, which corresponds to a standard deviation of 22.22° and a mean error of 0.87°. The mean error seems not significant, but it is important to remark that it is given for the entire EAF-FoV and not only for the zone with the highest error.

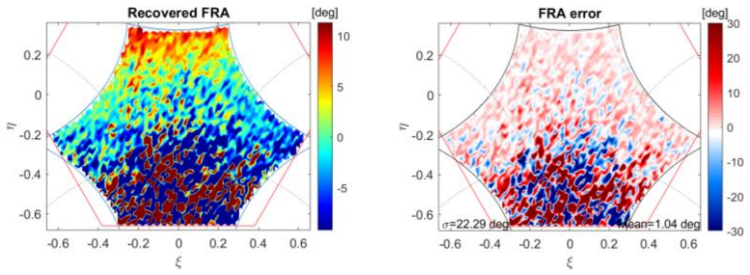

(a) (b)

Figure 3.17. Noisy FRA snapshot: (a) recovered FRA, (b) difference between the recovered FRA and the L1 FRA.

It can be noticed that the effect of the noise introduces an important error. This leads to developing a methodology that makes possible the recovery of the FRA without washing out the geophysical variation of the FRA.

Chapter 4

Faraday Rotation Angle and Vertical Total Electric Content from SMOS Radiometric Data

Estimating the FRA out of the SMOS radiometric data is not a straightforward nor an instantaneous process due to MIRAS radiometric sensitivity (thermal noise), relatively poor accuracy (spatial bias), and image reconstruction artifacts that a single snapshot presents. The retrieved FRA from a single snapshot would be masked by the effect of noise. Thus, to retrieve it with good accuracy, a methodology has to be implemented.

4.1. Recovery with SMOS Simulated Data

This methodology is based on deriving VTEC maps that are only dependent on the longitude and latitude coordinates from SMOS radiometric measurements themselves. These SMOS-derived VTEC maps could be then re-ingested by the L2 processors to correct for the Faraday rotation.

The FRA per snapshot is retrieved by using the SMOS radiometric data (Eq. (3.10)). This equation is shown again in (4.1) in order to make the reading easier.

$$\Omega_f = -\varphi - \frac{1}{2}\arctan\left(\frac{2\Re e\left(T_B^{xy}\right)}{T_B^{xx} - T_B^{yy}}\right) \tag{4.1}$$

Then, the VTEC per snapshot can be computed by solving Eq. (3.1) for VTEC:

$$VTEC = \frac{f^2 \Omega_f \cos\theta}{1.355 \times 10^4 B_0 \cos\Theta_B} \tag{4.2}$$

Once the VTEC is retrieved per snapshot, VTEC maps per each SMOS overpass can be generated and used for the FRA correction at each snapshot.

The analysis is going to be done firstly for a descending orbit (March 20th, 2014). As mentioned in section 3.1. , descending orbits present higher FRA and higher variability than ascending orbits.

4.1.1. FRA and VTEC Computation

As explained in section 3.3.1. , the brightness temperatures emitted by the Earth are simulated with the SMOS realistic measurement scenario; that is, every polarization is acquired in successive instants and the processing, assuming a unique instant. To consider the FRA, the L1 FRA and Eq. **¡Error! No se encuentra el origen de la referencia.** are used. Figure 4.1 shows the FRA and VTEC snapshots of the descending orbit (same date as Fig. 3.16): (a) the L1 FRA used in the simulation; (b) the recovered FRA by applying Eq. (4.1); and (c) the FRA error of the recovery with respect to the L1 FRA.

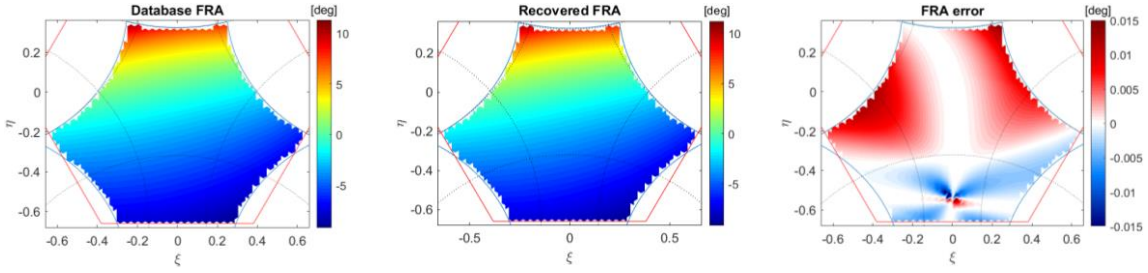

(a) (b) (c)

Figure 4.1. FRA snapshots of a descending orbit simulated with the realistic SMOS measurement scenario: (a) L1 FRA, (b) retrieved FRA, (c) difference between the retrieved FRA and the L1 FRA.

Several conclusions can be drawn. When simulating the SMOS operating mode, a blurring is introduced (Martin-Neira et al., 2002) in the FRA retrieval (Fig. 4.1c). The most affected part of the snapshot corresponds to the lower-incidence-angle (bottom part) because of the indetermination of Eq. (4.1), but actually, it is visible that the retrieval is affected mostly in the entire snapshot.

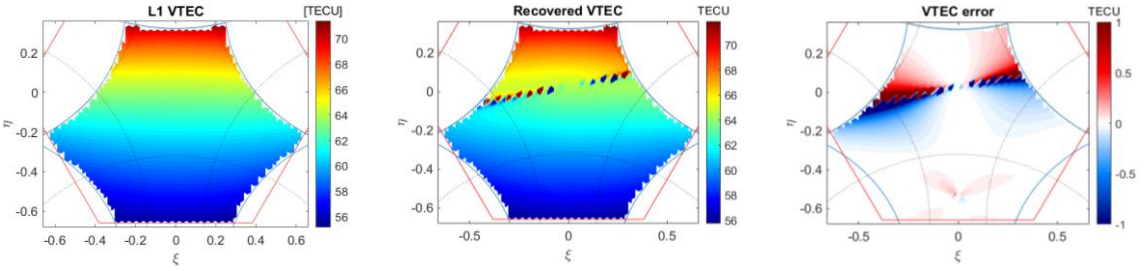

(a) (b) (c)

Figure 4.2. VTEC snapshots of a descending orbit simulated with the realistic SMOS measurement scenario: (a) L1 VTEC, (b) recovered VTEC, and (c) difference between the recovered VTEC and the L1 VTEC.

The retrieved VTEC snapshots from the FRA snapshots in Fig. 4.1 are shown in Figure 4.2. In the left there is the L1 VTEC; in the middle, the recovered VTEC using Eq. (4.2); and in the right, the error of the recovery with respect to the L1 VTEC.

In the recovered VTEC (Fig. 4.2b), it is noticeable that there is a zone where the retrieval is not possible (particularly in this snapshot, in the zone$-0.2 < \eta < 0.2$). This impossibility arises when the geomagnetic field is orthogonal to the wave propagation direction ($\cos\Theta_B \approx 0$) when solving the equation (4.2).

Figure 4.3 shows the recovered FRA, the FRA error, the recovered VTEC, and the VTEC error snapshots when considering the effect of noise.

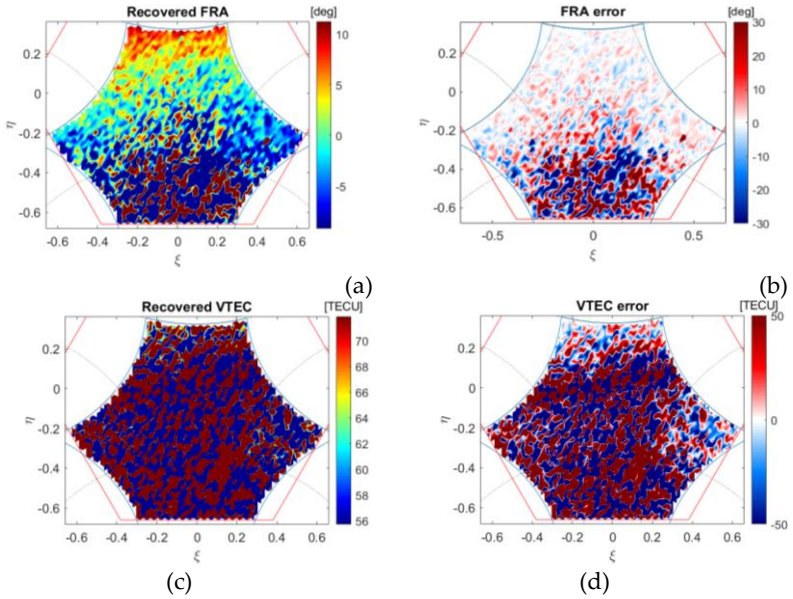

Figure 4.3. FRA and VTEC single snapshot of the descending orbit simulated with the realistic SMOS measurement scenario considering the effect of noise: (a) recovered FRA, (b) difference between the recovered FRA and the L1 FRA, (c) recovered VTEC, (d) difference between the recovered VTEC and the L1 VTEC.

As already mentioned in section 3.3.2. with respect to Fig. 3.17b, the effect of the noise masks the FRA and the VTEC retrieval. Such is the masking that the blurring effect introduced by the SMOS operating mode of measuring and processing at different instants is negligible. The most important issue to deal with is the effect of the noise (Rubino et al., 2018).

4.1.2. Geolocation

Once the VTEC snapshots are retrieved, the geolocation is done at an altitude of 450 km by using an ETOPO-5 grid (resolution of 5 minutes of latitude and longitude). All the measurements acquired over the same grid point are averaged. Figure 4.4 shows the VTEC

maps of a descending orbit over the Pacific (March 20, 2014): Fig. 4.4a, 4.4b, and 4.4c correspond to the L1 VTEC, the recovered VTEC, and the difference between the recovered one and the L1, respectively.

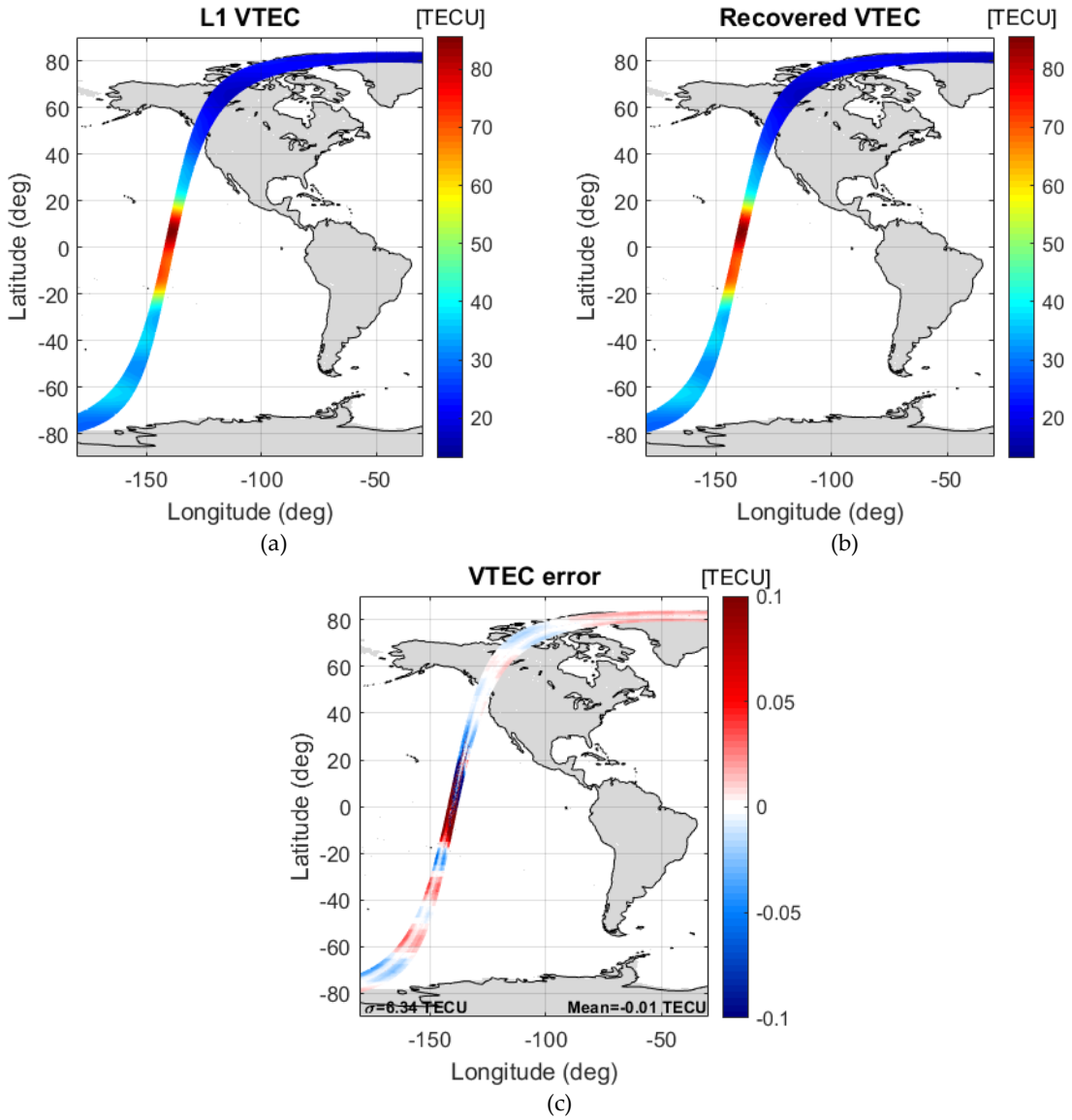

Figure 4.4. VTEC maps of a descending orbit over the Pacific simulated without taking into account the effect of noise: (a) L1 VTEC, (b) recovered VTEC, and (c) VTEC error.

Due to both indeterminations in Eq. (4.1) and Eq. (4.2), the recovery presents a considerable error, which is highest in the zone close to the equator because the geomagnetic field and the wave propagation direction are orthogonal. This error needs to be mitigated.

Figure 4.5 shows the number of averages done per pixel in the generation of the VTEC map. Because of the shape of the EAF-FoV of the snapshot, the laterals of the swath present

a smaller number of averages than the central part. The zone with approximately 20 averages corresponds to calibration events of the local oscillators (every 10 minutes) (Gabarro et al., 2013), (Brown et al., 2008).

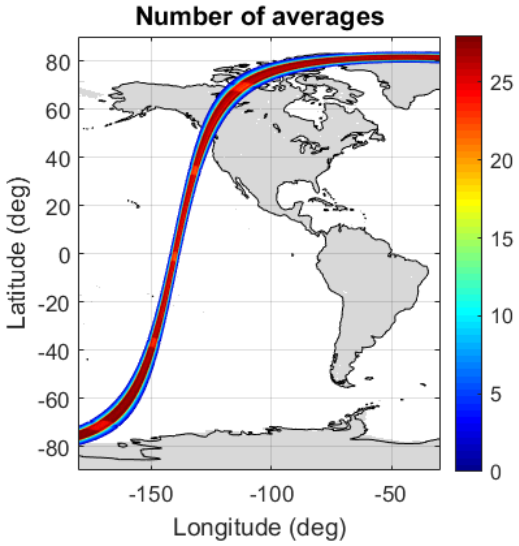

Figure 4.5. Number of averages done per pixel in the generation of the VTEC map.

Figure 4.6 shows the VTEC maps of the descending orbit when considering the effect of noise. The figure in the left corresponds to the recovery; the right one, to the difference between the recovery and the L1 VTEC.

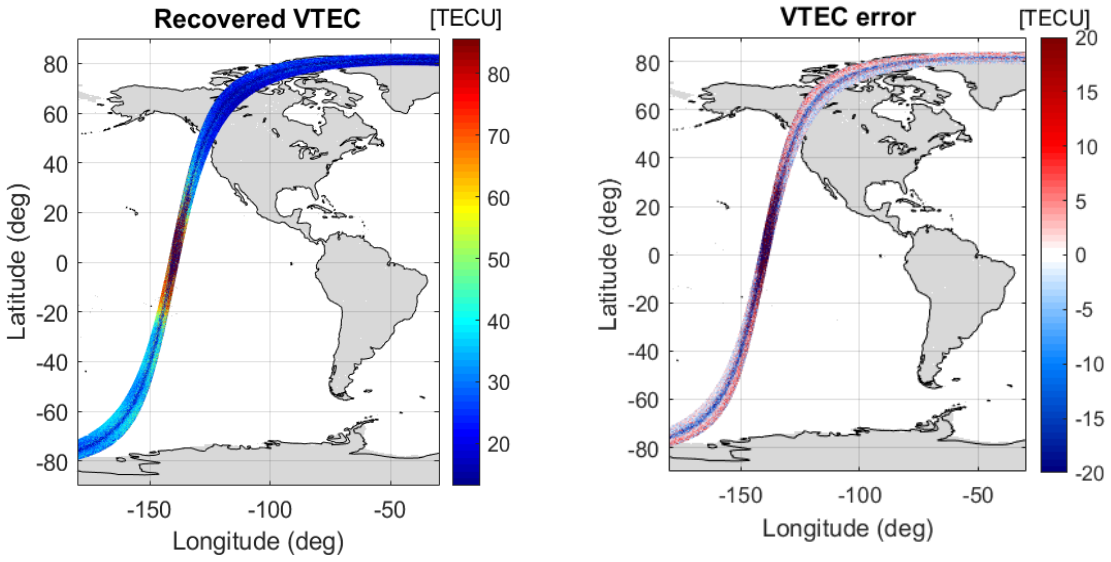

(a) (b)

Figure 4.6. VTEC maps of the descending orbit simulated considering the effect of noise: (a) recovered VTEC and (b) VTEC error.

Even though the VTEC recovery at snapshot level has an important degradation because of the effect of noise (Fig. 4.3d), it can be seen that the VTEC in the recovered map is not totally masked. This is thanks to the average that is done in the generation of the VTEC map (Fig. 4.5). Nevertheless, it is important to remark that the highest error is obtained in the zone where the indetermination in Eq. (4.2) arises. It can also be seen that the recovery in the central part of the swath presents an error that is present in the entire orbit. This is the one caused by the indetermination that emerges from Eq. (4.1).

To avoid introducing errors that are not part of the developed methodology and are negligible compared to the effects of noise, the simulator emulates the ideal SMOS measurements, i.e. all the full-polarization brightness temperatures are measured at the same instant. Figure 4.7 shows the errors in the retrieval of the descending orbit at snapshot level (FRA, Fig. 4.7a; VTEC, Fig. 4.7b) and over the VTEC map (Fig. 4.7c). By taking a look at the scale and the statistics, it is visible that the errors are much lower than when assuming the SMOS operating mode.

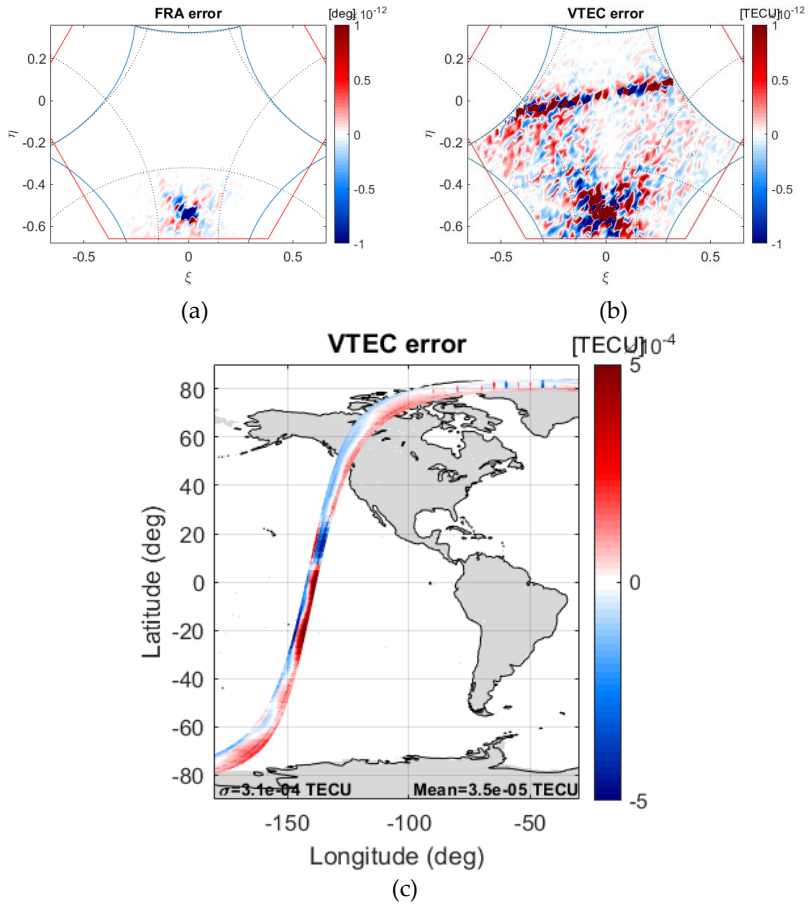

Figure 4.7. Recovery errors of the descending orbit when assuming the brightness temperatures measured at the same instant despite the polarization within each block (not taking into account the effect of noise): (a) FRA snapshot error, (b) VTEC snapshot error, and (c) VTEC map error.

4.1.3. Avoiding the Indetermination when Retrieving the FRA using the SMOS Radiometric Data

As already commented in section 3.3.2. , the indetermination that arises in Eq. (4.1) happens when both the numerator and the denominator tend to 0 ($T_B^{xx} \approx T_B^{yy}$ and $T3 \approx 0$); that occurs in the low-incidence-angle zone of the snapshot (bottom part of the snapshot). For this reason, to avoid this indetermination, measurements acquired under low incidence angles are rejected. The threshold has been empirically selected and corresponds to pixels with incidence angles lower than 25°. Figure 4.8 shows the recovered FRA snapshot and its FRA error.

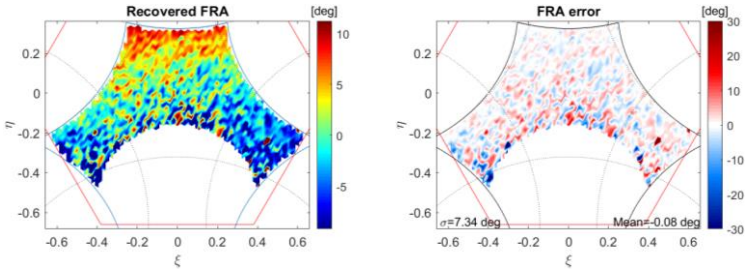

(a) (b)

Figure 4.8. FRA snapshots of the descending orbit avoiding indetermination when retrieving the FRA (taking into account the effect of noise): (a) recovered FRA and (b) FRA error.

Figure 4.9 shows VTEC maps of both the recovery and the error when those pixels that cause the indetermination in (4.1) are rejected. As it can be seen in the figure, even though there are pixels being rejected over the snapshot, the average in the geolocation allows to not have any gap of information in the recovered map.

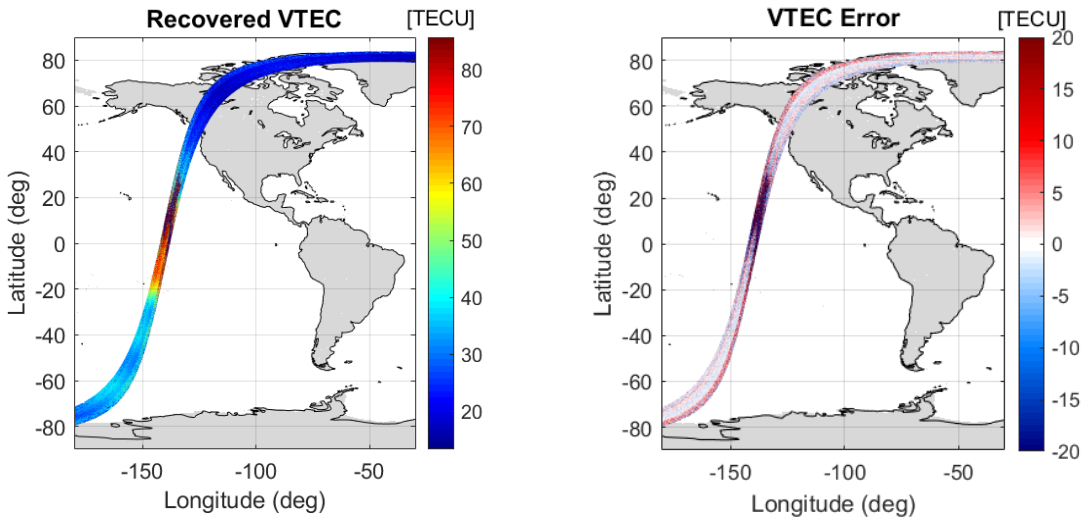

(a) (b)

Figure 4.9. VTEC maps of the descending orbit avoiding the indetermination when retrieving the FRA (taking into account the effect of noise): (a) recovered VTEC and (b) VTEC error.

It can be seen that the error that was in the middle of the swath when not rejecting these pixels (Fig. 4.6) is not present now.

Figure 4.10 shows the number of averages done per pixel in the generation of the VTEC map when avoiding the indetermination of (4.1). In this case, there are a maximum of 24 averages in contrast with the 31 done when not rejecting any pixels (Fig. 4.5). The pixels with the greatest number of averages correspond now to the ones close to the AF-FoV border with the EAF-FoV rather than the ones in the middle of the swath because, now, those are the ones being rejected.

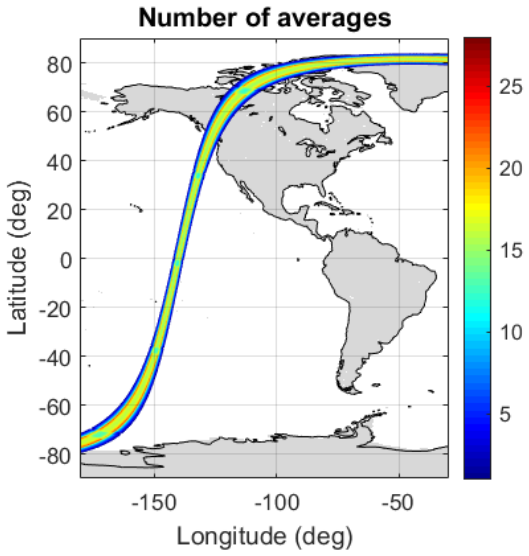

Figure 4.10. Number of averages done per pixel in the geolocation when avoiding the indetermination in Eq. (4.1).

Figure 4.11 shows the retrieved FRA (left) and the FRA error (right) of the ascending-orbit snapshot.

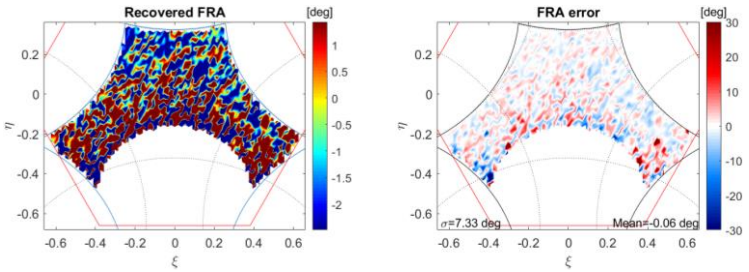

(a) (b)

Figure 4.11. FRA snapshots of the ascending orbit avoiding the indetermination when retrieving the FRA (considering the effect of noise): (a) recovered FRA and (b) FRA error.

4.1.4. Avoiding the Indetermination when Calculating the VTEC from the Retrieved FRA

As it has been mentioned before, Eq. (4.2) presents an indetermination when the direction of the wave propagation and the geomagnetic field are perpendicular. That happens close to the equator. However, this is not latitudinally fixed; it depends on both the geomagnetic direction variation and the type of orbit (descending or ascending).

In order to avoid this indetermination, measurements of pixels with a $\cos\Theta_B$ lower than a given threshold are rejected. The threshold has been empirically selected and corresponds to pixels with a $|\cos\Theta_B| < 0.05$ over TB snapshots (Rubino et al., 2022). Figure 4.12 shows TB snapshots in every polarization when avoiding the indeterminations of both Eq. (4.1) and Eq. (4.2) (in the geomagnetic equator); in the top, one snapshot where the indetermination of Eq. (4.2) starts to arise (the pixels rejected are in the top left corner of the snapshot), and in the bottom, one of the worst scenarios, i.e. most affected by this indetermination.

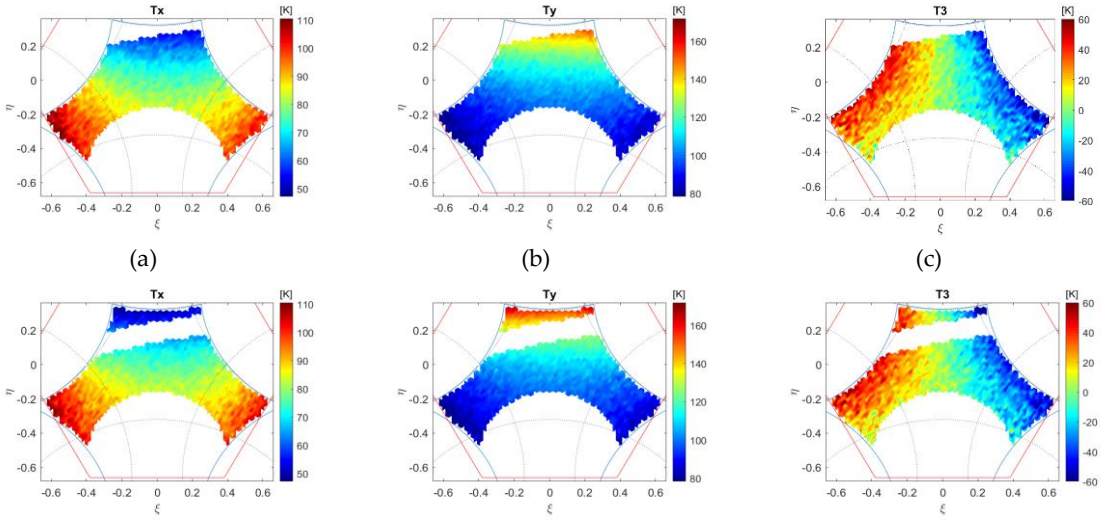

Figure 4.12. Filtered brightness temperature snapshots affected by the indetermination in Eq. (4.2) in the X polarization (left column), Y polarization (middle column), and T3 (right column): (top) snapshot less affected, (bottom) snapshot in the worst scenario.

Figure 4.13 shows the recovered VTEC map (left) and the VTEC error (right) of the descending orbit.

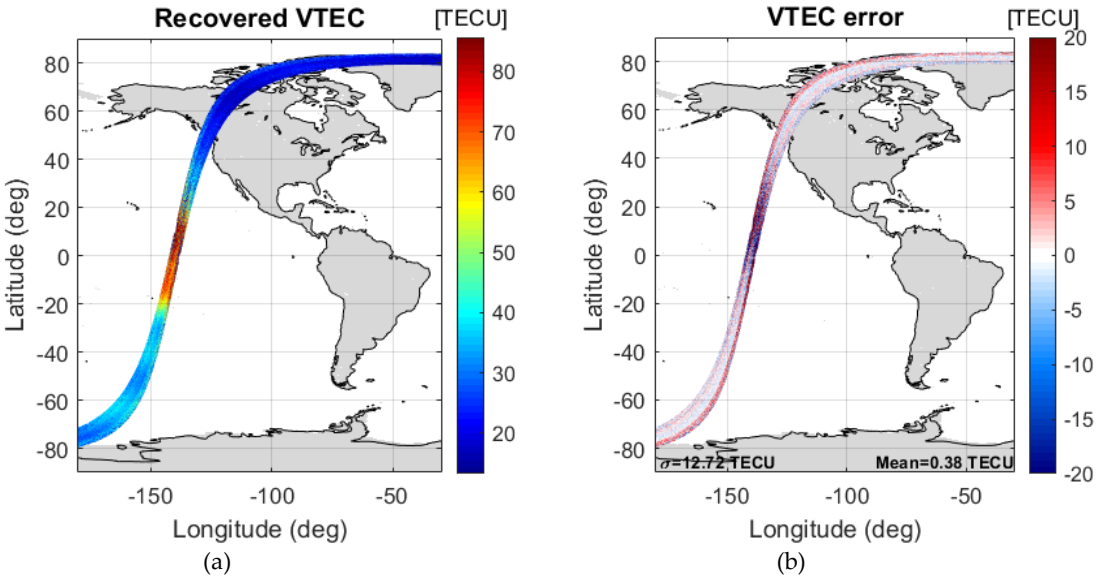

Figure 4.13. Recovered VTEC map of the descending orbit avoiding both indeterminations (considering the effect of noise): (a) recovered VTEC map, and (b) VTEC error map.

Figure 4.14 shows the number of averages done per pixel in the generation of the VTEC map when avoiding both indeterminations. The maximum number of averages per pixel stays the same, but where the geomagnetic field and the wave propagation direction are orthogonal, there are a smaller number of averages because of the rejection of pixels to avoid the indetermination.

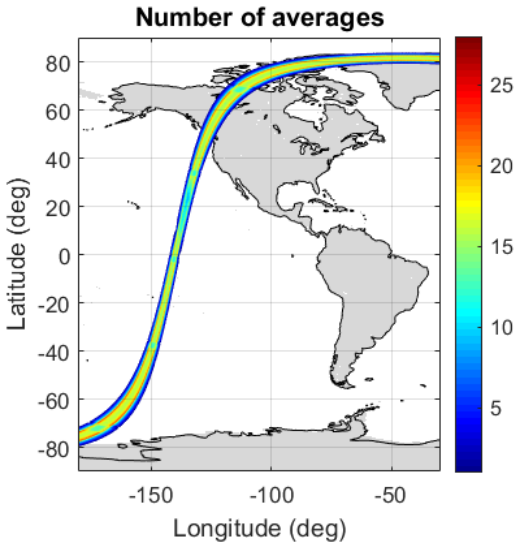

Figure 4.14. Number of averages when avoiding indeterminations in the equations needed in the retrieval.

Due to the rejection of pixels, close to the geomagnetic equator, there is a very small zone where recovery is not possible.

4.1.5. Spatio-temporal Filtering Techniques

To reduce the effect of noise and artifacts in the retrieved VTEC from SMOS data, spatio-temporal filtering techniques are required (Corbella et al., 2015). The sizes of both filters have been optimized with the simulator that considers the effect of noise. The size of both filters has to be carefully optimized considering that they are required to maintain the FRA/VTEC natural variability. The first step was to optimize the size of the temporal filter of TB measurements considering a fixed spatial filter. There are different options to implement the spatial filter: it could be applied at either FRA or VTEC snapshot level, or over the recovered VTEC map. The size of the spatial filter was set to 0.179 in the director cosine plane (10 times the minimum $\Delta\xi$=0.0179), and the temporal filter was applied to TB snapshots by varying its length from 15 to 83 snapshots with a step of 4. The temporal filter consists of an averaging triangular window considering the current snapshot with the highest weight. Figure 4.15 shows the Root Mean Square Error (RMSE) of the recovery with respect to the size of the temporal filter. The optimization was done with descending orbits of two different dates –March 21st, 2011 and March 20th, 2014– and same results were obtained (Rubino et al., 2019b).

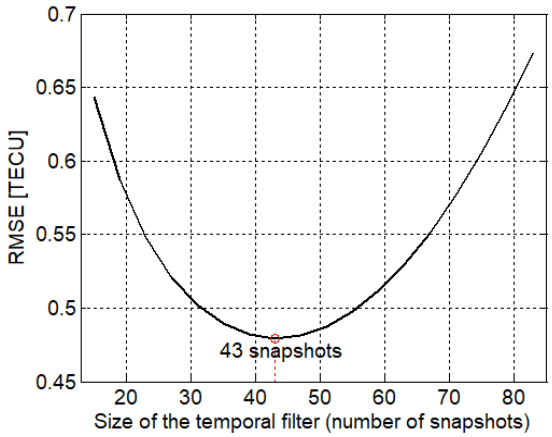

Figure 4.15. Optimization of the temporal filter with a coarse binning (4 snapshots): root mean square error (recovered VTEC - L1 VTEC) vs size of the temporal filter.

Once it is known that the optimal size of the temporal window is 43 snapshots, the spatial filter was optimized by varying its radius from 0.1253 to 0.2506 with a step of 0.0179 over VTEC snapshots. Figure 4.16 shows the RMSE of the recovery error when varying the size of the spatial filter.

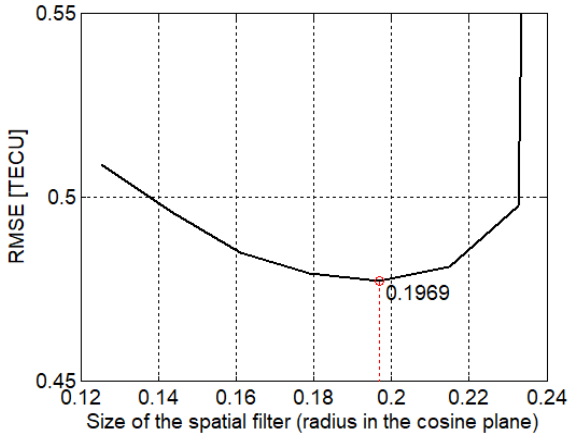

Figure 4.16. Optimization of the spatial filter fixing the temporal filter to 43 snapshots: RMSE vs size of the spatial filter.

Afterwards, a second optimization of the temporal filter was done with a refined binning. The radius size of the spatial filter was set to 0.1969 and the size of the temporal filter was varied from 33 to 69 snapshots with a binning of 2. This optimization is shown in Figure 4.17.

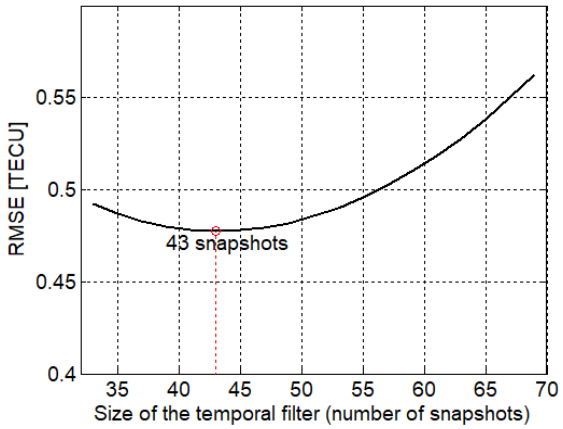

Figure 4.17. Optimization of the temporal filter fixing the spatial filter to 0.1969: RMSE vs size of the temporal filter.

Finally, the spatial filter was optimized with a finer binning. The temporal filter was fixed once again to 43 snapshots, and the radius of the spatial filter was varied to 0.169 to 0.239 with a step of 0.01, and its optimization is shown in Figure 4.18.

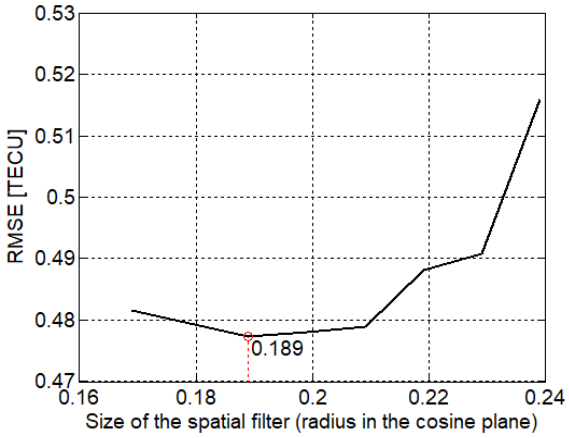

Figure 4.18. Optimization of the spatial filter fixing the temporal filter to 43 snapshots: RMSE error vs size of the spatial filter.

An assessment was done to verify if it is better to apply the spatial filter in the antenna plane (VTEC snapshots) or in the ground plane (recovered VTEC maps). The spatial filter was applied over the VTEC map with a radius of 190 km, which is equivalent to the size of the window used in the antenna plane. There was not a clear improvement in the retrieval, but there was an important difference in the execution time: the calculation over recovered VTEC maps was much slower. Therefore, the spatial filter was decided to be applied at the antenna reference frame.

When applying these spatio-temporal filtering techniques, the effects of noise and artifacts in the retrieval are reduced. Figure 4.19 shows several FRA snapshots of the descending orbit: the L1 FRA (Fig. 4.19a), the recovered FRA (Fig. 4.19b) and its error (Fig. 4.19c), the recovered FRA after applying the 43-snapshot temporal filter in the TB snapshots (Fig. 4.19d) and its error (Fig. 4.19e). The snapshot shown corresponds to a snapshot that does not have the indeterminacy of Eq. (4.2) to see the impact of the filters in all pixels of the snapshot.

The impact of applying the temporal filter can be seen when comparing Fig. 4.19b and Fig. 4.19d, considering the L1 FRA (Fig. 4.19a). When the filter is applied, the FRA physical variation is not as masked by the effect of the noise. This can also be corroborated by comparing the standard deviation (STD) of the error recovery when not applying (Fig. 4.19c) and when applying (Fig. 4.19e) the filter, the STD improves from 6.54° to 1.07°.

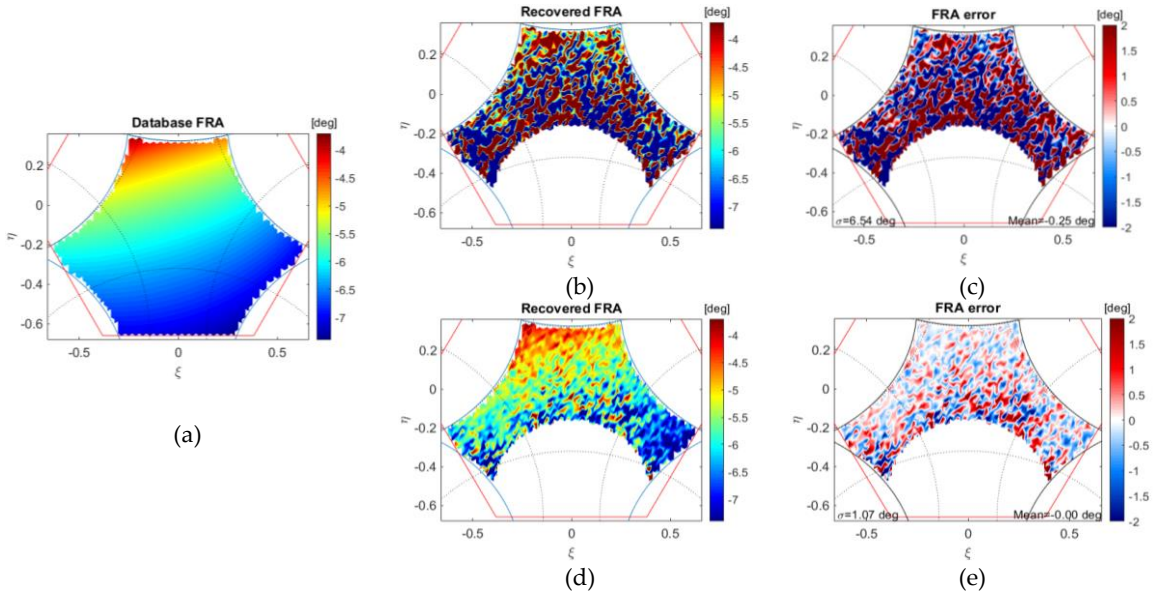

Figure 4.19. FRA snapshots of the descending orbit analyzing the application of the temporal filter: (a) L1 FRA, (b) recovery when not applying the temporal filter, (c) FRA error when not applying the temporal filter, (d) recovery when applying the temporal filter, (e) FRA error when applying the temporal filter.

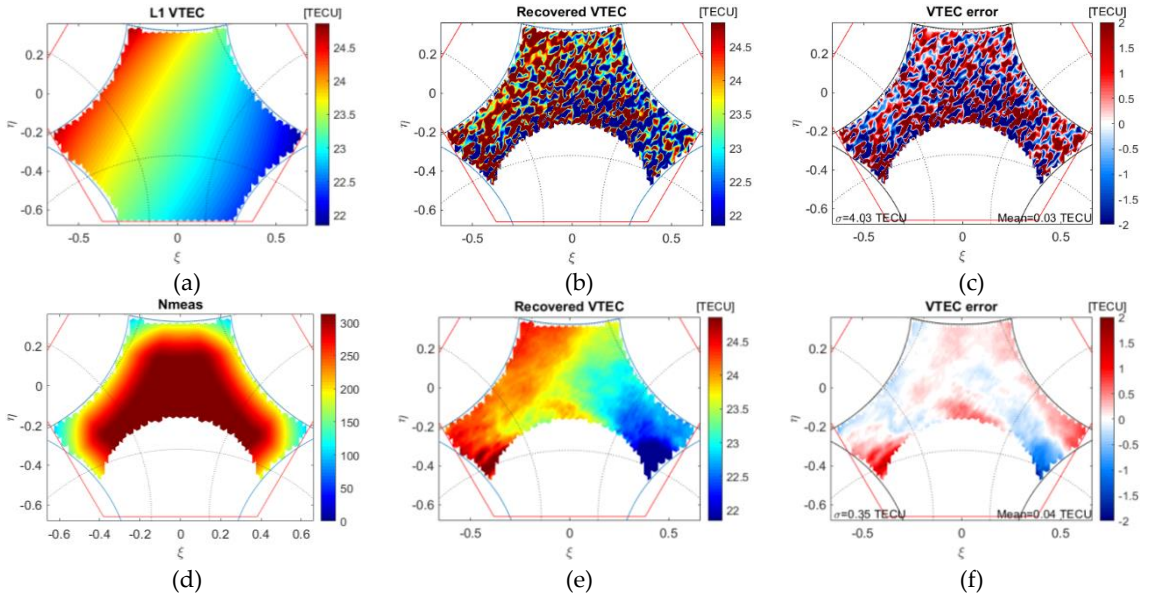

Figure 4.20. VTEC snapshots of the descending orbit analyzing the application of spatio-temporal filtering techniques: (a) L1 VTEC, (b) recovered VTEC before applying the spatial filter, (c) VTEC error before applying the spatial filter, (d) number of averages when applying the spatial filter, (e) recovered VTEC after applying the spatial filter, and (f) VTEC error after applying the spatial filter.

Figure 4.20 shows different VTEC snapshots related to the ones in Fig. 4.19: the L1 VTEC (Fig. 4.20a), the recovered VTEC –once the temporal was applied– (Fig. 4.20b) and its error (Fig. 4.20c), the number of averages done at snapshot level when applying the spatial filter (Fig. 4.20d), the VTEC recovery after applying the spatial filter (Fig. 4.20e) and its error (Fig. 4.20f).

Some conclusions can be drawn when applying the spatial filter to the VTEC snapshots. The improvement in the STD of the error in the recovery is very significant: 0.35 TECU versus 4.03 TECU (without the spatial filter). Regarding the number of averages done when applying this filter, it is much higher in the middle part of the snapshot than in the borders, as expected. As a result, the mitigation of the effect of noise is better in the middle of the snapshot than in the borders.

The VTEC map of the descending orbit when applying the spatio-temporal filtering techniques is shown in Figure 4.21. From now on, this methodology is going to be assumed as the first approach.

It can be seen that the effect of the noise is mitigated to a large extent. The STD of the recovery error goes from 12.72 TECU when not applying the filtering (Fig. 4.13c) to 0.69 TECU (Fig. 4.21b). Note the different scales in the two figures.

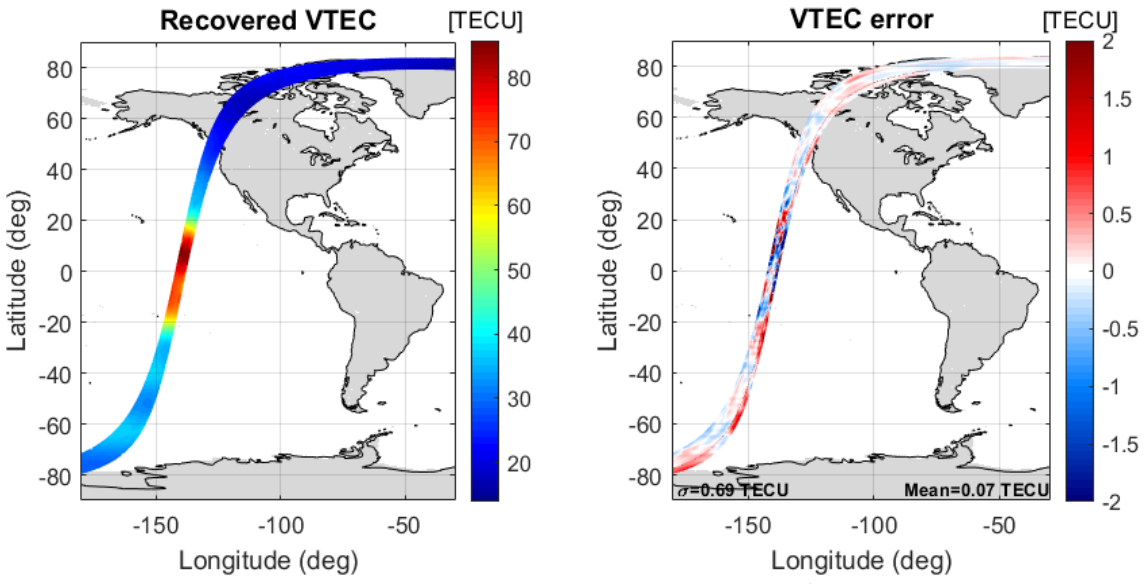

(a) (b)

Figure 4.21. VTEC maps of the descending orbit applying filtering techniques (once the indeterminations are avoided) using the first approach: (a) recovered VTEC and (b) VTEC error.

Figure 4.22 shows the number of averages done per pixel in the generation of the VTEC map once the filtering techniques have been applied.

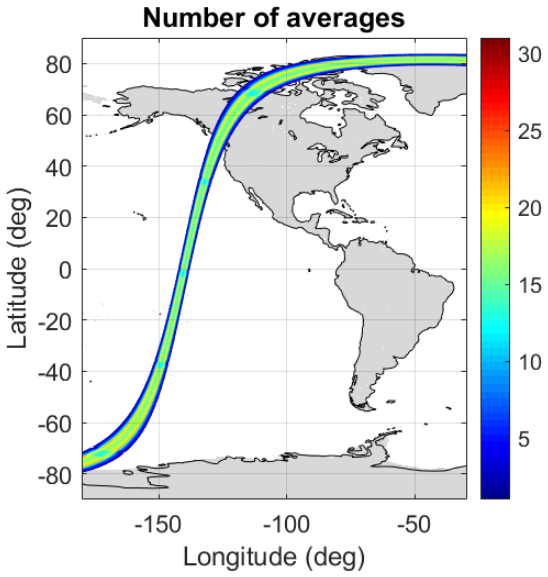

Figure 4.22. Number of averages after applying the filtering techniques.

Since the rejection of pixels to avoid the indetermination of Eq. (4.2) occurs before filtering techniques are applied, all snapshots present TB values in the entire EAF-FoV and this allows for the same number of average values done per pixel in the generation of the VTEC map in the entire orbit.

4.1.6. FRA Recovery from the SMOS-derived VTEC Maps Using the First Approach

Once the VTEC map has been retrieved, it can be used to calculate the FRA with Eq. (3.1). It is noteworthy to mention that even if there is a pixel rejection in the recovered FRA snapshots (section 4.1.3.), the FRA can be calculated for the entire snapshot (including the low-incidence-angle region) from the recovered VTEC maps because they do not present any miss of information.

Figure 4.23 shows plots of the FRA of a pixel in the center of the swath with respect to the latitude of the descending orbit: in the left, a comparison of the retrieved using the first approach (in green) and the L1 FRA (in red), and in the right, the error of the recovery with respect to the L1 FRA.

Even though this simulation considers the effect of the noise, it can be seen that its effect is so well mitigated that the recovery presents a negligible error.

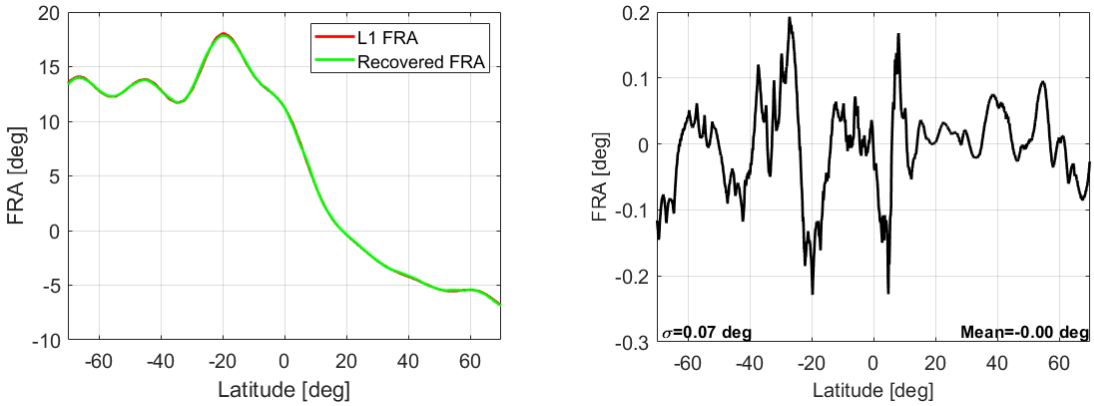

(a) (b)

Figure 4.23. FRA versus latitude of a pixel in the center of the swath along the descending orbit: (a) L1 FRA (red) and retrieved FRA from simulated data using the first approach (green), (b) error of the retrieved FRA with respect to the L1 FRA.

4.1.7. Analysis for Ascending Orbits

In the ascending orbit, there is not a different scenario with respect to a descending orbit. There are errors in the retrieval caused by both indeterminations in equations (4.1) and (4.2), and by the effect of the noise. Actually, for ascending orbits, the effect of noise causes a higher deterioration in the retrieval because of the small range of FRA variation, which makes the retrieval more challenging.

Figure 4.24 shows a FRA snapshots of the ascending orbit: the L1 FRA (Fig. 4.24a), the recovered FRA (Fig. 4.24b) and the FRA error (Fig. 4.24c) before applying the temporal filter, and the recovered FRA (Fig. 4.24d) and the FRA error (Fig. 4.24e) after applying the temporal filter.

Once again, it is verified the important improvement that the temporal filter introduces in the methodology even though the total FRA range in the snapshot is low. The STD of the recovery error improves from 6.55° to 1.01°.

In the calculus of the VTEC from the retrieved FRA at the antenna level, there is also an important improvement once the spatio-temporal filtering techniques are applied to the TB measurements. Figure 4.25 shows the L1 VTEC (Fig. 4.25a), the recovered VTEC (Fig. 4.25b) and the VTEC error (Fig. 4.25c) before applying the temporal filter, and the recovered FRA (Fig. 4.25d) and the FRA error (Fig. 4.25e) after applying the temporal filter.

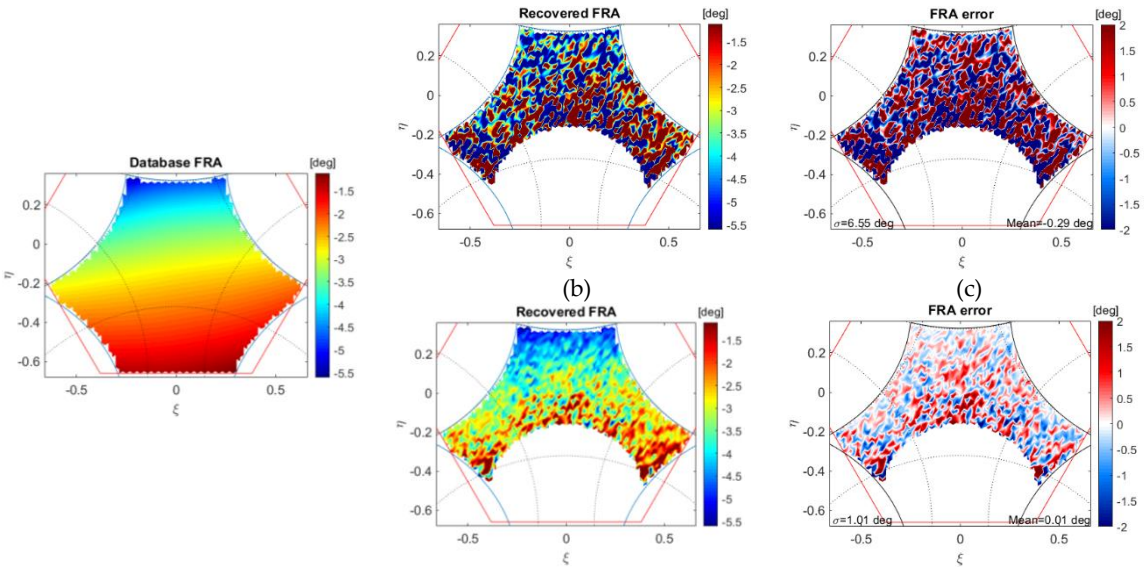

Figure 4.24. FRA snapshots of the ascending orbit analyzing the application of the temporal filter: (a) L1 FRA, (b) recovery when the temporal filter is not applied, (c) FRA error when not applying the temporal filter, (d) recovery when applying the temporal filter, (e) FRA error when applying the temporal filter.

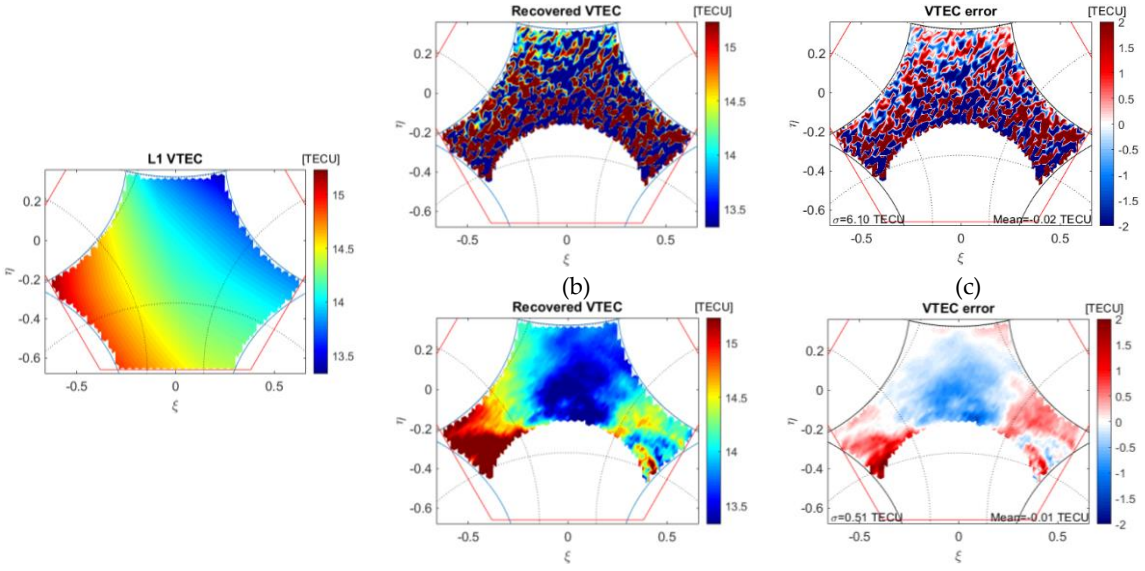

Figure 4.25. VTEC snapshots of the ascending orbit analyzing the application of spatio-temporal filtering techniques: (a) L1 VTEC, (b) recovered VTEC before applying the spatial filter, (c) VTEC error before applying the spatial filter, (d) number of averages before applying the spatial filter, (e) recovered VTEC after applying the spatial filter, (f) VTEC error after applying the spatial filter.

In this case, as mentioned before, when the spatial filter is not applied, the VTEC retrieval is highly affected by the effect of noise due to the small range of VTEC. The STD of the recovery error is 6.10 TECU; but, when applying the filter, it decreases to 0.51 TECU.

The VTEC maps of the ascending orbit are shown in Figure 4.26.

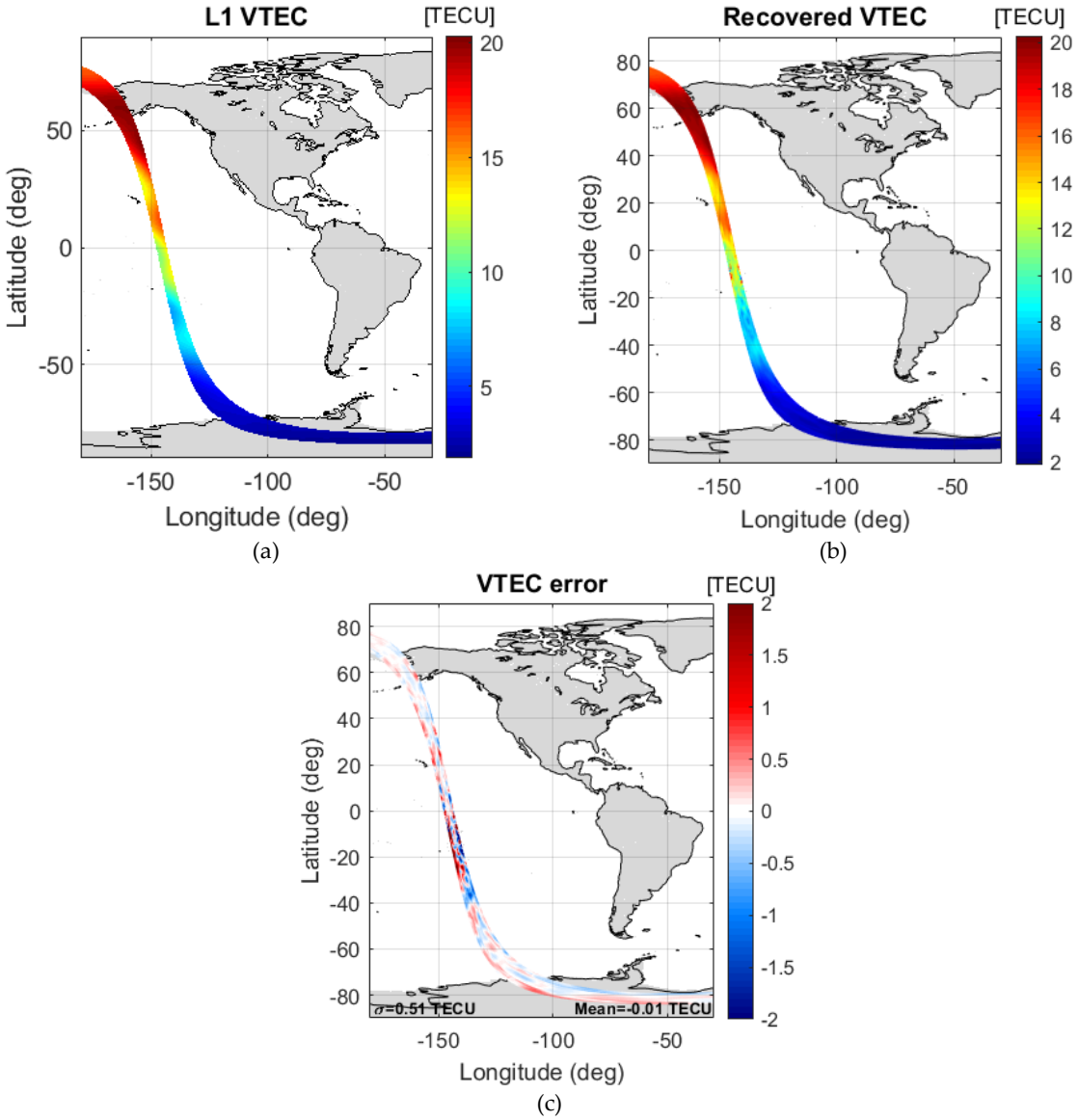

Figure 4.26. VTEC maps of the ascending orbit: (a) L1 VTEC (b) recovered VTEC using the first approach, and (c) VTEC error.

Even though the FRA range of the ascending orbit is small and the effect of noise has an important affectation in the data, the using the first approach is able to retrieve VTEC with good accuracy. The STD of the recovery corresponds to 0.51 TECU.

In Figure 4.27, the plot of the FRA of a pixel in the center of the swath with respect to the latitude of the ascending orbit is shown: in the left, the comparison of the retrieved using the first approach (in green) and the L1 FRA (in red), and in the right, the error of the recovery with respect to the L1 FRA.

An important detail to comment is that, in the ascending orbit, the geomagnetic field is orthogonal to the wave propagation direction in latitudes around 20°S (Fig. 4.26c) instead of around 20°N as is the case in the descending orbit (Fig. 4.21c). That error in the retrieval does not represent a handicap when calculating the FRA from the recovered VTEC because is in the zone where it tends to zero due to the presence of the orthogonality ($\cos\Theta_B \approx 0$ in Eq. (4.2)).

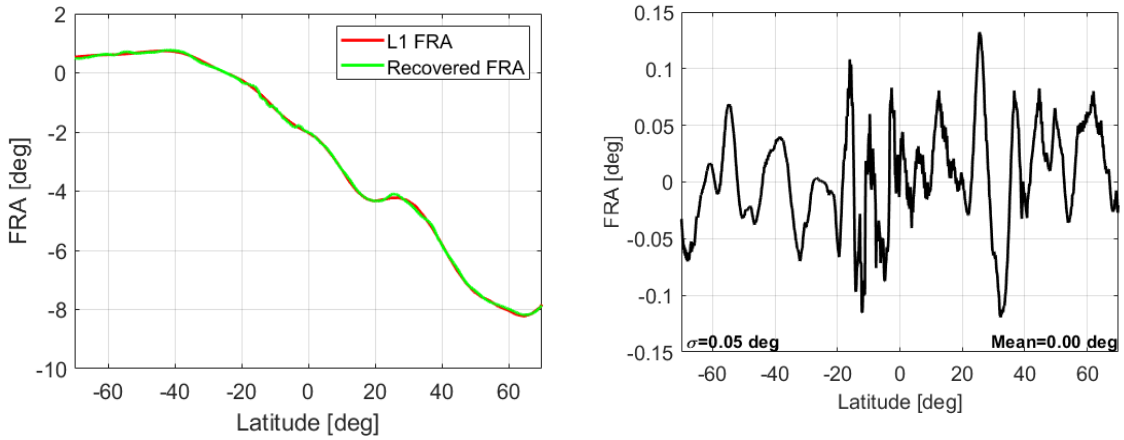

(a) (b)

Figure 4.27. FRA vs latitude of a pixel along the ascending orbit: (a) L1 FRA (red) and retrieved FRA with simulated data (green), (b) error of the retrieved FRA with respect to the L1 one.

4.2. Recovery with SMOS Radiometric Data Using the First Approach

Once the methodology was refined, SMOS radiometric data was processed. To do so, the MIRAS Testing Software (MTS) (Corbella et al., 2008) has been used. This software is an independent processor developed at the UPC to process from SMOS raw data up to geolocated brightness temperatures (L1C level). The MTS is used in the context of the ESL L1 activities as a breadboard for testing new calibration and image reconstruction algorithms, previously to their inclusion in the SMOS L1 Operational Processor (L1OP). All TB used in this thesis have been processed by the MTS.

Figure 4.28 shows the FRA snapshots of the descending orbit when processing SMOS radiometric data: the recovered FRA (Fig. 4.28a) and the difference between the recovery and the L1 FRA snapshot (Fig. 4.28b). The L1 FRA is used as the reference to compare with the recovery.

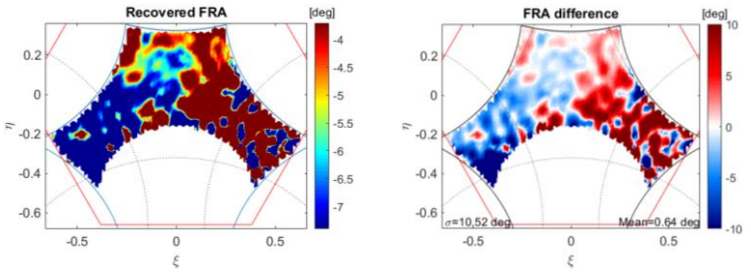

(a) (b)

Figure 4.28. FRA snapshots from SMOS radiometric data in the descending orbit: (a) recovered FRA, (b) difference between the recovered and the L1 FRA.

As it can be seen, when processing the SMOS radiometric data, it can be said that both the effect of the noise and image reconstruction artifacts degrade the quality of the recovery. This is evident comparing the STD of the FRA difference when processing SMOS radiometric data and when using simulated data. In the first case (Fig. 4.28b), it is 10.52°, whereas in the second case (Fig. 4.19e) it is 1.07°. These results were expected because in the simulator only the radiometric sensitivity per polarization was taken into account, but in SMOS, there are other error sources that are not able to be simulated such as spatial biases, among others, that are going to be deal with in the following sections.

It must be pointed out that in the case of the simulated data, the error in the recovery can be computed, since the FRA that is used to generate the TB at the antenna reference frame is known (computed from the L1 VTEC). Therefore, the difference between the retrieved FRA and the L1 FRA is the error that the retrieval has. In the case of the real SMOS data, the recovery is simply compared with the L1 VTEC to have a reference, but these are differences and not errors.

Figure 4.29 shows VTEC snapshots of the descending orbit when processing the SMOS radiometric data once the temporal filter is already applied. The recovered VTEC before applying the spatial filter, the difference between that recovery and the L1 VTEC, the recovery after applying the spatial filter, and the difference between that retrieval and the used reference are shown in Fig. 4.29a, 4.29b, 4.29c, and 4.29d, respectively.

By looking at the recovery before and after the spatial filter (Fig. 4.29a and 4.29c), it can be said that in both cases the recovery has a poor quality. It has to be considered that this is at snapshot level and its total VTEC range is small. By comparing the STD in Fig. 4.29b and 4.29d, 37.49 TECU and 16.21 TECU, it is clear that there is an important impact when applying the filter. Nevertheless, 16.21 TEC represents a high STD value.

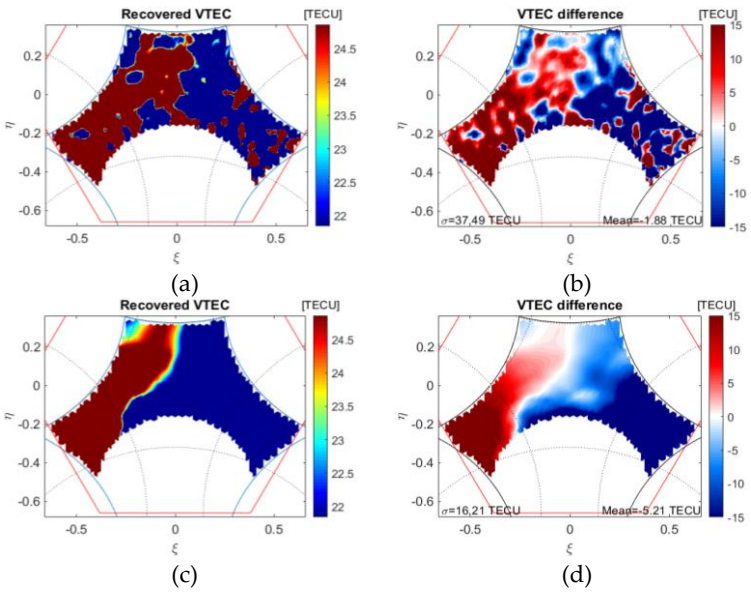

Figure 4.29. VTEC snapshots retrieved from SMOS radiometric data in the descending orbit: (a) the SMOS-derived VTEC before applying the spatial filter, (b) the difference between the SMOS-derived (before applying the spatial filter) and the L1 VTEC, (c) the SMOS-derived VTEC after applying the spatial filter, (b) the difference between the SMOS-derived (after applying the spatial filter) and the L1 VTEC.

The VTEC maps of the descending orbit when processing the SMOS radiometric data are shown in Figure 4.30. In the top, there is the recovery using the first approach; in the bottom left, the difference between the retrieval and the L1 VTEC over ocean, showing the statistics of the difference in the range of latitudes [60°S 60°N]; and in the bottom right, the difference over land.

Even though the recovery at snapshot level (Fig. 4.29c) does not seem to have enough quality, the VTEC geophysical variation is recovered when generating the VTEC map (Fig. 4.30a). It is important to remember that, when generating the VTEC map, all the measurements acquired over the same grid cell are averaged, which helps to improve the quality of the SMOS-derived VTEC map.

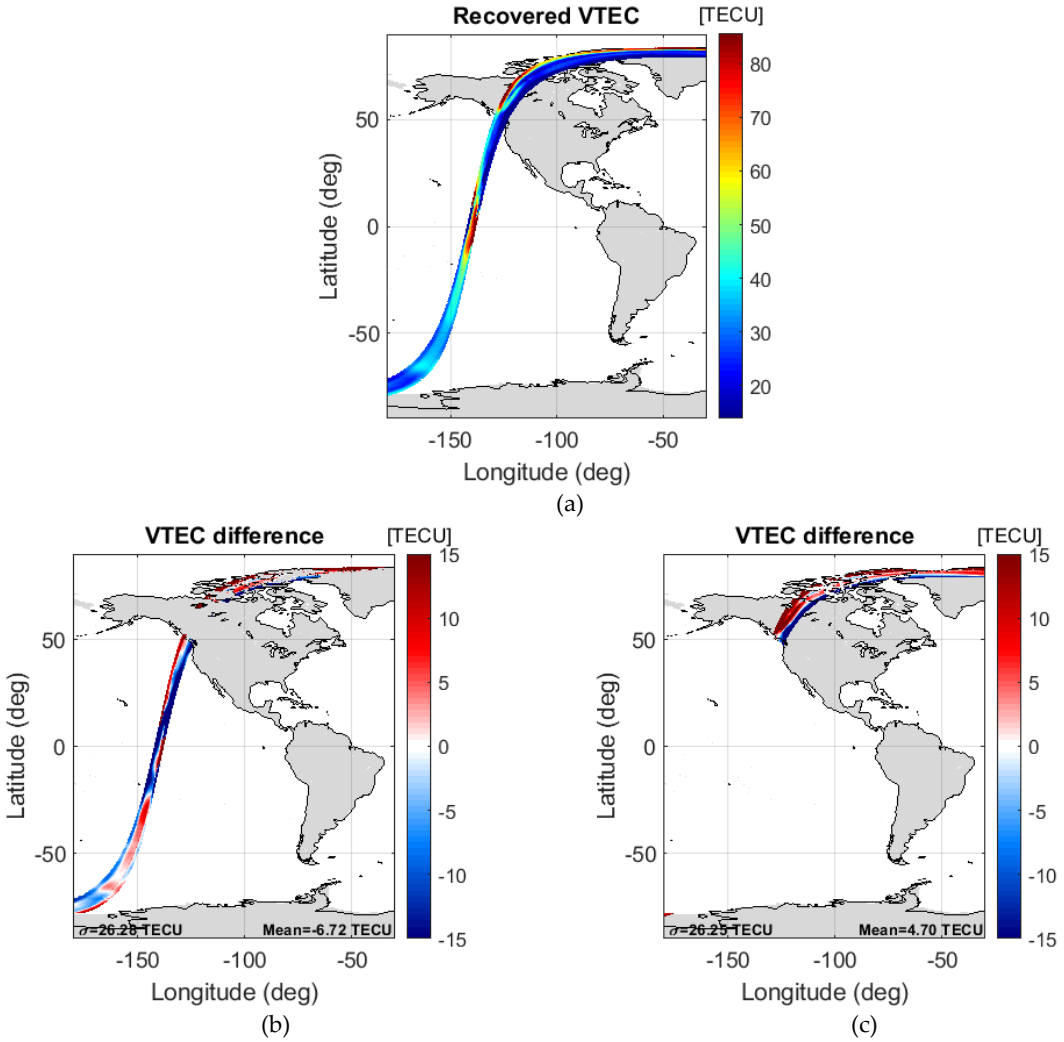

Figure 4.30. VTEC maps of the descending-orbit SMOS radiometric data: (a) recovery using the first approach, and difference between the retrieval and the L1 VTEC (b) over ocean and (c) over land.

Analyzing the difference between the recovered and the L1 VTEC map, it can be said that, as it happens at snapshot level, when processing SMOS radiometric data, the STD of the difference is much greater than the one processing simulated data (26.28 and 26.25 TECU with respect to 0.69 TECU. It is noteworthy that the SMOS measurements over land are much more contaminated, in particular by the RFI sources, and less stable than over ocean, being hard to reach a conclusion only analyzing one orbit.

Additionally, the recovered VTEC using the first approach presents a systematic pattern with higher differences in the edges of the swath. This pattern did not appear in the retrieved VTEC when processing simulated data.

4.2.1. Improving the Recovered Systematic Pattern in the Laterals of the Swath

To mitigate the effects on swath laterals lines, which occur during VTEC recovery, several empirical approaches were assessed. The first approach used only the AF-FoV instead of using the EAF-FoV region. By doing so, the retrieval could only be performed over a much narrower swath of the SMOS overpass. Hence, a second attempt was based on assigning the average VTEC of the AF-FoV to the entire EAF-FoV in each snapshot (similarly to what was done in Corbella et al., 2015, where the average in the AF-FoV was assigned to the FRA of boresight). With this approach, the TEC variability along the snapshot is not considered. The third and selected technique consists of extending the value of the VTEC in the closest pixels of the AF-FoV to the EAF-FoV (Rubino et al., 2019a). The methodology including this step is going to be assumed from now on as the second approach.

Figure 4.31 shows the descending-orbit VTEC snapshots to analyze the application of the selected technique. Fig. 4.31a shows the recovered VTEC snapshot with a wider range – to perceive its variation within the snapshot– when not extending the VTEC value of AF-FoV closest pixels to the EAF-FoV; Fig. 4.31b, the difference between this recovery and the L1 VTEC; Fig. 4.31c, the retrieved snapshot after extending the AF-FoV VTEC border value to the EAF-FoV; and Fig. 4.31d, the difference between the Fig. 4.31c and the L1 VTEC.

As it can be seen, the zones with more error in the retrieval in the VTEC snapshot when not extending to the EAF-FoV (Fig. 4.31a) are the laterals of the overpass, as previously mentioned. By applying this extension (Fig. 4.31c), the error in the retrieval is slightly corrected. In the left part of the snapshot, the saturated pixels with a value greater than 50 TECU take a more realistic VTEC value with this new assignment. There is another important comment from Fig. 4.31a. The VTEC is a parameter that is always positive. As an effect of the error in the retrieval, it can be seen that there are some negative values in the snapshot. These pixels could be rejected at this point, but it is not done in order to not vary the width of the swath, and not forgetting that the recovery improves with the averaging done when generating the VTEC maps. A better indicator of the improvement is the comparison of the STD of the differences of both recoveries with respect to the L1 VTEC; in the first case, it is 16.21 TECU and in the second, 11.96 TECU. Even though this is the analysis of just one snapshot, it can be expected that a significant improvement in the recovered VTEC map can be obtained.

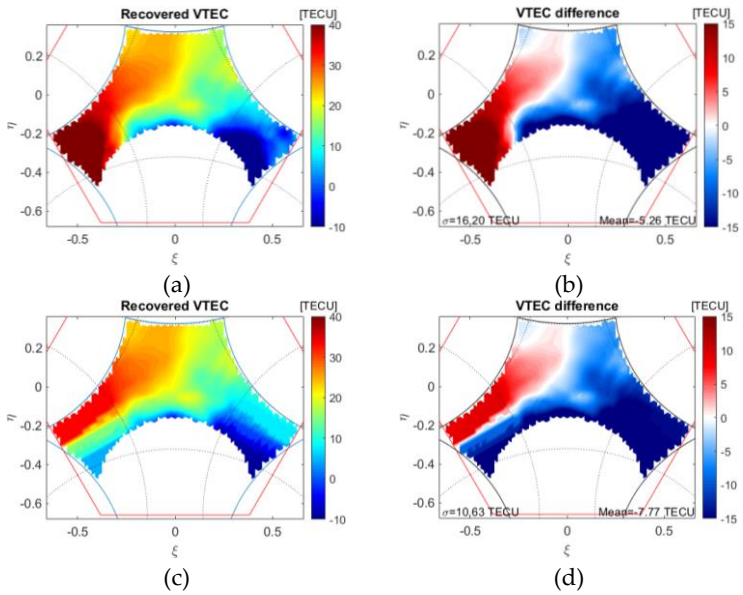

Figure 4.31. VTEC snapshots analyzing the approach application in the EAF-FoV: (a) recovered VTEC when not extending to the EAF-FoV, (b) VTEC difference between the recovery when extending to the EAF-FoV and the L1 VTEC, (c) retrieval when extending to the EAF-FoV, and (d) VTEC difference between the retrieval when extending to the EAF-FoV and the L1 VTEC.

Additionally, when comparing the recoveries using the first approach –when not extending– (Fig. 4.30a) and when using the second approach –extending to the EAF-FoV– (Fig. 4.32a), it can be seen that systematic pattern in the laterals is partially mitigated. As expected, the impact of introducing this approach affects only the swath laterals of the recovery. The sidebands of the Southern Hemisphere become softer. In the Northern Hemisphere, a similar softening happens, though not as noticeable as in the Southern one. This can be noticeable in Figure 4.32d, which shows the differences between the recovery when using the second approach and the first one. The improvements are also reflected in the STD of the difference with respect to the L1 VTEC. Over ocean, it improves from 26.28 TECU (Fig. 4.30b) to 15.57 TECU (Fig. 4.32b); and over land, from 26.25 TECU (Fig. 4.30c) to 9.56 TECU (Fig. 4.32c).

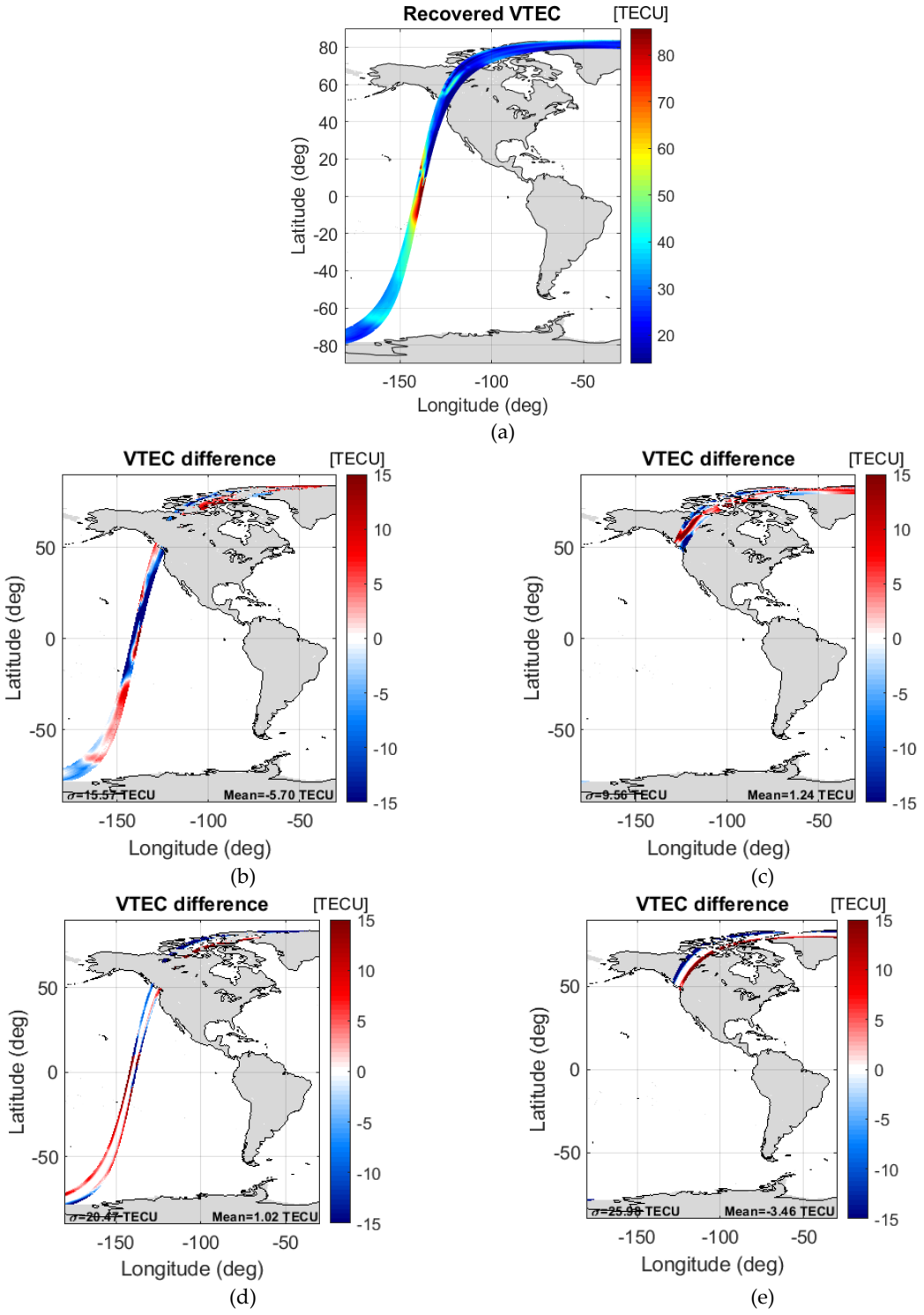

Figure 4.32. VTEC maps of the descending orbit when using the second approach: (a) recovered VTEC, (b) difference between the recovery and the L1 VTEC over ocean, (c) difference between the recovery and the L1 VTEC over land, and difference between the recovery when using the second approach and the first one (d) over ocean and (e) over land.

In the following figures, VTEC maps of the ascending orbit are shown. In Figure 4.33, the recovered VTEC is shown, in the left, when using the first approach for the recovery –not extending the laterals of the VTEC AF-FoV value to the EAF-FoV–, and in the right, when using the second approach recovery – extending the laterals of the VTEC AF-FoV value to the EAF-FoV–.

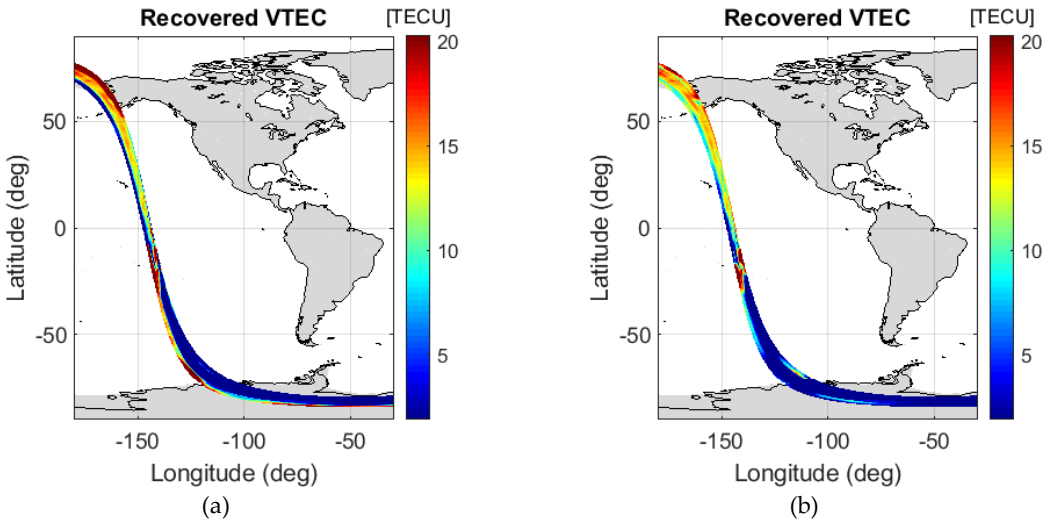

Figure 4.33. Recovered VTEC maps of the ascending orbit: (a) recovered VTEC using the first approach, (b) recovery using the second approach.

In Figure 4.34a and c (figures in the left), the difference between the recovery and the L1 VTEC over both ocean and land are shown, respectively, when using the first approach; Fig. 4.34b and d (figures in the right), are the same images but when using the second approach. Finally, Fig. 4.34e and f are the differences between both solutions over ocean and land respectively.

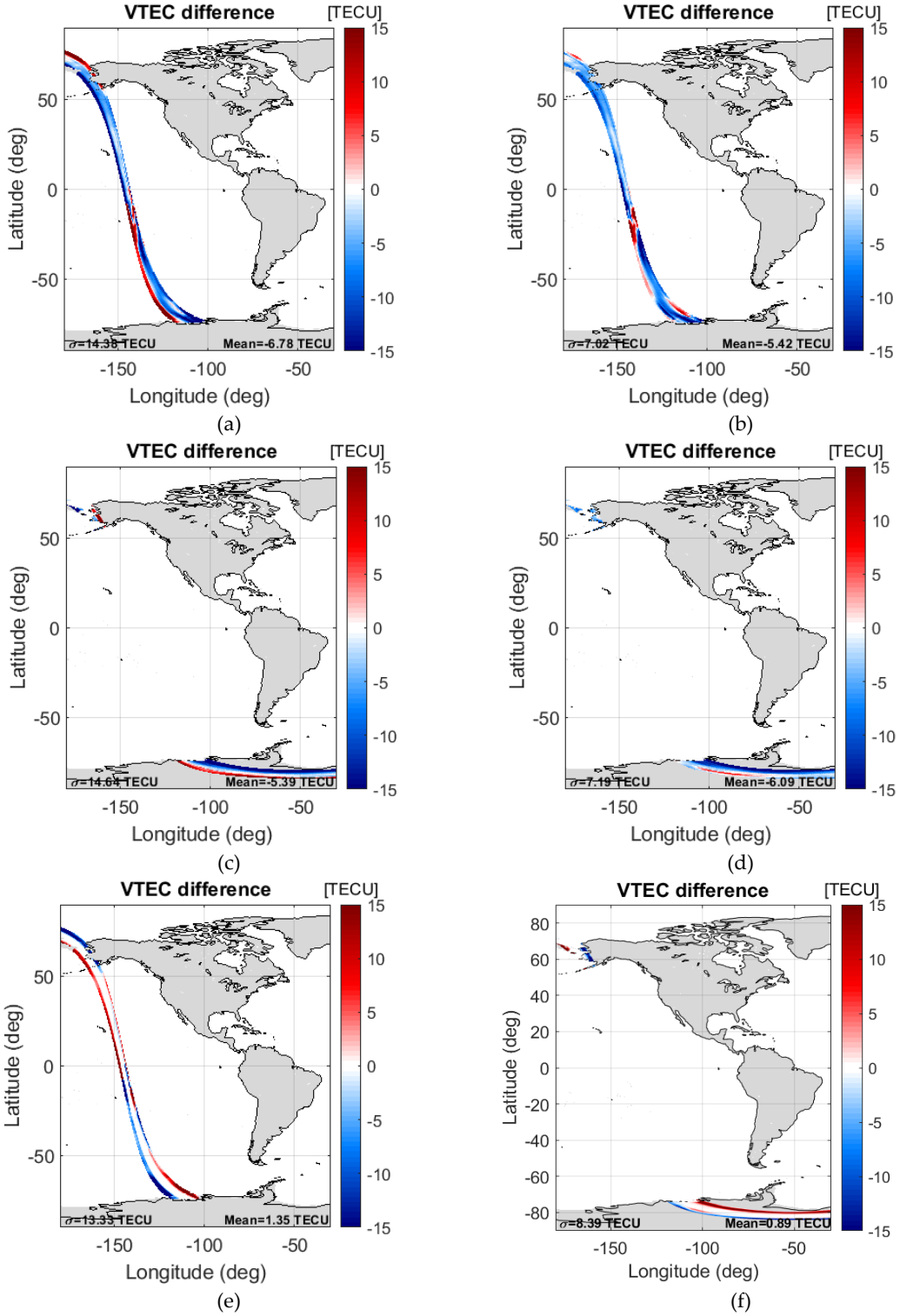

Figure 4.34. Difference between the recovery Top: recovering in the EAF-FoV and the L1 VTEC over ocean, (a) using the first approach and (b) using the second approach; middle: recovering in the EAF-FoV and the L1 VTEC over land (c) using the first approach and (d) using the second approach; bottom: difference between applying the second and first approach over (e) ocean and (f) land.

There is an important improvement in the STD of the comparison with respect to the L1 VTEC when not applying and when applying it. The STD goes from 14.38 TECU (Fig. 4.34a) to 7.02 TECU (Fig. 4.34b) over the ocean and from 14.64 TECU (Fig. 4.34c) to 7.19 TECU (Fig. 4.34d) over land. More importantly, it is visible in the mitigation of the systematic error in the lateral of the swath, which do not correspond to the geophysical variation of the VTEC.

4.2.1.1. FRA Recovery from the Retrieved VTEC Maps from SMOS Radiometric Data Using the Second Approach

As done with simulated data, the FRA can also be calculated from the VTEC maps retrieved from SMOS radiometric data.

Figure 4.35 shows plots of the FRA of a pixel in the center of the swath with respect to the latitude of the descending orbit as shown in Fig. 4.23, but in this case, when retrieving the maps with SMOS radiometric data using the second approach: in the left, a comparison of the retrieved (in green) and the L1 FRA (in red), and in the right, the difference of the recovery with respect to the L1 FRA. The statistics are shown only for the range of latitudes of [60°S 60°N].

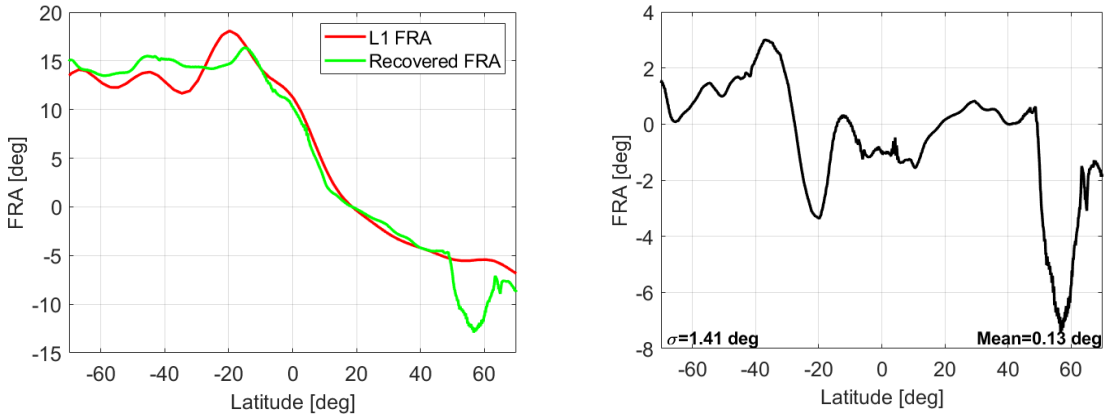

Figure 4.35. FRA vs latitude of a pixel along the descending orbit: (a) L1 FRA (red) and retrieved FRA with SMOS radiometric data when using the second approach (green), (b) difference between the retrieved FRA with respect to the L1 one.

It can be seen in Fig. 4.35a that the recovery follows the geophysical variation of the FRA, especially over the ocean (latitude range of [70°S 50°N]). This is verified with the STD on Fig. 4.35b which corresponds to only 1.41° taking into account that the SMOS radiometric data is highly masked by the effect of noise among other factors. On the contrary, over land (latitudes higher than 50°N), there is an error in the retrieval, that, as mentioned when showing the recovered VTEC maps using SMOS radiometric data, can be caused by several reasons.

The same images are shown for the ascending orbit in Figure 4.36.

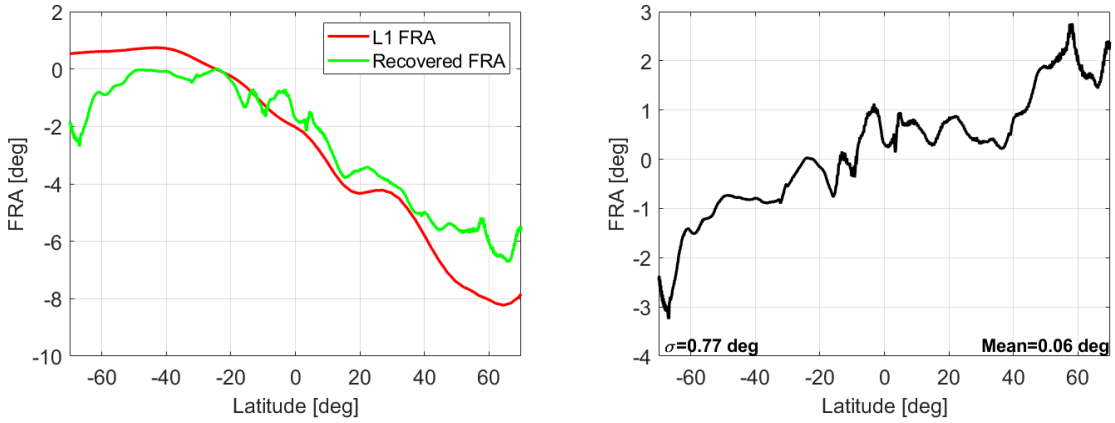

(a) (b)

Figure 4.36. FRA vs latitude of a pixel along the ascending orbit: (a) L1 FRA (red) and retrieved FRA with SMOS radiometric data when using the second approach (green), (b) difference between the retrieved FRA with respect to the L1 one.

Despite the fact that in the ascending orbit the recovery is much more challenging because of the low FRA range and that it is highly masked by the effect of noise, the FRA retrieval follows the geophysical variation as well (STD of the difference equals to 0.77°), and the mean difference between the recovery and the used reference tends to 0°. As mentioned when showing the results of the descending orbit, these results cannot be conclusive because they are from only one orbit. Different orbits were analyzed (not shown) and the conclusions are the same.

4.2.1.2. Comparison of the Retrieved VTEC from SMOS with other VTEC Sources

A comparison of the VTEC retrieved with the second approach and those from the other VTEC sources introduced in section 3.2.2. is presented in Figure 4.37 for the descending orbit of March 20th, 2014 over the Pacific Ocean (Rubino et al., 2019b). Recalling (section 3.2.2.4.2.1.), the A3TEC is computed as a single value per snapshot. Therefore, the best way to compare the different VTEC sources is in a plot of VTEC with respect to the latitude of a unique pixel which corresponds to the center of the swath. The black line corresponds to the IGS VTEC (coming from GPS); the red one, to the L1 VTEC; the one in green, to the SMOS-retrieved VTEC; and the one in magenta, to the A3TEC.

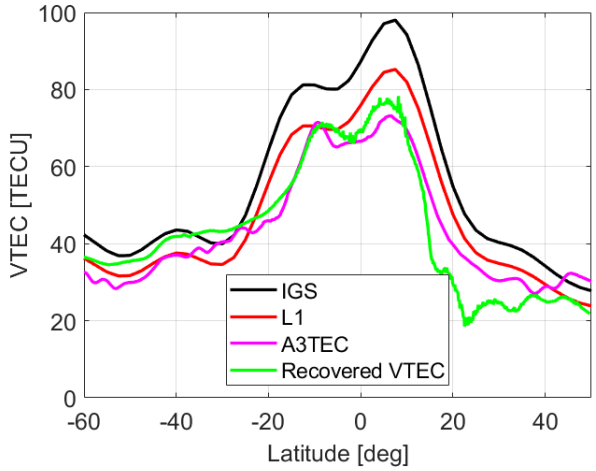

Figure 4.37. Comparison of the descending-orbit VTEC coming from different sources.

As mentioned in section 3.2.2.3. , the IGS VTEC is calculated at 20000 km of altitude. Therefore, it considers a higher total electron content, which makes it to be above the other sources. On the other hand, both sources coming from SMOS radiometric data –the retrieval with the second approach (green line) and the A3TEC (magenta line)– follow the temporal-geophysical variation that the L1 VTEC presents over ocean, but more similarly one to the other with respect to the source used as the reference (L1 VTEC). In latitudes 10°N to 30°N, the A3TEC tends to the L1 VTEC. This is expected because in the procedure to retrieve it, the L1 VTEC is used as a first guess. Furthermore, the green line presents an unexpected VTEC drop caused by an error in the recovery due to the indetermination that arises in Eq. (4.2) when the geomagnetic field and the wave propagation direction are orthogonal. This does not represent an issue when correcting the FRA over the mission because in that zone, the FRA vanishes. Moreover, the recovered VTEC has less ripples than the A3TEC. It was found that the origin of those ripples is due to remaining noise as reported in Vergely et al., 2014. Over land, it can be seen that the recovered VTEC has a drastically unexpected change of VTEC value that could be caused by a RFI source among other reasons. It is noteworthy to remark that the A3TEC does not provide data over land.

Figure 4.38 shows the comparison of the different VTEC sources of section 3.2.2. for the ascending orbits.

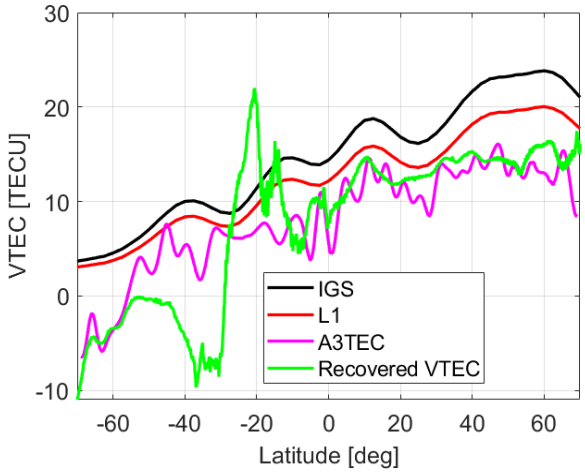

Figure 4.38. Comparison of the ascending-orbit VTEC coming from different sources.

As expected after analyzing Fig. 4.34b, the recovery using the second approach follows the geophysical variation of the L1 VTEC, but it is generally below the L1 VTEC. In the ascending orbit, the orthogonality between the geomagnetic field and the wave propagation direction occurs around 20°S. This causes the unexpected VTEC peak in the retrieval that can be seen in the plot. Once again it is noteworthy to mention that this does not represent an issue when correcting the FRA over the mission because in that zone, the FRA vanishes.

Additionally, to the comments already done for the plot of the descending orbit (Fig. 4.37), it can be added that both the A3TEC and the recovered VTEC negative values at southern high latitudes, which do not have geophysical sense. This does not happen in the descending orbit. It is important to mention once again that in the ascending orbits, the effect of noise causes a higher deterioration in the retrieval because of the small range of FRA variability, and this is reflected in Fig. 4.36. It is important to remark that this analysis is only for one orbit, which is not representative to draw conclusions.

Different orbits were analyzed (not shown) and the conclusion of the results in both types of orbits, descending and ascending ones, are the same.

4.2.1.3. Daily VTEC Maps Using SMOS Radiometric Data Retrieving with the Second Approach

In order to analyze the performance of the second approach on a global scale, the analysis has been extended to all the descending orbits of March 21st, 2011. The impact of the RFI contamination on the quality of the VTEC maps has been also evaluated (Rubino et al., 2019b).

The VTEC provided by the L1 VTEC and the retrieved VTEC with the second approach are shown in Figure 4.39.

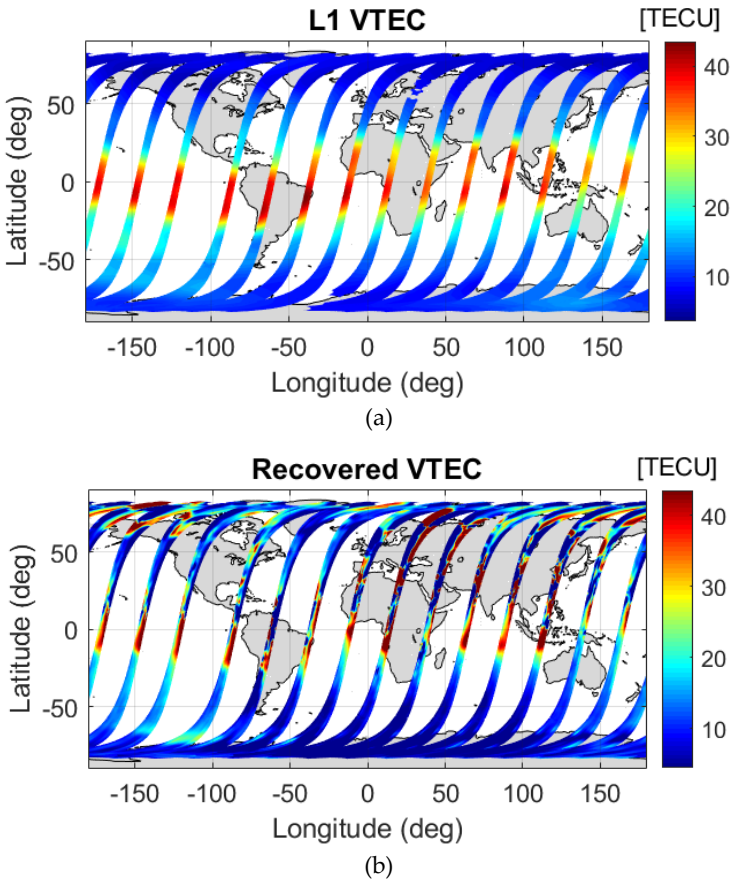

Figure 4.39. VTEC maps of the descending orbits of March 21st, 2011: (a) L1 VTEC and (b) recovered VTEC using the second approach.

The difference between them over ocean and over land are shown in Figure 4.40. It is known that in the geophysical VTEC variation there should not be any negative values. Those grid points with negative VTEC values are rejected. The VTEC retrievals that are affected by the presence of RFI sources or by the singularities in Eq. (4.1) are rejected as well, applying a threshold of 120 TECU. It was chosen by studying the L1 VTEC in the descending orbits of 2014, the year with the highest solar activity in the mission, knowing that a higher VTEC value than that one does not have geophysical sense.

Fig. 4.39b shows that the second approach is able to recover the spatio-temporal geophysical and variability of the VTEC, even though there are some issues in the retrieval, such as the remaining systematic error pattern (more noticeable in the Northern Hemisphere Fig. 4.39b). This systematic error pattern (not present in the simulation experiments) might be induced by the instrument when measuring the Faraday rotation.

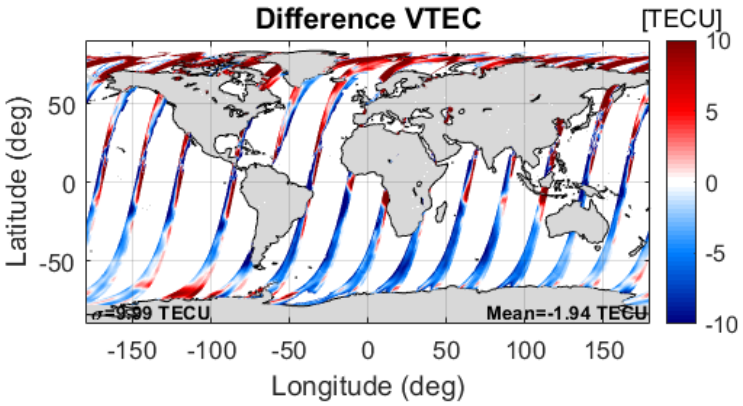

(a)

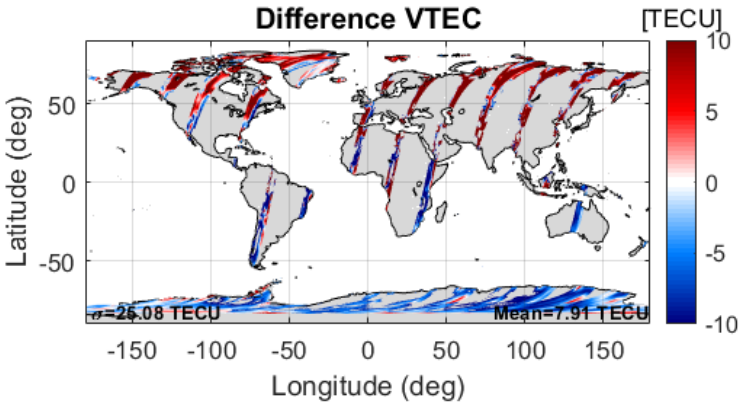

(b)

Figure 4.40. Difference between the recovered VTEC maps using the second approach and the L1 VTEC of the descending orbits of March 21st, 2011: (a) over ocean and (b) over land.

The greatest differences between the recovered and the L1 VTEC are concentrated at northern-high latitudes, close to ice edges. There are also significant differences over the Bering, the Beaufort, and the Barents Seas on that date. Figure 4.41 shows, in the top left and in the bottom left, a zoom of the recovered VTEC over the Bering Sea and over the Barents Sea, respectively. It is known that at the beginning of the mission, there was a RFI source close to these affected zones (Fig. 2.25a). On the other hand, it is known from Oliva et al., 2016 that there was a RFI source affecting the Bering Sea that was switched off in 2012. Consequently, a descending orbit was retrieved over the same region on March 20th, 2012 to compare with that of the previous year, and it is shown in Fig. 4.41b. Similarly, a descending orbit over the Barents Sea was processed on March 20th, 2014 (when the RFI source was already switched off) and it is shown in Fig. 4.41d.

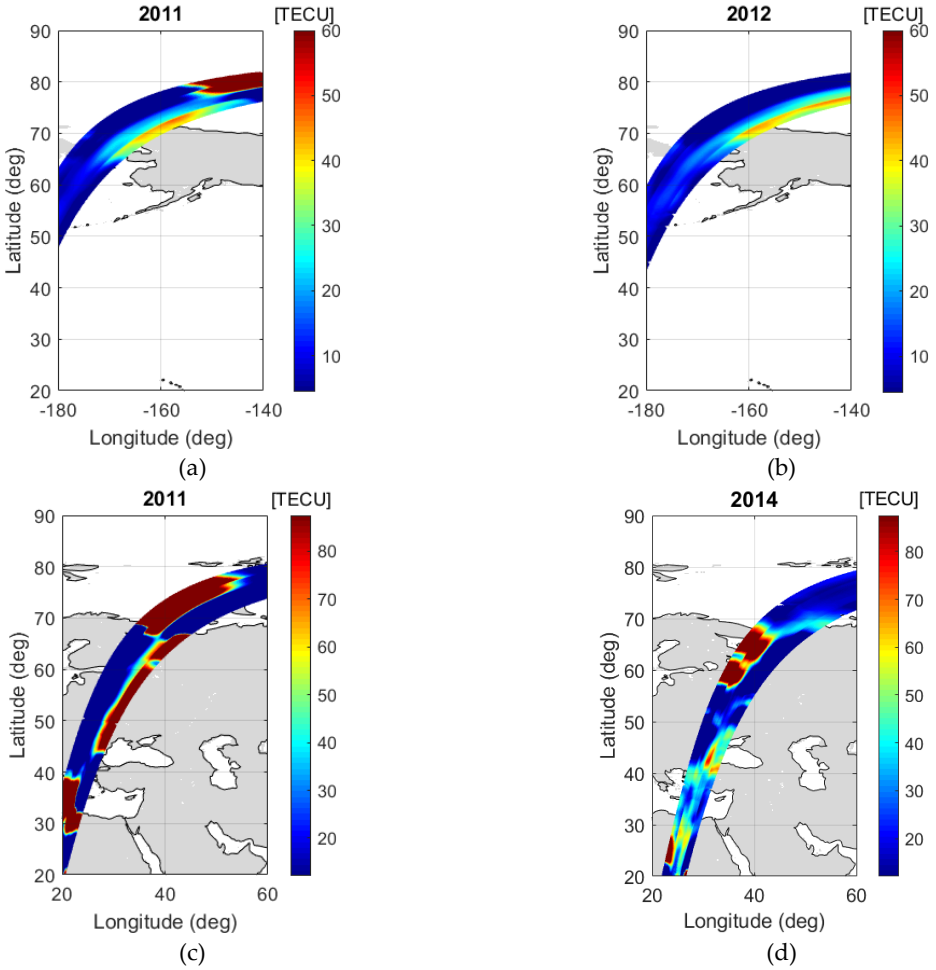

Figure 4.41. Zoomed recovered VTEC of descending orbits (using the second approach) over: a) the Bering Sea on March 21st, 2011 (RFI contaminated), b) the Bering Sea on March 20th, 2012 (RFI not contaminated), c) the Barents Sea on March 21st, 2011 (RFI contaminated), d) Barents Sea on March 20th, 2014 (RFI not contaminated).

In both cases, it can be seen that when the RFI source was shut down, the recovery improves. In the East of Canada, at 80°N, in 2012 (Fig. 4.41b), the error in the retrieved VTEC has been mitigated to a large extent. In 2011, the Barents Sea had an important error in the retrieval. In 2014 (Fig. 4.41d), the recovery over the Barents Sea was possible mitigating the error; and over Finland, it was possible the retrieval.

In the analysis of Fig. 4.40b, there are significant differences with respect to the L1 VTEC. This could be due to the presence of RFI over land, considering the RFI probability map in Fig 2.25a. To verify whether this is related to the TB contamination by RFI, the descending orbits on March 20th, 2014 (note that many RFI sources were switched off) were processed and shown in Figure 4.42. By comparing Fig. 4.39 and Fig. 4.42, a significant improvement can be observed over ocean in the northern-high latitudes as well as a general improvement in the retrievals over land.

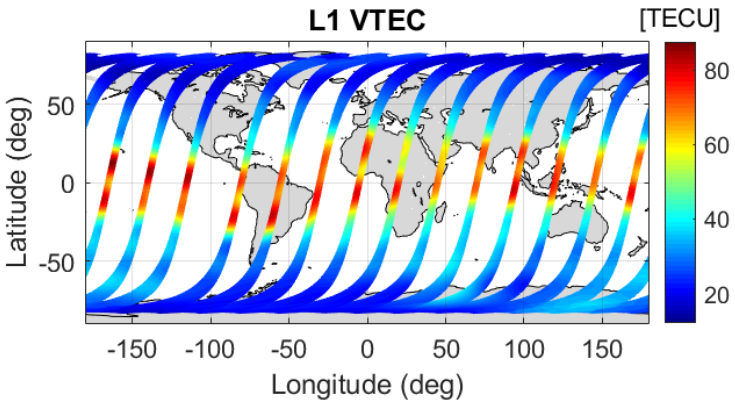

(a)

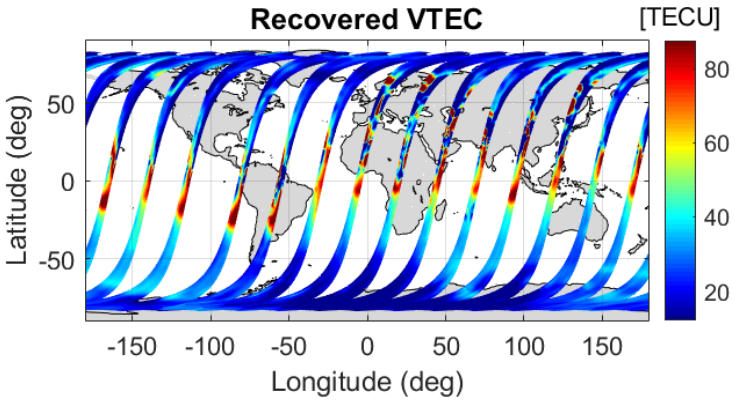

(b)

Figure 4.42. VTEC maps of the descending orbits on March 20th, 2014: (a) L1 VTEC and (b) recovered VTEC using the second approach.

The difference between the recovered VTEC using the second approach and the L1 VTEC over ocean and over land are shown in Figure 4.43, top and bottom, respectively.

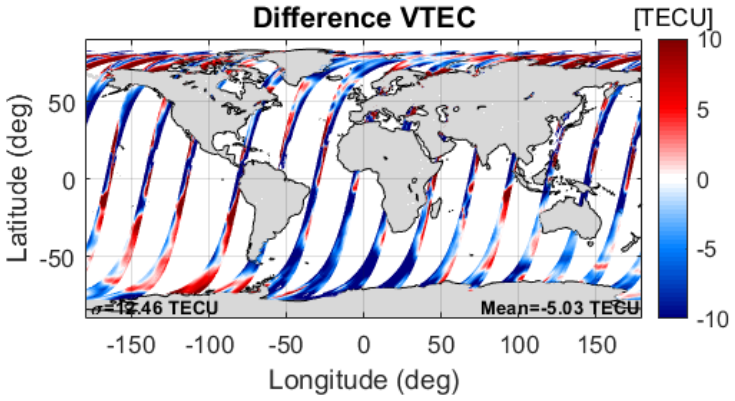

(a)

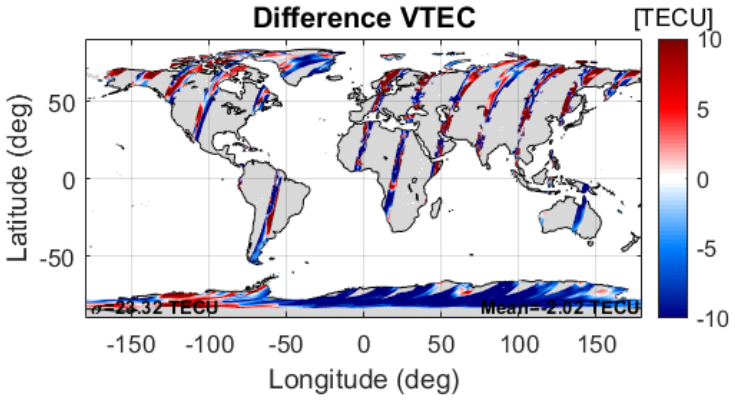

(b)

Figure 4.43. Difference between the recovered VTEC maps using the second approach and the L1 VTEC of the descending orbits on March 20th, 2014: (a) over ocean and (b) over land.

Over land, not only RFI contamination is degrading the quality of the VTEC maps. As mentioned in 3.2.2.4.2.2. (1st case), when the TB in the X polarization and the Y polarization are similar, and the T3 tends to 0 K, the recovery of the FRA is not possible because an indetermination arises in the equation to solve the FRA (Eq. (4.1)). This does not represent an issue when correcting the FRA in the mission because it vanishes and independently on the VTEC value used in Eq. (4.2), the FRA tends to 0°.

A map of T_B^{xx} minus T_B^{yy} and T3 were calculated for March of both 2011 and 2014 and are shown in Figure 4.44 (in the top, 2011; in the bottom, 2014; in the left, $T_B^{xx} - T_B^{yy}$; in the right, T3). The plot uses all SMOS orbits, descending and ascending, of 9 consecutive days (from March 1st to the 9th). This condition happens in zones of dense forest (such as in the Amazon, Russia and Canada).

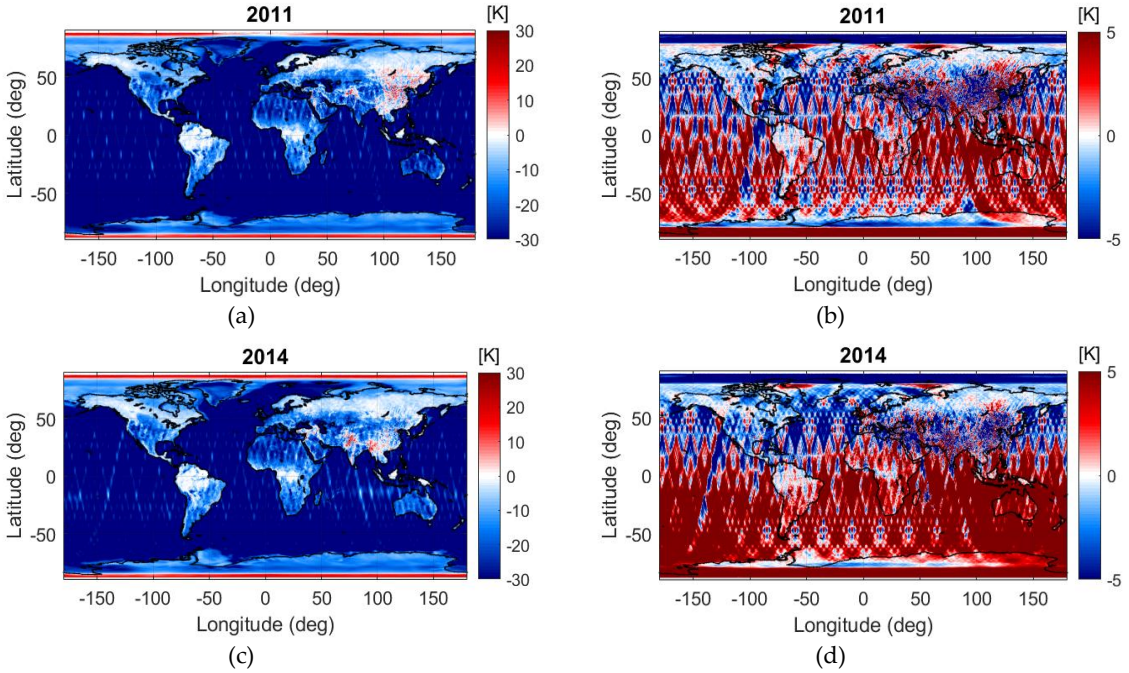

Figure 4.44. 9-day TB maps: (a) difference between T_B^{xx} and T_B^{yy} in March 2011, (b) T3 in March 2011, (c) difference between T_B^{xx} and T_B^{yy} in March 2014, and (d) T3 in March 2014.

In both years of Fig. 4.44, it happens the same. Over Amazon rainforest and over Alaska and part of Russia, T_B^{xx} minus T_B^{yy} tends to 0 as well as T3. This is one of the main limitations in the methodology to retrieve VTEC over land, together with areas affected by RFI contamination.

VTEC maps from ascending orbits of March 21st, 2011 are shown. In Figure 4.45.

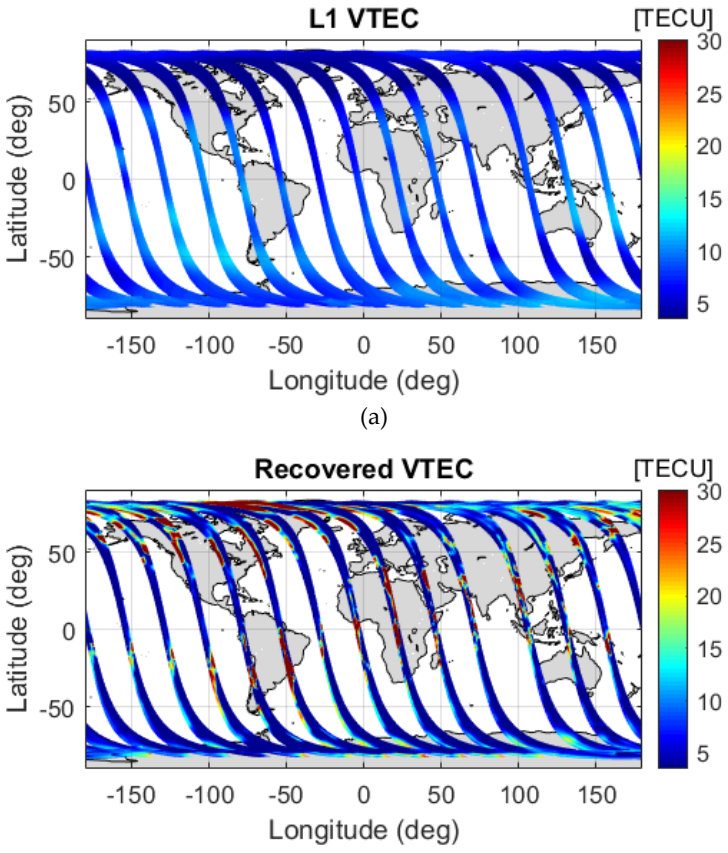

Figure 4.45. VTEC maps of the ascending orbits of March 21st, 2011: (a) L1 VTEC and (b) recovered VTEC using the second approach.

Figure 4.46 shows the difference between both VTEC maps, the recovered one when using the second approach and L1 VTEC, over ocean and land in the top and bottom, respectively. VTEC negative values and higher than 40 TECU have been rejected. This threshold has been chosen studying the ascending-orbit L1 VTEC of 2014.

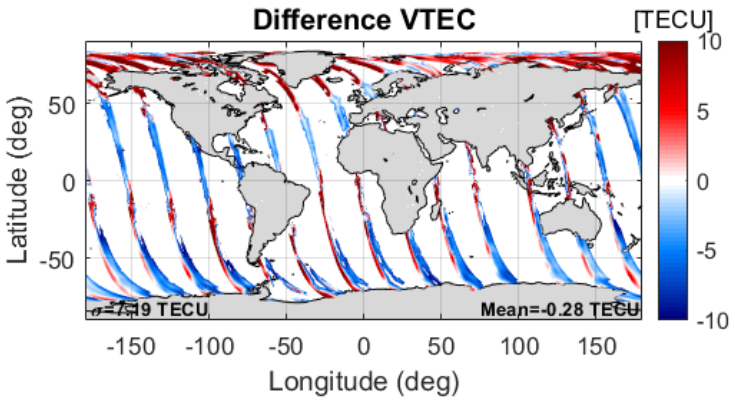

(a)

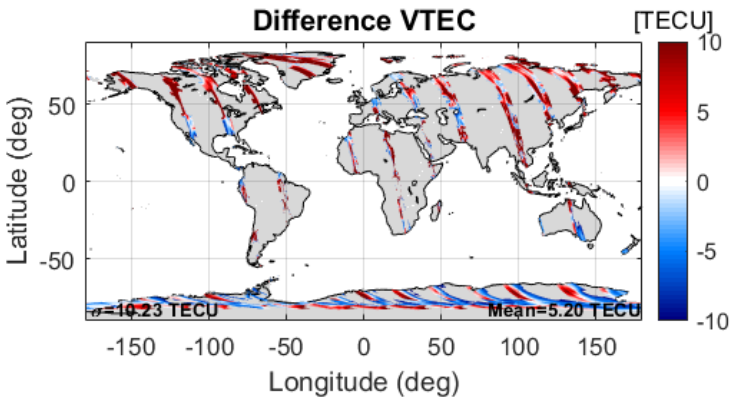

(b)

Figure 4.46. Difference between the recovered VTEC maps using the second approach and the L1 VTEC of the ascending orbits on March 21st, 2011: (a) over ocean and (b) over land.

VTEC maps from ascending orbits on March 20th, 2014 are shown. In Figure 4.47, the L1 VTEC and the recovered VTEC are shown in the top and the bottom, respectively, and in Figure 4.48, the difference between both VTEC maps over ocean and land, respectively.

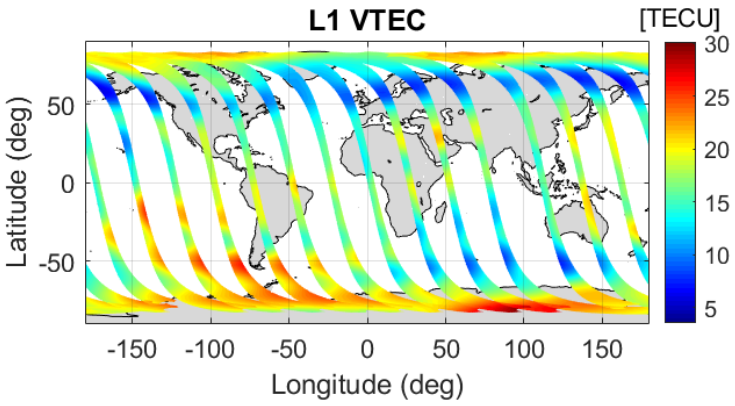

(a)

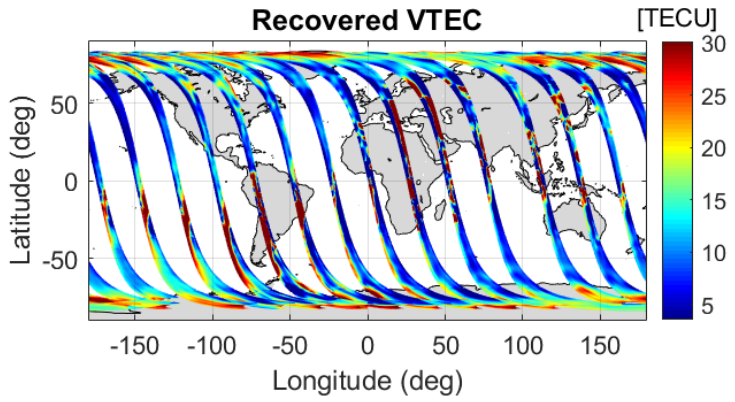

(b)

Figure 4.47. VTEC maps of the ascending orbits on March 20th, 2014: (a) L1 VTEC and (b) recovered VTEC using the second approach.

When comparing the recoveries of both years (Fig. 4.45b and 4.47b), it might seem that the one from 2014 has apparently a better quality. The VTEC total range of that year is much higher than the one of 2011 ([3.52 30.13] TECU with respect to [2.19 12.70] TECU). As a result, the recovery is less masked by the effect of the noise than the one of 2011.

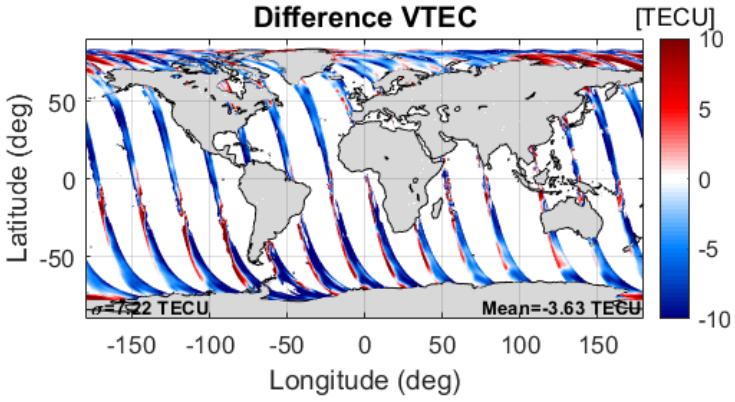

(a)

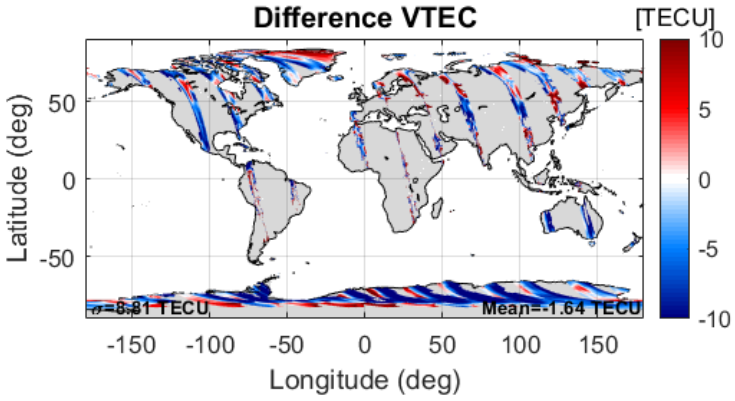

(b)

Figure 4.48. Difference between the recovered VTEC maps using the second approach and the L1 VTEC of the ascending orbits on March 20th, 2014: (a) over ocean and (b) over land.

By comparing the STD of the difference of the recovery when using the second approach with respect to L1 VTEC over ocean in both years (Fig. 4.46a and Fig. 4.48a) –7.19 TECU and 7.22 TECU, respectively–, it is clarified that, actually, the recovery of the latest year does not have a much better accuracy, at least, with respect to the L1 VTEC. In fact, because some RFI sources in 2014 had been switched off with respect to 2011, the recovery of the latest year should have a better STD, and that does not happen. This shows that even when the RFI sources can be switched off, still, the recovery of ascending orbits is challenging, and this is because of the lower VTEC total range that they have.

4.3. Conclusions

Measuring the Faraday rotation from radiometric data allows the estimation of the total electron content of the ionosphere by using an inversion procedure. This leads to the

possibility of deriving a VTEC product from SMOS data. This product can then be re-ingested in the SMOS level 2 processor to improve the geophysical retrievals.

The proposed methodology consists of the usage of spatial-temporal filtering techniques to mitigate the effect of noise. It allows to derive VTEC maps independently of the target seen by the instrument, and this is an important difference with respect to the other methodology that also derives VTEC maps from SMOS radiometric data (Vergely et al., 2014), which is focused over the ocean and uses a forward radiative model. Besides, the developed methodology is able to estimate the VTEC in the entire swath with information from different incidence angles. This is in contrast to other methodologies that assigns an unique VTEC value for the entire FoV, as is the case of Corbella et al., 2015 and Vergely et al., 2014.

The retrieval of VTEC maps is more challenging for ascending orbits than for descending orbits because the effect of noise masks to a larger extent the geophysical VTEC variation since its range of the VTEC variability is much smaller. On the other hand, the methodology presents several limitations to obtain accurate TEC retrievals over land in (i) presence of RFI sources that degrade the quality of the TBs, and (ii) regions where the brightness temperature in H and V polarizations are very similar and the third Stokes parameter tends to 0 K (such as in the dense forests).

The retrieved VTEC maps have been inter-compared with the L1 VTEC (both over ocean and land) and the IGS VTEC and the A3TEC products over ocean. They provide values generally lower than the ones from the external VTEC databases (L1 and IGS VTEC), which is in agreement with the differences found when comparing over the ocean the other SMOS-derived product (A3TEC) with the same two external data sources (Vergely et al., 2014). Additionally, it has fewer ripples than the A3TEC. In other words, the recovered VTEC is smoother than the A3TEC.

The retrieved VTEC maps present a remaining systematic error pattern (more noticeable in the Northern Hemisphere, as shown in Figure 4.39b and 4.45b) that might be introduced by the instrument when measuring the Faraday rotation (not present in the simulation experiments). Next chapter is focused on characterizing this FRA systematic error pattern in a region and for a period with very low FRA values, so the measurement can be assumed as a systematic error of the instrument and a correction can be applied.

Chapter 5

Characterization and Correction of Systematic Error Patterns in the Faraday Rotation Angle

Even when applying the technique of extending the VTEC value of the AF-FoV border to the EAF-FoV (second approach), it can be seen in the VTEC recovery that there is a systematic error pattern affecting more drastically the laterals of the swath (Rubino et al., 2020), (Rubino et al., 2022). It is known that the VTEC has an important variation in latitude, but not in longitude; at least, it should not be perceived across the SMOS swath. Figure 5.1 shows the recovered VTEC when using the second approach of an orbit of March 20th, 2014 in a saturated scale to make more visible the presence of this error pattern (more visible in the Northern Hemisphere).

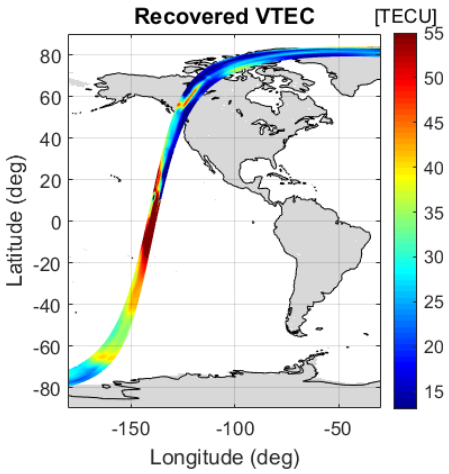

Figure 5.1. Recovered VTEC map when using the second approach (descending orbit of March 20th, 2014).

This effect is noticeable along all longitudes. When taking a look at the comparison between the recovery and the L1 VTEC over ocean, in the case of the descending orbits (Fig. 4.40a and 4.43a), it is more visible in the Northern Hemisphere; and, in the ascending ones

(Fig. 4.46a and 4.48a), in the Southern Hemisphere. This led to a thorough research to find a way to characterize and compensate for this error contribution.

5.1. Characterization of the FRA Systematic Error Pattern

Obtaining the VTEC from the recovered FRA snapshots is just a theoretical calculus using Eq. (4.2). Therefore, it is assumed that the error is introduced when calculating the measured FRA (Ω_f^m) using the radiometric data as shown in the following equation:

$$\Omega_f^m = -\varphi - \frac{1}{2}\arctan\left(\frac{2\Re e\left(T_B^{xy}\right)}{T_B^{xx} - T_B^{yy}}\right) \tag{5.1}$$

It can be then inferred that the estimated FRA calculated with Eq. (5.1) is in fact the addition of two components: the actual FRA (Ω_f) and the FRA systematic error pattern, called delta (Δ) from now on.

$$\Omega_f^m = \Omega_f + \Delta \tag{5.2}$$

From Figure 3.4b two conclusions can be drawn: the FRA tends to 0° around 20°S, and 2017 is a year with low FRA –because it is a year with low solar activity–. As shown in Figure 3.2, values are lower for JJA (June, July, and August). Consequently, SMOS radiometric data of the year 2017 was used to calculate Δ. All ascending-orbit TB per polarization as well as φ (although it does not vary significantly along the orbit) of three consecutive days of July (15th to the 17th) in the latitude range between 30°S and 5°S were averaged. Then, Eq. (5.1) was applied to calculate Ω_f^m. The error term Δ is computed by subtracting $\Omega_f^m - \Omega_f$, where Ω_f is calculated using Eq. (5.3) and L1 FRA as reference.

$$\Omega_f = 1.355 \times 10^4 f^{-2} B_0 \cos\Theta_B \sec\theta \; VTEC_{L1} \tag{5.3}$$

Finally, to mitigate the effect of the noise, a spatial filter with a radius of 0.189 in the director cosine plane was applied. The resulting FRA systematic error pattern is shown in Figure 5.2. As it can be seen, it is calculated for incidence angles greater than 25°. This is because this is the range used by the proposed methodology (section 4.2.1.).

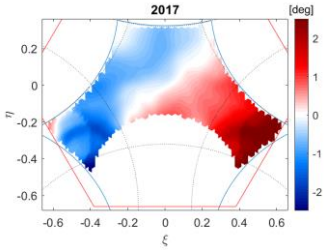

Figure 5.2. FRA systematic error pattern computed using data in 2017.

The characterization of the FRA systematic error was repeated by using other years to assess whether Δ can be considered stable over the entire mission. This computation was repeated for three different periods (see Figure 5.3): December 2018, July 2014 (year with much higher solar activity), and using three consecutive days (15th to 17th) of July per each year in the period 2010-2019.

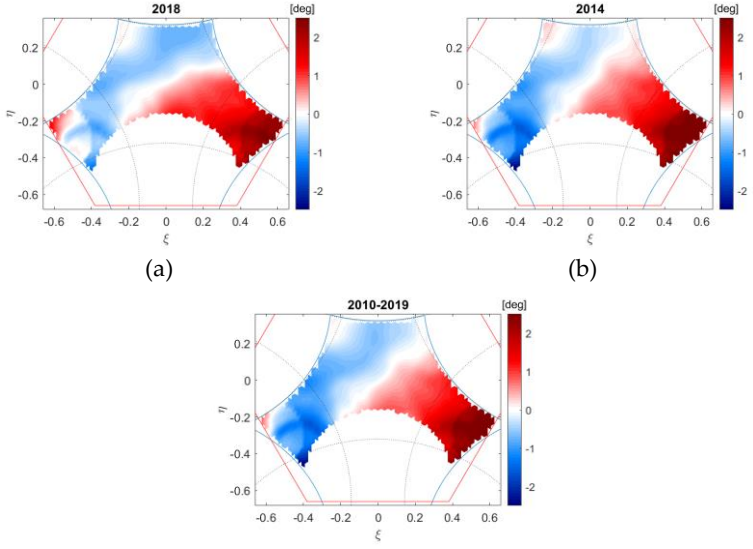

Figure 5.3. Δ three consecutive days of: (a) December 2018, (b) July 2014, and (c) July 2010-2019.

Patterns found from different years agree, corroborating that Δ remains temporally stable along the mission. From this analysis, it was decided to use the same systematic error pattern in the correction for the entire mission, the one computed by using data in the period 2010-2019 (Fig. 5.3c).

By including the correction of the FRA systematic error pattern in the second approach in section 4.2.1. , the bias is expected to be mitigated.

5.2. Recovering VTEC Maps Using the Third Approach

The second approach that retrieves VTEC maps stays the same but with a new step for correcting the FRA systematic error pattern. It is going to be assumed from now on as the third approach. It consists on:

1. Pixels with $|\cos\Theta_B| < 0.05$ over TB snapshots are rejected to avoid the indetermination of Eq. (4.2), shown again as follows to make easier the reading.

$$VTEC = \frac{f^2 \Omega_f \cos\theta}{1.355 \times 10^4 B_0 \cos\Theta_B} \tag{5.4}$$

2. A temporal filter is applied with a window size of 43 TB snapshots.
3. The measured FRA is calculated by using Eq. (5.1).
4. Pixels with an incidence angle lower than 25° are rejected in order to avoid the indetermination in Eq. (5.1).
5. Δ is subtracted to Ω_f^m to obtain the actual FRA Ω_f by using Eq. (5.5). Δ had been previously calculated for the entire mission using three consecutive days from years 2010 to 2019.

$$\Omega_f = \Omega_f^m - \Delta \tag{5.5}$$

6. The VTEC is calculated using Eq. (5.4).
7. A spatial filter with a radius of 0.196 is applied over the VTEC snapshots.
8. The VTEC AF-FoV value is extended to the EAF-FoV.
9. The geolocation is done over an ETOPO-5 grid.

Figure 5.4 shows a FRA snapshot of March 20th, 2014 of the L1 (left), before (middle) and after (right) the correction of Δ to the recovered FRA. In the image, it can be seen the impact that causes the correction of Δ: the recovery is less saturated when eliminating the FRA systematic error pattern.

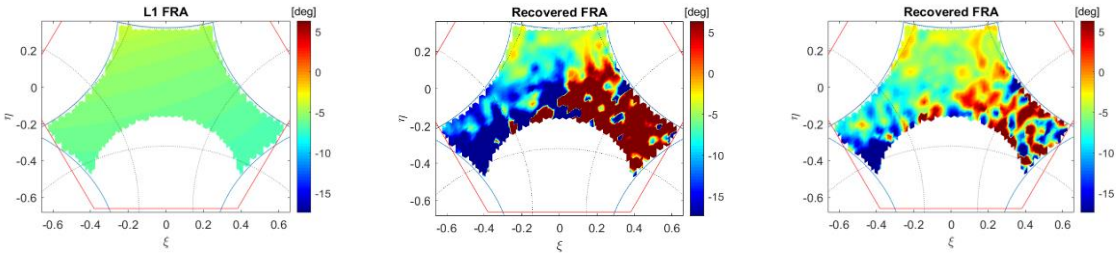

(a) (b) (c)

Figure 5.4. FRA snapshots of date: (a) L1 FRA, (b) recovered FRA when the Δ is not corrected and (b) recovered FRA once Δ is subtracted.

Figure 5.5 shows the VTEC snapshots: (a) the L1 VTEC, (b) the recovery when the Δ is not corrected and (c), its difference with the L1 VTEC, (d) the recovery once Δ is subtracted and (e), its difference with respect to the L1 VTEC.

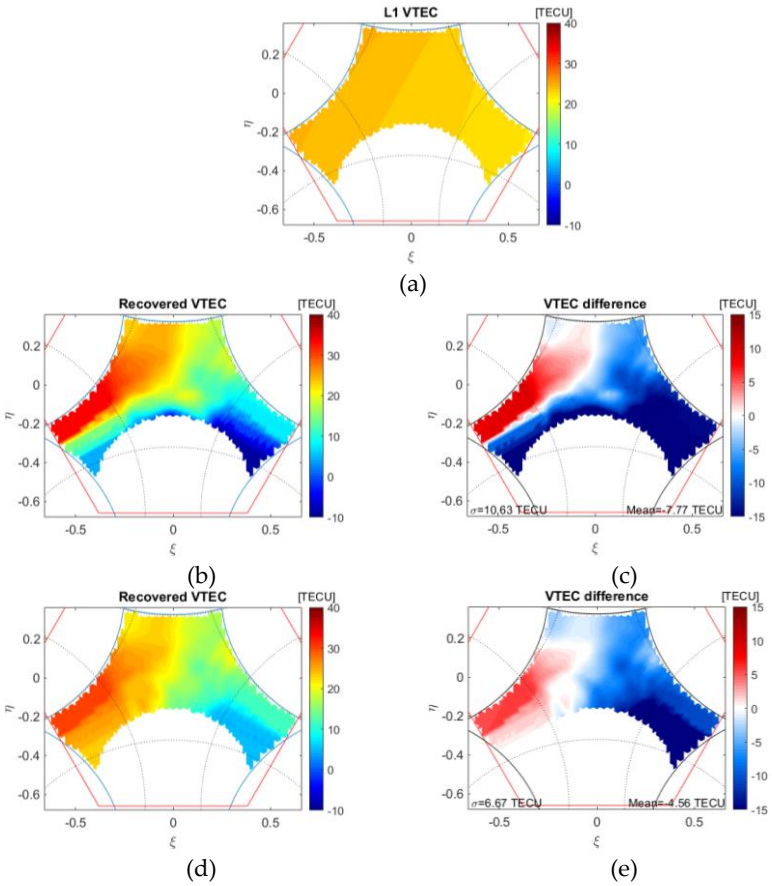

(a) (b) (c) (d) (e)

Figure 5.5. VTEC snapshot: (a) L1 VTEC, (b) recovery when the Δ is not corrected, (c) the difference between (b) and the L1 VTEC, (d) recovery once Δ is subtracted, (e) the difference between (d) and the L1 VTEC.

When comparing Fig. 5.5b and d it is clearly noticeable that, by subtracting Δ in the retrieved FRA snapshots, the pattern in the VTEC that does not correspond to a geophysical

variation is mitigated. Additionally, this also is reflected in the STD of the difference with respect to the L1 when not correcting the FRA systematic pattern (10.63 TECU) and when doing it (6.67 TECU), being the most important reason of this improvement the correction for the systematic error pattern.

5.3. VTEC Maps Using the Third Approach

Figure 5.6 shows the VTEC maps of the descending orbit: in the left, the recovered VTEC when using the second approach –Δ is not corrected–, its difference with respect to the L1 VTEC over ocean and over land (figures a, c, and e), and in the right, the recovered VTEC when using the third approach –once Δ is subtracted–, its difference with respect to the L1 VTEC over ocean and over land (figures b, d and f). It is important to remark that, the VTEC pixels with VTEC both lower that 0 TECU (pixels close to 55° of latitude and 120° of longitude) and higher than 120 TECU were rejected because it is known that they correspond to errors in the retrieval since the VTEC should not present any negative values nor higher than 120 TECU in its geophysical variation.

When comparing the recovery in the descending orbit when using the second approach (Fig. 5.6a) and when using the third one (Fig. 5.6b), it can be seen –more noticeable in the Northern Hemisphere ocean– that the asymmetric longitudinal pattern in the swath that does not correspond to the geophysical variability of the VTEC is mitigated once Δ is subtracted. This can also be perceived in the difference between the retrievals with respect to the L1 VTEC over ocean in Fig. 5.6c and Fig. 5.6d. It has to be recalled that the L1 VTEC is used just as a reference, but, as it can be seen in the STD in both plots, there is an important improvement –13.41 TECU to 10.56 TECU–. This is caused mainly because of the mitigation of the systematic pattern error.

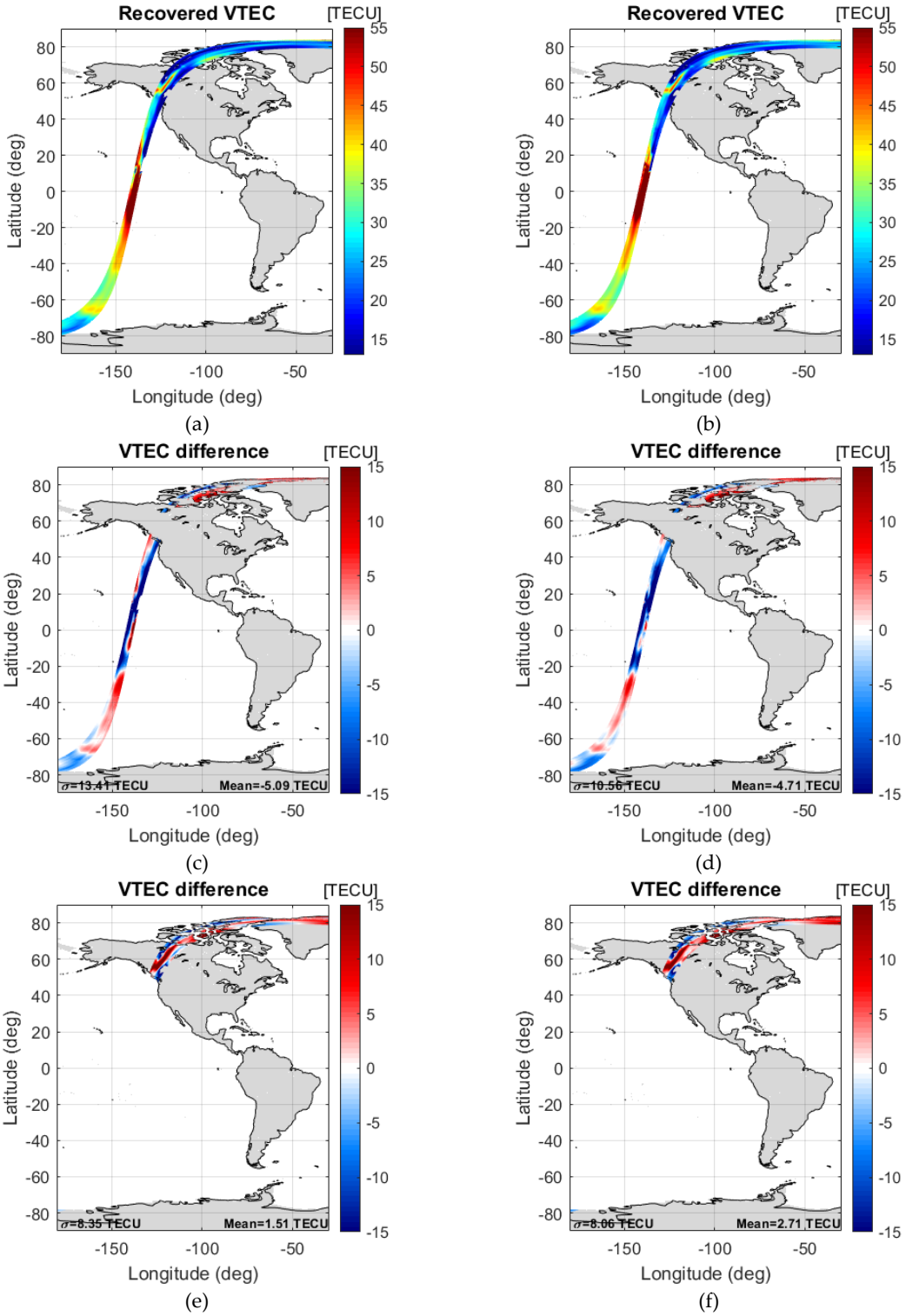

Figure 5.6. VTEC maps of the descending orbit: (a) using the second approach, (b) using the third approach, (c) difference between the recovery when using the third approach and the L1 VTEC over ocean, (d) the same but using the third approach, (e) difference between the recovery when using the second approach and the L1 VTEC over land, (f) the same but using the third approach.

Figure 5.7, which shows the difference between the recovery when using the second approach and using the third one, in the left, over ocean and in the right, over land.

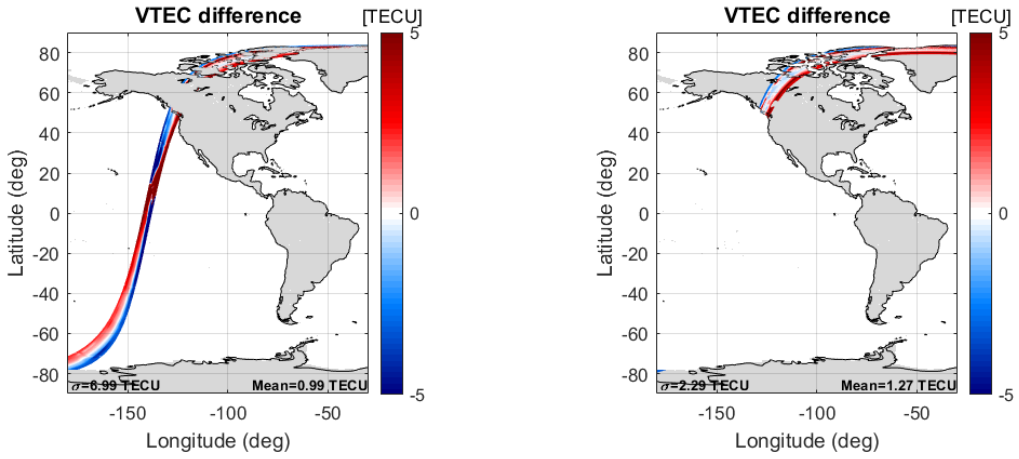

(a) (b)

Figure 5.7. Difference between the recovery when using the third approach and the second one in the descending orbit: (a) over ocean and (b) over land.

The magnitude of Δ, approximately [-2.5° 2.5°], represents a variation of the VTEC retrieval of approximately 5 TECU.

Figure 5.8 shows the VTEC maps of the ascending orbit: in the left, the recovered VTEC when using the second approach, its difference with respect to the L1 VTEC over ocean and over land (figures a, c and e), and in the right, the recovered VTEC when using the third approach, its difference with respect to the L1 VTEC over ocean and over land (figures b, d and f). Figure 5.9a and b show the difference between the recovery when using the third approach and when using the second one over ocean and over land, respectively. In the plots of the right, also the pixels with negative VTEC value are rejected, and, as it can be seen, much more pixels are discarded in comparison with the descending orbit. This is due, as it has been mentioned, that the ascending orbits are more challenging to retrieve because of the effect of noise and its small VTEC range.

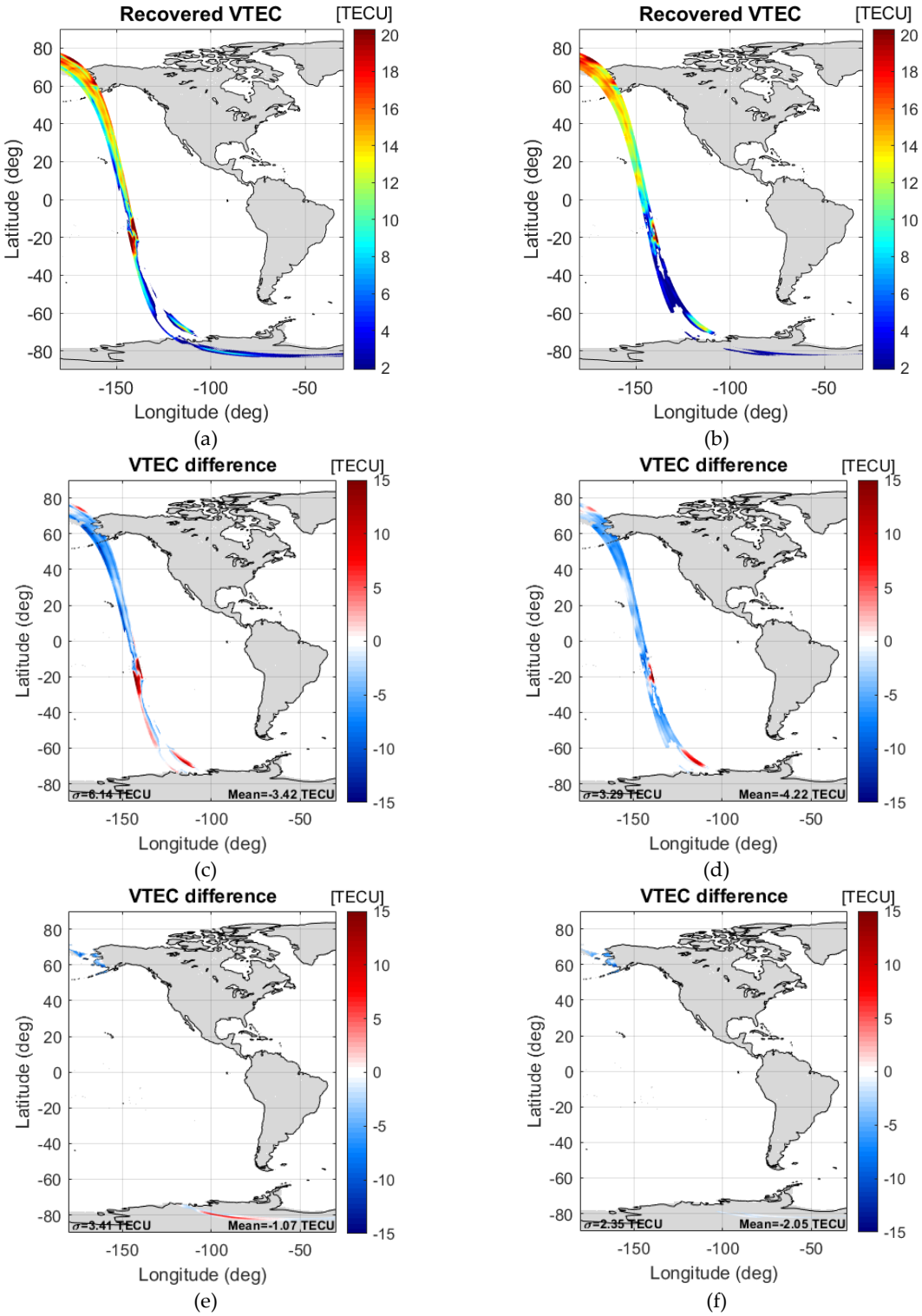

Figure 5.8. VTEC maps of the ascending orbit: (a) using the second approach, (b) using the third approach, (c) difference between the recovery when using the second approach and the L1 VTEC over ocean, (d) the same but when using the third approach, (e) difference between the recovery when using the second approach and the L1 VTEC over land, (f) the same but when using the third approach.

When comparing the retrievals in the ascending orbit when using the second approach (Fig. 5.8a) and when using the third approach (Fig. 5.8b), it happens the same as with the descending orbit. The swath longitudinal pattern that clearly does not correspond to the geophysical variability of the VTEC is mitigated once Δ is subtracted. This is more noticeable in the Northern Hemisphere Ocean. The STD with respect to the L1 VTEC over the ocean (Fig. 5.8c and Fig. 5.8d) also shows the improvement, from 6.14 TECU to 3.29 TECU.

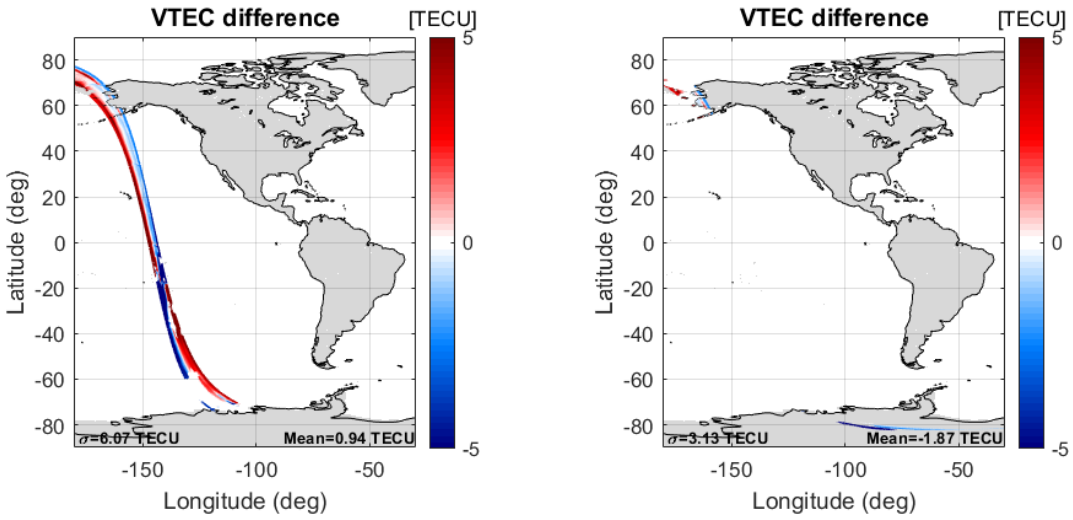

Figure 5.9. Difference between the recovery when using the second approach and using the second one in the ascending orbit: (a) over ocean and (b) over land.

5.3.1. FRA Recovery from the Retrieved VTEC Maps from SMOS Radiometric Data

Figure 5.10 shows plots of the FRA with respect to the latitude of the descending orbit calculating it with different VTEC sources. In the left, there is the FRA using the L1 VTEC (red line), the recovered VTEC when using the third approach (green line), and the recovered VTEC when using the second approach (blue line). In the right, there is the difference between the recovered FRA when using the third approach and the L1 FRA (green line), and the recovered FRA when using the second approach (blue line). Both, the STD and the average of the difference with respect to the L1 FRA is shown in the respective colors. The plots in the top correspond to a pixel in the center of the swath; the ones in the middle, to a pixel in the right part of the swath; and the ones in the bottom, to a pixel in the left part of the swath.

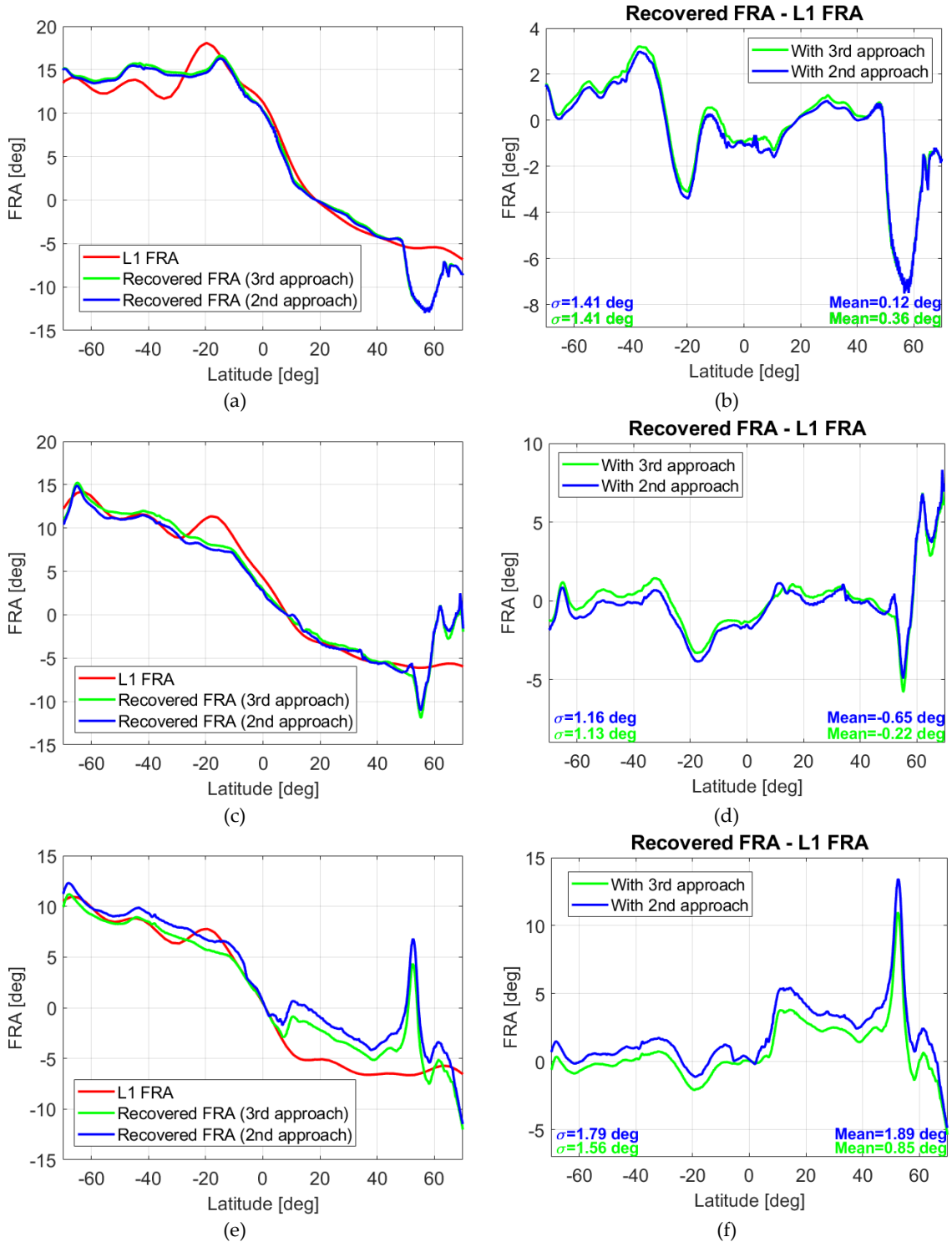

Figure 5.10. FRA vs latitude of a pixel along the descending orbit comparing when using different VTEC sources: (left plots) using the L1 VTEC in red, using the third approach in green, using the second approach in blue; (right plots) difference between the recovered FRA using the third approach and the L1 FRA in green, and the recovered FRA using the second approach and the L1 FRA in blue: (a) and (b) of a pixel in the center of the swath, (c) and (d) of a pixel in the right part of the swath, and (e) and (f) of a pixel in the left part of the swath.

When analyzing the plots, it can be seen that in the center pixel of the swath the subtraction of Δ (Fig. 5.10a) does not have an important impact. On the contrary and as expected, in pixels of the lateral of the swath, the correction of Δ (Fig. 5.10c and Fig. 5.10e) has a higher impact. It catches the attention that, close to 20°N, in the left lateral (Fig. 5.10e), there is an important FRA jump of magnitude. It is caused by the recovered VTEC value, which is higher with respect to the one that the geophysical VTEC variability should have at that range of latitudes (Fig. 5.6a and Fig. 5.6b) with respect to the L1 VTEC. This is improved by using the third approach. In all plots, in latitudes higher than 50°N, the same effect is observed: there is a drastic change in the FRA value. This happens over land in the presence of RFI or in the cases when the indetermination of Eq. (5.1) arises. Finally, it has to be recalled that the L1 FRA has been used just as a reference. It is perceived that when using the third approach (green line), the recovery is smoother than when using the second approach, as the FRA geophysical variation should be.

The same images are shown for the ascending orbit in Figure 5.11.

The conclusions are the same as with the descending orbit. The highest impact when applying this new step in the methodology is in the laterals of the swath, especially in the right lateral. This is due to the fact that, in the ascending orbit, this lateral is the one more mitigated with the FRA systematic error pattern correction in all range of latitudes (comparison between Fig. 5.8a and Fig. 5.8b).

It is important to remark again that, when analyzing just one orbit, the results cannot be conclusive. That is why orbits of daily VTEC maps are analyzed afterwards.

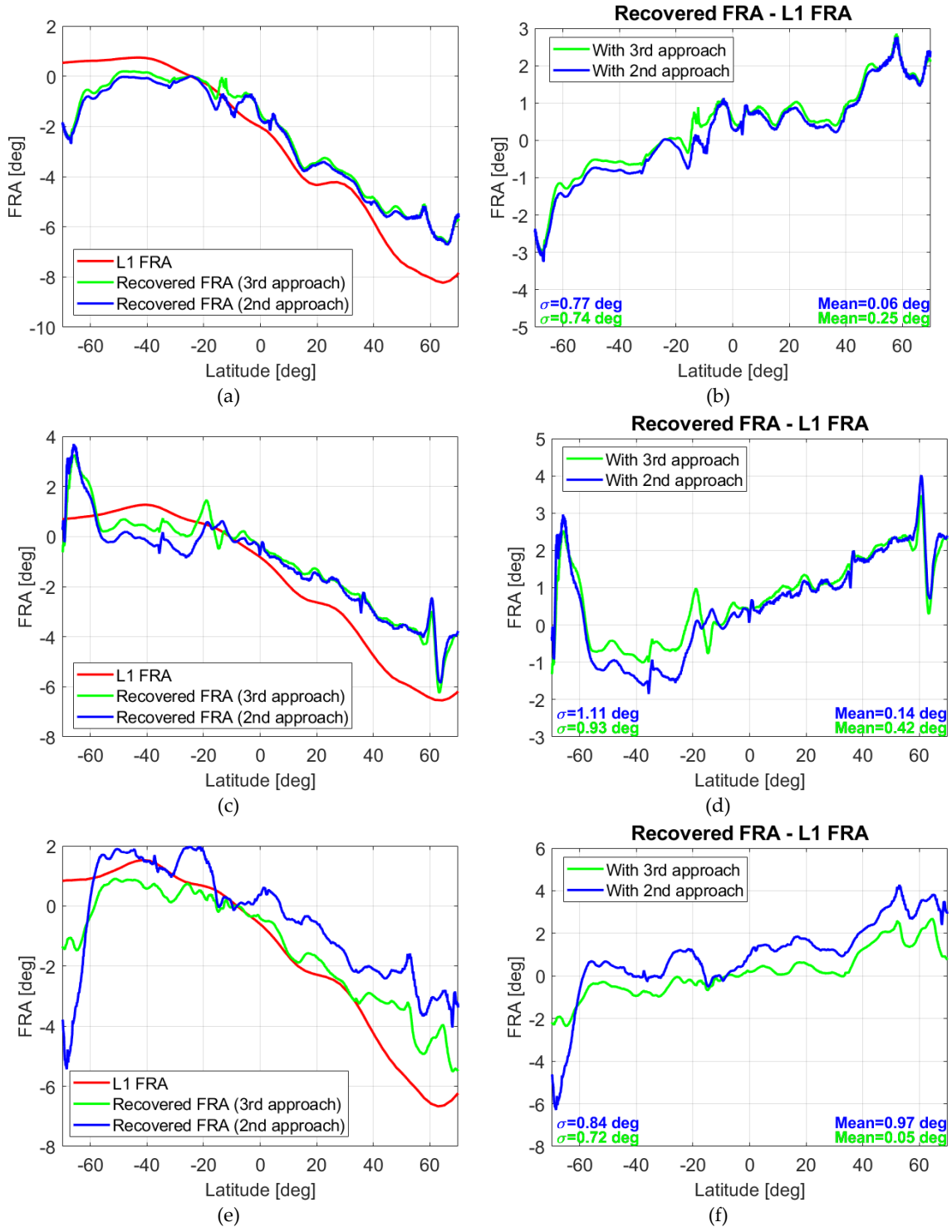

Figure 5.11. FRA vs latitude of a pixel along the ascending orbit comparing when using different VTEC sources: (left plots) using the L1 VTEC in red, using the third approach in green, using the second approach in blue; (right plots) difference between the recovered FRA using the third approach and the L1 FRA in green, and the recovered FRA using the second approach and the L1 FRA in blue: (a) and (b) of a pixel in the center of the swath, (c) and (d) of a pixel in the right part of the swath, and (e) and (f) of a pixel in the left part of the swath.

5.3.2. Comparison of the Retrieved VTEC using the third approach from SMOS with other VTEC Sources

Figure 5.12 shows the VTEC of different sources with respect to the latitude. The value corresponds to the one of the middle pixel of the swath of the descending orbit. The line in black refers to the IGS VTEC; the one in red, to the L1 VTEC; the one in magenta, to the A3TEC; the one in green, to the recovery using the third approach; and in blue, the recover using the second approach.

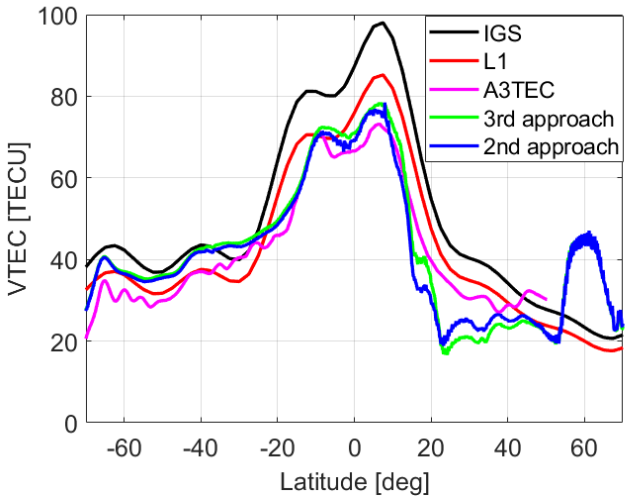

Figure 5.12. Comparison of the descending-orbit VTEC coming from different sources when correcting Δ.

The results are very similar to Fig. 4.37. The main important difference once again is that, in this case, the recovery has fewer small ripples. Also, the VTEC drop when using the third approach at 20°N is not as low as when using the second approach.

Figure 5.13 shows the different VTEC sources with respect to the latitude of the middle pixel of the swath, in this case, for the ascending orbit.

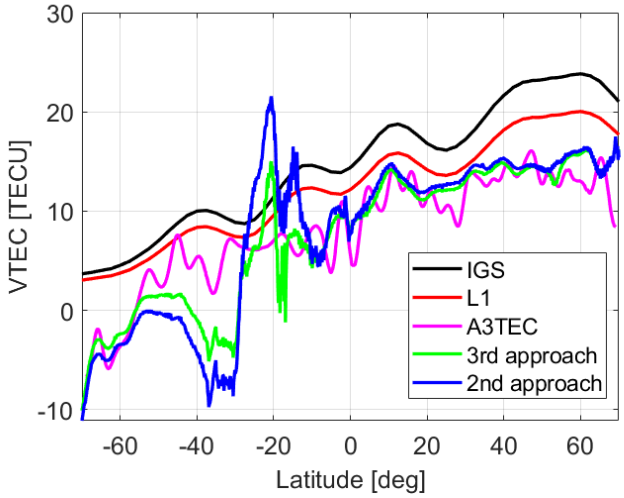

Figure 5.13. Comparison of the ascending-orbit VTEC coming from different sources when correcting Δ.

In this case, there are more differences when introducing the new step in the methodology. The recovery not only presents fewer small ripples, but also around latitude 20°S it is much stable.

In contrast with Fig. 5.8b, Fig. 5.13 shows the negative VTEC values along the orbit in the retrieval that corrects for the FRA systematic error (green line). This shows the impact of introducing the correction in the third approach. As it can be seen, the retrieval is less negative from latitudes 70°S to 30°S, and, in particular in latitudes from 55°S to 40°S, it is not negative any more. These two facts as well as the enhancement in the error close to 20°S show the improvement that adds the correction of Δ.

5.3.2.1. Daily VTEC Maps Using SMOS Radiometric Data Retrieving with the Third Approach

Figure 5.14 shows the L1 VTEC and the recovery of all descending orbits of March 21st, 2011 when using the third approach –applying the correction of the FRA systematic error pattern–. Not only pixels with negative values have been rejected, but also pixels higher than 120 TECU, knowing that they correspond to an error in the retrieval caused by the singularities in Eq. (5.1) or by the presences of RFI sources.

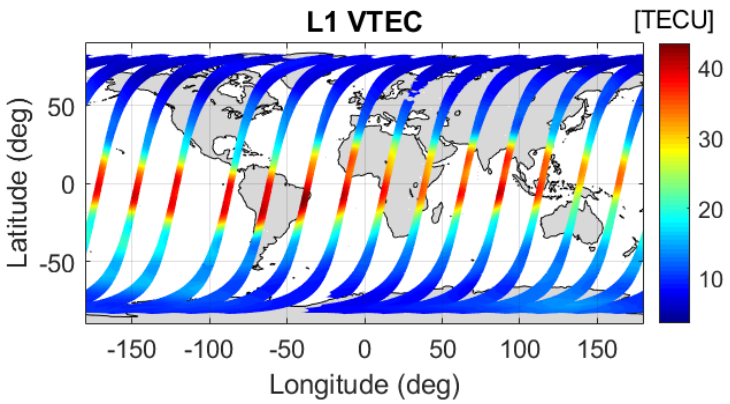

(a)

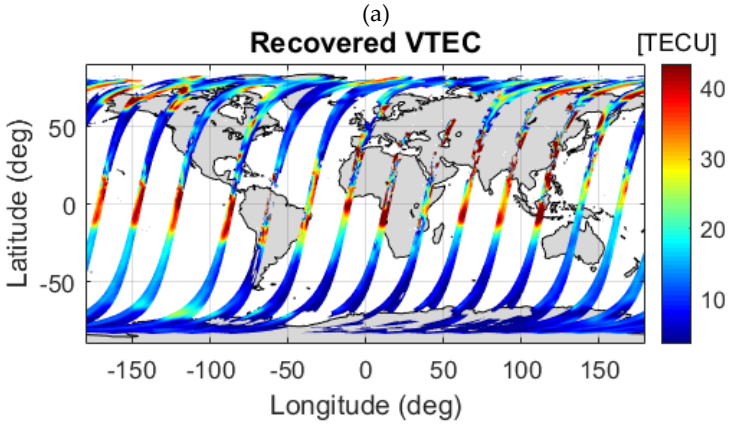

(b)

Figure 5.14. VTEC maps of the descending orbits of March 21st, 2011: (a) L1 VTEC and (b) recovered VTEC using the third approach.

Figure 5.15 shows the VTEC difference between the recovery using the third approach and the L1 over ocean (top) and land (bottom) of the descending orbit of March 21st, 2011.

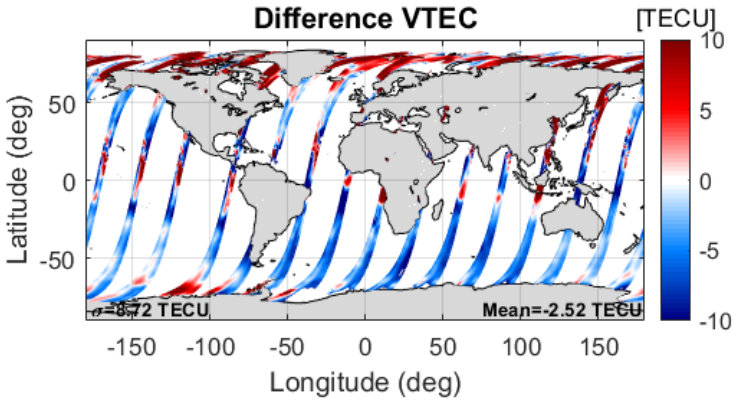

(a)

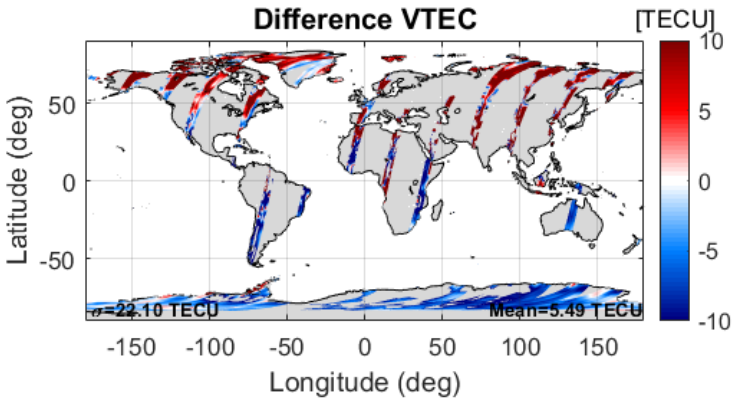

(b)

Figure 5.15. Difference between the recovered VTEC maps using the third approach and the L1 VTEC of the descending orbits of March 21st, 2011: (a) over ocean and (b) over land.

The main differences between Fig. 4.39 and Fig. 5.14 are more visible over ocean instead of over land. In magnitude, the statistics do not have a significant improvement, but an important impact is visible in the geophysical VTEC longitudinal variability (Fig. 4.40a with respect to Fig. 5.15a).

Figure 5.16 shows the difference between using the third approach and the second one in the daily map of March 21st, 2011 in order to see with more detail the impact of the correction of the FRA systematic error pattern. Main differences can be seen over the Pacific and the Atlantic Ocean, where it is realized that the plot is more saturated than over land. It is important to recall that over Europe and Asia there are presence of RFI sources. By this reason, the comparison over that zone is not reliable.

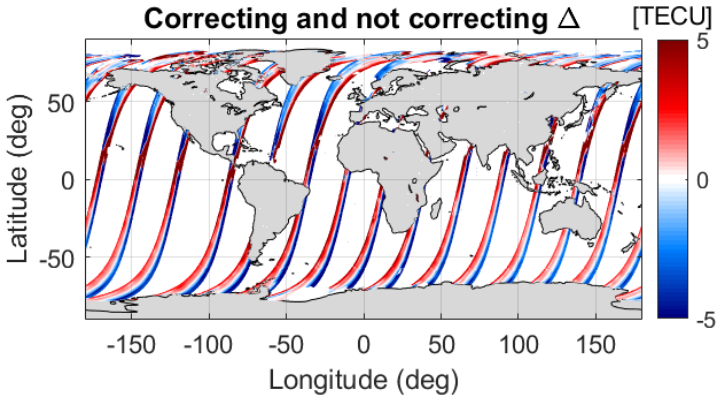

(a)

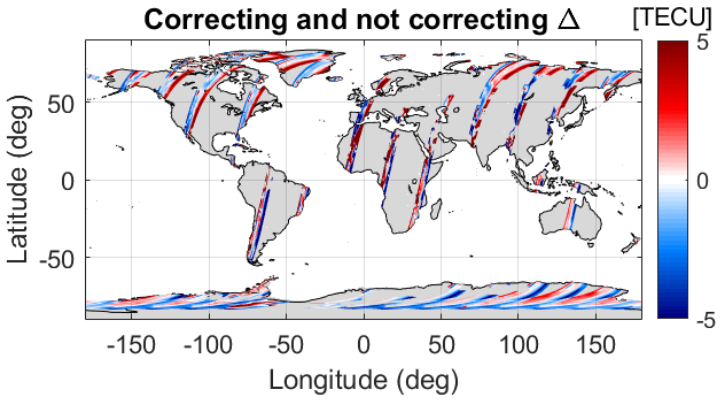

(b)

Figure 5.16. Difference between the recovered VTEC maps when using the third approach and when using the second one of the descending orbits of March 21st, 2011: (a) over ocean and (b) over land.

Figure 5.17 shows the L1 and the recovery VTEC of all descending orbits of March 20th, 2014 using the third approach.

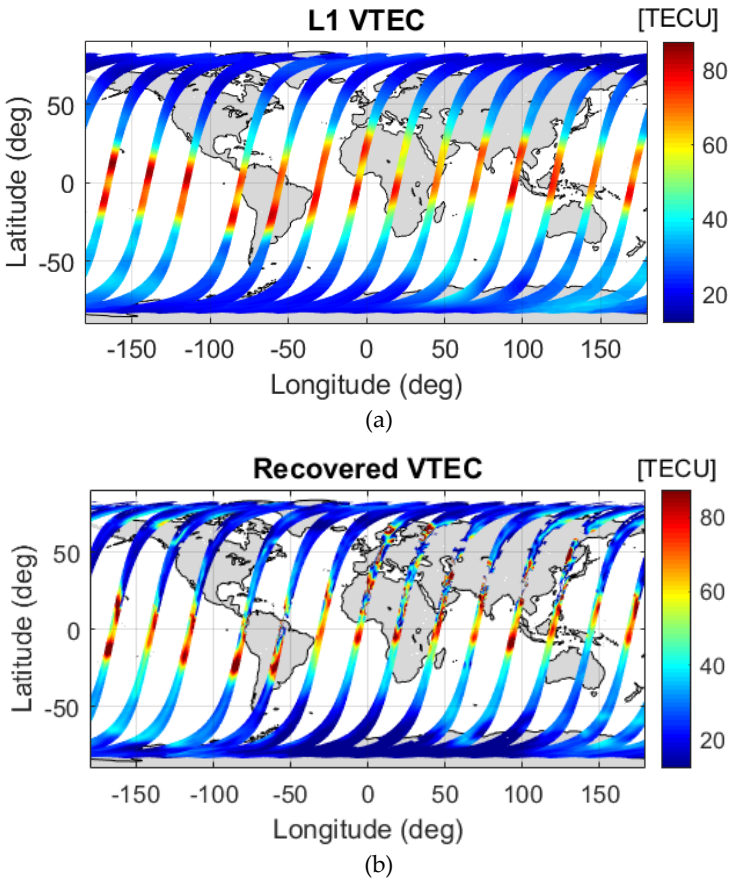

Figure 5.17. VTEC maps of the descending orbits of March 20th, 2014: (a) L1 VTEC and (b) recovered VTEC using the third approach.

Figure 5.18 shows the VTEC difference between the recovery using the third approach and the L1 over ocean (top) and land (bottom) of the descending orbits from March 20th, 2014.

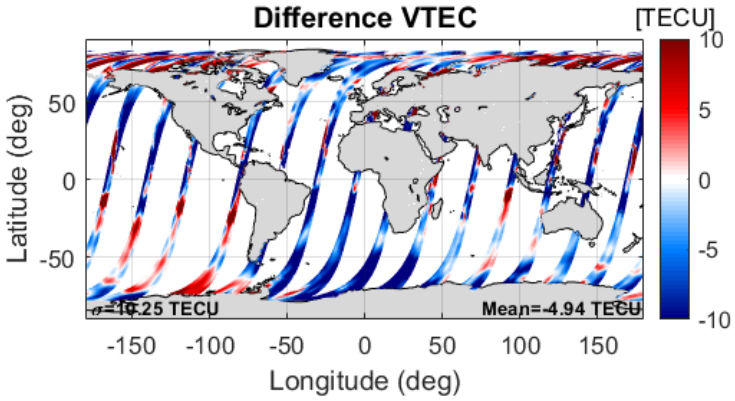

(a)

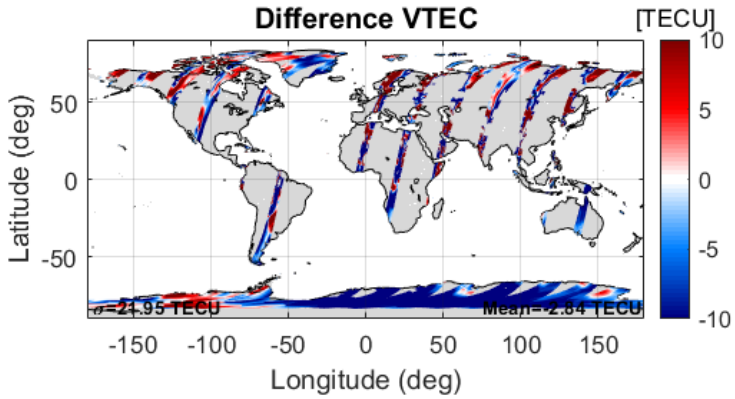

(b)

Figure 5.18. Difference between the recovered VTEC maps using the third approach and the L1 VTEC of the descending orbits of March 20th, 2014: (a) over ocean and (b) over land.

Once more, there are not many differences when comparing both Fig. 4.42 and Fig. 5.17, and Fig. 4.43 and Fig. 5.18 but in the geophysical longitudinal VTEC variability.

Figure 5.19 shows the difference between the recovered VTEC maps when using the third approach and when using the second approach over ocean (top) and over land (bottom). Same conclusions as the ones from 2011 can be drawn. There is a higher impact over ocean than over land when applying the correction of Δ.

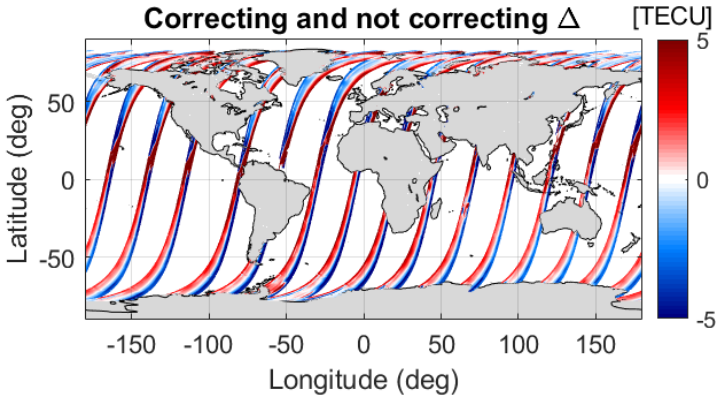

(a)

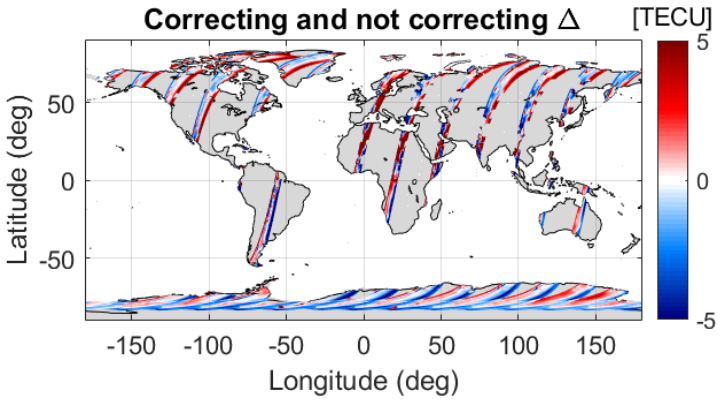

(b)

Figure 5.19. Difference between the recovered VTEC maps when using the third approach and when using the second one of the descending orbits of March 20th, 2014: (a) over ocean and (b) over land.

The ascending orbits of March 21st, 2011 have been also recovered using the third approach. The L1 VTEC and the recovered VTEC are shown in Figure 5.20 and the difference between both are shown in Figure 5.21, in the top, over ocean; in the bottom, over land. VTEC values lower than zero and higher than 40 TECU are rejected once again, knowing that they correspond to an error in the retrieval.

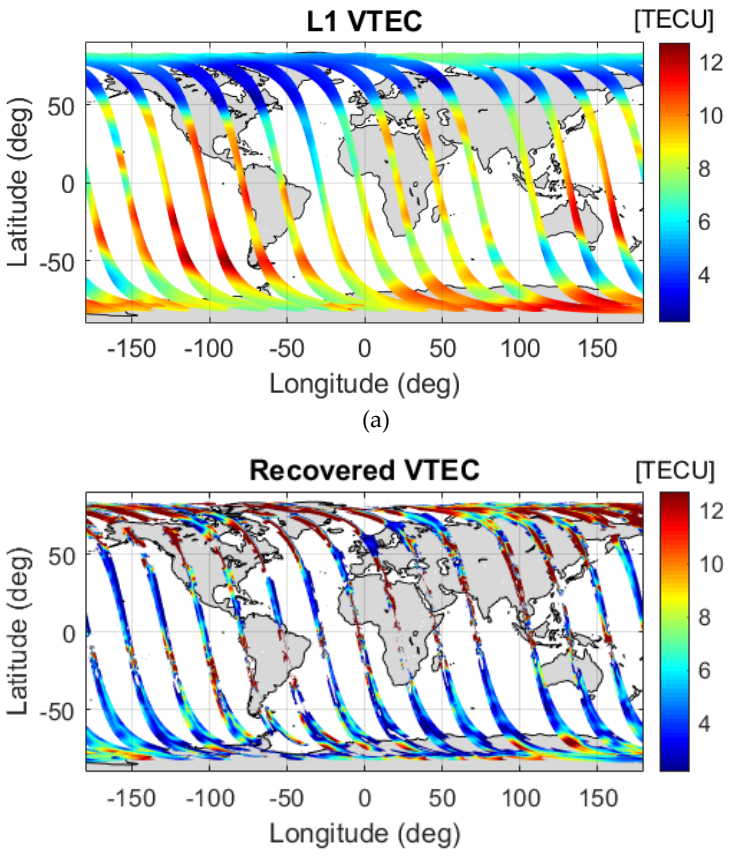

Figure 5.20. VTEC maps of the ascending orbits of March 21st, 2011 correcting the FRA systematic error: (a) L1 VTEC and (b) recovered VTEC using the third approach.

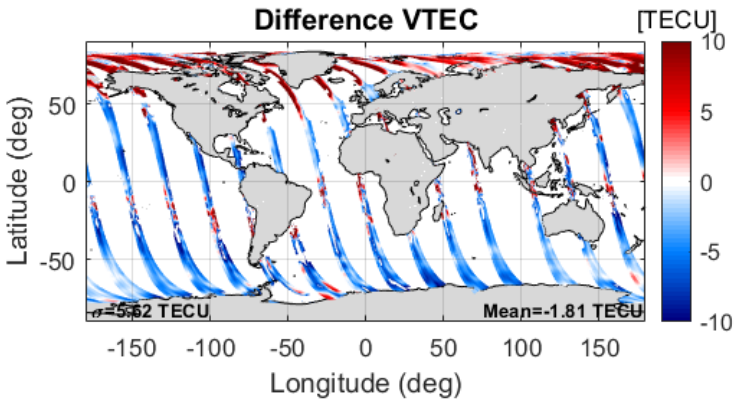

(a)

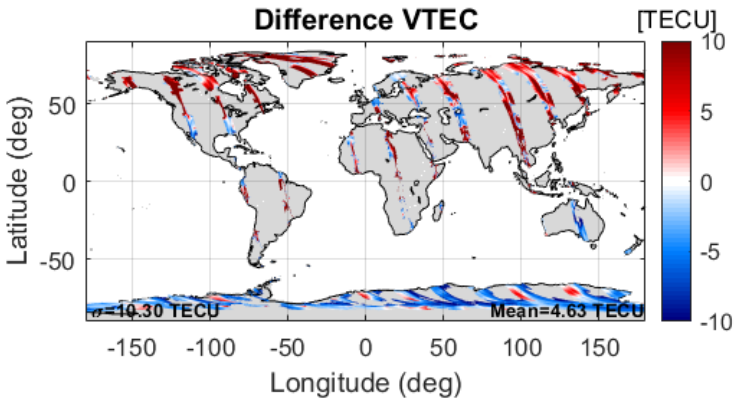

(b)

Figure 5.21. Difference between the recovered VTEC maps using the third approach and the L1 VTEC of the ascending orbits of March 21st, 2011: (a) over ocean and (b) over land.

The difference between the recovered VTEC maps when using the third approach and when using the second approach is shown in Figure 5.22. It can be seen over ocean in the top, and over land in the bottom.

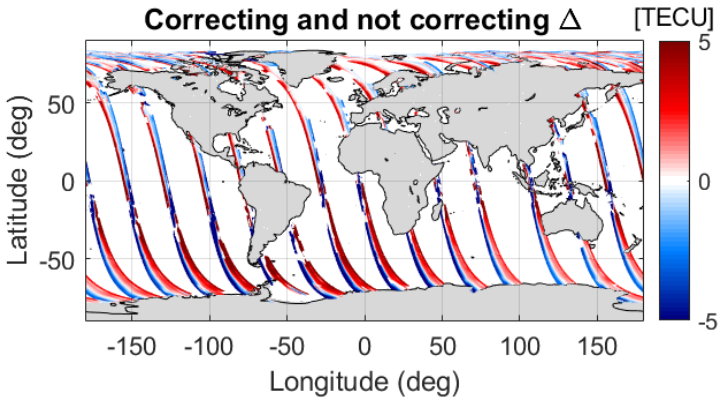

(a)

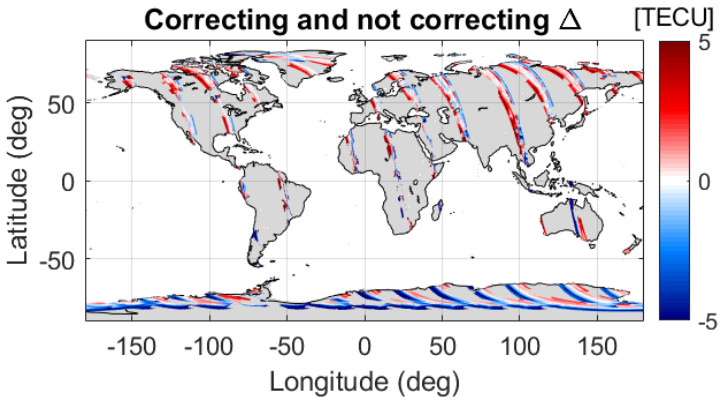

(b)

Figure 5.22. Difference between the recovered VTEC maps when using the third approach and when using the second one of the ascending orbits of March 21st, 2011: (a) over ocean and (b) over land.

Same plots are shown in Figure 5.23, Figure 5.24, and Figure 5.25 for March 20th, 2014.

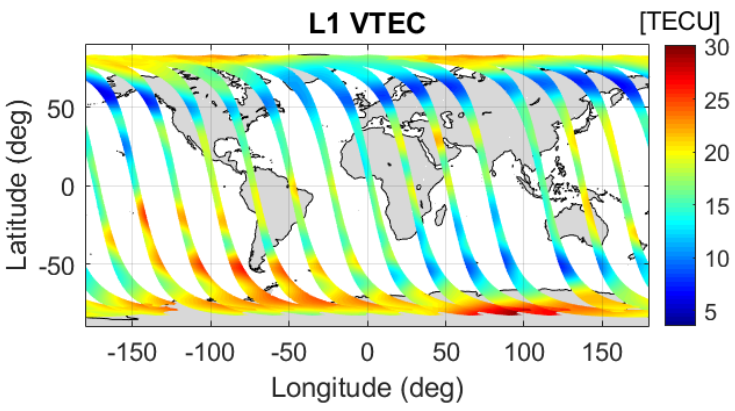

(a)

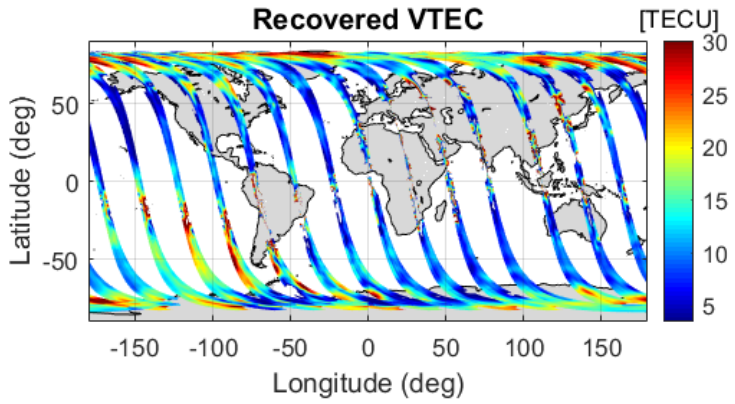

(b)

Figure 5.23. VTEC maps of the ascending orbits of March 20th, 2014: (a) L1 VTEC, (b) recovered VTEC using the third approach.

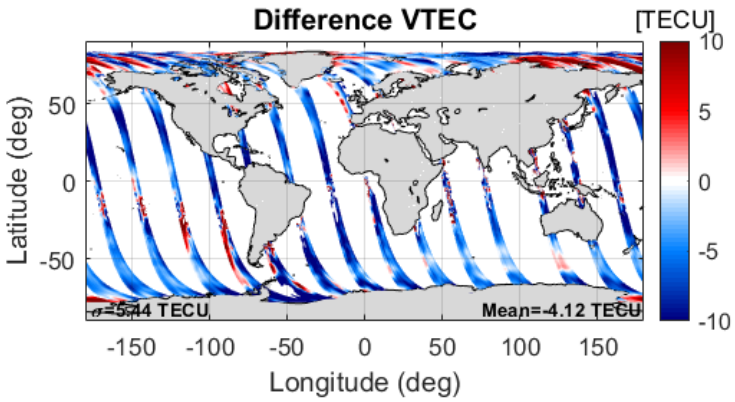

(a)

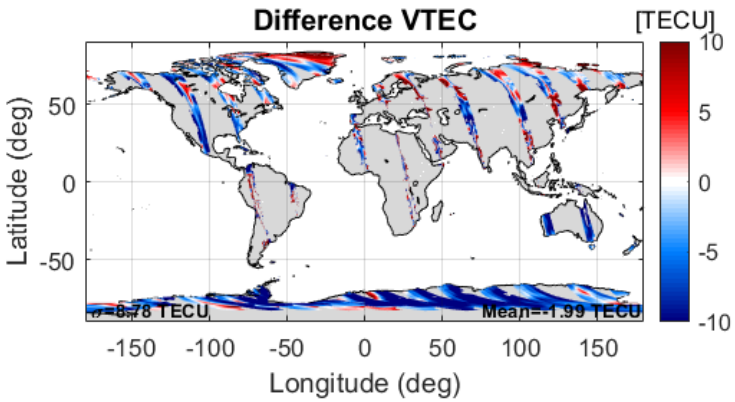

(b)

Figure 5.24. Difference between the recovered VTEC maps using the third approach and the L1 VTEC of the ascending orbits of March 20th, 2014: (a) over ocean and (b) over land.

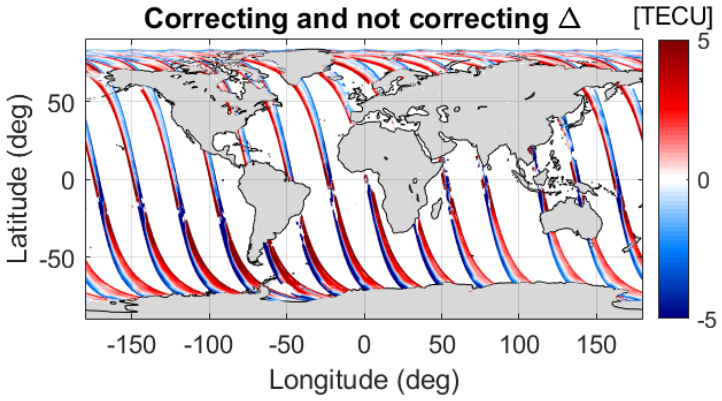

(a)

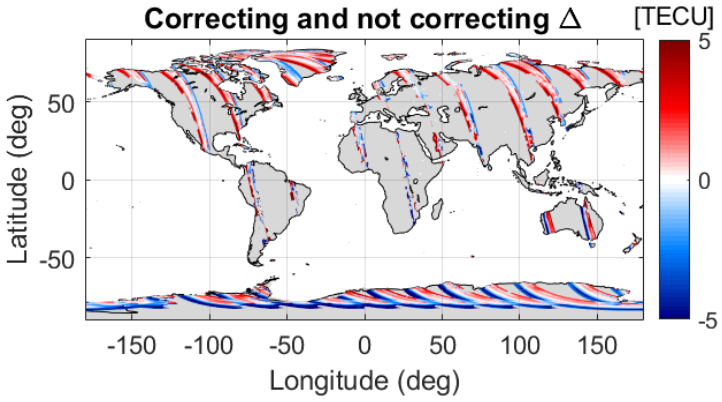

(b)

Figure 5.25. Difference between the recovered VTEC when using the third approach and when using the second one of the descending orbits of March 20th, 2014: (a) over ocean and (b) over land.

In both dates, it also happens, as in the descending case, that the recovery follows a more geophysical variation to what the VTEC is expected to be. It also can be seen by comparing the figures of the ascending orbits from Chapter 4 and from this chapter (Fig. 4.46 and Fig. 5.21, Fig.4.48 and Fig. 5.24) that less pixels are rejected out of the range of 0 to 40 TECU. This means that the retrieval using the third approach is within the expected range.

5.4. Conclusions

It was realized from Chapter 4 that there was a systematic error pattern when estimating the FRA from SMOS measurements. As a result, the retrieved VTEC maps were also affected in its longitudinal variability.

This systematic error pattern has been characterized in regions, periods and the type of orbits where the FRA should tend to zero. These correspond to zones with latitudes between 35°S and 5°S of ascending orbits and during JJA. In order to mitigate the effect of noise in its computation, the TB of three consecutive days have been averaged. The analysis has been

done for mid-July (low solar activity) of different years (2014, 2017, and 2018 and for the period 2010-2019). It has been corroborated that it can be considered temporally stable along the mission despite the variation of the solar activity. This temporal stability led to use the correction computed with the period 2010-2019 for the entire mission.

The addition in the methodology of the FRA systematic error subtraction to the retrieved FRA leads to an important improvement in the SMOS-derived VTEC maps, especially in the laterals of the swath. It not only improves the recovery of the descending orbits but also of the ascending orbits. Because the VTEC range of the ascending orbits is lower than the one of the descending orbits, the impact of adding this correction in the methodology is more visible. It is important to remark that the L1 VTEC is being used just as a reference to compare with, which means that all the shown statistics do not show the quality of the improvement. What it actually shows the improvement on the VTEC maps is the more geophysical consistent VTEC retrieved when correcting first the FRA from the systematic error pattern.

The correction of the FRA also causes an impact in the smoothness of the VTEC recovery, which also has an effect in the calculus of the FRA from the VTEC maps in order to correct the FRA in the mission.

Next chapter is devoted to assess the impact of using these SMOS-derived VTEC maps on the TB quality with respect to the case of using the L1 VTEC. The assessment has been focused over the ocean, where the impact of ionospheric corrections is stronger because of the limited sensitivity of the brightness temperatures to sea surface salinity, which is higher for soil moisture.

Chapter 6

Assessment of the Recovered Vertical Total Electron Content

The main objective of this chapter is the quality assessment of the VTEC maps retrieved with the third approach and the analysis of the impact that their use can have in the SMOS geophysical retrievals. From now on, the recovered VTEC maps with the third approach are going to be assumed as SMOS-derived VTEC maps.

As part of this analysis, global monthly SMOS-based VTEC maps have been generated and analyzed with respect to the L1 VTEC maps. After this, the analysis has been focused over ocean, where the impact of the ionospheric corrections is stronger. Some of the usual L1 metrics, such as the spatial biases, the Hovmöller diagrams to show the stability, are used to evaluate the performance of SMOS-derived VTEC maps with respect to the L1 VTEC.

6.1. Hovmöller Diagrams of VTEC

In order to evaluate the temporal variability of the VTEC, three years (2014 to 2016) were chosen to calculate a Hovmöller diagram. These years were selected because they are the ones with the highest solar activity along the SMOS mission. One orbit over the Pacific was selected per day (shown in Figure 6.1), and the SMOS-derived VTEC maps are calculated within an ETOPO-5 grid (equivalent to 5 minutes or 0.08°). Then, this resolution is interpolated to the one of the L1 VTEC –a much coarser one (2.5°)– to be able to compare them.

Figure 6.2 shows the VTEC Hovmöllers for descending orbits: in the top, the one using the L1 VTEC; in the middle, with the SMOS-derived VTEC; and in the bottom, the difference between the second one and the first one.

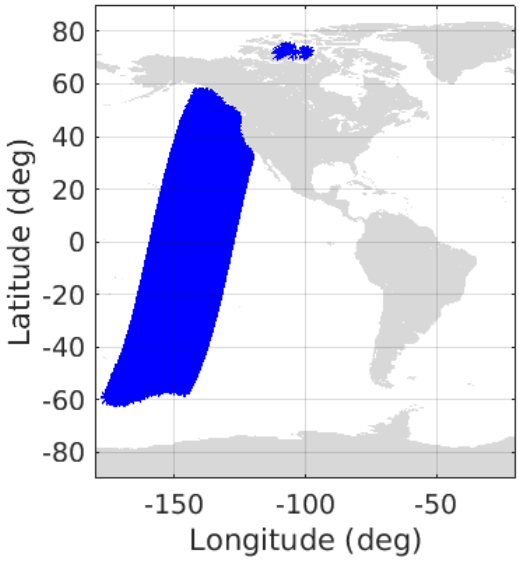

Figure 6.1. Descending orbits selected for the VTEC Hovmöller.

It can be seen that in latitudes from 40°N to 60°N there are some orbits with data gaps. That is because, in these plots, only the VTEC over ocean is shown, and, as it can be seen in Fig. 6.1, there are some orbits that are over land.

The SMOS-derived VTEC Hovmöller does not present any bias throughout the mission, at least, over the Pacific Ocean. As expected, the SMOS-derived VTEC is mostly below the L1 VTEC over the years except for zones close to the descending-orbit geomagnetic equator (latitudes around 20°N, especially in the beginning and the end of the year). In addition, as it was noted in Fig. 3.4a, 2014 was the year with the highest VTEC, and it decreases over the years.

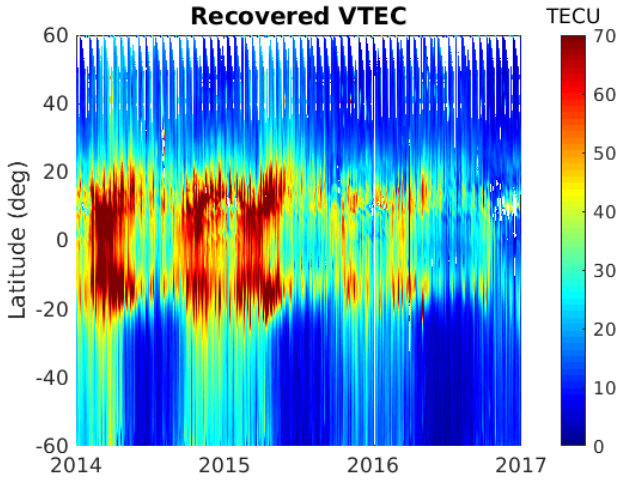

(a)

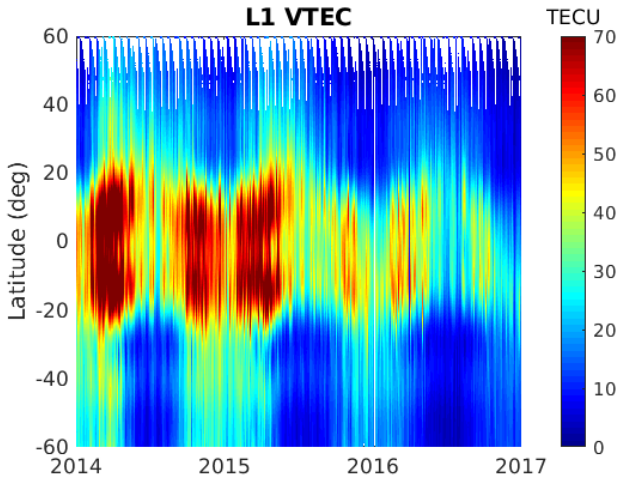

(b)

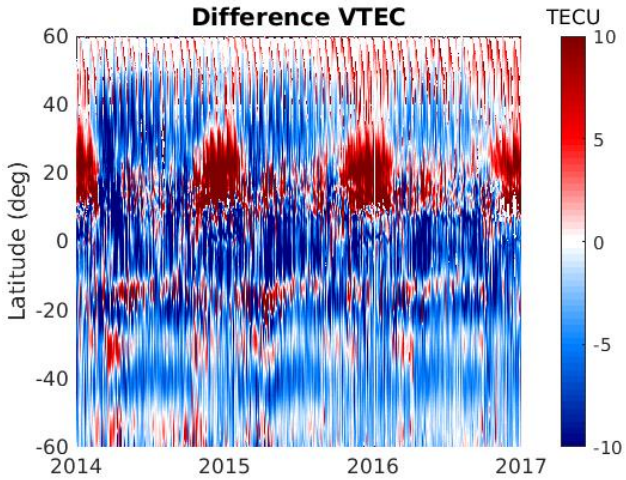

(c)

Figure 6.2. VTEC Hovmöllers of the descending orbits: (a) L1 VTEC, (b) SMOS-derived VTEC, and (c) difference between the SMOS-derived VTEC and the L1 VTEC.

Plots for the ascending orbits are shown in Figure 6.3 and Figure 6.4. In the first one, the selected orbits for the Hovmöller diagram are shown, and in the second one, in the top, middle, and bottom there is the L1 VTEC Hovmöller, the SMOS-derived VTEC one, and the difference between the second one and the first one.

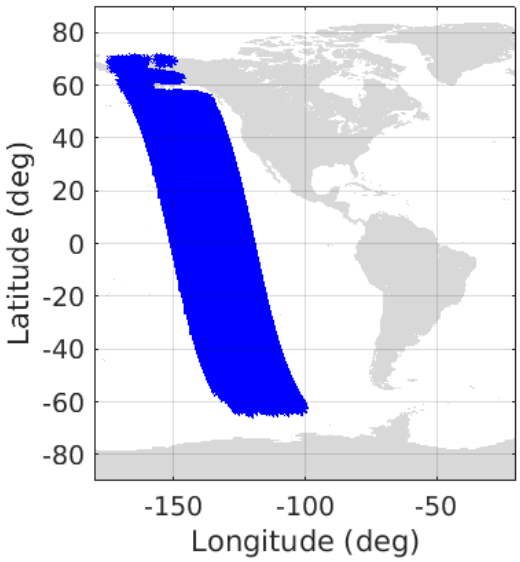

Figure 6.3. Ascending orbits selected for the VTEC Hovmöller.

As noted in the SMOS-derived VTEC Hovmöller of descending orbits, in ascending orbits, differences between the SMOS-derived VTEC and L1 VTEC are similar throughout the different years. Once again, it is shown that SMOS-derived VTEC is mainly below the L1 VTEC except for the zone close to the geomagnetic equator (latitudes around 20°S). Note that the scales used for ascending and descending orbits are quite different.

In Fig. 6.4b and c, in the range of latitudes between 40°S and 20°S there is no recovery data, mainly in the second half of each year. This corresponds to pixels with SMOS-derived VTEC lower than 0 TECU that were rejected in order to show only VTEC values that have geophysical sense. The error in that zone occurs because the VTEC range of those pixels are low, and both, the effect of noise and the closeness to the indetermination of Eq. (5.4) affect the recovery. It is noteworthy mentioning that the lower the solar activity per year, the higher the number of rejected pixels.

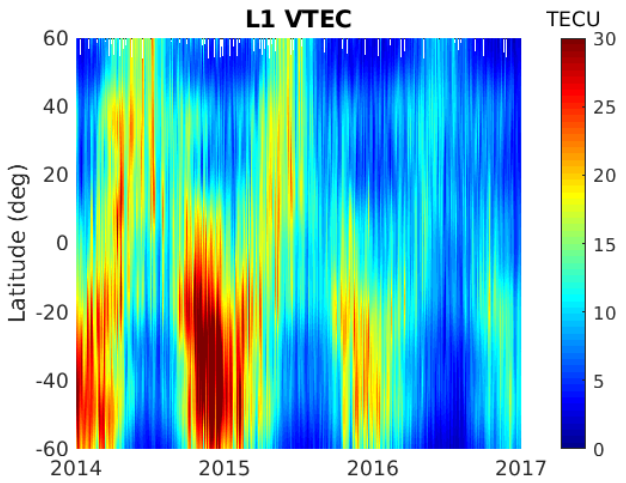

(a)

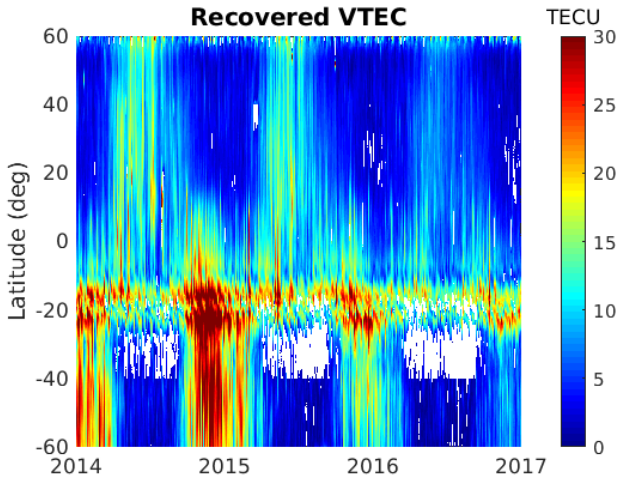

(b)

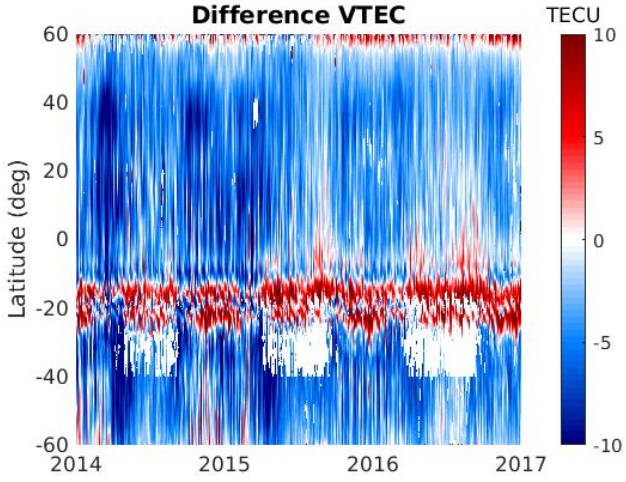

(c)

Figure 6.4. VTEC Hovmöllers for ascending orbits: (a) L1 VTEC, (b) SMOS-derived VTEC, and (c) difference between the SMOS-derived VTEC and the L1 VTEC.

6.2. Monthly VTEC Global Maps

To evaluate the geographical variability of the SMOS-derived VTEC along the mission, the year 2014 was chosen to calculate global VTEC maps since it is the year with the highest solar activity. All the VTEC descending overpasses were recovered and plotted per month in global maps. In the following images, the L1 VTEC is shown in subfigure (a); in the (b), the SMOS-derived VTEC map; and in the (c), the difference between the second one and the first one. Only plots of January (Figure 6.5) and March (Figure 6.6) are shown because they are the months with lowest and highest VTEC, respectively. The rest of the plots can be seen in Appendix A.

It is important to recall that the VTEC has a significant variation along the day, and, even more, along a month. Therefore, it is noteworthy to remark that these global VTEC maps are shown just to have a worlwide overview of the SMOS-derived VTEC and its comparison with respect to the L1 VTEC. They also show that there are not any systematic patterns in the retrieval.

These monthly maps can be helpful to detect systematic errors in the SMOS-based VTEC maps and which are the main limitations in the VTEC retrieval both over land and ocean.

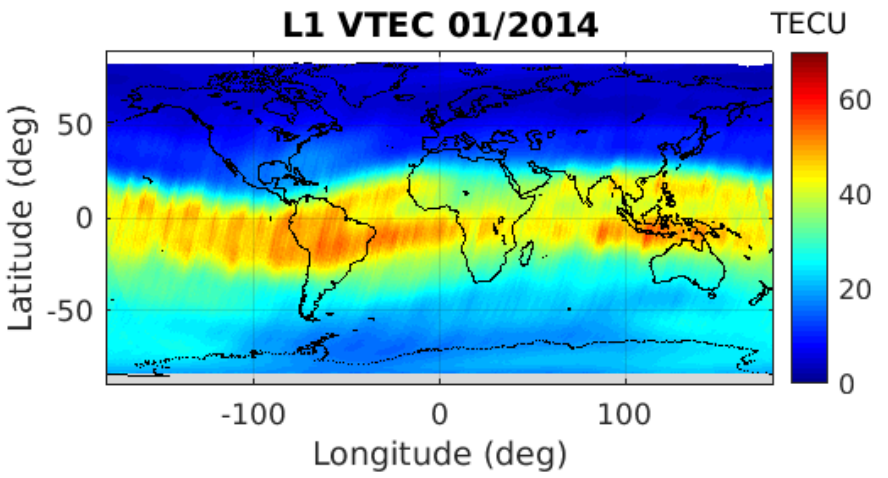

(a)

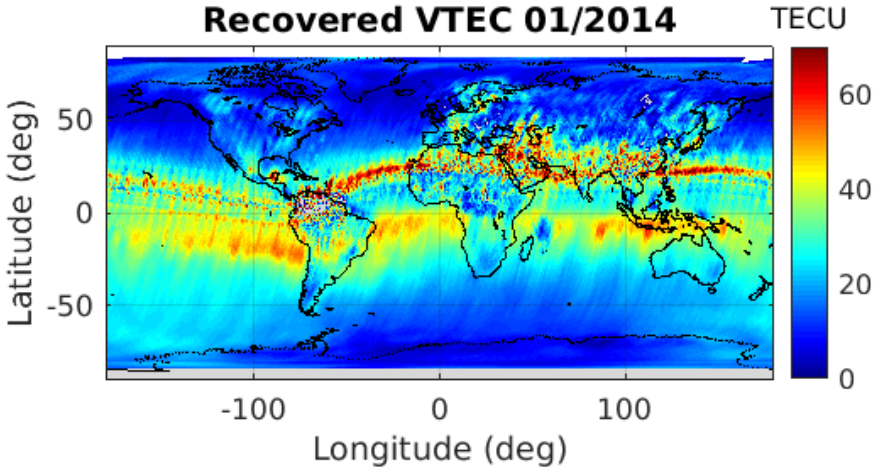

(b)

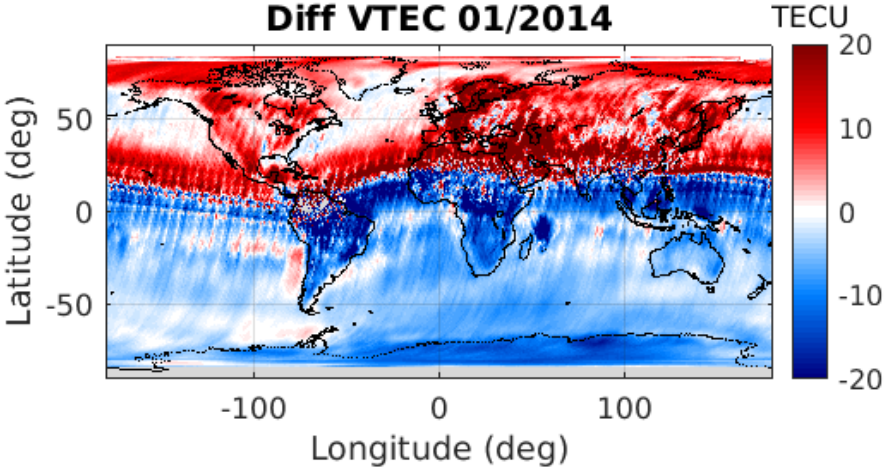

(c)

Figure 6.5. VTEC global maps of January 2014 (descending orbits): (a) L1 VTEC, (b) SMOS-derived VTEC, and (c) difference between the SMOS-derived VTEC and the L1 VTEC.

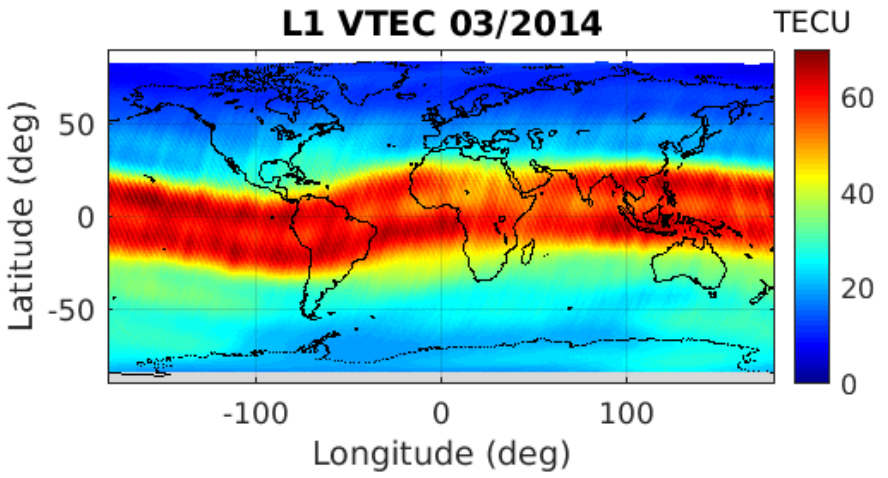

(a)

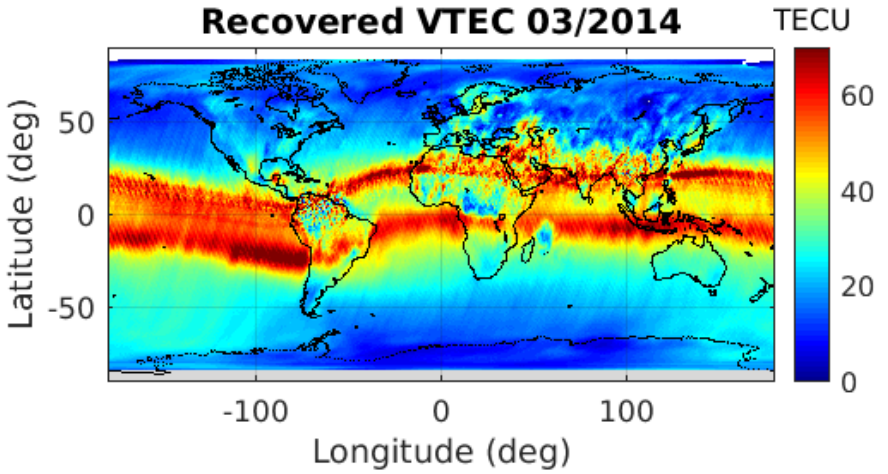

(b)

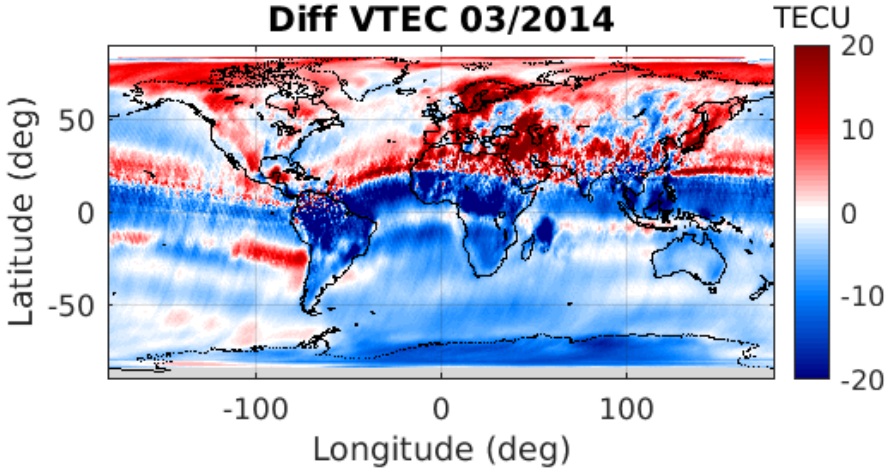

(c)

Figure 6.6. VTEC global maps of March 2014 (descending orbits): (a) L1 VTEC, (b) SMOS-derived VTEC, and (c) difference between the SMOS-derived VTEC and the L1 VTEC.

When taking a look at the SMOS-derived VTEC maps per month (plot (b) of every of the previous figures), there are some points to remark. The month with the lowest VTEC corresponds to January, and the ones with the highest, to March and April. Differences between the SMOS-derived VTEC and the L1 VTEC are spatially consistent in the different months. It can be observed in all months in the zone of Europe and Asia how the recovery over land is strongly affected by the presence of RFI sources. This affectation can be also observed in the Japan Sea. On the other hand, it can be seen that over tropical forests (such as in the Amazon and the zone of Africa around the Equator among others) the TEC retrieval is highly ill-conditioned, since the TB in the X and Y polarizations have similar strength, causing an indetermination in the Eq. (5.1), as it was previously discussed (see section 3.2.2.4.2.2.). In these cases, the $T_B^{hh} \approx T_B^{xx}$ and $T_B^{vv} \approx T_B^{yy}$, and the error in the SMOS-derived VTEC does not represent an issue in the compensation of the FRA. Figure 6.7 shows a map of the world's forests, where it happens this condition.

Once again, it is noteworthy that this methodology is independent of any forward model and it is able to provide globally VTEC retrievals, although as above-mentioned, the retrieval over land presents some limitations. Regardless of that, there are not any systematic patterns that can be noticed but in the zone close to the geomagnetic equator, where there are errors in the retrieval because of the fact that the term $\cos\Theta_B$ of the denominator of Eq. (5.4) tends to 0 and it causes an indetermination. This is not a problem from the point of view of the Faraday rotation correction, since it vanises, independently of the TEC, when the geomagnetic field is aligned with the signal path. It is important to remark that the retrieval over Australia does not present any abnormal features. Moreover, the retrieval over the coast and ices edges is challenging due to the fact that there is an abrupt change of brightness temperatures. Nonetheless, there is nor land-sea contamination neither ice-sea contamination effects (Martín-Neira et al., 2016) in the retrieval of the VTEC maps.

When comparing the global L1 VTEC map with the SMOS-derived VTEC one (plot (c) of every of the previous figures), there are systematic patterns that happen in the geomagnetic Northern Hemisphere (latitudes higher than approximately 20°N) –hereafter, called NH– and in the geomagnetic Southern Hemisphere –hereafter, called SH–. Over the months, over land, in the NH, the recovery is always above the L1 VTEC; whereas, in the SH, it tends to be below the L1 VTEC. Along the months, over ocean, in the SH, the recovery tends to be mainly below the L1 VTEC; whereas in the NH, there is not a specific systematic pattern of the recovery with respect to the L1 VTEC.

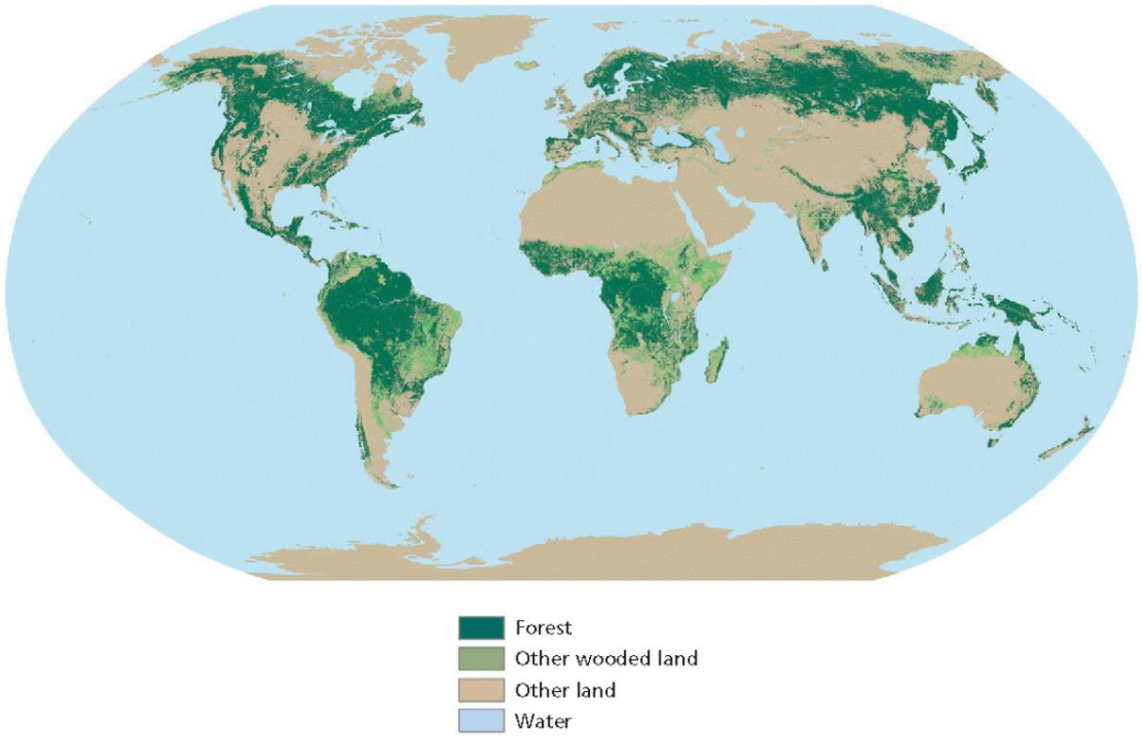

Figure 6.7. The world's forests (Food and Agriculture Organitation, FAO, n.d.)

In the following figures, the global VTEC maps of January (Figure 6.8) and March (Figure 6.9) are shown because they are the months with lowest and highest VTEC, respectively. The rest of the plots can be seen in Appendix B. The top plot corresponds to the L1 VTEC map; the middle one, to the SMOS-derived VTEC and the bottom one, to the difference between the SMOS-derived VTEC and the L1 VTEC.

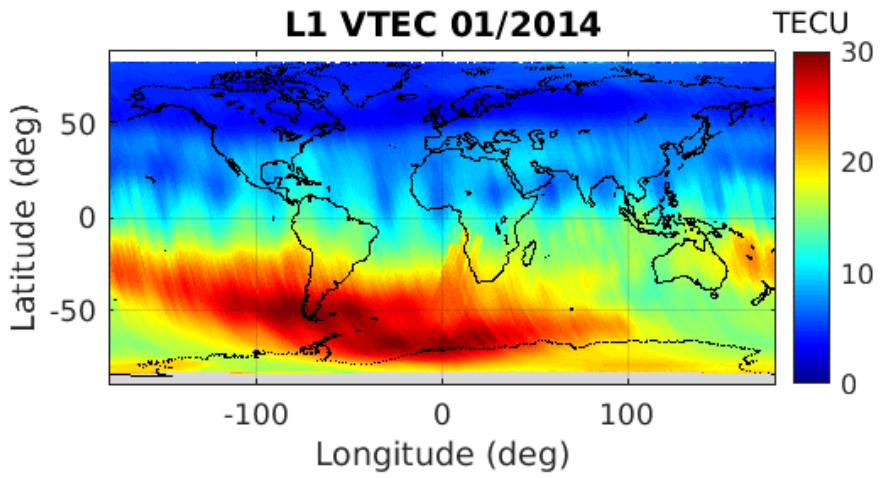

(a)

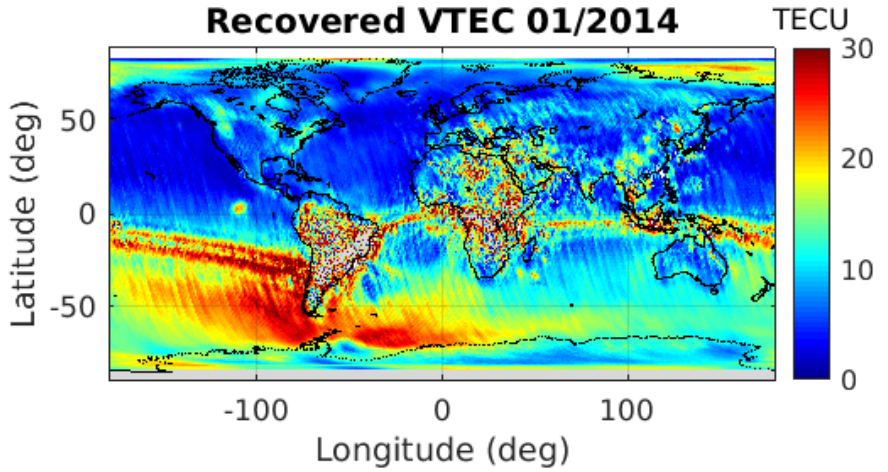

(b)

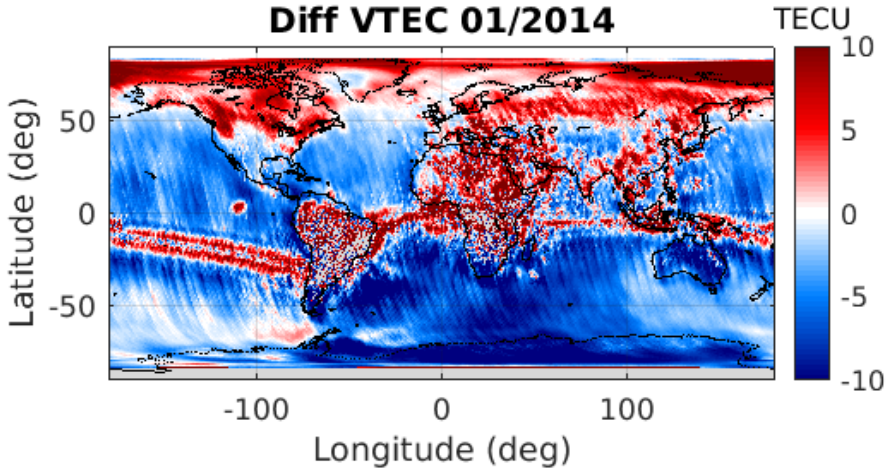

(c)

Figure 6.8. VTEC global maps of January 2014 (ascending orbits): (a) L1 VTEC, (b) SMOS-derived VTEC, and (c) difference between the SMOS-derived VTEC and the L1 VTEC.

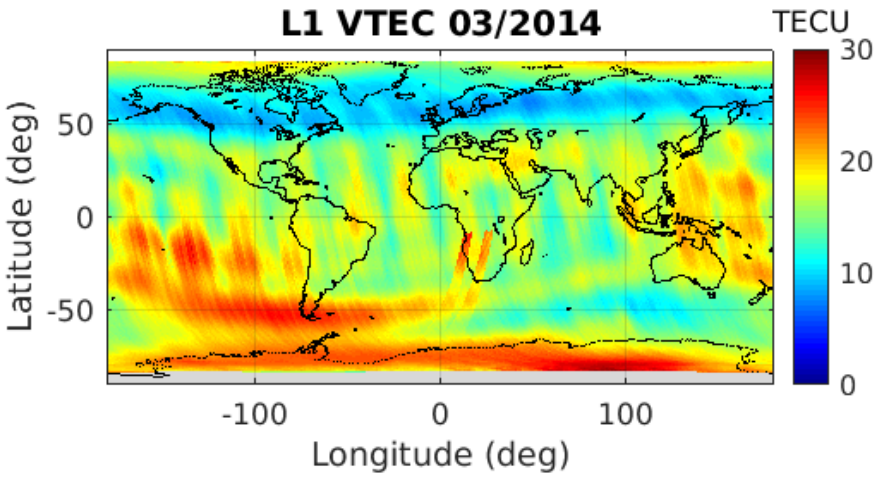

(a)

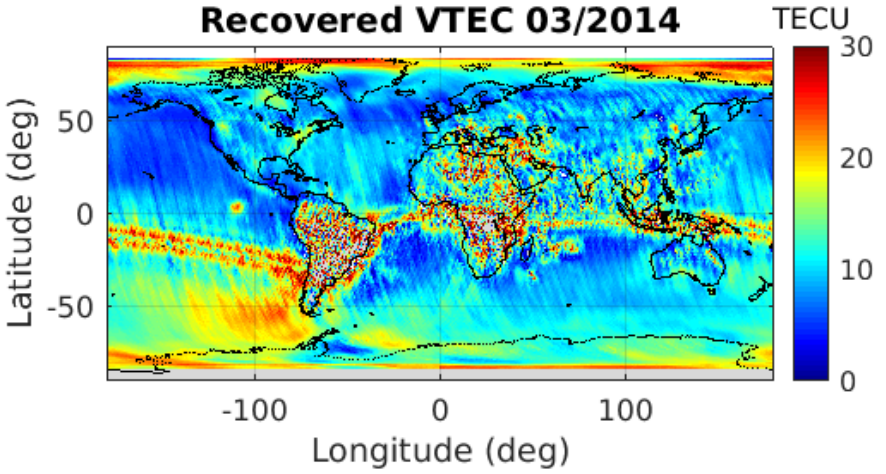

(b)

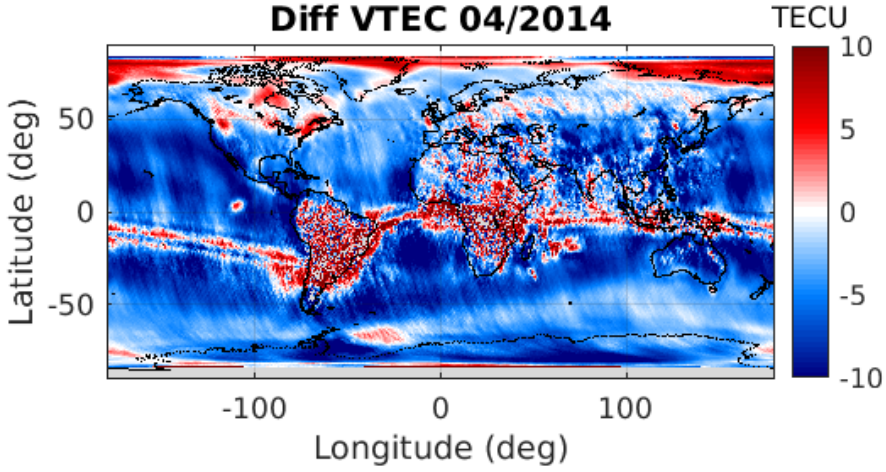

(c)

Figure 6.9. VTEC global maps of March 2014 (ascending orbits): (a) L1 VTEC, (b) SMOS-derived VTEC, and (c) difference between the SMOS-derived VTEC and the L1 VTEC.

The results obtained for the ascending orbits follow the same pattern of the ones addressed for the descending ones. In this case, the presence of RFI in Europe and Asia affects the recovery with a higher impact. Additionally, once again the affectation over tropical forests due to the similarity of the polarization X and Y in the TB and the T3 tending to 0 TECU is more drastic, as well as the retrieval over both the continental ice and the land-sea transition. It has to be consider for both conclusions that the VTEC scale range in this type of orbits is lower, which emphasizes visually the higher affectation in the recovery. Finally, along the months, over ocean, the recovery is always below the L1 VTEC, but close to the zone where the geomagnetic field is aligned with the signal path, as it happens in the retrieval of the descending orbit.

6.3. Spatial Bias on Brightness Temperatures

To analyze the impact of using the SMOS-derived VTEC maps on the TB spatial biases, the differences between the measured and the theoretically modeled brightness temperatures as a function of the spatial direction (i.e, in (ξ,η) antenna coordinates) are computed. This is done over a very stable region in the South Central Pacific Ocean (Tenerelli & Reul, 2010). Typically, ten orbits in ascending/descending orbits are used and the temporal median of the difference between measurements and model are computed.

The modeled TB are derived by evaluating the Geophysical Model Function (GMF) presented in (Zine et al., 2008), using geophysical priors for SSS (climatology from World Ocean Atlas 2009 (Antonov et al., 2010)), SST (Sea Surface Temperature) and wind speed at time of the acquisition provided by the European Center for Medium-Range Weather Forecasts (ECMWF) (Sabater et al., 2010). VTEC products are used to transform modeled TB at ocean surface to antenna reference frame.

The spatial biases using the SMOS-derived VTEC products have been compared with respect to the ones obtained when the L1 VEC product is used. It is noteworthy to recall that even if in the methodology developed in this research, there is a pixel rejection in the recovered FRA snapshots (section 4.1.3.), the FRA can be calculated for the entire snapshot (including the low-incidence-angle region) from the SMOS-derived VTEC maps because they do not present any miss of information.

The particular metric used for the assessment of the spatial biases corresponds to the standard deviation of the difference between SMOS and modeled TB normalized by the radiometric accuracy, quantity that should be close to 1 (Oliva & ESA team, 2015). Figure 6.10 shows this metric (descending orbits from April 27th to May 6th, 2012 over the South Pacific have been used) for the X polarization, in the left (Fig. 6.10a), when using the L1 VTEC to generate modeled TB at antenna reference; in the right (Fig. 6.10b), when using the SMOS-derived VTEC maps.

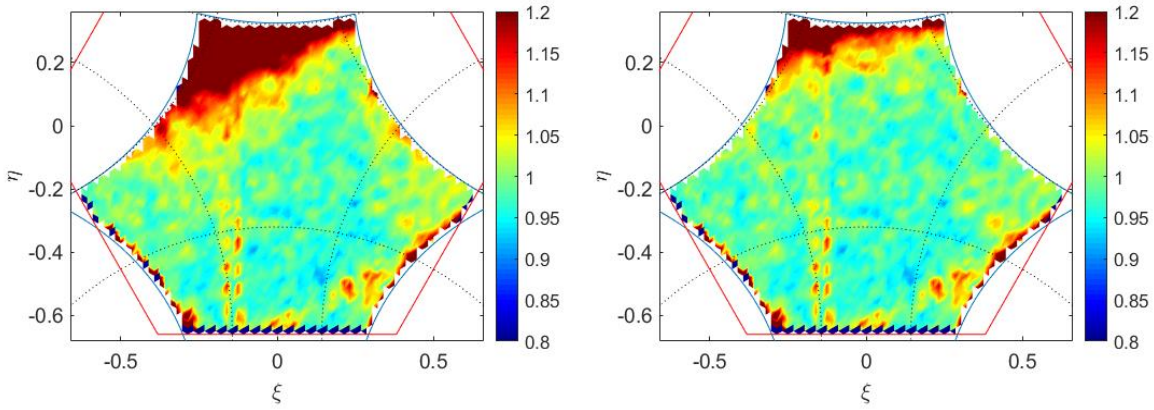

(a) (b)

Figure 6.10. Standard deviation of the difference between SMOS and modeled TB normalized by the radiometric accuracy for the X polarization (descending orbits of April 27th to May 6th, 2012): (a) when the L1 VTEC is used to transform modeled TB at ocean surface to antenna frame, and (b) when the SMOS VTEC is used.

Figure 6.11 shows the same plots but for the Y polarization: in the left, when using the L1 VTEC and in the right, when using the SMOS VTEC.

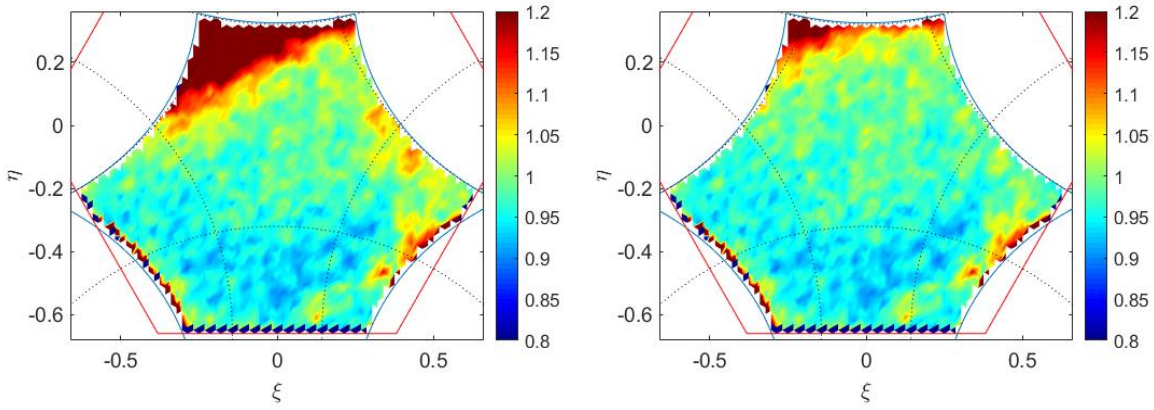

(a) (b)

Figure 6.11. Standard deviation of the difference between SMOS and modeled TB normalized by the radiometric accuracy for the Y polarization (descending orbits of April 27th to May 6th, 2012): (a) when the L1 VTEC is used to transform modeled TB at ocean surface to antenna frame, and (b) when the SMOS VTEC is used.

Figure 6.12 shows the plots of the T3.

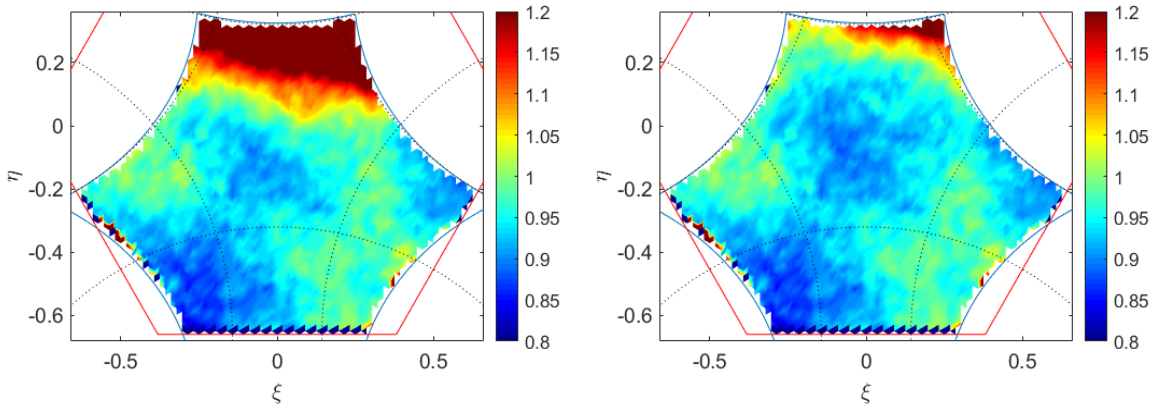

(a) (b)

Figure 6.12. Standard deviation of the difference between SMOS and modeled TB normalized by the radiometric accuracy for T3 (descending orbits of April 27th to May 6th, 2012): (a) when the L1 VTEC is used to transform modeled TB at ocean surface to antenna frame, and (b) when the SMOS VTEC is used.

A clear significant improvement is observed in all polarizations when using the SMOS-derived VTEC products. In the area of the FoV with highest sensitivity to TEC (as reported in Figure 1 of Vergely et al., 2014), with high incidence angles (top part of the snapshot). This result demonstrates that part of the spatial biases was, in fact, due to a poor estimation of the TEC.

The spatial biases have been also computed for a different date (descending orbits from May 26th to June 5th, 2014) and they are shown in Figure 6.13, Figure 6.14, and Figure 6.15 for the X, Y polarization, and T3, respectively.

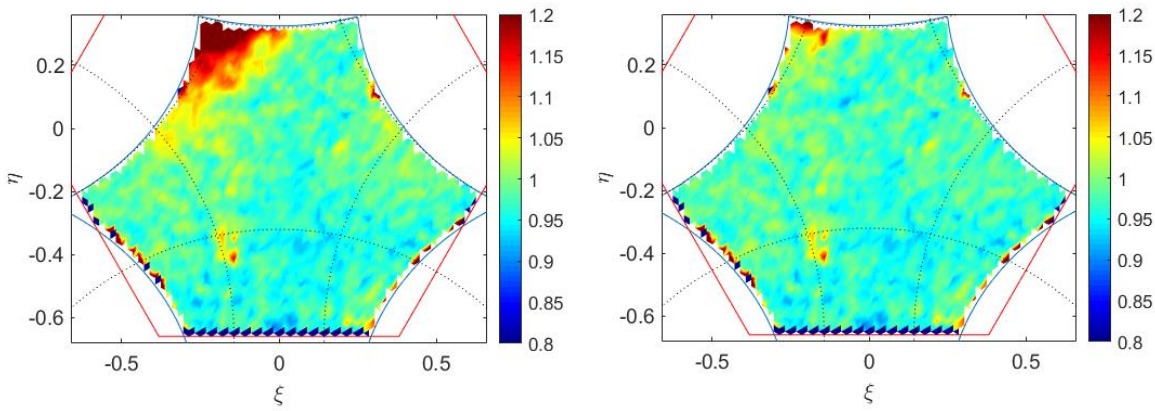

(a) (b)

Figure 6.13. Standard deviation of the difference between SMOS and modeled TB normalized by the radiometric accuracy for the X polarization (descending orbits of May 26th to June 5th, 2014): (a) when the L1 VTEC is used to transform modeled TB at ocean surface to antenna frame, and (b) when the SMOS VTEC is used.

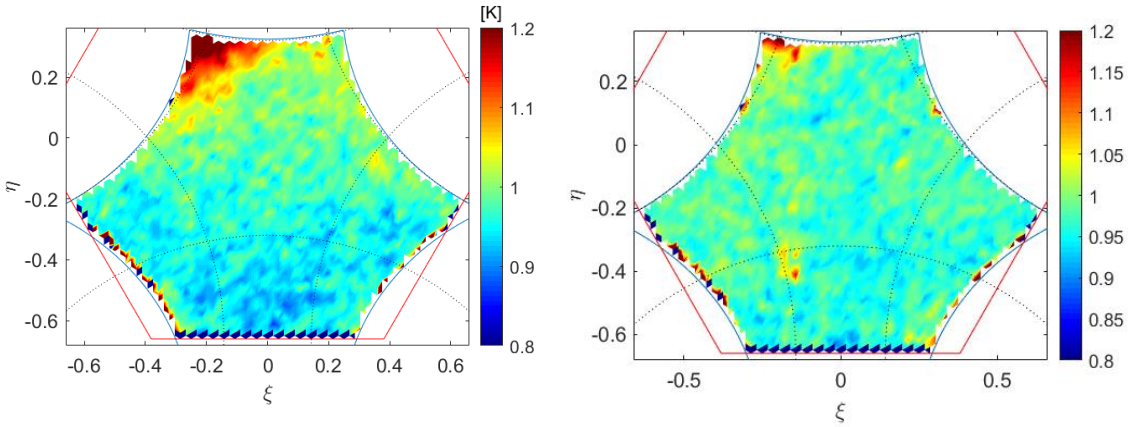

(a) (b)

Figure 6.14. Standard deviation of the difference between SMOS and modeled TB normalized by the radiometric accuracy for the Y polarization (descending orbits of May 26th to June 5th, 2014): (a) when the L1 VTEC is used to transform modeled TB at ocean surface to antenna frame, and (b) when the SMOS VTEC is used.

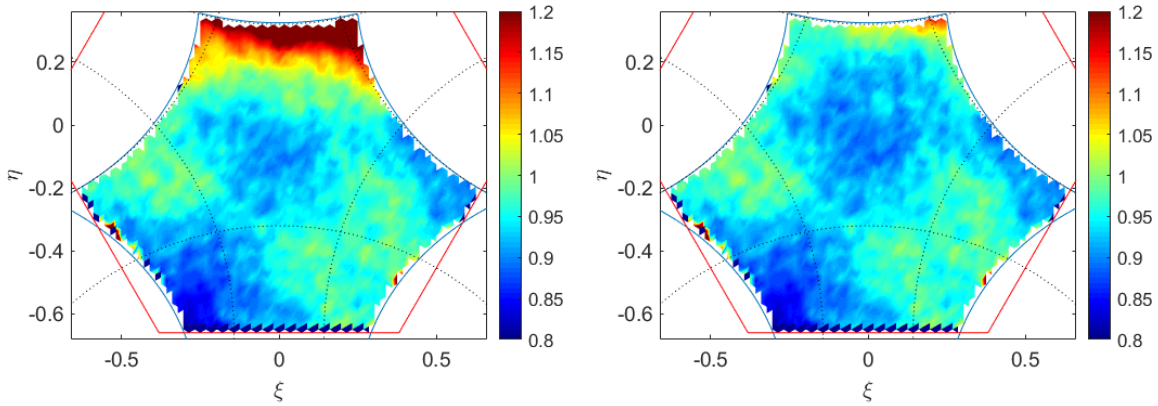

(a) (b)

Figure 6.15. Standard deviation of the difference between SMOS and modeled TB normalized by the radiometric accuracy for T3 (descending orbits of May 26th to June 5th, 2014): (a) when the L1 VTEC is used to transform modeled TB at ocean surface to antenna frame, and (b) when the SMOS VTEC is used

In the plots of 2014, there is also a significant improvement for all the polarizations in the region of the field of view with higher incidence angles. The impact of this improved stability is expected to be quite significant in terms of retrieved salinities, since it is used in the correction for the spatial bias worldwide even though it is computed only in the region South Pacific Ocean.

6.4. Assessment on Brightness Temperature Stability

The next step has been the assessment of the impact using the SMOS-derived VTEC maps to correct the FRA instead of the L1 VTEC products on the brightness temperature stability. In order to analyze the stability using the two VTEC products, Hovmöller diagrams of the difference between the SMOS and the modeled TBs at antenna reference frame have been generated per each polarization. This is a usual metric in the SMOS Level 1 Expert Support Laboratories (ESL) for the assessment of TB stability (Oliva & ESA team, 2015). Those orbits over the Pacific Ocean (one ascending orbit and one descending per day) in the period 2014-2016 have been used in this analysis. This period has been chosen because it includes the year 2014, which is the one with the highest VTEC along the mission.

The color represents the mean difference of SMOS TB with respect to the model. All the TBs in the AF-FoV have been averaged per each snapshot. The y axis corresponds to the boresight latitude at which the TB measurement has been acquired (using bins of 0.25° in latitude), and the x axis corresponds to time. It must be pointed out that the mean bias along the mission has been subtracted to the Hovmöller diagram.

Figure 6.16 and Figure 6.17 show the descending-orbit TB Hovmöllers for the X and Y polarizations, respectively. The top plot corresponds to the one when using the L1 VTEC in the rotation of the modeled TB from the surface plane to antenna plane reference, and the bottom one, to the one when using the SMOS-derived VTEC map.

It is important to remark that, as it can be seen in Figures 6.2 and 6.4, the VTEC Hovmöllers cover latitudes from 60°N to 60°S and all TB Hovmöller plots shown as follows cover latitudes 40°N to 50°S. This is because the first ones were calculated using the entire SMOS overpasses but cut over land, and the second ones were calculated using only the latitudes of the orbit where the complete AF-FoV is over the ocean.

In both polarizations, the main differences can be seen between 20°S and 0° of latitude. Also, where there is a negative bias along the Hovmöller, the one that uses the SMOS-derived VTEC is less saturated than the one that uses L1 VTEC.

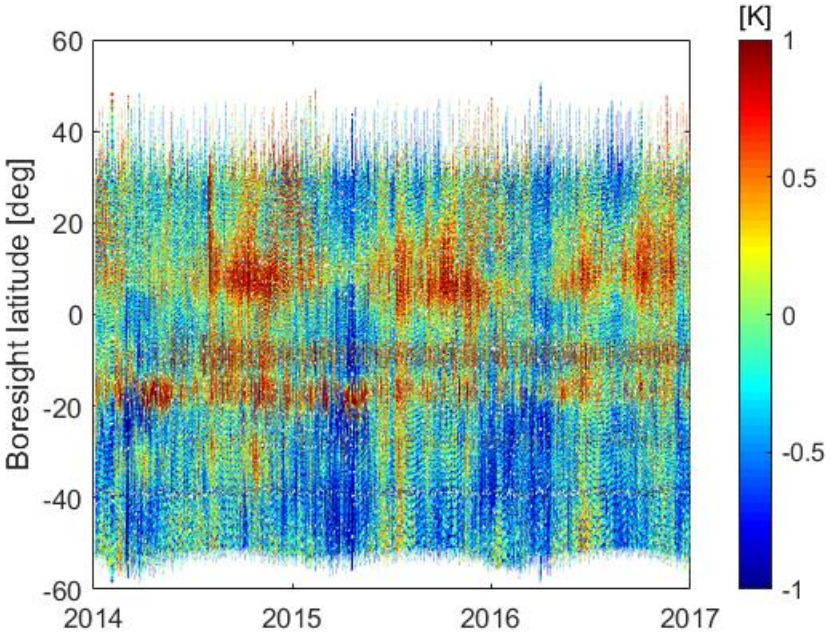

(a)

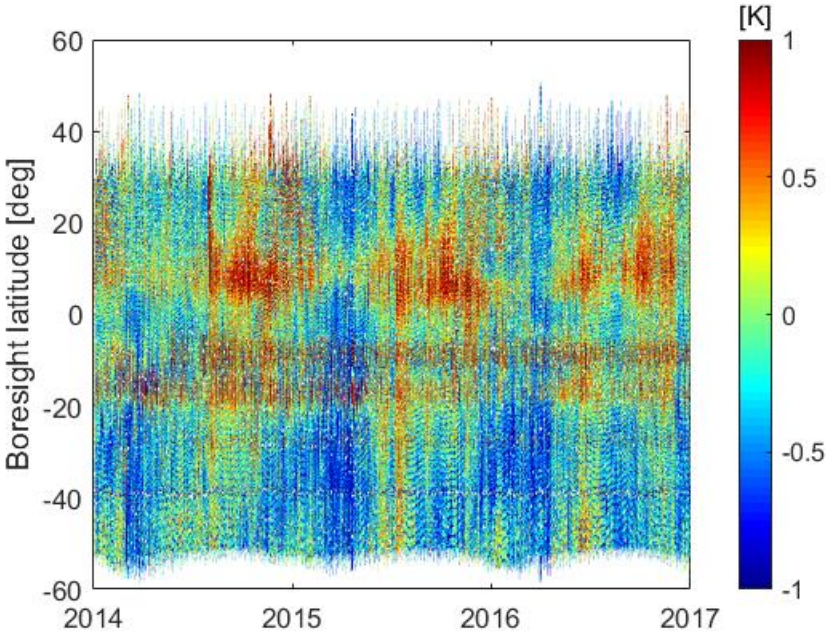

(b)

Figure 6.16. Hovmöller diagram of the difference between the SMOS TB and the modeled TB (averaged in the AF-FoV) for the X polarization at antenna reference for descending orbits: (a) the L1 VTEC product has been used to correct for the FR in the modeled TB, and (b) SMOS-derived VTEC maps have been used for the FR correction.

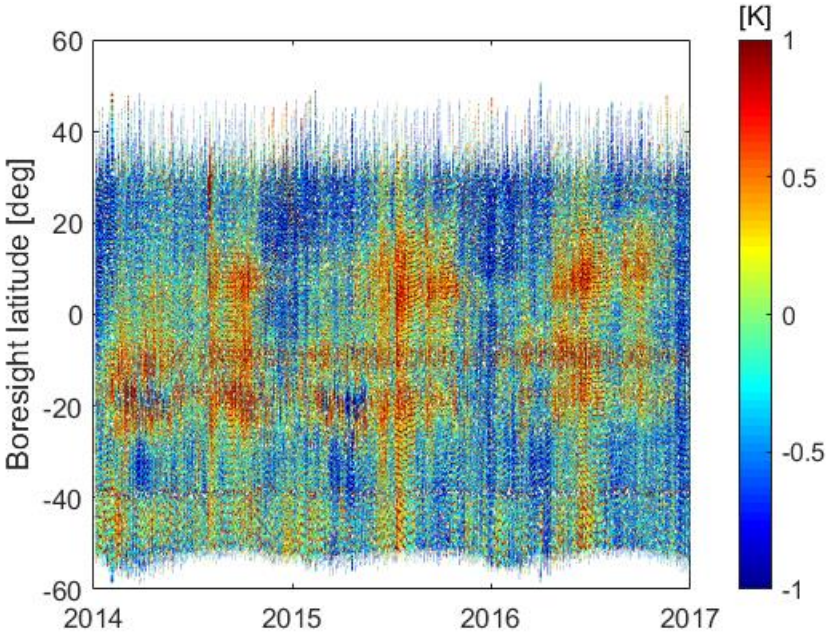

(a)

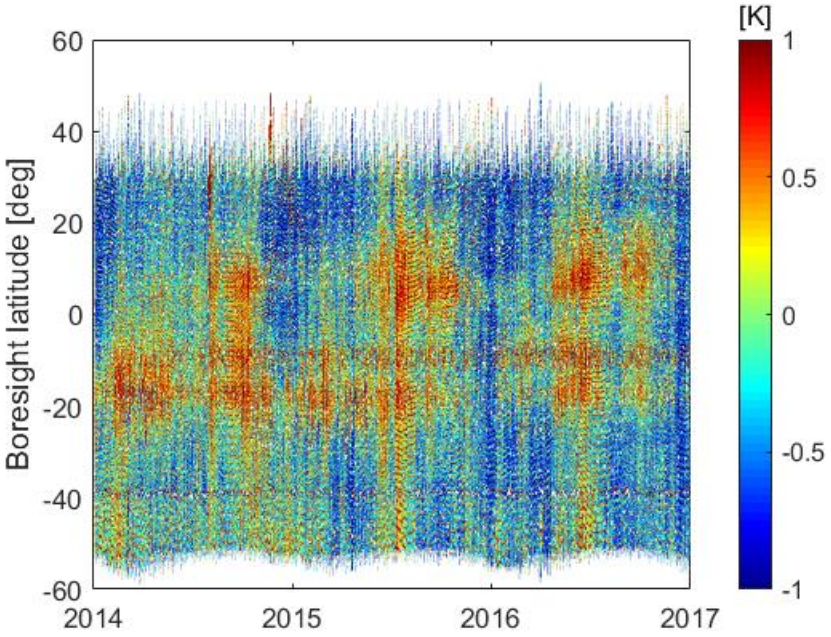

(b)

Figure 6.17. Hovmöller diagram of the difference between the SMOS TB and the modeled TB (averaged in the AF-FoV) for the Y polarization at antenna reference for descending orbits: (a) the L1 VTEC product has been used to correct for the FR in the modeled TB, and (b) SMOS-derived VTEC maps have been used for the FR correction.

In order to analyze more in detailed, some orbits from the TB Hovmöller were taken separately and plotted with respect to the latitude. In the following figures, the SMOS TB

minus the TB model rotated with the L1 VTEC is shown in red, and when rotated with the SMOS-derived VTEC, in blue.

Figure 6.18 shows the X-polarization TB bias with respect to the latitude of different descending orbits along 2014.

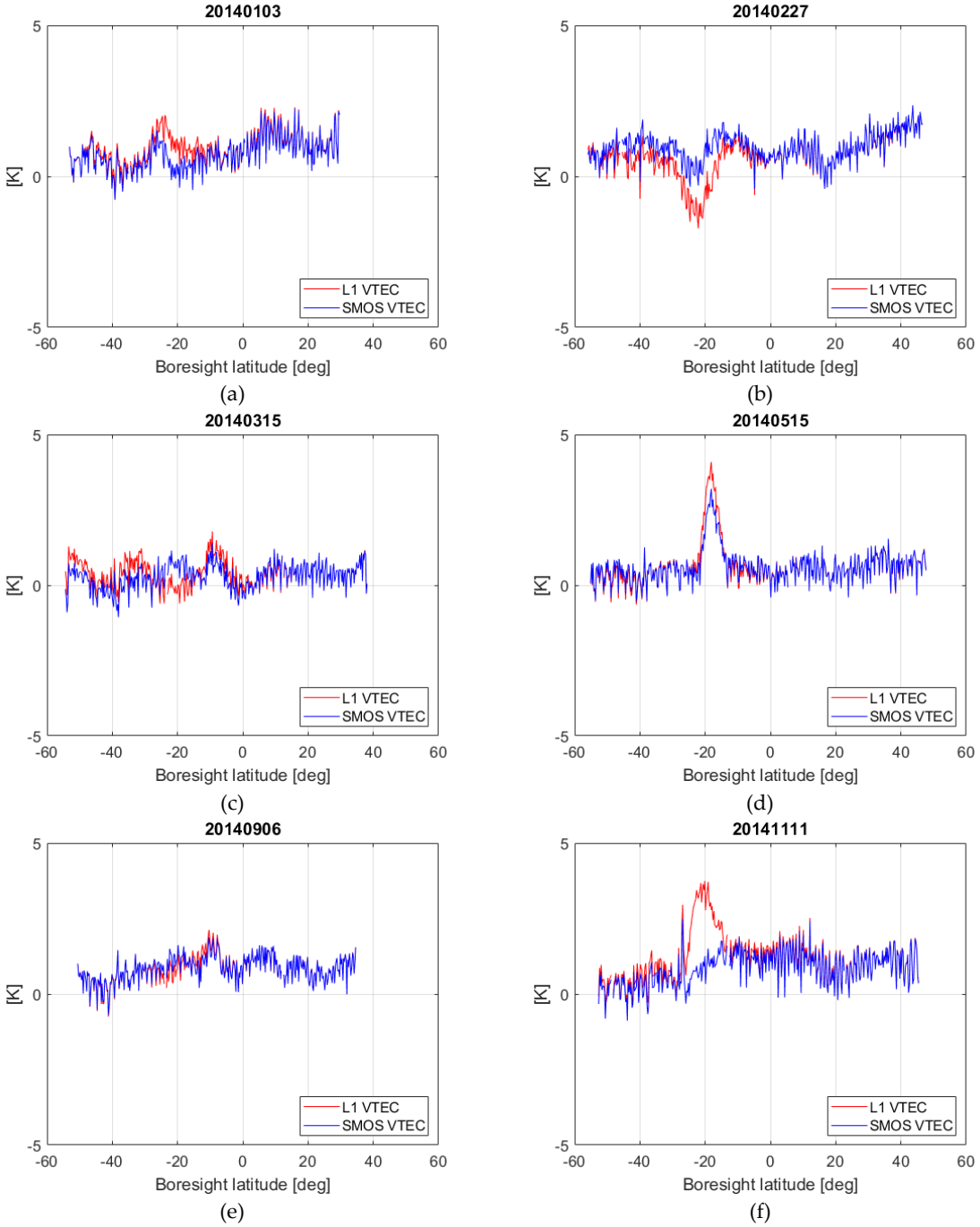

Figure 6.18. X-polarization TB bias vs latitude of different descending orbits along 2014: (a) January 3rd, (b) February 27th, (c) March 15th, (d) May 15th, (e) September 6th, and (f) November 11th.

As it can be seen in Fig. 6.18, independently on the date, the impact of using the SMOS-derived VTEC instead of the L1 VTEC is clearly much higher in the SH, where the sensitivity of TB to TEC is higher (see Fig. 3a in Vergely et al., 2014). In this figure, there are only some examples within the year, but it can be seen that mainly, when using the SMOS-derived VTEC, the obtained stability is better, particularly around latitudes of 20°S.

Figure 6.19 shows the X-polarization TB bias with respect to the latitude of different descending orbits along 2015. The bias is similar or better in several orbits when the SMOS-derived VTEC is used. In the cases where it is worse, there is not much difference.

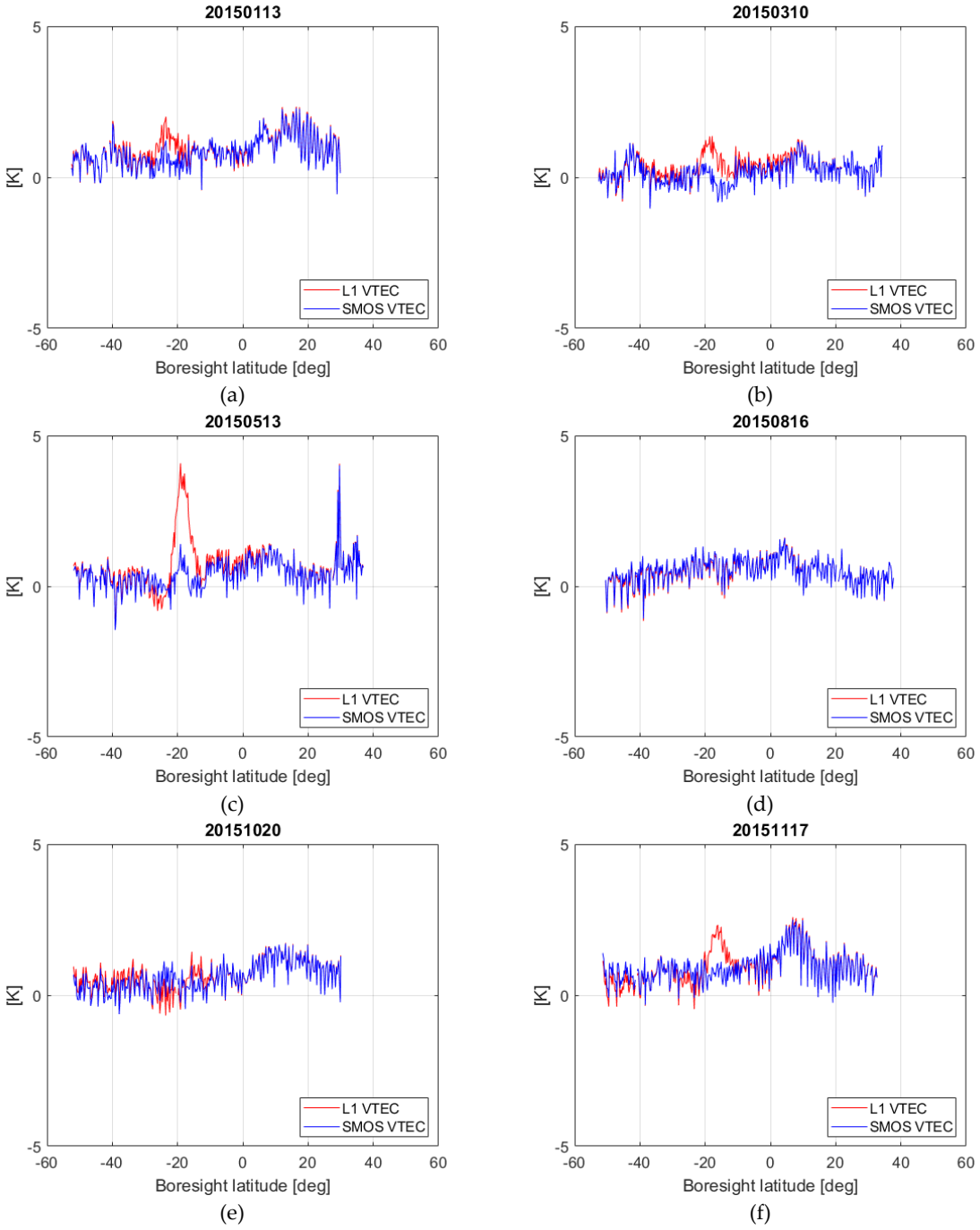

Figure 6.19. X-polarization TB bias vs latitude of different descending orbits along 2015: (a) January 13th, (b) March 10th, (c) May, 13th, (d) August 16th, (e) October 20th, and (f) November 17th.

Figure 6.20 shows the X-polarization TB bias with respect to the latitude of different descending orbits along 2016. The bias behaves similarly to year 2015: there is no much difference when using one or another VTEC source. In Fig. 6.2, it can be seen that since half of 2015, the VTEC has a lower magnitude. This is why the impact of using one or another VTEC is not as important as in 2014.

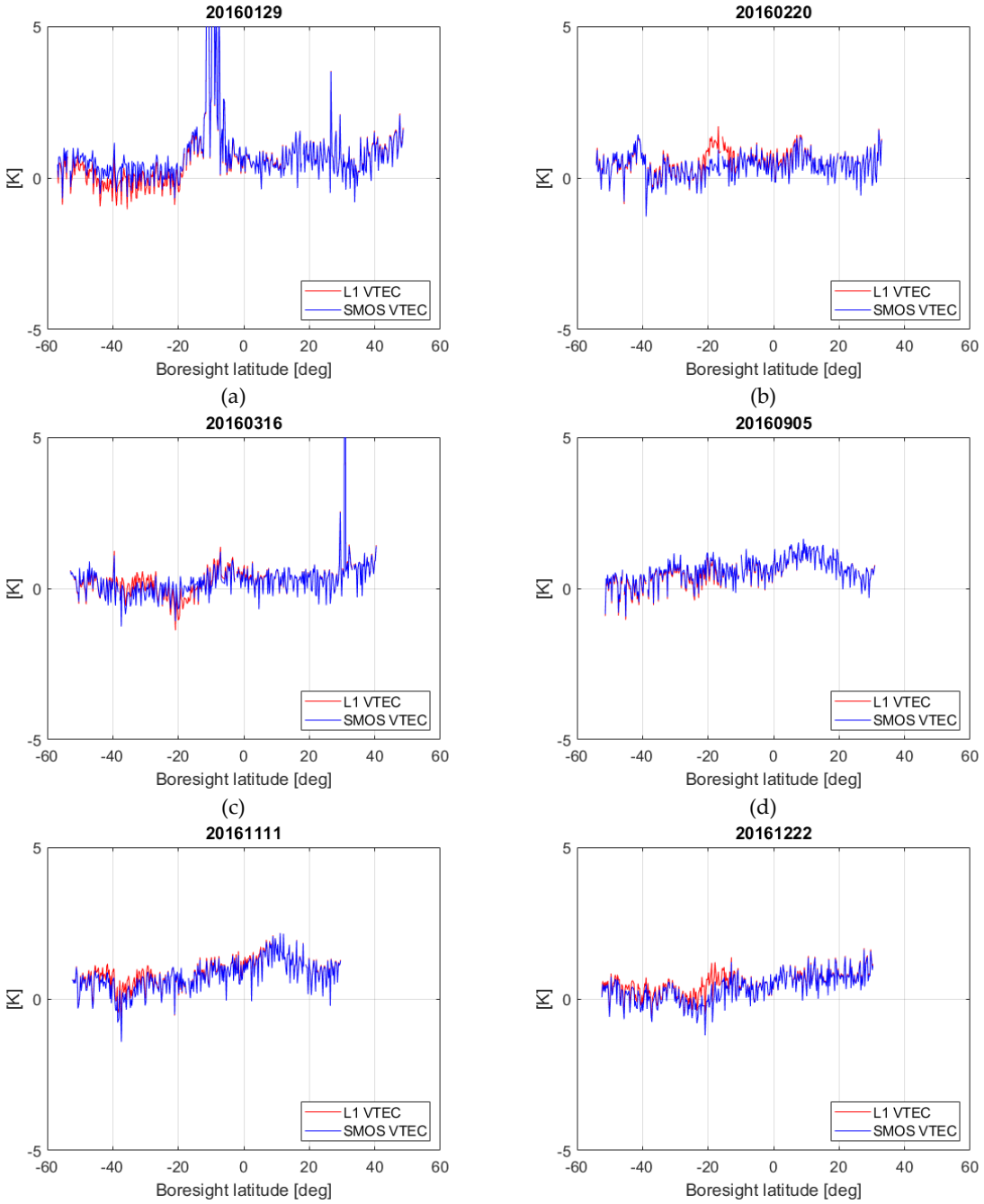

Figure 6.20. Figure 6.20 shows the X-polarization TB bias with respect to the latitude of different descending orbits along 2016.

Figure 6.21 shows the Y-polarization TB bias with respect to the latitude of the several descending orbits of 2014. The dates of the orbits correspond to the same as the ones shown for the X polarization (Fig. 6.18).

Figure 6.22 and Figure 6.23 show the Y-polarization TB bias with respect to the latitude of the descending orbits of 2015 and 2016 with the same date as Fig. 6.19 and 6.20, respectively.

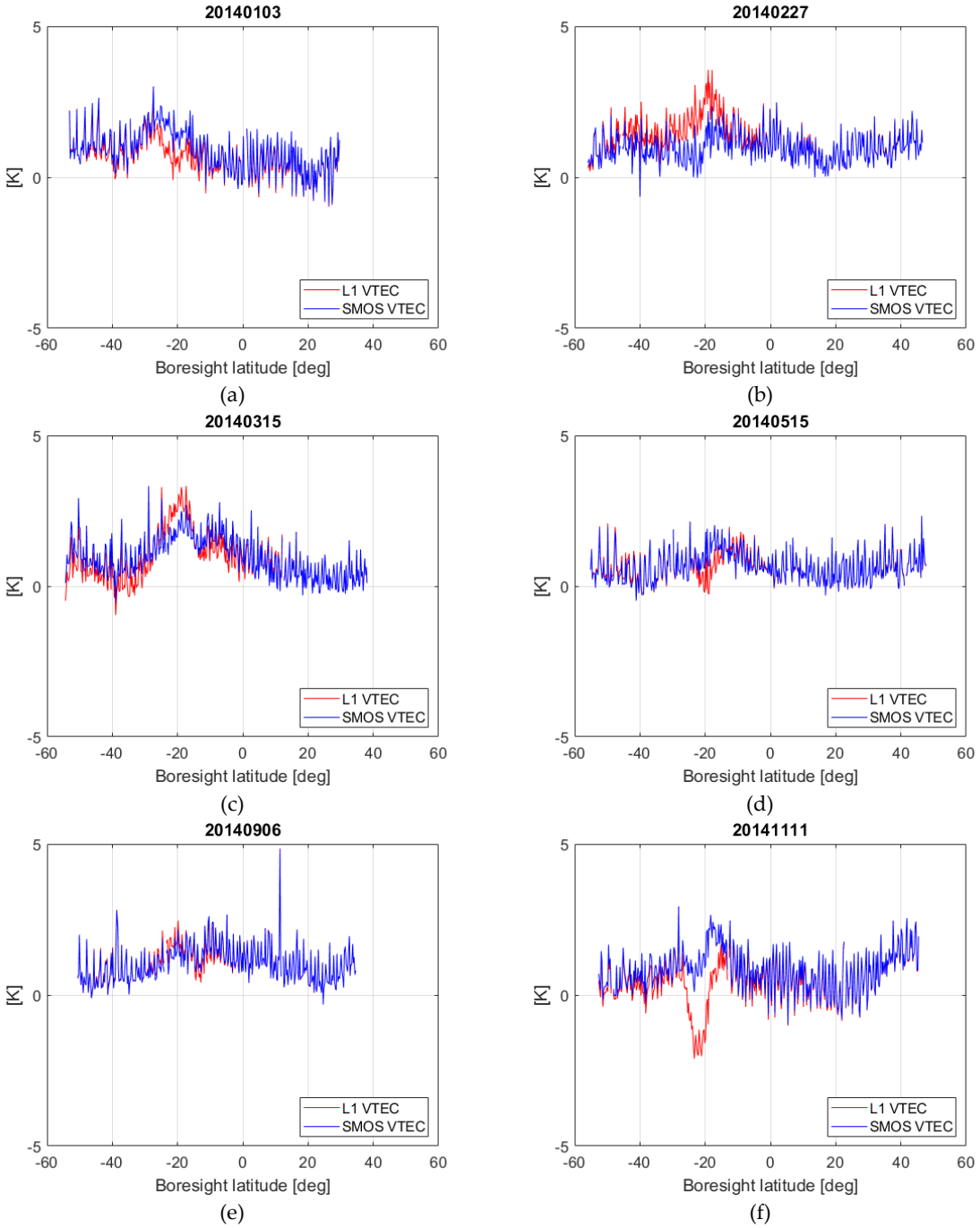

Figure 6.21. Y-polarization TB bias vs latitude of different descending orbits along 2014: (a) January 3rd, (b) February 27th, (c) March 15th, (d) May 15th, (e) September 6th, and (f) November 11th.

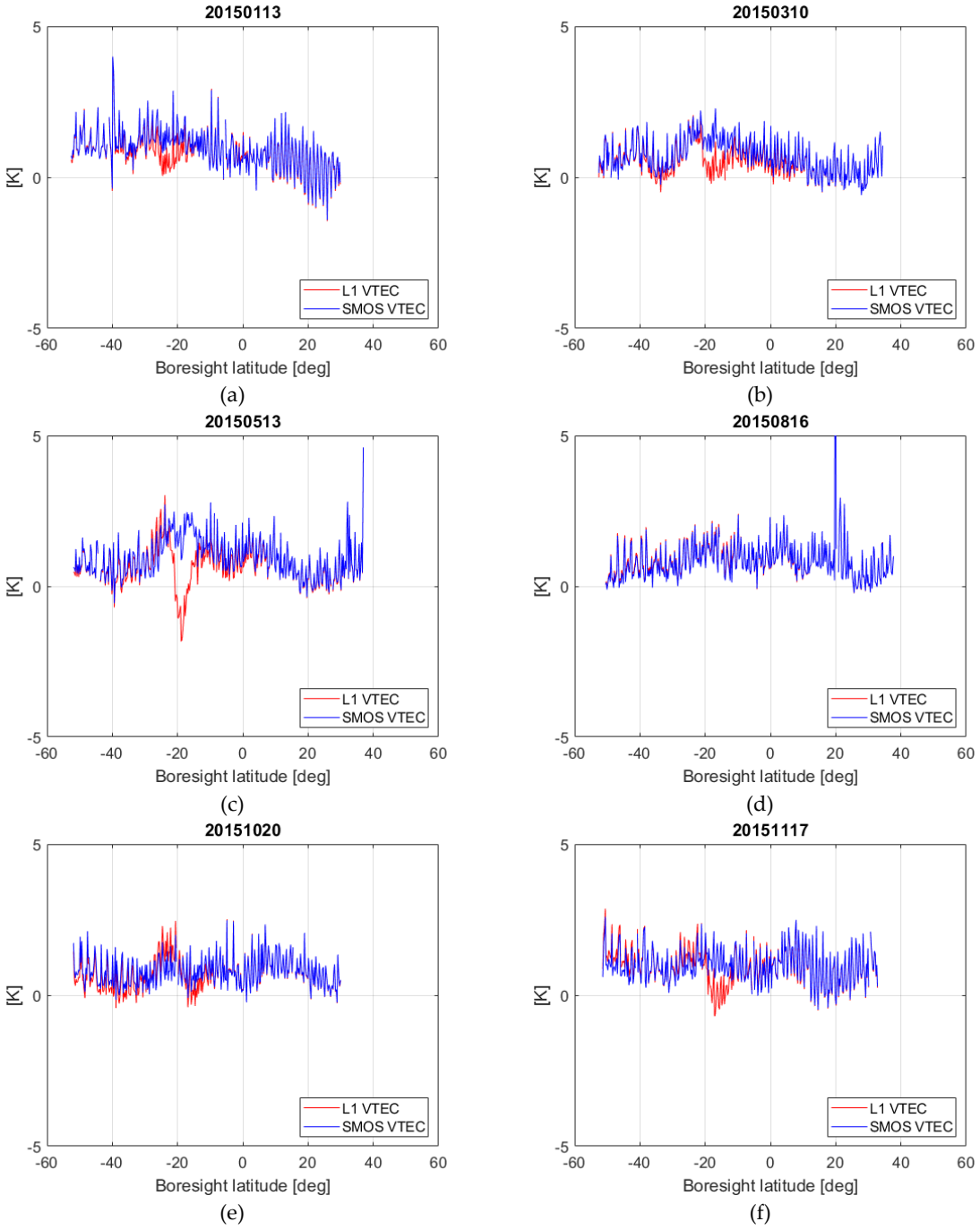

Figure 6.22. Y-polarization TB bias vs latitude of different descending orbits along 2015: (a) January 13th, (b) March 10th, (c) May, 13th, (d) August 16th, (e) October 20th, and (f) November 17th.

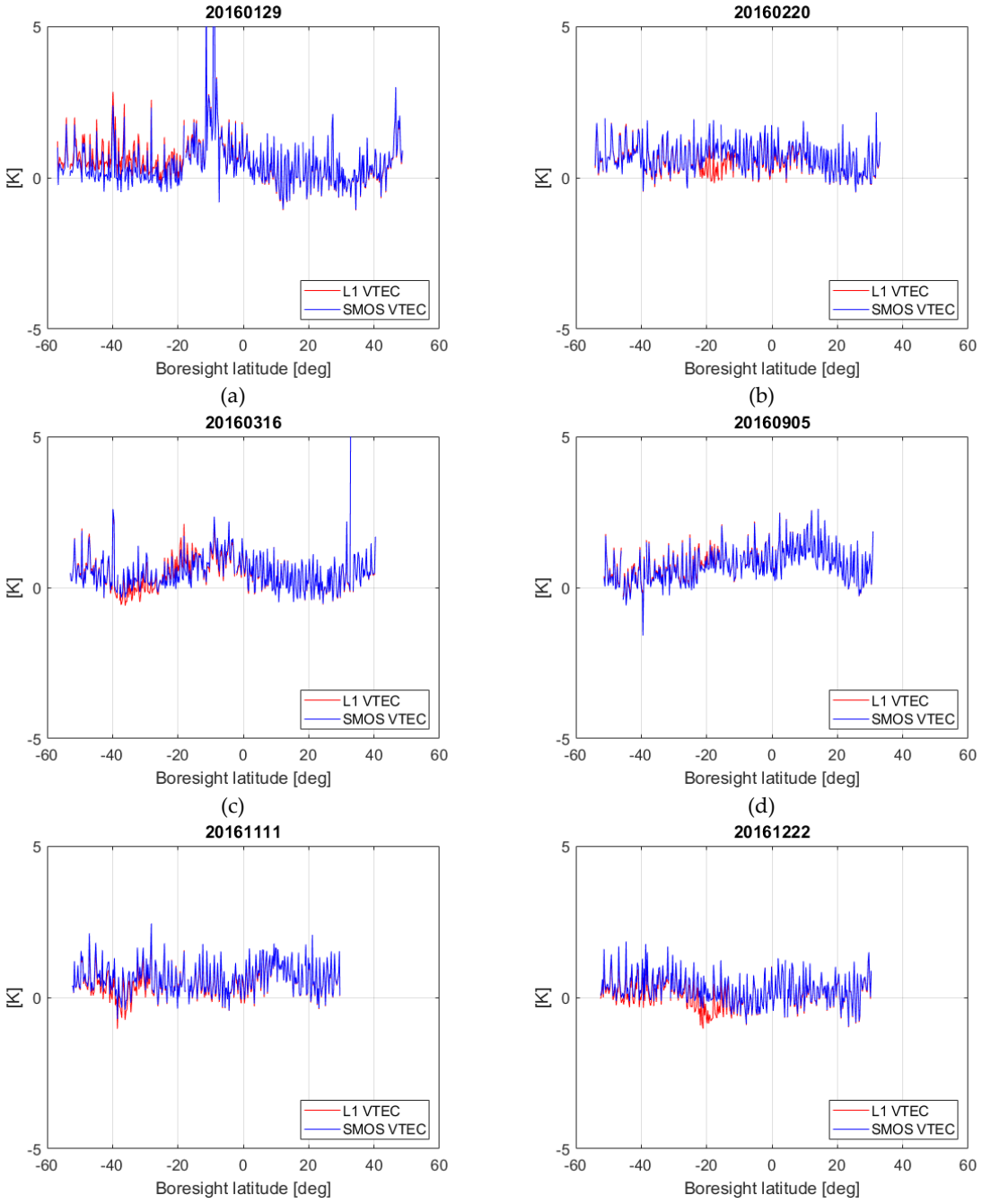

Figure 6.23. Y-polarization TB bias vs latitude of different descending orbits along 2016: (a) January 29th, (b) February 20th, (c) March 16th, (d) September 5th, (e) November 11th, and (f) December 22nd.

The Y-polarization TB bias when using the VTEC sources to rotate the model from the Earth surface to the antenna plane in every year follow the same pattern as the one of the X polarization.

Figure 6.24 shows the Hovmöller diagram of the difference between the SMOS TB and the modeled TB for the third Stokes parameter for descending orbits.

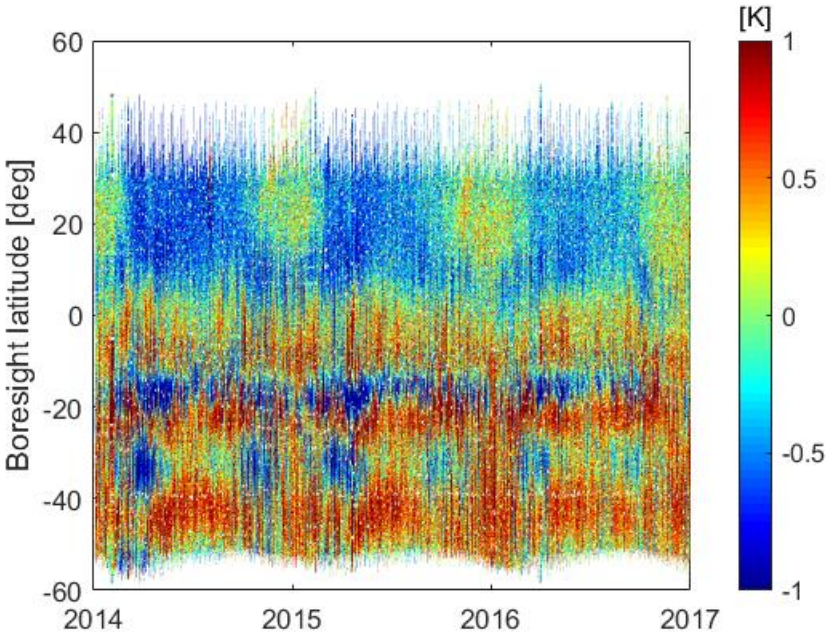

(a)

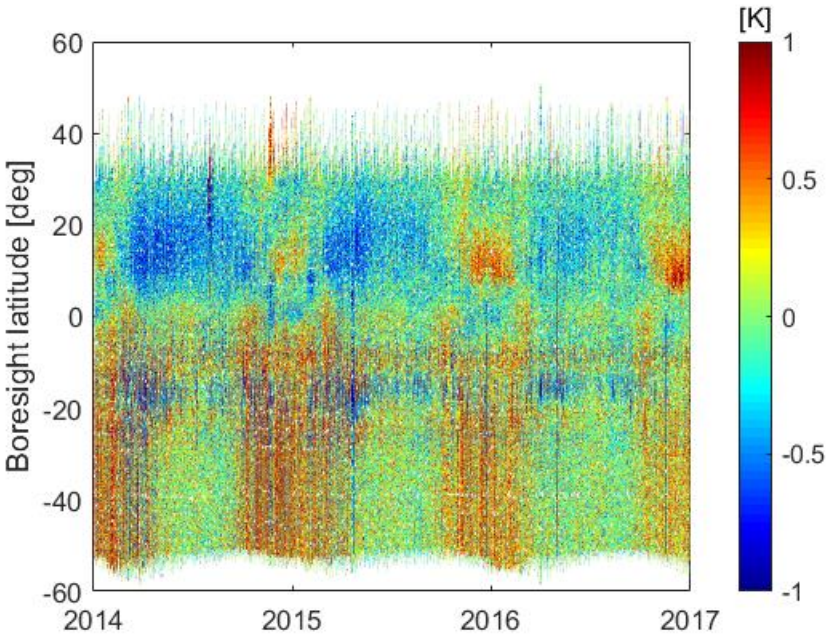

(b)

Figure 6.24. Hovmöller diagram of the difference between the SMOS TB and the modeled TB (averaged in the AF-FoV) for the third Stokes parameter at antenna reference for descending orbits: (a) the L1 VTEC product has been used to correct for the FR in the modeled TB, and (b) SMOS-derived VTEC maps have been used for the FR correction.

In Oliva, 2020, a strong latitudinal gradient in T3 when using the L1 VTEC for correcting the FR was reported. This is also reproduced in Fig. 6.24a. On the contrary, as evidenced in these Hovmöllers, the latitudinal gradient in T3 has been substantially reduced when using the SMOS-derived VTEC maps (Fig. 6.24b), improving the stability with respect to the usage of the L1 VTEC product (Fig. 6.24a).

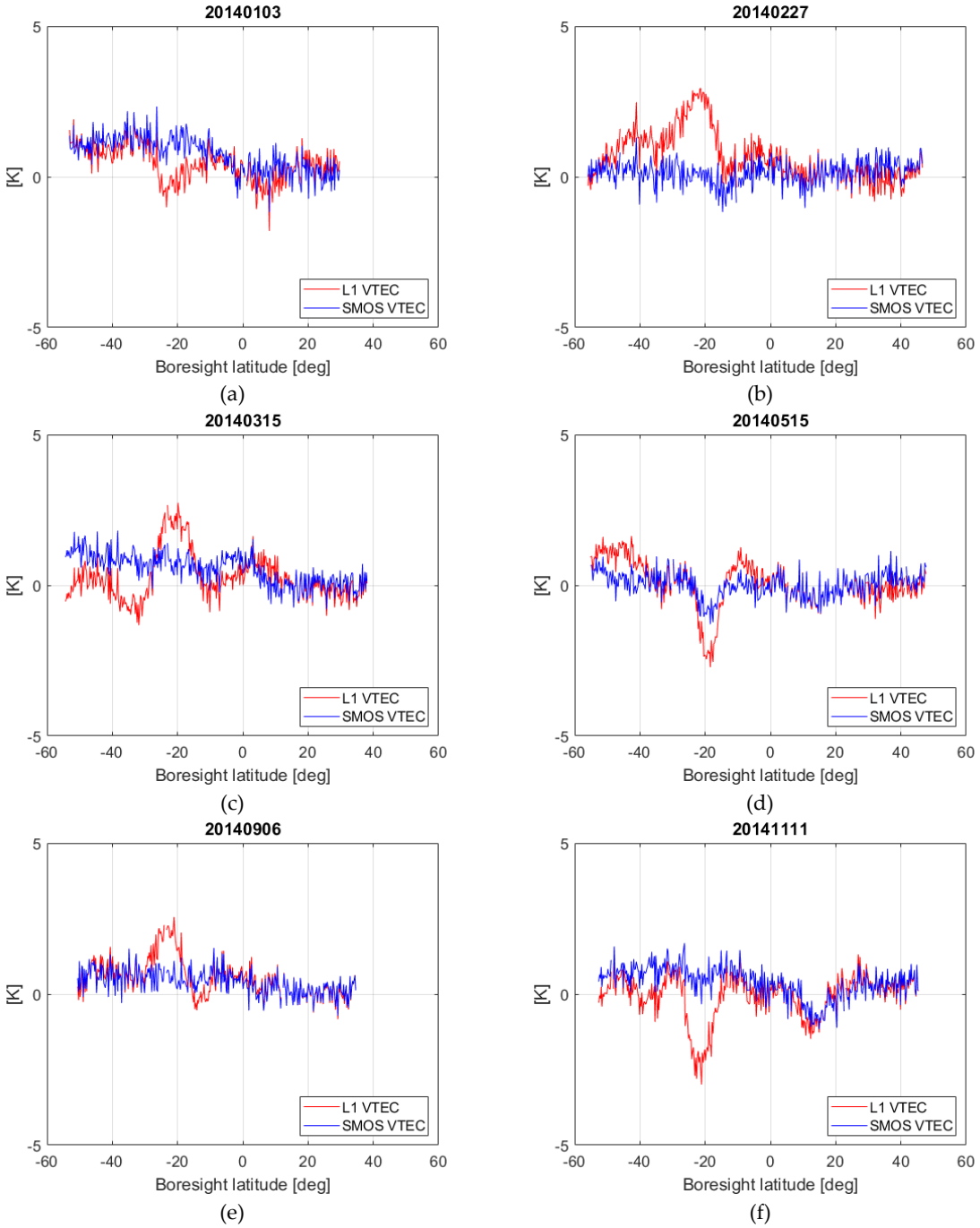

Figure 6.25. T3 bias vs latitude of different descending orbits along 2014: (a) January 3rd, (b) February 27th, (c) March 15th, (d) May 15th, (e) September 6th, and (f) November 11th.

Figure 6.25 shows the T3 bias with respect to the latitude of several descending orbits of 2014 (same dates as for X and Y polarizations).

Figure 6.26 shows the T3 bias with respect to the latitude of several descending orbits along 2015.

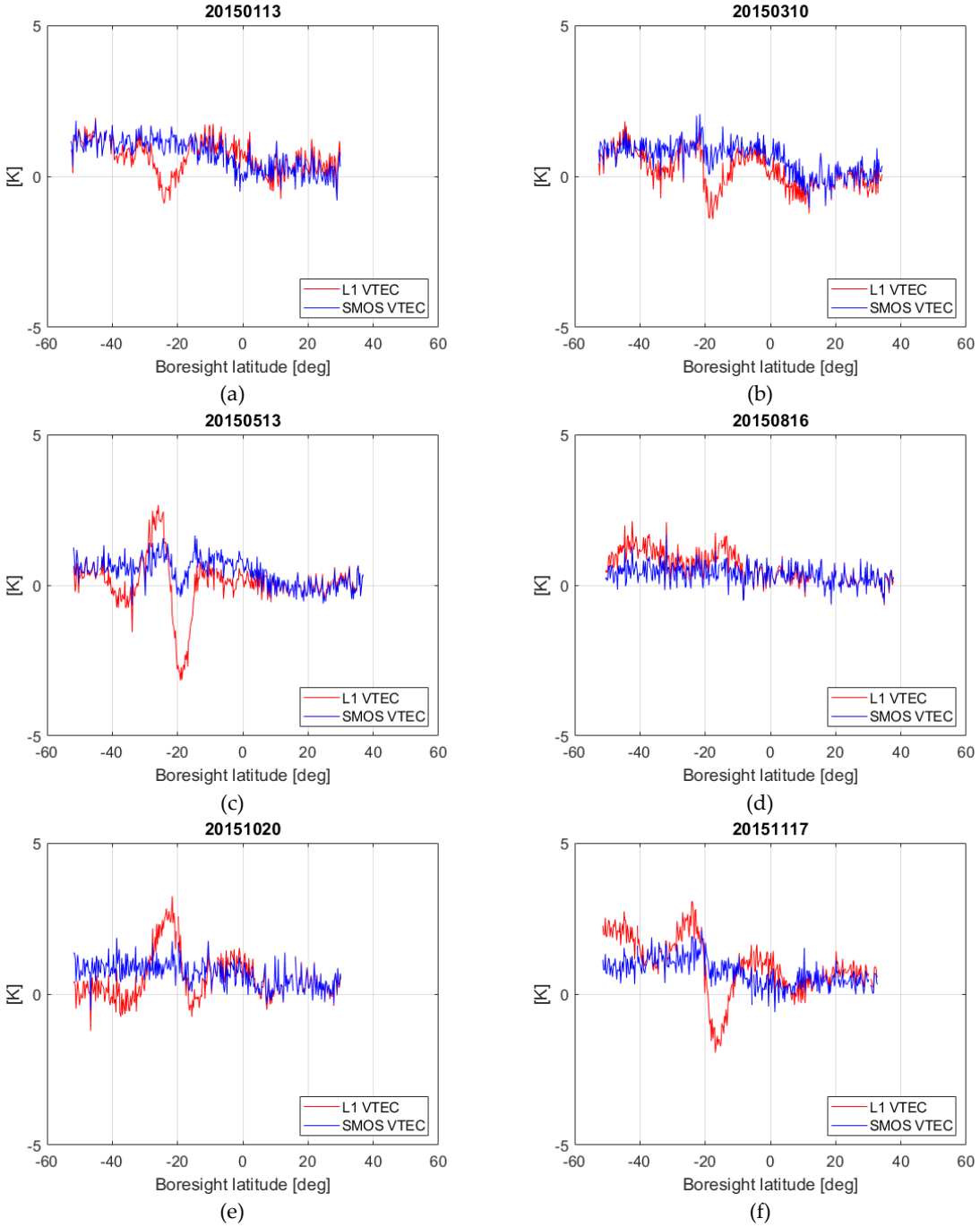

Figure 6.26. T3 bias vs latitude of different descending orbits along 2015: (a) January 13th, (b) March 10th, (c) May, 13th, (d) August 16th, (e) October 20th, and (f) November 17th.

Figure 6.27 shows the T3 bias with respect to the latitude of the different descending orbits along 2016.

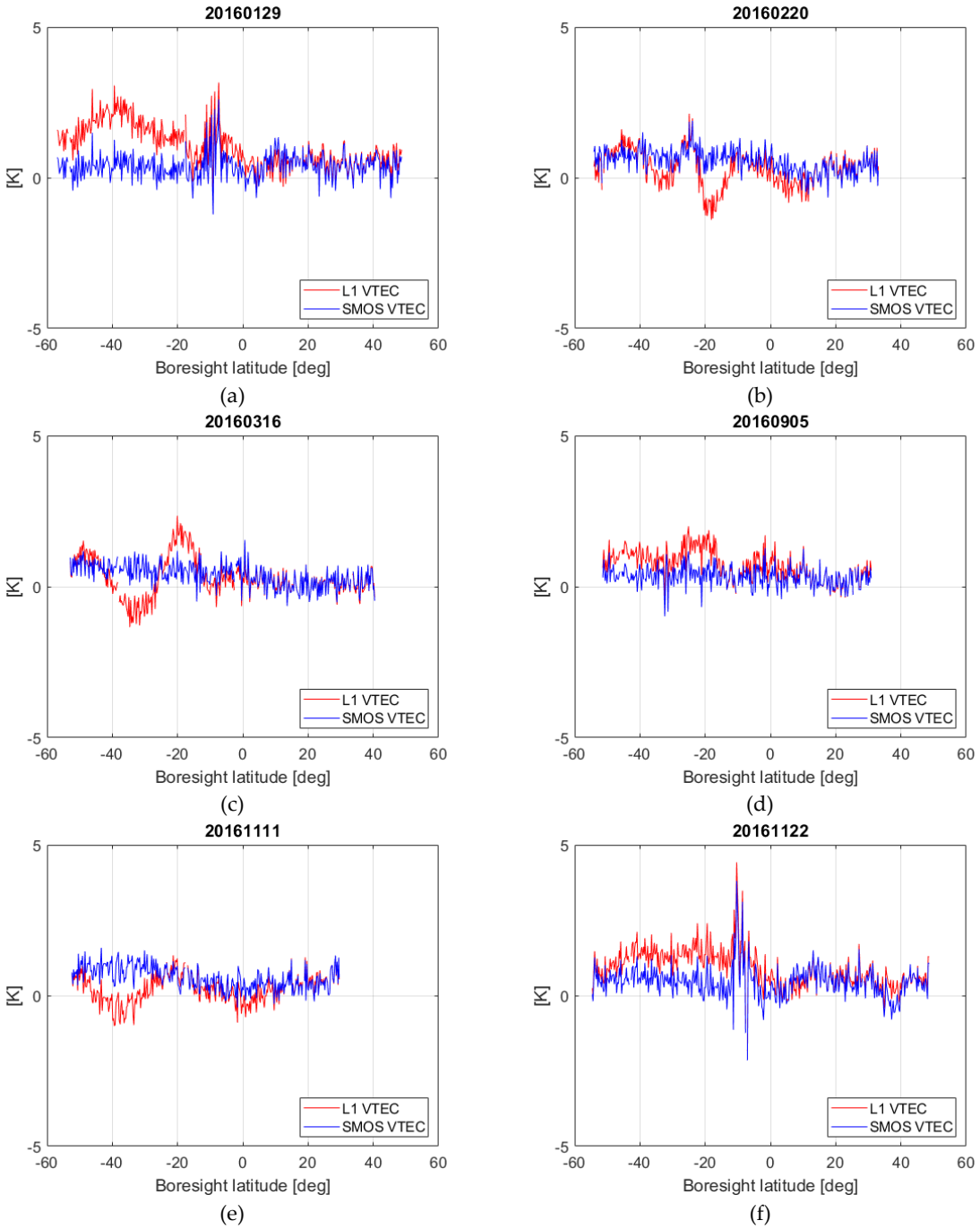

Figure 6.27. T3 bias vs latitude of different descending orbits along 2016 (a) January 29th, (b) February 20th, (c) March 16th, (d) September 5th, (e) November 11th, and (f) December 22nd.

As expected from Fig. 6.24b, when analyzing more deeply the T3 bias, the latitudinal gradient has been mitigated to a large extent when using the SMOS-derived VTEC,

improving also the stability with respect to the case of using the L1 VTEC. Unlike what happens along the latitudes in the X and Y polarizations that the main differences between using one or another VTEC source occur in the Southern Hemisphere, some slight differences in the bias of T3 are noticeable along the North Hemisphere as well.

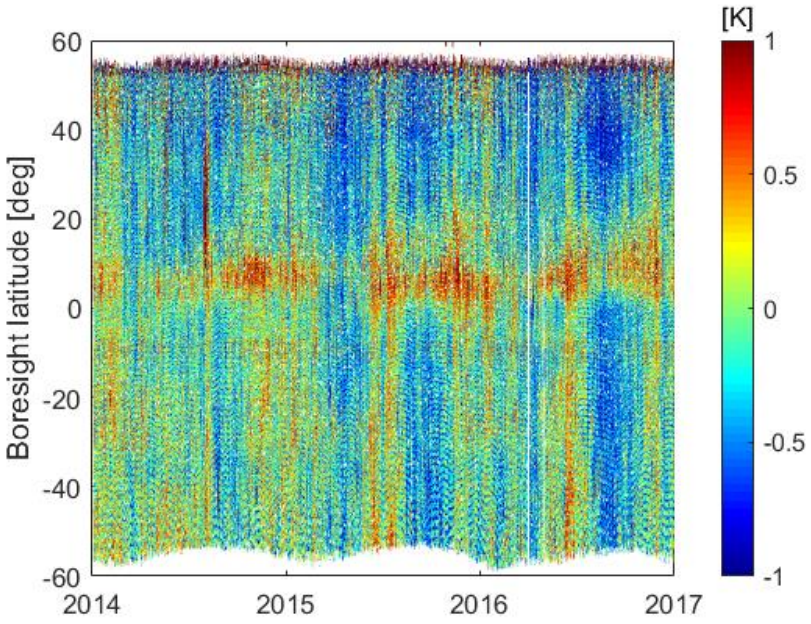

(a)

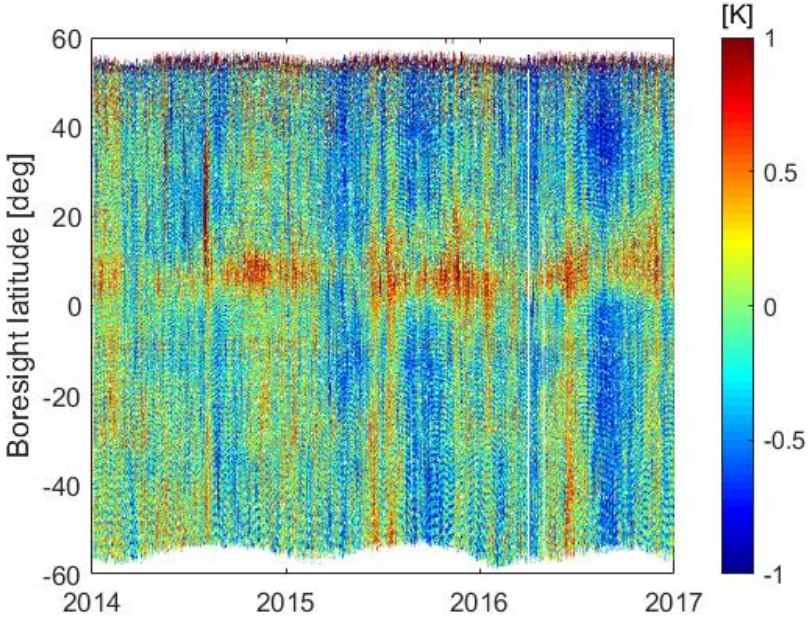

(b)

Figure 6.28. Hovmöller diagram of the difference between the SMOS TB and the modeled TB (averaged in the AF-FoV) for the X polarization at antenna reference for ascending orbits: (a) the L1 VTEC product has been used to correct for the FR in the modeled TB, and (b) SMOS-derived VTEC maps have been used for the FR correction.

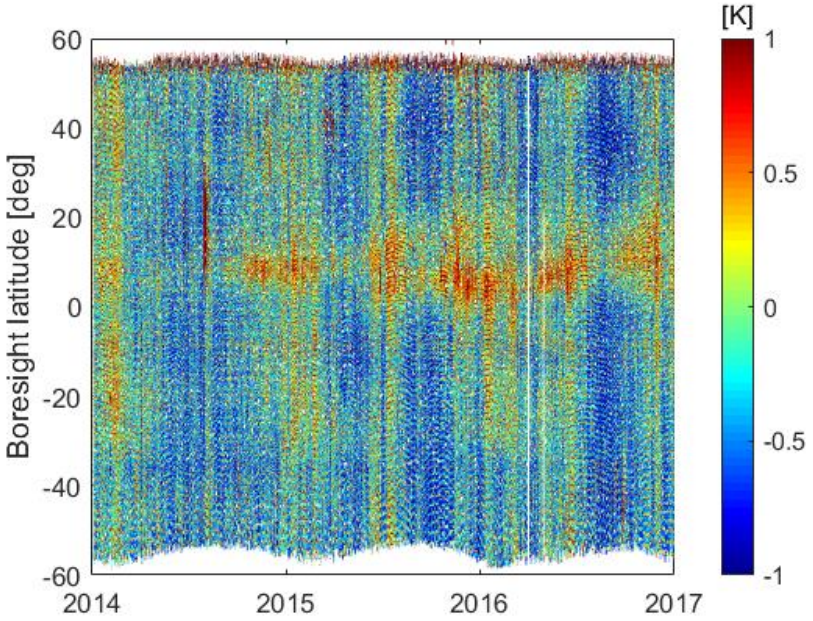

(a)

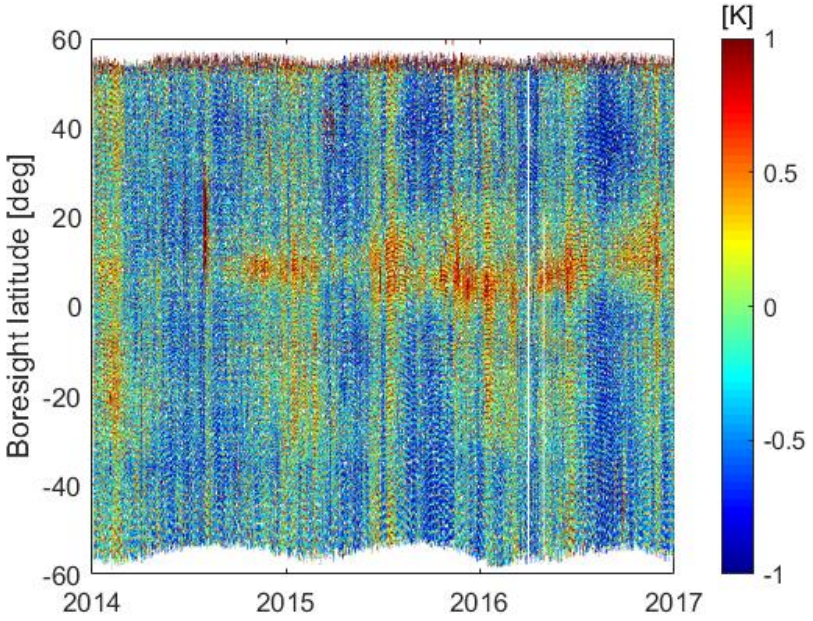

(b)

Figure 6.29. Hovmöller diagram of the difference between the SMOS TB and the modeled TB (averaged in the AF-FoV) for the Y polarization at antenna reference for ascending orbits: (a) the L1 VTEC product has been used to correct for the FR in the modeled TB, and (b) SMOS-derived VTEC maps have been used for the FR correction.

Figure 6.28 and Figure 6.29 show the ascending-orbit TB Hovmöller for the X and Y polarization, respectively. When using the SMOS-derived VTEC, the negative bias in the TB Hovmöller of both polarizations is less saturated, even though the improvement is not as noticeable as in the descending orbits.

Figure 6.30 shows the ascending-orbit TB Hovmöller for the third Stokes parameter.

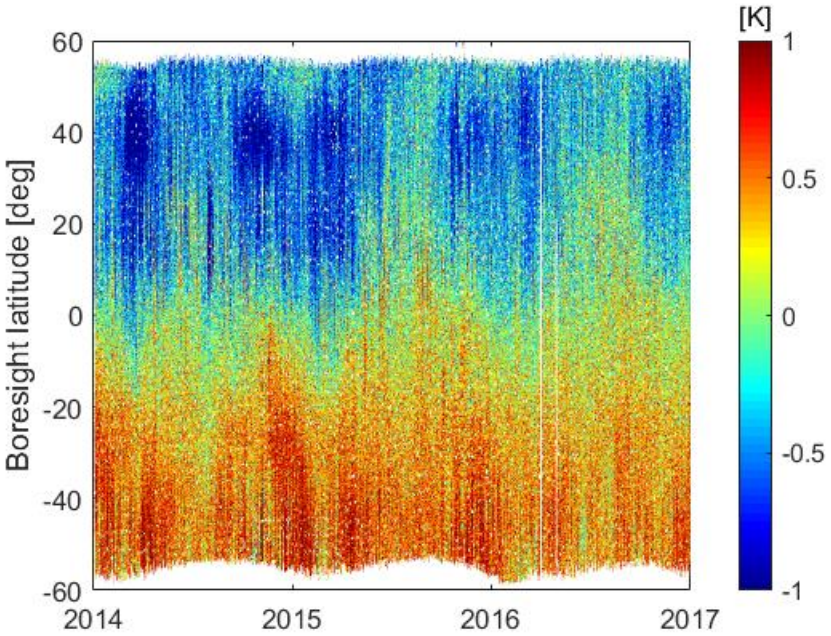

(a)

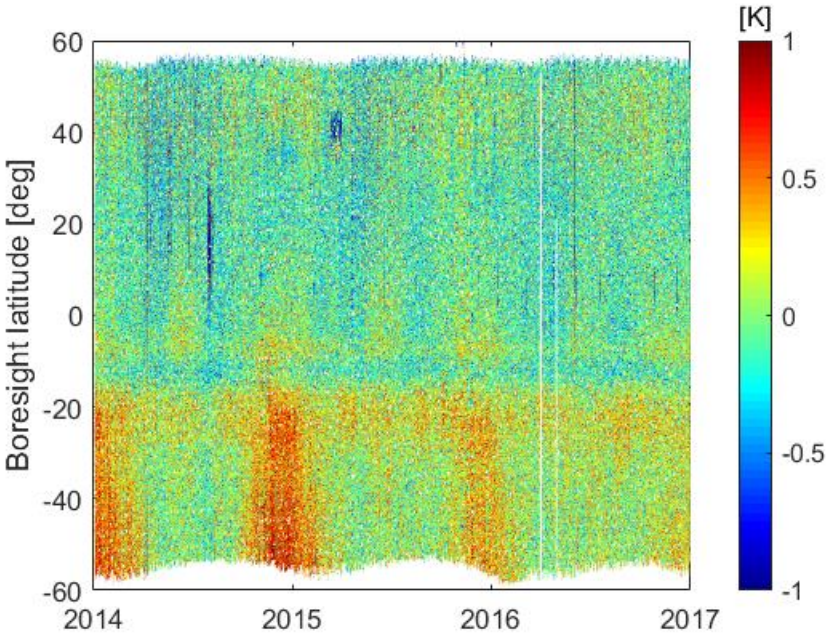

(b)

Figure 6.30. Hovmöller diagram of the difference between the SMOS TB and the modeled TB (averaged in the AF-FoV) for the third Stokes parameter at antenna reference for ascending orbits: (a) the L1 VTEC product has been used to correct for the FR in the modeled TB, and (b) SMOS-derived VTEC maps have been used for the FR correction.

In the T3 Hovmöller of the ascending orbits, the latitudinal gradient present in the Hovmöller generated using the L1 VTEC is substantially mitigated when using the SMOS-derived VTEC maps, as in the descending orbits. In fact, the Hovmöllers for the descending and ascending orbits are more similar when using the SMOS-derived VTEC maps.

The TB bias of several ascending orbits of year 2014, 2015 and 2016 for the X (left column) and Y polarizations (right column) are shown in Figure 6.31.

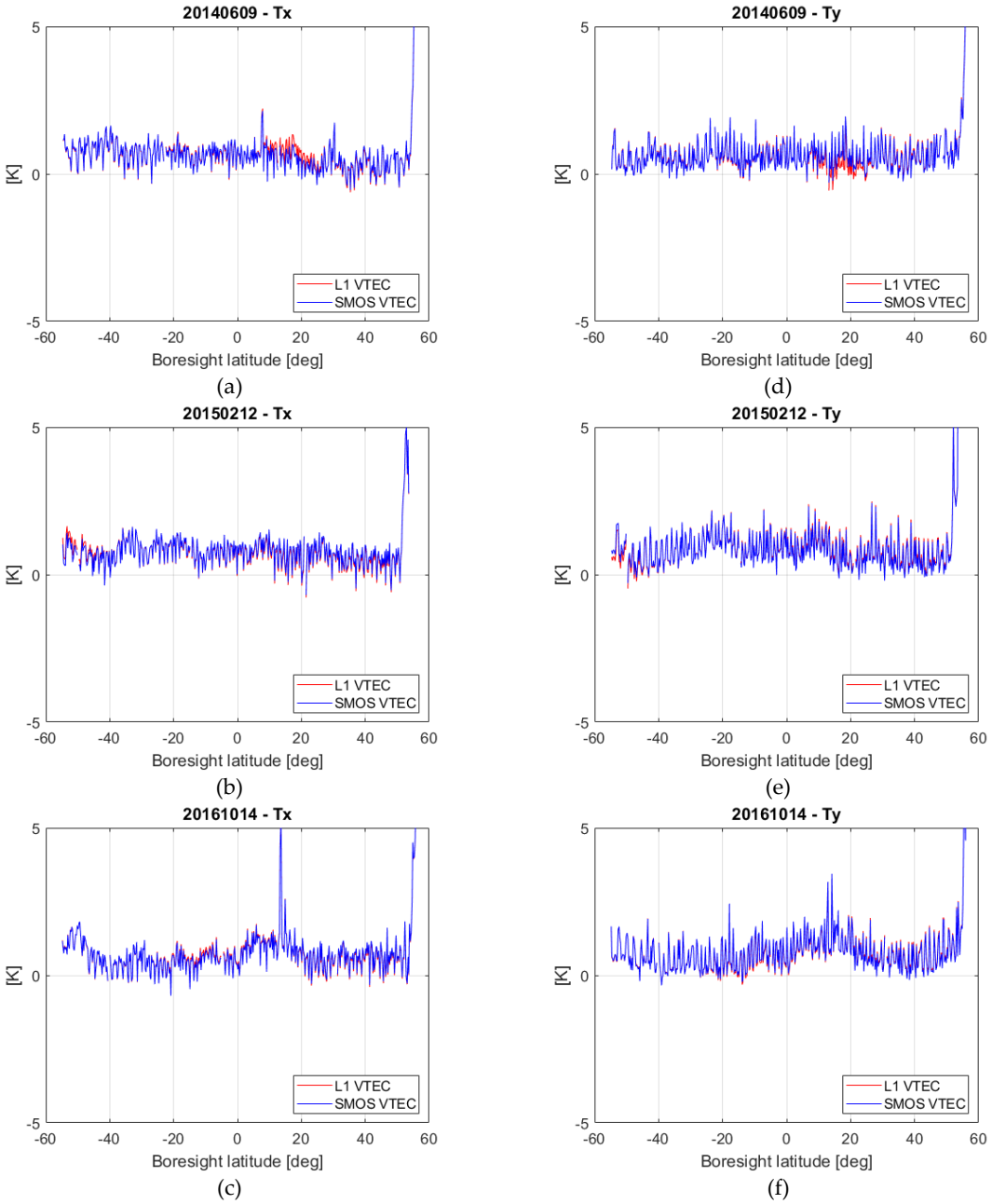

Figure 6.31. Bias of different ascending orbits: Left: X polarization of (a) June 9th, 2014; (b) February 12th, 2015; (c) October 14th, 2016, Right: Y polarization of (d) June 9th, 2014; (e) February 12th, 2015; (f) October 14th, 2016.

In Figure 6.32, there are plots for the T3 of an orbit of 2014, 2015, and 2016.

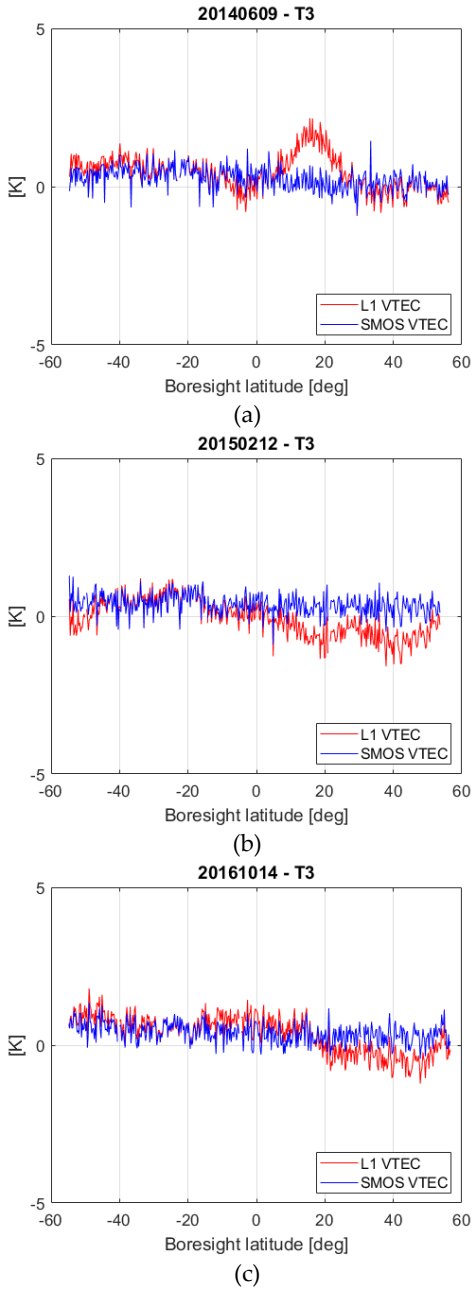

Figure 6.32. T3 Bias of different ascending orbits: (a) June 9th, 2014; (b) February 12th, 2015; and (c) October 14th, 2016.

In the case of ascending orbits, the impact of using one or the other VTEC product on TB in X and Y polarizations is quiet low despite of the hemisphere to be analyzed, which is expected due to the low VTEC values in ascending orbits as compared to descending ones. On the other hand, in the T3, even though not in a large scale as it happens in the descending

orbits, the bias is much more stable along the different orbits (latitudinal gradient has been clearly mitigated) over the years when using the SMOS-derived VTEC.

6.5. Ocean Anomaly Global Maps

The impact of using the SMOS-based VTEC maps instead of the L1 VTEC has been also analyzed on daily global maps of the ocean TB anomaly (defined as the difference between SMOS TB once corrected for spatial biases (Tenerelli & Reul, 2010) and the theoretically modeled TB). This is the magnitude that enters in the sea surface salinity (SSS) retrieval scheme in order to calculate it. Therefore, it is a first quality indicator for the SSS retrievals.

In the L2 Sea Surface Salinity team, the temporal median of the TB difference between the SMOS measured TB and the modeled TB as a function of the spatial direction is known as the Ocean Target Transformation (OTT) (Tenerelli & Reul, 2010). The OTT is calculated on a daily basis and it is applied worldwide over the ocean to correct for the spatial biases. As mentioned in section 6.3. , it is computed in a very stable zone in the South Central Pacific using ten orbits per each direction (Figure 6.33): for the descending ones, those orbits passing through the region defined by the longitude-latitude coordinates [112°W±16 at 5°S, 123°W±16 at 45°S] (Fig. 6.33a), and for the ascending ones, those orbits passing through the region defined by the longitude-latitude coordinates [121°W±16 at 5°S, 111°W±16 at 45°S] (Fig. 6.33b), zones where the presence of land/island is minimized. Plots correspond to the Figure 1 of Yin et al., 2013.

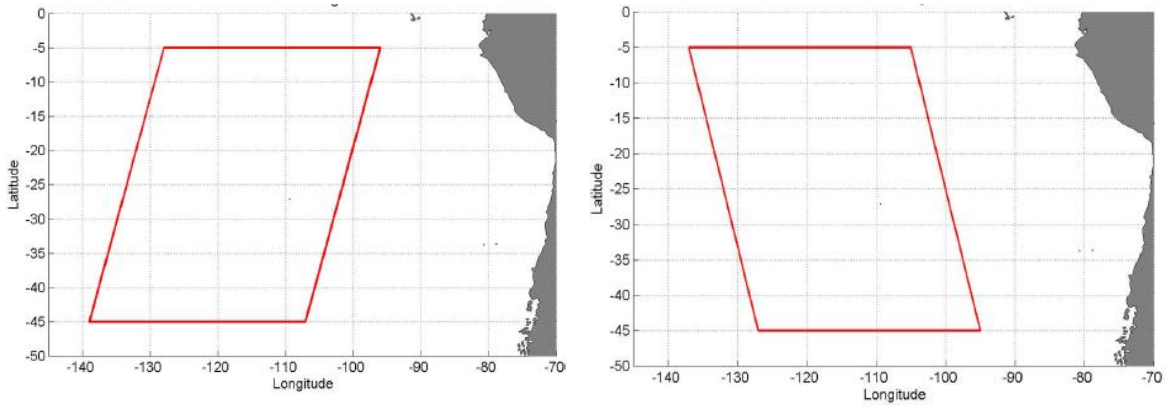

(a) (b)

Figure 6.33. Zone of the South Pacific where the OTT is computed: (a) for descending orbits and (b) for ascending orbits (figure 1 of Yin et al., 2013).

The SMOS TB per polarization of all orbits in the diamond region shown in Figure 6.33 are averaged as well as the modeled TB at antenna reference frame, hence previously rotated with the VTEC source. Then, the temporal median of the TB difference of them is calculated over the director cosine (ξ, η) coordinates. This OTT is then subtracted to each ocean snapshot to correct for the spatial biases on TB and then, the ocean TB anomaly is computed.

The assessment had been only done in descending orbits, knowing that they are the ones more affected by the FRA. Figure 6.34 shows the ocean TB anomaly in the X polarization of a descending orbit over the Pacific Ocean on May 30th, 2014. In the top left, the L1 VTEC is used for both the OTT computation and the rotation of the model; in the top right, the SMOS-derived VTEC. In the bottom, the difference between the second one and the first one is shown.

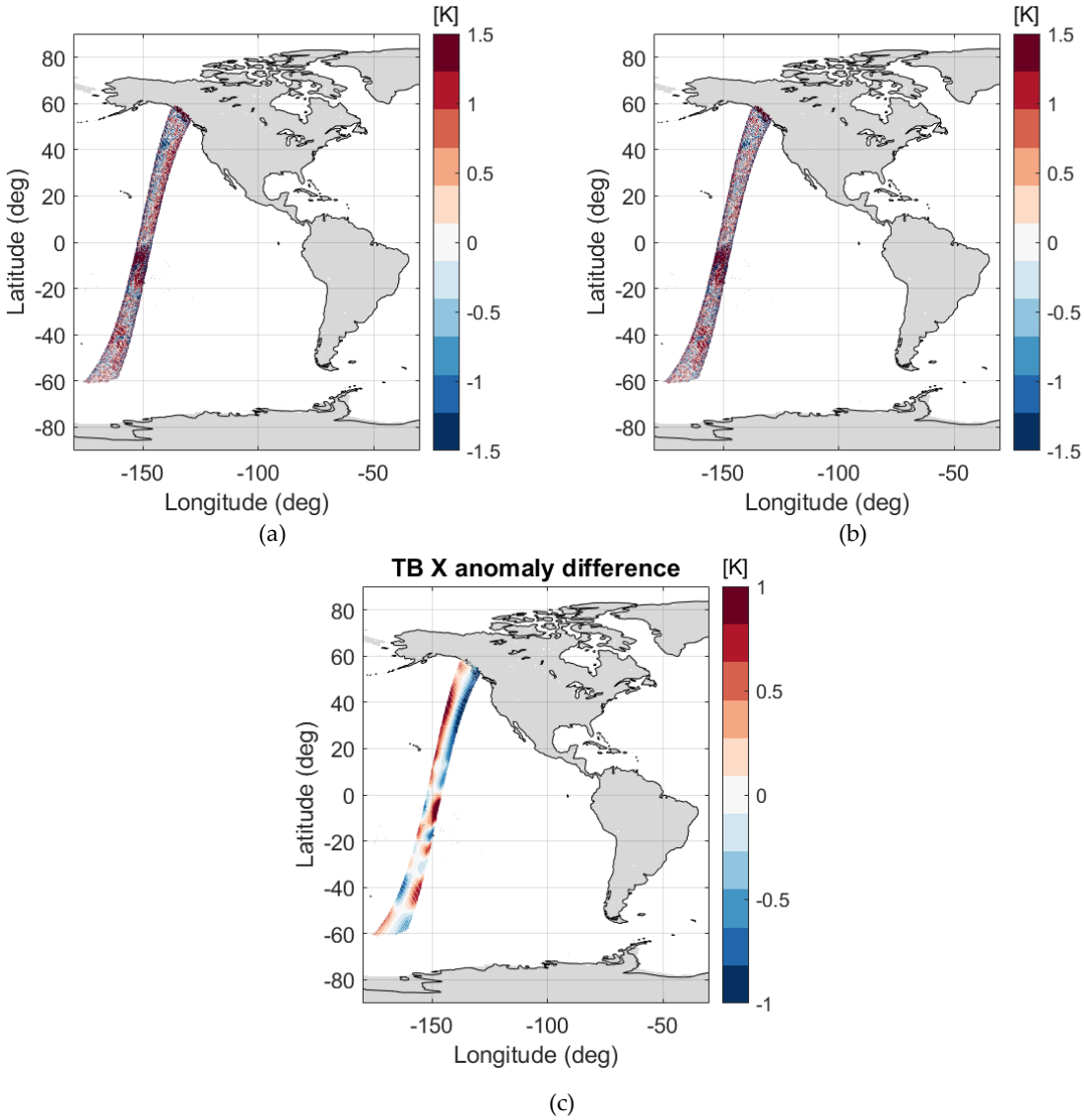

Figure 6.34. X-polarization ocean TB anomaly of a descending orbit on May 30th, 2014 when using: (a) the L1 VTEC, (b) the SMOS-derived VTEC, and (c) difference between (a) and (b).

It catches the attention the results in the range of latitudes between 20°S and 0° in both shown in the top. By taking a look to the TB at that latitude range, it is realized that there is an RFI source that is affecting SMOS measurements. On the other hand, systematic errors found when the L1 VTEC is used (Fig. 6.34a) are largely mitigated when using the SMOS-

derived VTEC maps (Fig 6.34b). This is particularly evidenced in Fig 6.34c. the dipole error pattern has been corrected.

Figure 6.35 shows the TB anomaly of the Y polarization of the same date when using the L1 VTEC (top left plot), the SMOS-derived VTEC (top right plot), and the difference between the second one and the first one (bottom plot).

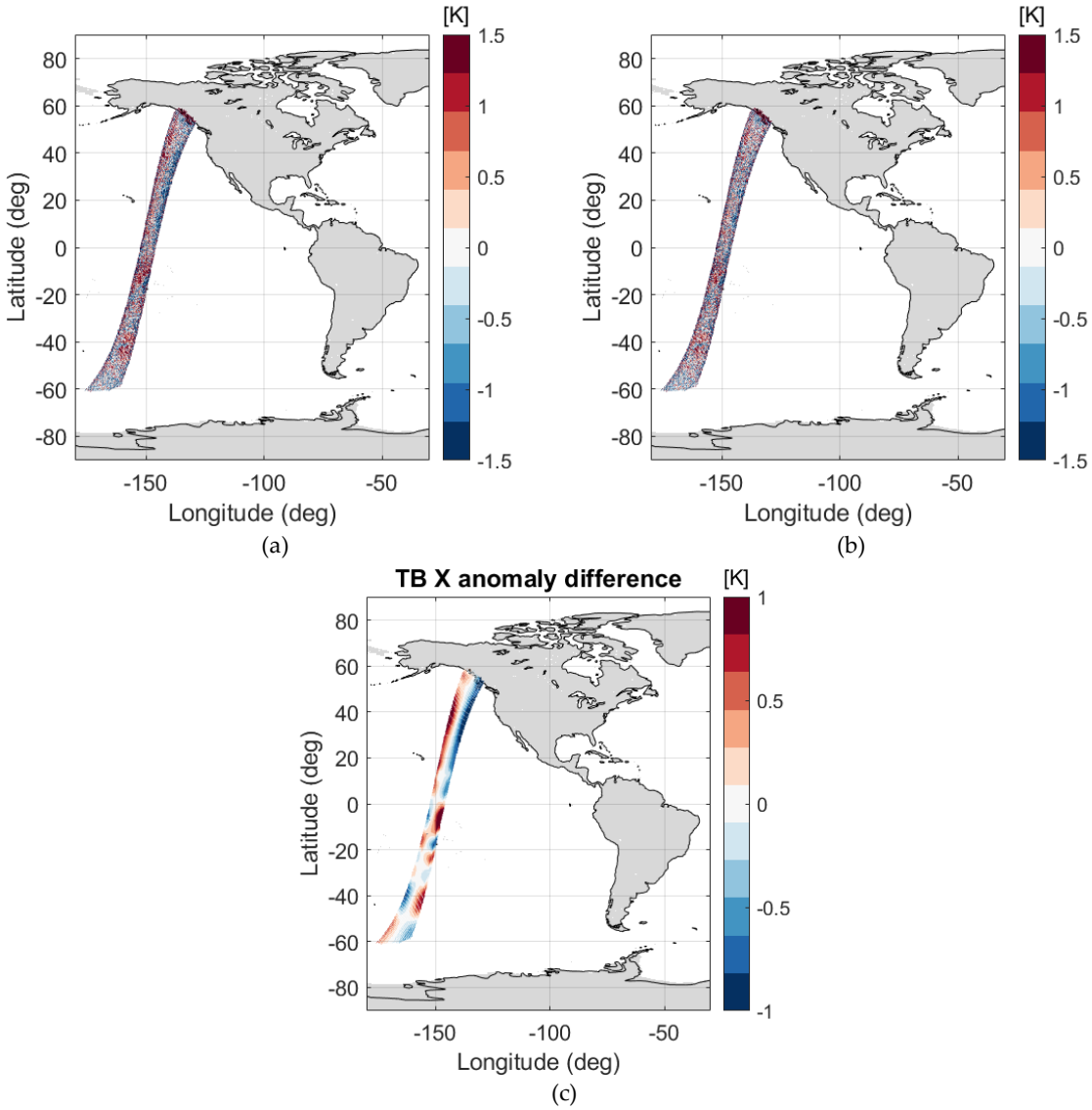

Figure 6.35. Y-polarization ocean TB anomaly of a descending orbit on May 30th, 2014 when using: (a) the L1 VTEC, (b) the SMOS-derived VTEC, and (c) difference between when using the SMOS-derived VTEC and the L1 VTEC.

The results in the Y polarization are similar to the ones in the X polarization. The systematic errors found when the L1 VTEC (Fig. 6.35a) are mitigated when using the SMOS-derived VTEC (Fig. 6.35b).

To corroborate the improvement when using the SMOS-derived VTEC instead of the L1 VTEC, the TB anomaly of a different date over the Pacific was computed. It corresponds to a descending orbit on June 3rd, 2014 and it is shown in Figure 6.36 and Figure 6.37 for the X and Y polarization, respectively.

Once again, it can be seen that, when using the SMOS-derived VTEC instead of the L1 VTEC in both the calculus of the OTT and the modeled TB rotation, the systematic errors in the longitudinal axis are mitigated. It catches the attention the saturation at latitude 20°N in the top plots of the figures. It corresponds to a localized RFI source that is affecting.

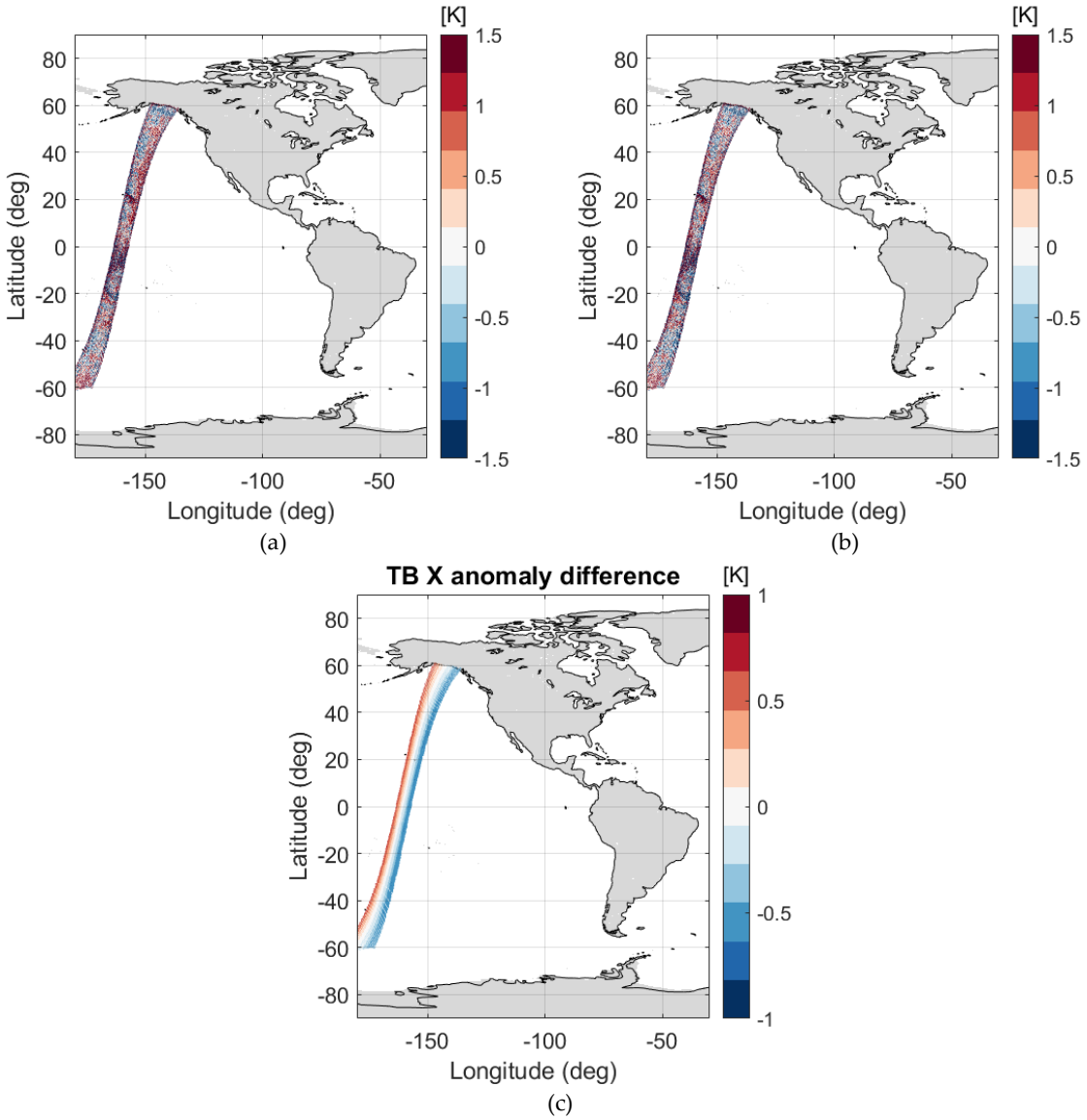

Figure 6.36. X-polarization ocean TB anomaly of a descending orbit on June 3th, 2014 when using: (a) the L1 VTEC, (b) the SMOS-derived VTEC, and (c) difference between (a) and (b).

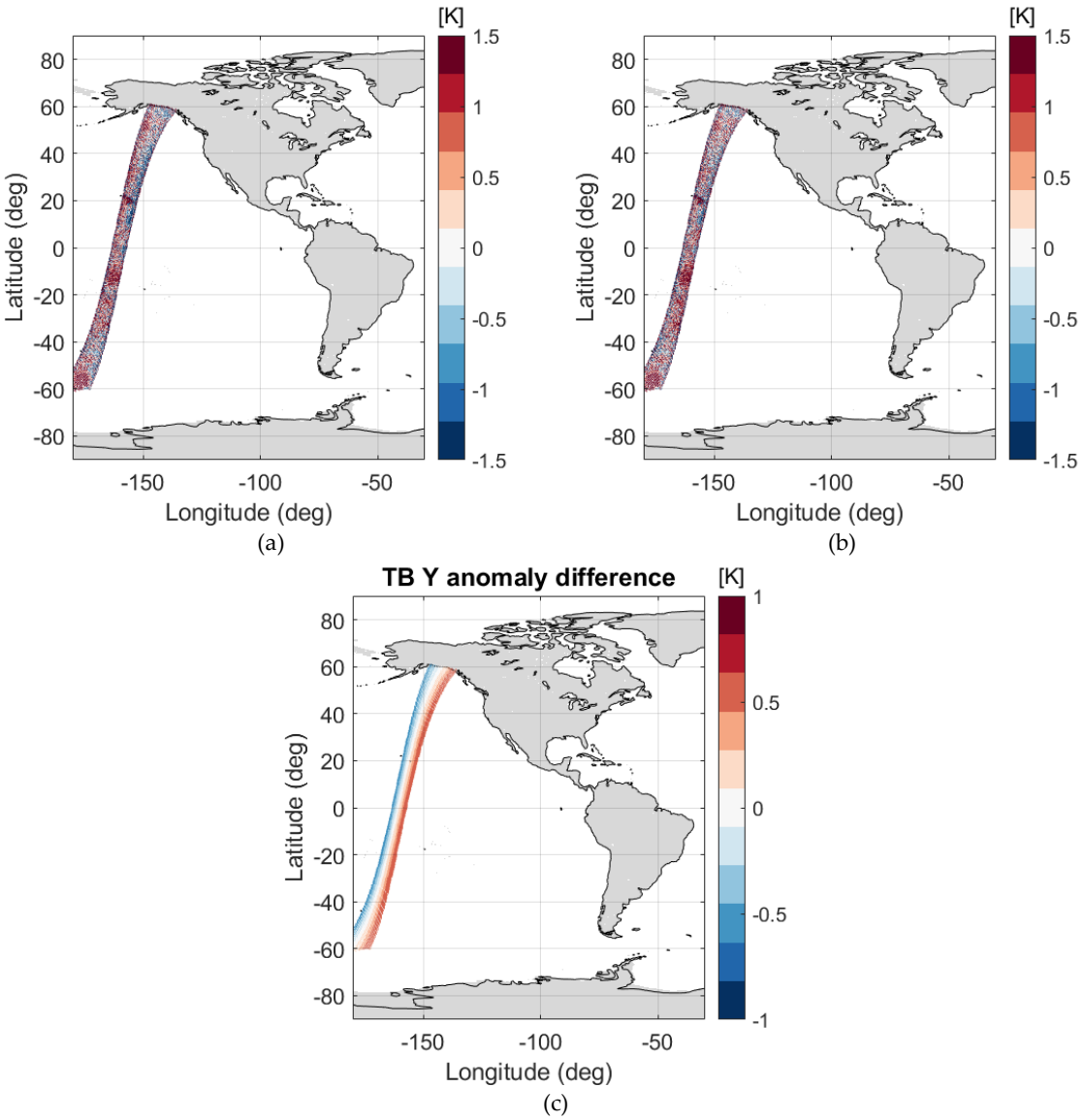

Figure 6.37. Y-polarization ocean TB anomaly of a descending orbit on June 3th, 2014 when using: (a) the L1 VTEC, (b) the SMOS-derived VTEC, and (c) difference between (a) and (b).

In a further step, the TB anomaly map of the descending orbits of a day has been calculated. Figure 6.38 shows the map in the X polarization –in the left, when using the L1 VTEC; in the right, when using the SMOS-derived VTEC– in two regions: over the Pacific Ocean in the top, and over the Indian Ocean in the bottom. A different date for the analysis was chosen to corroborate the results. It corresponds to June 5th, 2014.

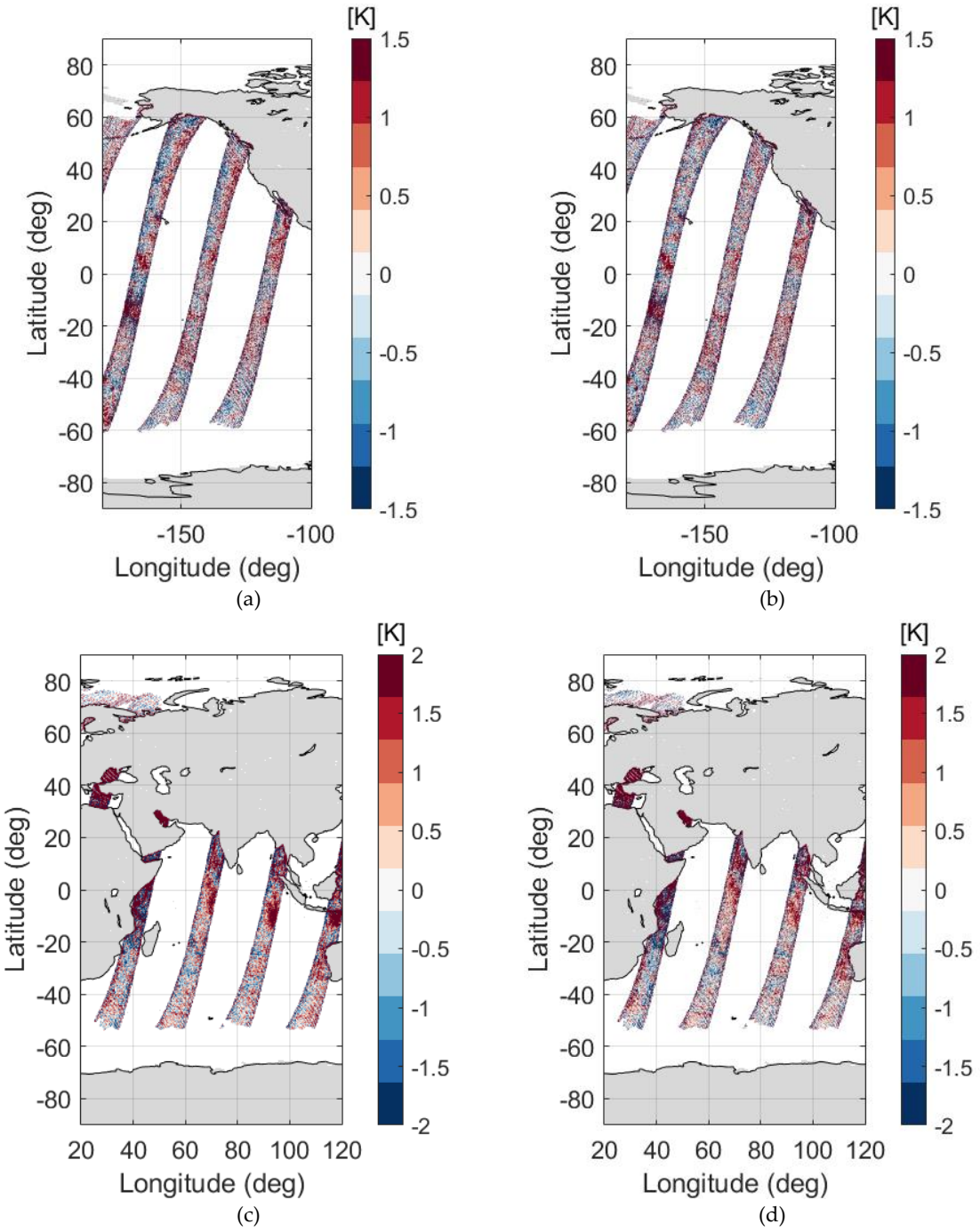

Figure 6.38. X-polarization ocean TB anomaly of all descending orbits on June 5th, 2014 over the Pacific Ocean, when using (a) the L1 VTEC and (b) the SMOS-derived VTEC; over the Indian Ocean, when using (c) the L1 VTEC and (d) the SMOS-derived VTEC.

Over the Pacific, it can be noticed that when using the SMOS-derived VTEC instead of the L1 VTEC, the ocean TB anomaly map has a more symmetric variability in the longitudinal axis as it should be in terms of geophysical variability. Over the Indian Ocean,

when using the SMOS-derived VTEC instead of the L1 VTEC, it can be seen that in latitudes between 10°S and 0°, it is less saturated.

To perceive when using one or another VTEC source in the rotation, Figure 6.39 shows the difference of the TB anomaly when using the SMOS-based VTEC and the L1 VTEC of all descending orbits on June 5th, 2014 over both the Pacific Ocean (left plot) and the Indian Ocean (right plot).

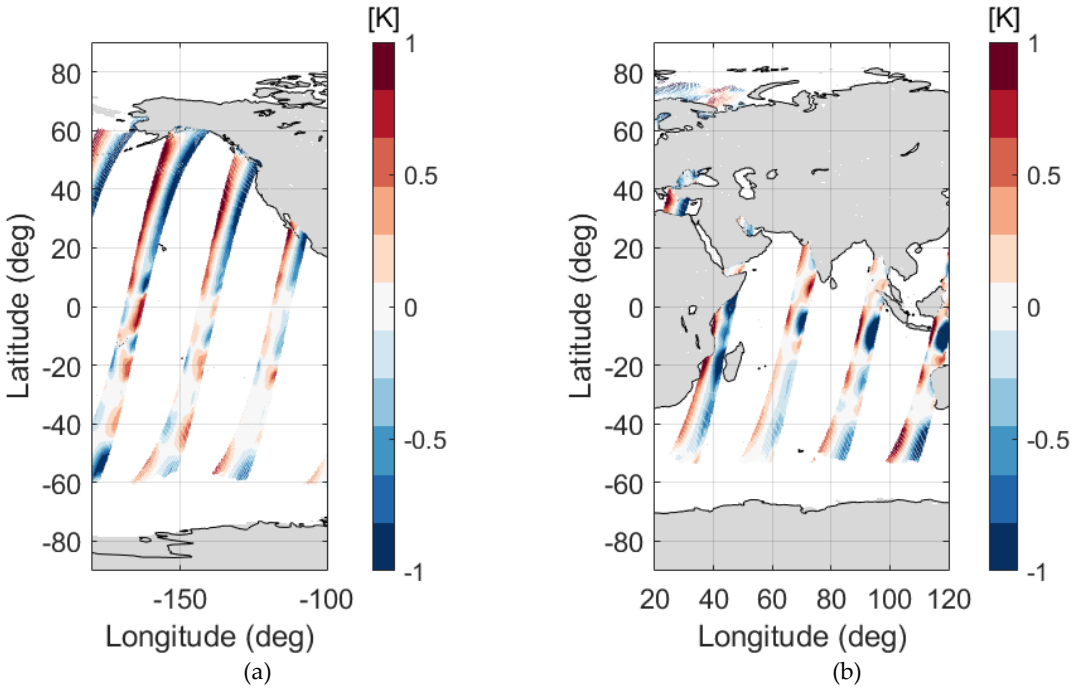

Figure 6.39. Difference of the X-polarization ocean TB anomaly when using the SMOS-based VTEC and the L1 VTEC of all descending orbits on June 5th, 2014 over (a) the Pacific Ocean and (b) the Indian Ocean.

Figure 6.40 shows the map in the Y polarization of the same date as in Fig. 6.38, June 5th, 2014.

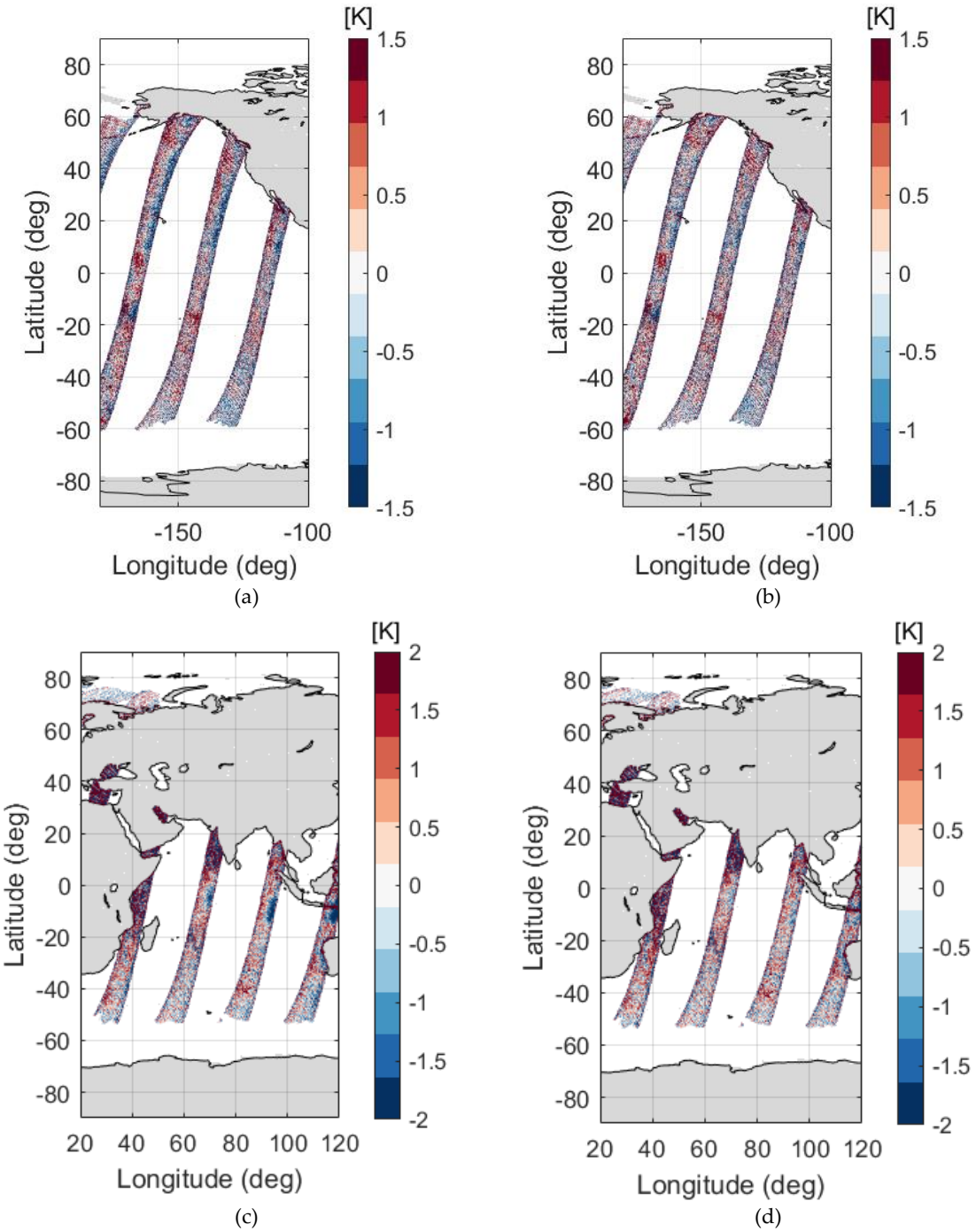

Figure 6.40. Y-polarization ocean TB anomaly of all descending orbits on June 5th, 2014 over the Pacific Ocean, when using (a) the L1 VTEC and (b) the SMOS-derived VTEC; over the Indian Ocean, when using (c) the L1 VTEC and (d) the SMOS-derived VTEC.

Once again, it can be seen in this polarization that by using the SMOS-derived VTEC, the systematic error in the laterals is mitigated given a much better stability in the retrieval

worldwide. The difference of using both sources in the Y polarization is shown in Figure 6.41.

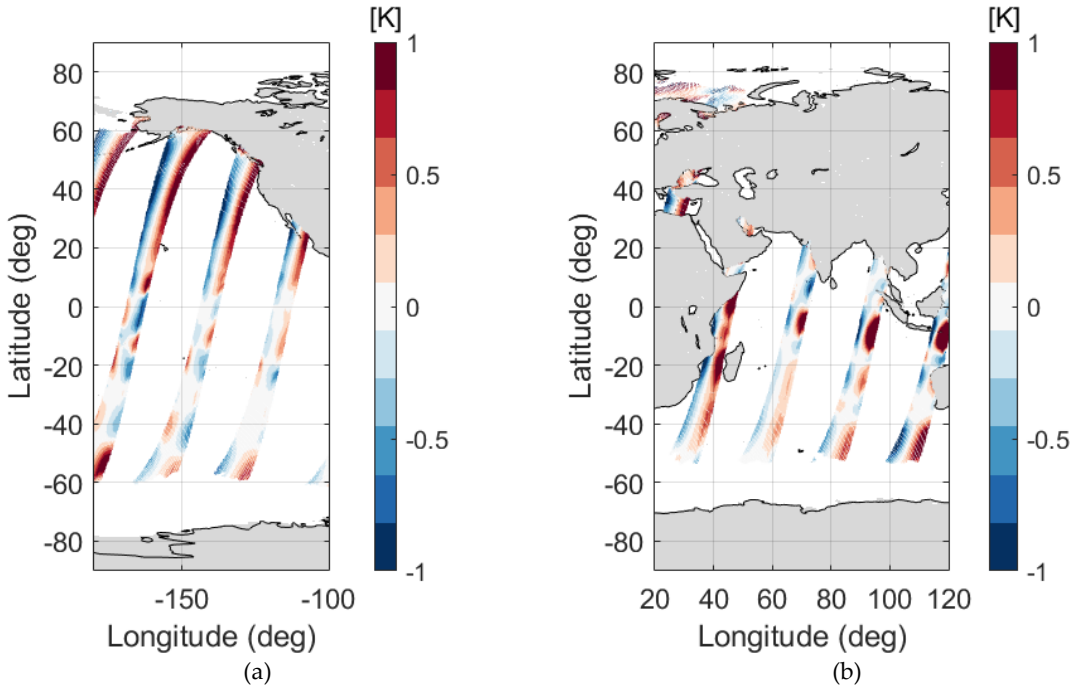

Figure 6.41. Difference of the Y-polarization ocean TB anomaly when using the SMOS-based VTEC and the L1 VTEC of all descending orbits on June 5th, 2014 over (a) the Pacific Ocean and (b) the Indian Ocean.

6.6. Conclusions

In Chapter 6, the performance of the SMOS-derived VTEC has been analyzed both temporally and geophysically. For the former, the Hovmöller diagrams of the retrieved VTEC along three years of the mission (2014-2016) over the Pacific Ocean for ascending and descending orbits have been analyzed. In those plots, high differences are found between the SMOS-based VTEC and the L1 VTEC, with the first one generally below the L1 VTEC despite the season. This is in agreement to the results found in the other VTEC retrieval from SMOS data (Vergely et al., 2014) and also in the case of Aquarius (Dinnat et al., 2014).

Monthly global maps show that the methodology is also capable to retrieve the VTEC independently to the target that is measuring, even though over land it is more challenging. The main reasons for that are firstly, because there is presence of RFI sources that corrupts the TB causing an affectation in the VTEC retrieval, and secondly, due to the fact that the TB over tropical forests are similar in the X and the Y polarizations and also T3 tends to 0 K, which causes an indetermination in Eq. (5.1). It can be also be appreciated that the VTEC retrieval does not seem to be affected by residual land-sea nor ice-sea contaminations. In the case of ascending orbits, errors in the retrieval are higher, since the VTEC range is much lower than for descending orbits. Close to the region where the geomagnetic field is aligned

with the signal path, for both ascending and descending orbits errors in the retrieved VTEC are high due to the indetermination ($\cos\Theta_B \approx 0$). However, this is not an issue for correcting the Faraday rotation, since it vanishes.

The impact of using the SMOS-derived VTEC maps on the spatial biases instead of the L1 VTEC is also positive. The part of the FoV of higher incidence angles improves very significantly in all the polarizations. The overall impact will be quite important in terms of retrieved salinity, since spatial biases are significant reduced.

In terms of the stability of the ocean brightness temperatures, in the X and Y-polarization TB Hovmöllers of both descending and ascending orbits, it cannot be seen an important improvement when using the SMOS-derived VTEC or the L1 VTEC. However, when analyzing descending orbits in more detail, plotting them separately with respect to the latitude, there is a clear improvement when using the SMOS-based VTEC. Main improvements are located in the Southern Hemisphere, where the sensitivity to TEC is higher. For ascending orbits, the impact on TB bias in X and Y polarizations is very low, since the VTEC range is much lower than in descending orbits. On the other hand, significant improvements are observed in the third-Stokes-parameter stability. The latitudinal gradient that there is when using L1 VTEC is mostly mitigated when using the SMOS-derived VTEC maps in both descending and ascending orbits, which improves the stability.

Daily maps of the difference between SMOS TB and modeled TB are also improved when using SMOS-derived VTEC maps. There is a clear reduction of systematic patterns, more evident in the Northern Hemisphere.

The assessment of the impact of these SMOS VTEC maps on the TB quality has been focused over the ocean, where the impact of ionospheric corrections is stronger. However, as already mentioned, the VTEC maps are derived from SMOS radiometric data independently of the target seen by the instrument. As part of the L1 ESL activities, future activities would be aimed at using these SMOS global VTEC maps for correcting the FRA and then, retrieve salinity and soil moisture to assess the final impact on the geophysical retrievals. Previously, a feasibility study for improving the quality of VTEC retrievals over RFI-contaminated regions is foreseen. The idea is to use improved brightness temperatures resulting from the application of techniques such as Nodal Sampling (González-Gambau et al., 2016) and the RFI mitigation technique (Oliva, 2018) to reduce the artifacts in TB images by RFI contamination.

Chapter 7

Conclusions and Future lines

7.1. Main Conclusions

At L-band, Faraday rotation is not negligible and must be corrected for obtaining accurate geophysical retrievals from satellite measurements. This is the case of the brightness temperatures measurements provided by SMOS. A classical theoretical formulation can be used to calculate the FRA (Le Vine & Abraham, 2002). However, the retrieval of the Faraday rotation from SMOS radiometric data in a continuous way would allow to improve the quality of the geophysical retrievals. As shown in Corbella et al., 2015, estimating the Faraday rotation directly from radiometric data at each snapshot and for all the pixels in the field of view is not straightforward, mainly due to the radiometric sensitivity and accuracy of MIRAS radiometer.

The methodology developed in this thesis is based on estimating the total electron content of the ionosphere for each SMOS overpass by using an inversion procedure from the measured Faraday rotation angle. These SMOS-derived VTEC maps can then be re-ingested to dynamically correct the Faraday rotation at each snapshot and for the complete SMOS field of view. This methodology allows to derive VTEC maps independently of the target seen by the instrument, and this is an important difference with respect to other methodology that also corrects the FRA by using SMOS radiometric data (Vergely et al., 2014), which is focused over the ocean and uses a forward radiative model. Besides, the methodology developed in this work allows to retrieve the VTEC for all the pixels in the SMOS field of view. This is in contrast to other methodologies that assign a unique VTEC value for the entire FoV, as is the case of Corbella et al., 2015 and Vergely et al., 2014.

The development of a FRA end-to-end simulator has allowed to select the best one between the different approaches to derive the SMOS-VTEC maps. By using this simulator, studies to select the size of the temporal filter applied to the brightness temperature and the radius of the spatial filter applied to VTEC snapshots have been addressed, leading to minimum errors in the VTEC and FRA retrievals. The simulator has also allowed the definition of different filters (such as the filtering of TBs acquired at low incidence angles to avoid the indetermination when $T_B^{xx} \approx T_B^{yy}$ and $T3 \approx 0$, and the filtering when the signal

propagation direction is orthogonal to the magnetic field). The optimization was done by using simulated data and then, confirmed with real SMOS TB measurements.

The SMOS-derived VTEC maps have been inter-compared with the L1 VTEC (both over ocean and land) and the IGS VTEC and the other SMOS-derived VTEC product (A3TEC) products over ocean. The SMOS-derived VTEC is smoother than the A3TEC. They provide values generally lower than the ones from the external VTEC databases (L1 and IGS VTEC), which it is in agreement with the differences found when comparing over the ocean the A3TEC product (Vergely et al., 2014) and also when comparing the Aquarius TEC (Dinnat et al., 2014) with the same two external data sources.

It was found that the SMOS-derived VTEC maps presented a remaining systematic error pattern that could be introduced by the instrument when measuring the Faraday rotation (it was not present in the simulation experiments). This FRA systematic error pattern has been characterized by using data in a region (latitude range [35°S 5°S]) and for a period (ascending orbits during summer months) with very low FRA values, so the measurement can be assumed as a systematic error of the instrument and a correction can be derived. The analysis has been done for different years (2014, 2017, 2018 and for the period 2010-2019). The FRA systematic error has been shown to be stable along the mission, despite the variation of the solar activity. This temporal stability led to the decision of using the same correction for the entire mission. The FRA systematic error subtraction to the retrieved FRA for each snapshot has led to an important improvement in the SMOS-derived VTEC maps, which are more geophysical consistent. It not only improves the recovery of the descending orbits but also of the ascending orbits.

The performance of the SMOS-derived VTEC has been analyzed both temporally and geographically. The temporal performance has been analyzed through the Hovmöller diagrams of the retrieved VTEC along three years of the mission (2014-2016) over the Pacific Ocean for ascending and descending orbits. High differences have been found between the SMOS-based VTEC and the L1 VTEC, with the first one generally below the L1 VTEC despite the season. This is in agreement to the results found in the A3TEC (Vergely et al., 2014) and also in the case of Aquarius (Dinnat et al., 2014). The spatial analysis has been performed by analyzing monthly global VTEC maps along 2014, the year with the highest TEC along the mission. These SMOS-derived VTEC maps have been compared to L1 VTEC maps and the main performance and limitations have been analyzed. The methodology is capable of retrieving VTEC maps independently to the target that is measuring, even though over land it is more challenging. Main limitations to obtain accurate TEC retrievals over land are in (i) RFI-contaminated regions, since interferences degrade the quality of the SMOS brightness temperatures and therefore, of the VTEC maps, and (ii) regions where the brightness temperature in X and Y polarizations are very similar and the third Stokes parameter tends to 0 K, such as in the case of dense forests. In addition, the retrieval of VTEC maps is more challenging for ascending orbits than for descending orbits because the effect

of noise masks to a larger extent the VTEC since its range of variability is much lower. However, the FR effect is lower in ascending orbits, and then, the impact of using these SMOS-derived VTEC maps or the L1 VTEC is also lower than for descending orbits. Errors in the SMOS-derived VTEC maps are higher close to the region where the geomagnetic field is aligned with the signal path due to the indetermination ($\cos\Theta_B \approx 0$). This can be an issue depending on the use of the SMOS-derived VTEC maps. Nevertheless, this is not a real problem when using the maps for the conversion of SMOS brightness temperatures from antenna to ground coordinates, since the FRA vanishes in that specific zone and it does not need to be corrected.

The analysis of the impact of using these SMOS-derived VTEC maps on the quality of the brightness temperatures has been focused over the ocean, where the effect of the ionospheric corrections is stronger. The analysis of the spatial biases has revealed that there is a significant reduction when using SMOS-derived VTEC maps instead of L1 VTEC in the region of the field of view with the highest sensitivity of TB to TEC (high incidence angles). The impact of this improved stability is expected to be quite significant in terms of the retrieved salinity. Once the improvement on the spatial biases has been shown, the TB stability has been analyzed by means of Hovmöller diagrams of the difference between the SMOS and the modeled TBs per each polarization at antenna reference frame H. The latitudinal gradient found in T3 when using the L1 VTEC for correcting the FRA has been substantially mitigated when using the SMOS-derived VTEC maps, improving the stability with respect to the usage of L1 VTEC products both in ascending and descending orbits. The stability of TB in X and Y polarizations has also been improved for descending orbits when using SMOS-derived VTEC maps (particularly in the Southern Hemisphere, where the sensitivity of TB to TEC is also higher), although the impact is lower than in the bias of T3. In the case of ascending orbits, the impact of using one or the other VTEC product on TB in X and Y polarizations is really low, which is expected due to the low VTEC values in ascending orbits as compared to descending ones. Finally, it has been assessed the impact on daily global maps of the ocean TB anomaly, that is, the magnitude that enters in the sea surface salinity retrieval scheme in order to calculate it, and therefore, it is a quality indicator for the SSS retrievals. Daily maps of the TB anomaly are also improved when using SMOS-derived VTEC maps. There is a clear reduction of systematic patterns, lowering the differences between SMOS measurements and modeled TB.

7.2. Thesis Outcomes

The original contributions of this work can be summarized as follows:

- Implementation of a L-band brightness temperature simulator mimicking the SMOS synthetic aperture radiometer able to retrieve the Faraday rotation angle and to derive the Vertical Total Electron Content of the ionosphere.

- Estimation of the VTEC for all the pixels in the AF-FOV with information of different incidence angles by using spatial and temporal filtering techniques.
- Detection of systematic patterns in the retrieved Faraday Rotation Angle (FRA) from SMOS radiometric data. These systematic patterns are characterized and corrected to improve the quality of the retrieved VTEC maps.
- Generation of VTEC maps over any type of surface (land, ocean, and ice) for the first time from only SMOS measurements, without using any prior information nor forward models.
- Demonstration of the quality improvement in terms of spatial biases, brightness temperature stability, and latitudinal gradient in the third Stokes parameter when using SMOS-derived VTEC maps with respect to L1 VTEC.

These contributions have resulted in a number of publications in international journals and conference proceedings.

Journal papers:

- Rubino, R., Duffo, N., González-Gambau, V., Torres, F., Corbella, I., Durán, I., & Martín-Neira, M. (2020a). Deriving VTEC Maps from SMOS Radiometric Data. *Remote Sensing*, *12*(10), 1604. https://doi.org/10.3390/rs12101604.
- Rubino, R., Duffo, N., González-Gambau, V., Corbella, I., Torres, F., Oliva, R., & Martín-Neira, M. (2022). Correcting the FRA Systematic Error in VTEC Maps from SMOS Radiometric. *IEEE Transactions on Geoscience and Remote Sensing*, *in revision*.

Conference proceedings:

- Rubino, R., Torres, F., Duffo, N., González-Gambau, V., Corbella, I., & Martin-Neira, M. (2017). Direct Faraday rotation angle retrieval in SMOS field of view. *2017 IEEE International Geoscience and Remote Sensing Symposium (IGARSS)*, 697–698. https://doi.org/10.1109/IGARSS.2017.8127047
- Rubino, R., Duffo, N., González-Gambau, V., Torres, F., Corbella, I., & Martin-Neira, M. (2018). New Methodology for the Faraday Rotation Angle Retrieval in the SMOS Field of View. *IGARSS 2018 - 2018 IEEE International Geoscience and Remote Sensing Symposium*, 3089–3092. https://doi.org/10.1109/IGARSS.2018.8517502
- Rubino, R., Duffo, N., González-Gambau, V., Corbella, I., Torres, F., Durán, I., & Martín-Neira, M. (2019a). New Methodology to Retrieve the Faraday Rotation Angle Using SMOS Data. *LPS19 -Living Planet 2019*. LPS19 -Living Planet 2019, Milan
- Rubino, R., Duffo, N., González-Gambau, V., Corbella, I., Torres, F., Durán, I., & Martín-Neira, M. (2019b). Refining the Methodology to Correct the Faraday

Rotation Angle from SMOS Measurements. *IGARSS 2019 - 2019 IEEE International Geoscience and Remote Sensing Symposium*.

- Rubino, R., Duffo, N., González-Gambau, V., Corbella, I., Torres, F., & Martin-Neira, M. (2020b). Characterizing Systematic Errors in the Faraday Rotation Retrieval from SMOS Measurements. *IGARSS 2020 - 2020 IEEE International Geoscience and Remote Sensing Symposium*, 6431–6433. https://doi.org/10.1109/IGARSS39084.2020.9323288

In addition, the main activities have been presented in the regular SMOS Payload Calibration Meetings maintained by the SMOS Expert Support Laboratories of Level 1:

- Rubino, R. "VTEC Maps from SMOS Data to Correct the Faraday Rotation Effect." Presented at the SMOS Payload Calibration Meeting #37, Barcelona, May 2019.
- Rubino, R. "New L1 TEC Product - Methodology and Assessment." Presented at the SMOS Payload Calibration Meeting #41, Online, June 2020.
- Rubino, R. "Support to New SMOS Data Products." Presented at the SMOS Payload Calibration Meeting #42, Online, September 2020.
- Rubino, R. "SMOS VTEC over All Surfaces." Presented at the SMOS Payload Calibration Meeting #43, Online, December 2020.
- Rubino, R. "Development of TEC Product & Analysis of Its Performance." Presented at the SMOS Payload Calibration Meeting #44, Online, March 2021.
- Rubino, R. "Evaluation of the Patched L1C Product." Presented at the SMOS Payload Calibration Meeting #45, Online, June 2021.
- Rubino, R. "Assessment of VTEC Products and Impact on the Geophysical Retrievals." Presented at the SMOS Payload Calibration Meeting #46, Online, September 2021.
- Rubino, R. "Assessment of VTEC Products and Impact on the Geophysical Retrievals." Presented at the SMOS Payload Calibration Meeting #47, Online, December 2021.
- Rubino, R. "VTEC Product – Assessment and Impact on the Geophysical Retrievals." Presented at the SMOS L1/L2OS Joint Meeting #6, Barcelona, June 2022.

7.3. Future Research Lines

In the short term, as part of the L1 ESL activities, the impact of using currently implemented techniques, such as the Nodal Sampling (González-Gambau et al., 2016) and the RFI mitigation technique (Oliva, 2018) on the quality of the VTEC maps will be assessed. Besides, the impact of using the VTEC map at its recovered resolution (ETOPO5, which is equivalent to 0.08°) rather than at the resolution of L1 VTEC (which is equivalent to 2.5°) will be evaluated. Thereafter, the next steps will be using these SMOS-derived VTEC maps

to correct for FRA in SMOS and then, retrieving salinity and soil moisture to assess the final impact on these geophysical variables.

In the mid-term, it is planned to test the usage of SMOS VTEC products for other L-band missions, such as SMAP and Copernicus Imaging Microwave Radiometer CIMR (Donlon, 2020). This would require the generation of global VTEC maps (not just for SMOS overpasses) by using appropriate techniques such as optimal interpolation. One could think of doing a longitudinal interpolation between one to the next orbit in such a way that a global daily VTEC map will be obtained.

In the long term, SMOS-derived VTEC products could be useful to other communities. Furthermore, in the frame of SMOS follow-on programs and other current and/or future missions that have an interferometric radiometer on board (e.g. the Water Cycle Observation Mission WCOM Chinese mission (Shi et al., 2016)), this work paves the way for future algorithms to derive VTEC maps and correct the Faraday rotation.

Appendix A

Monthly VTEC Global Maps of Descending Orbits

This appendix is devoted to show the monthly SMOS-derived VTEC maps of the descending orbits of the months that are not shown in section 6.2.

In the following images, the L1 VTEC is shown in subfigure (a); in the (b), the SMOS-derived VTEC map; and in the (c), the difference between the second one and the first one.

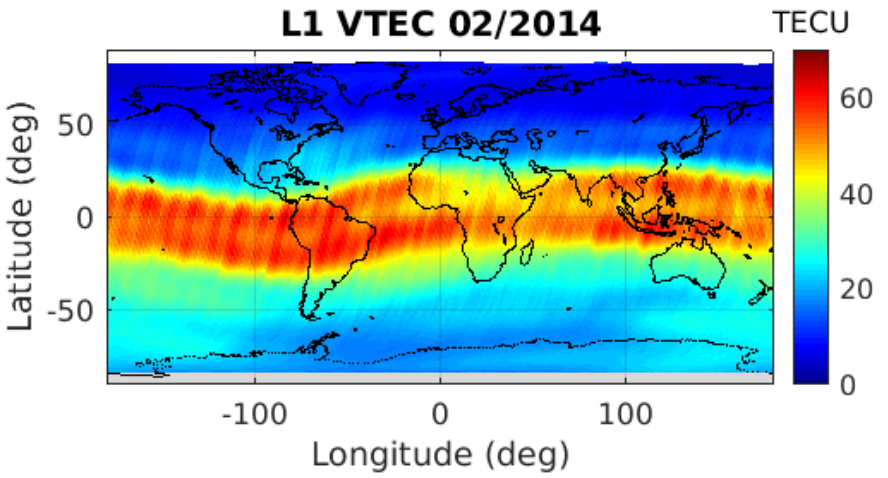

(a)

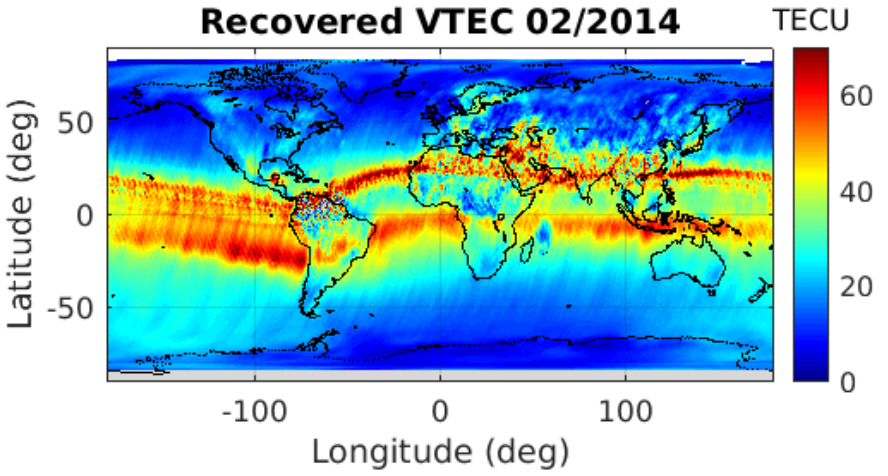

(b)

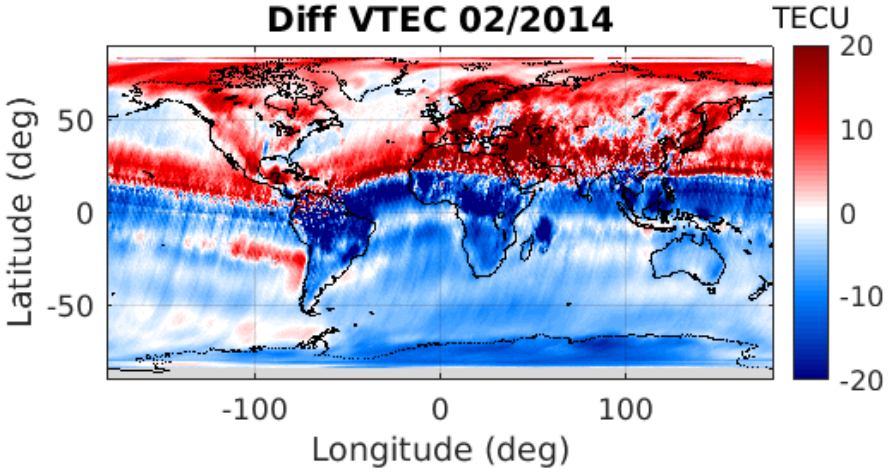

(c)

Figure A. 1. VTEC global maps of February 2014 (descending orbits): (a) L1 VTEC, (b) SMOS-derived VTEC, and (c) difference between the SMOS-derived VTEC and the L1 VTEC.

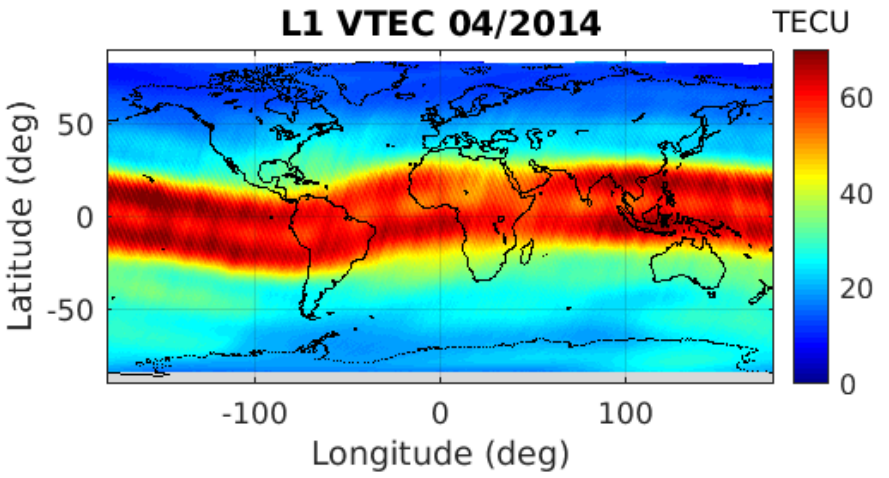

(a)

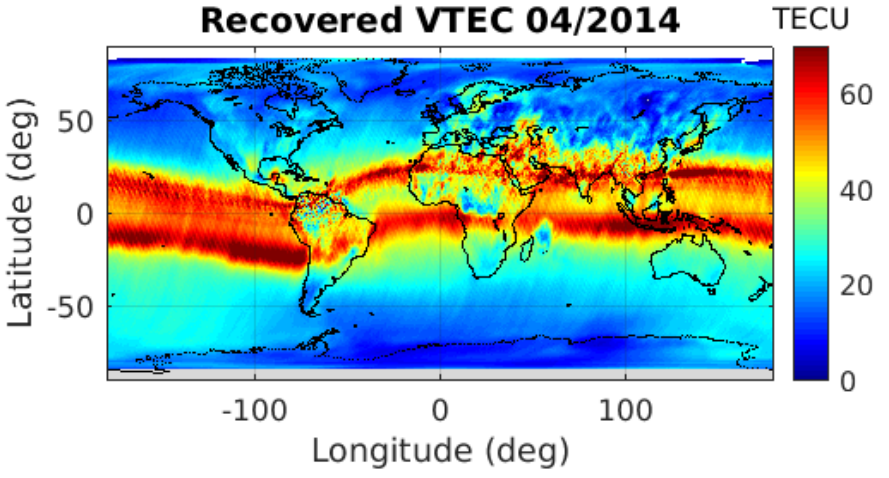

(b)

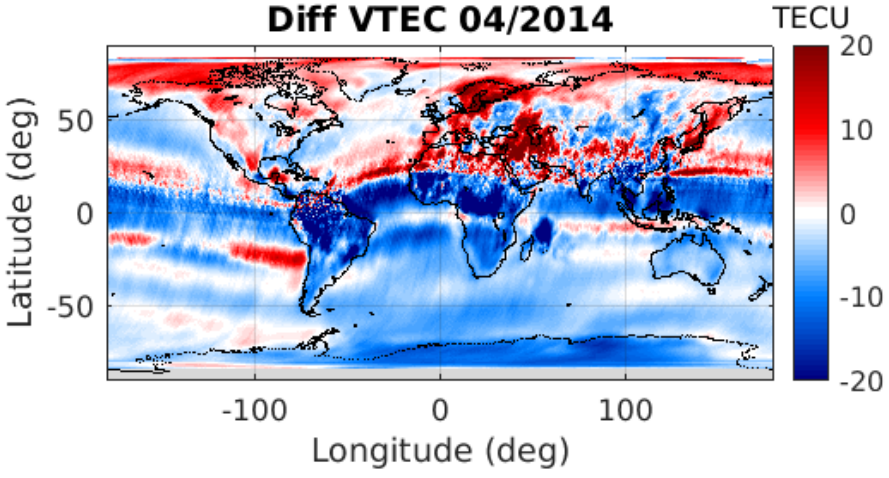

(c)

Figure A. 2. VTEC global maps of April 2014 (descending orbits): (a) L1 VTEC, (b) SMOS-derived VTEC, and (c) difference between the SMOS-derived VTEC and the L1 VTEC.

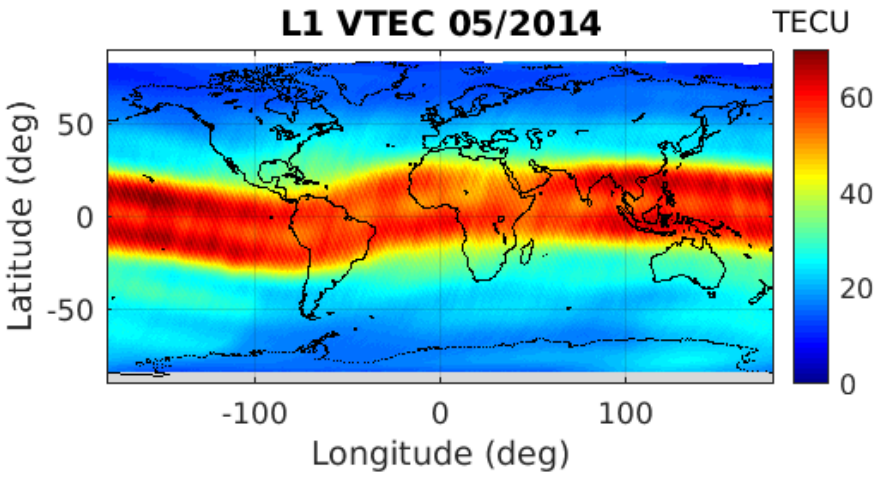

(a)

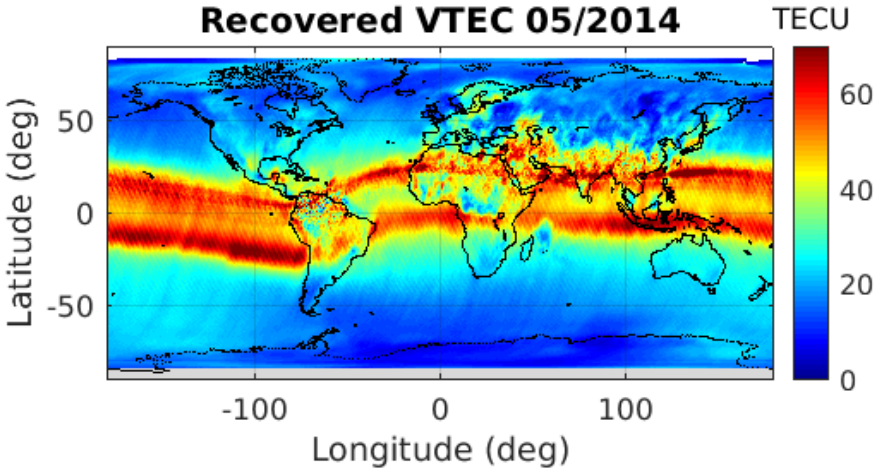

(b)

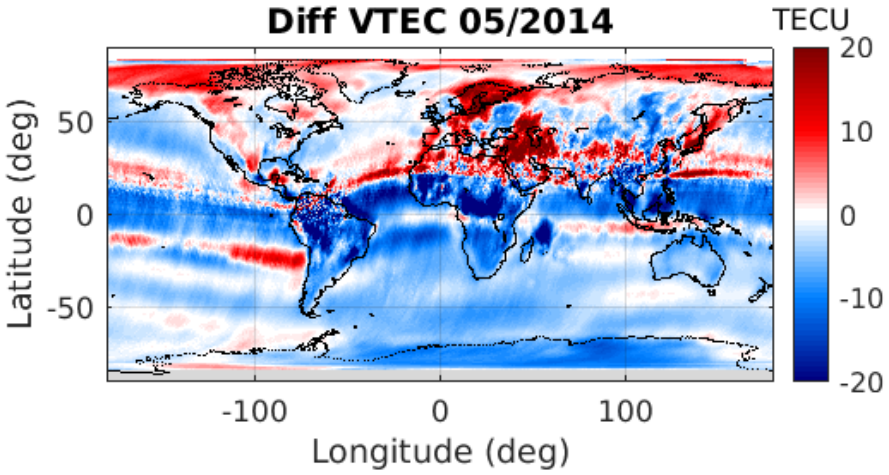

(c)

Figure A. 3. VTEC global maps of May 2014 (descending orbits): (a) L1 VTEC, (b) SMOS-derived VTEC, and (c) difference between the SMOS-derived VTEC and the L1 VTEC.

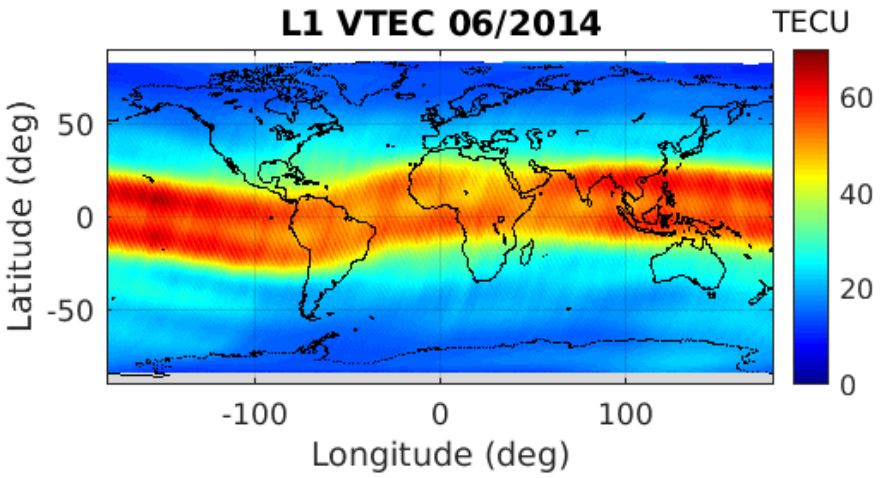

(a)

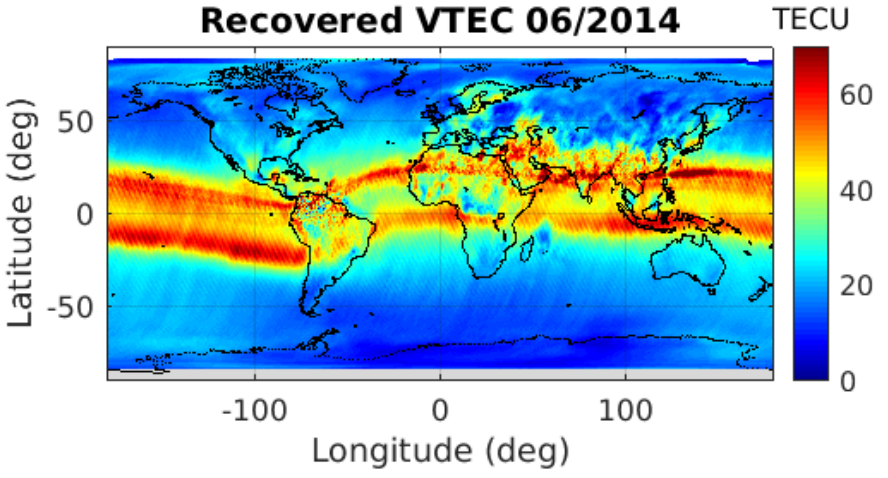

(b)

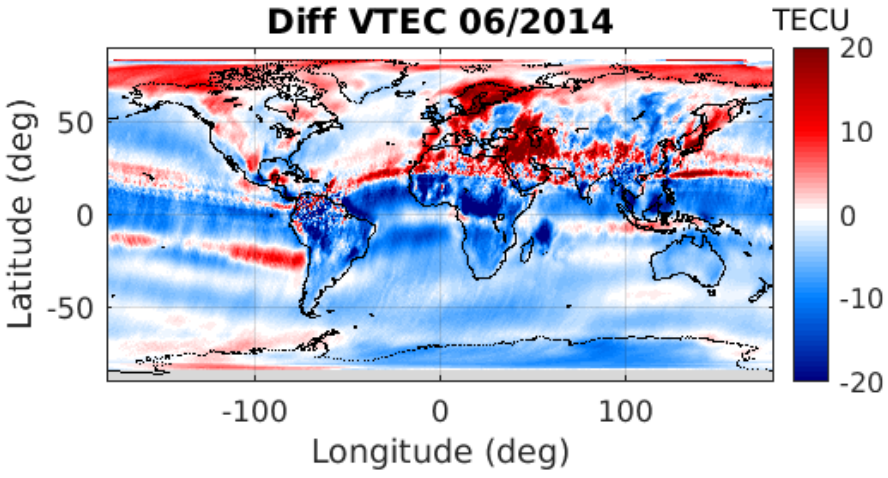

(c)

Figure A. 4. VTEC global maps of June 2014 (descending orbits): (a) L1 VTEC, (b) SMOS-derived VTEC, and (c) difference between the SMOS-derived VTEC and the L1 VTEC.

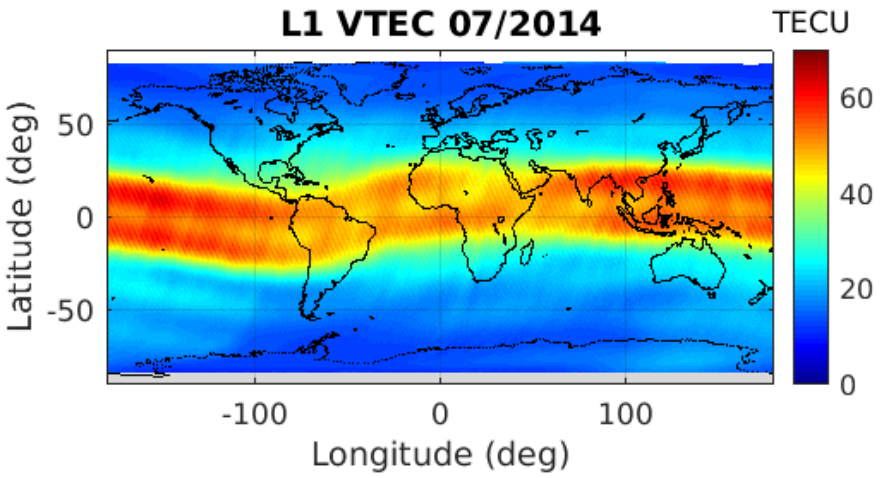

(a)

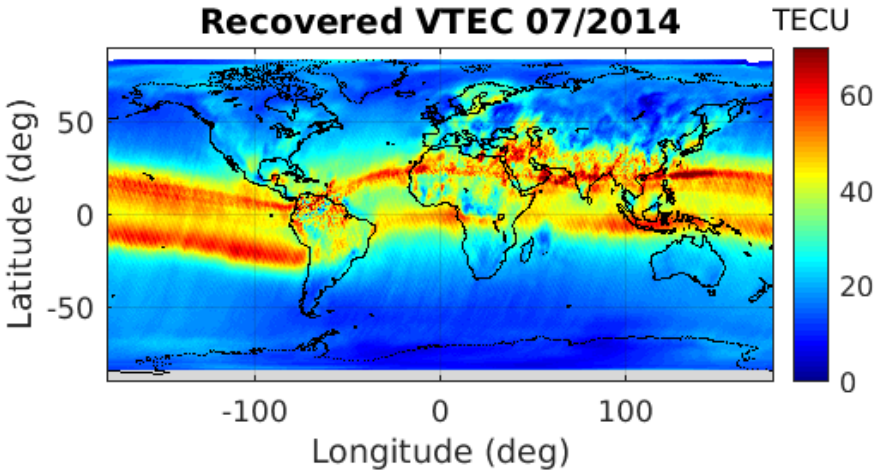

(b)

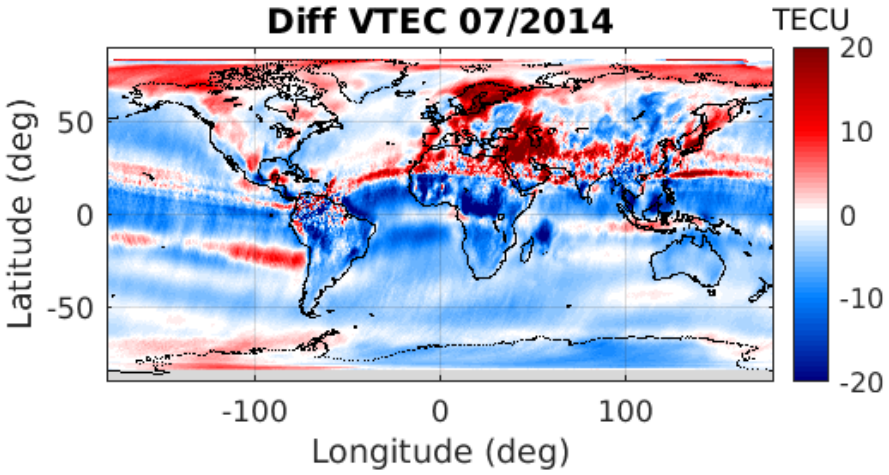

(c)

Figure A. 5. VTEC global maps of July 2014 (descending orbits): (a) L1 VTEC, (b) SMOS-derived VTEC, and (c) difference between the SMOS-derived VTEC and the L1 VTEC.

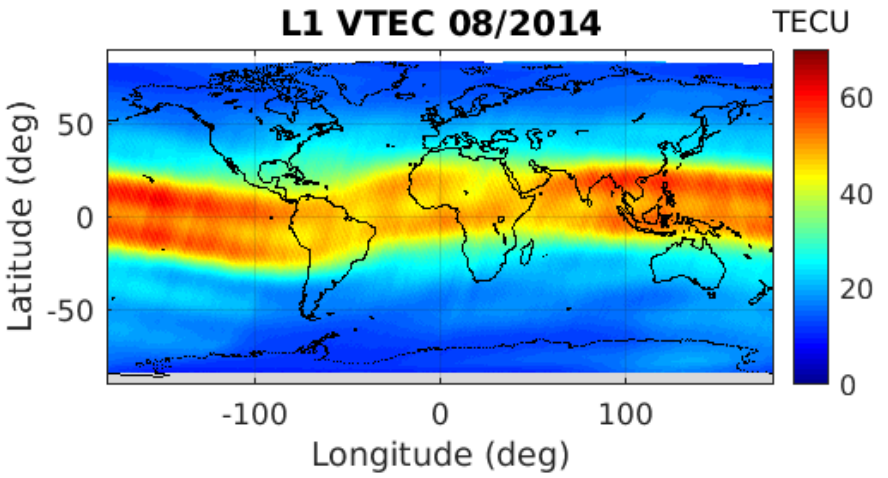

(a)

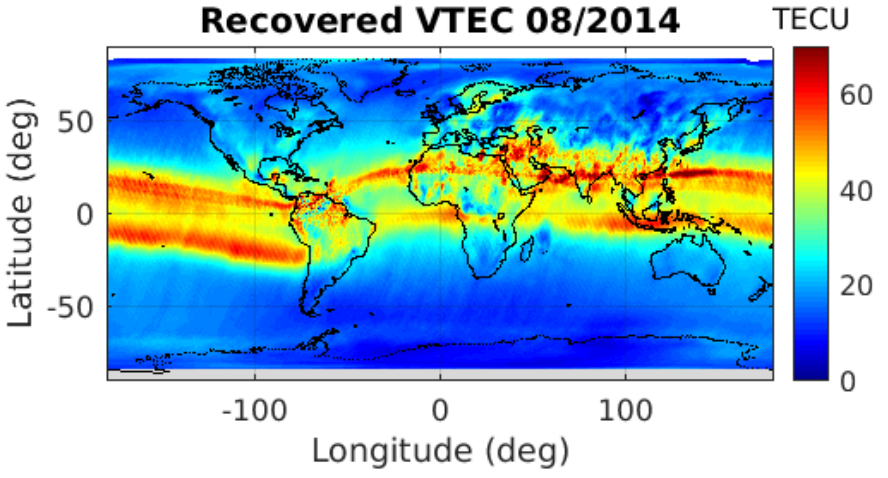

(b)

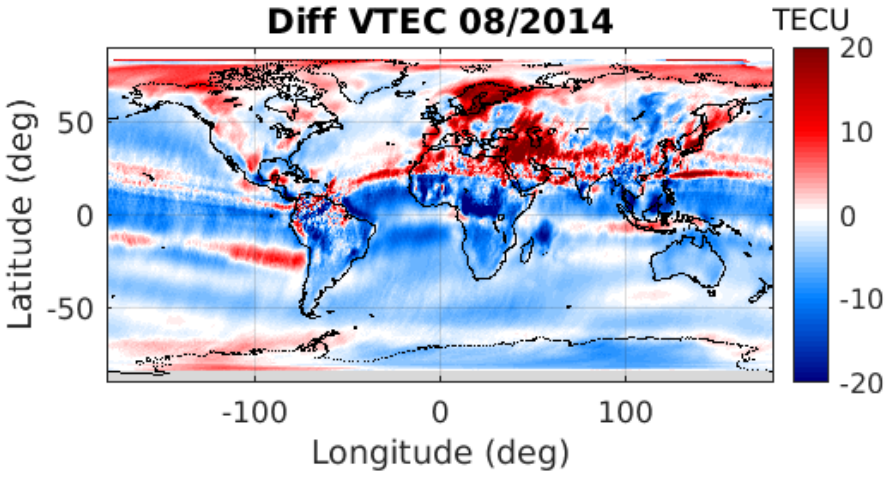

(c)

Figure A. 6. VTEC global maps of August 2014 (descending orbits): (a) L1 VTEC, (b) SMOS-derived VTEC, and (c) difference between the SMOS-derived VTEC and the L1 VTEC.

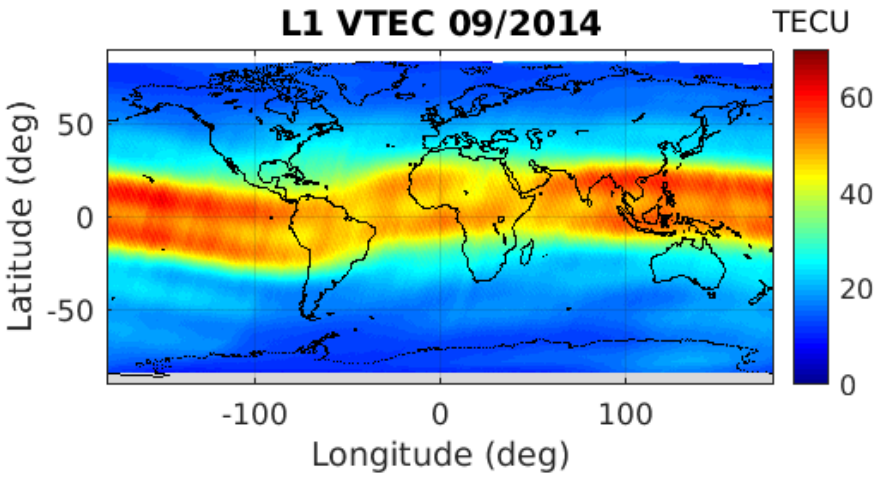

(a)

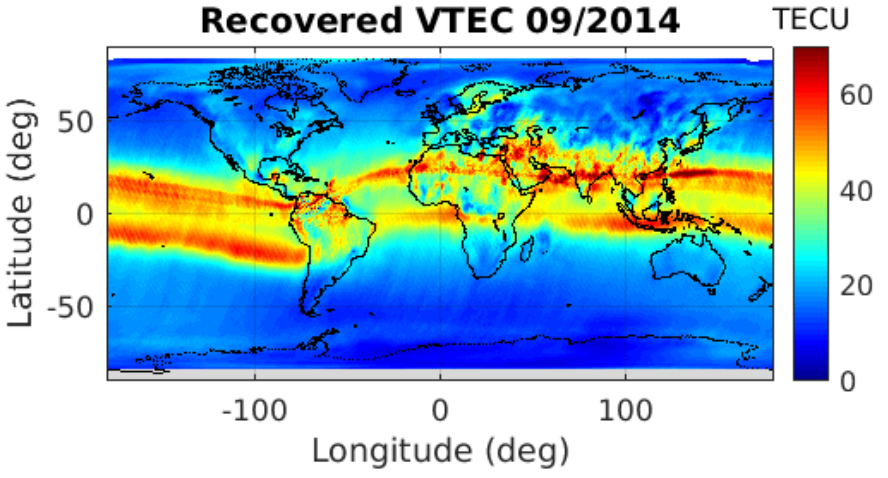

(b)

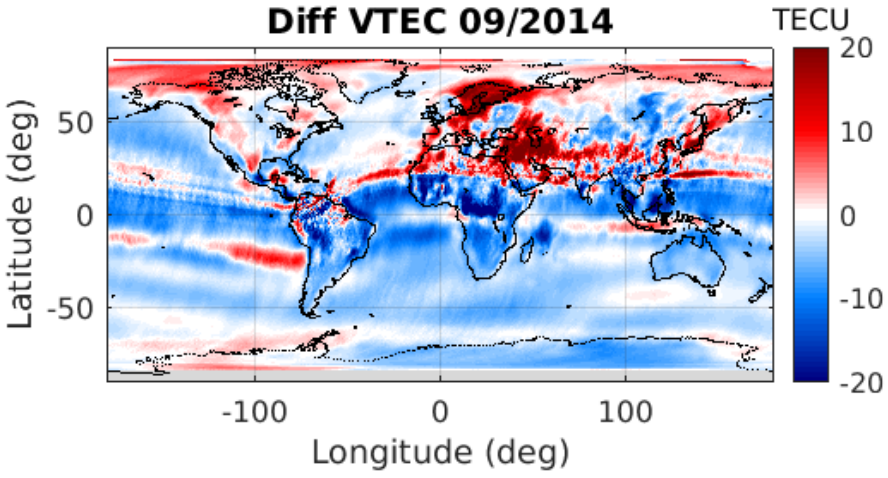

(c)

Figure A. 7. VTEC global maps of September 2014 (descending orbits): (a) L1 VTEC, (b) SMOS-derived VTEC, and (c) difference between the SMOS-derived VTEC and the L1 VTEC.

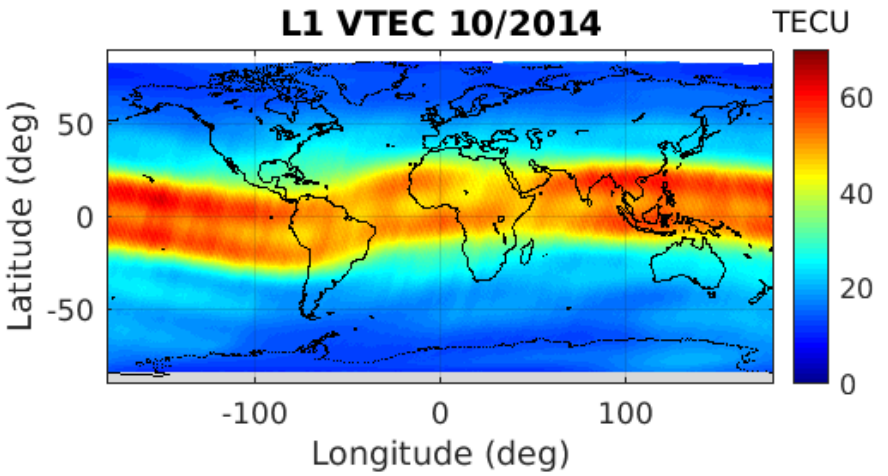

(a)

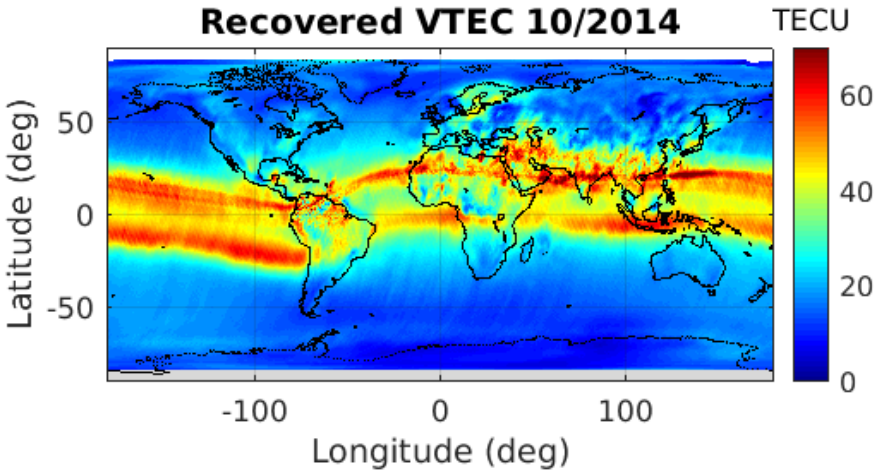

(b)

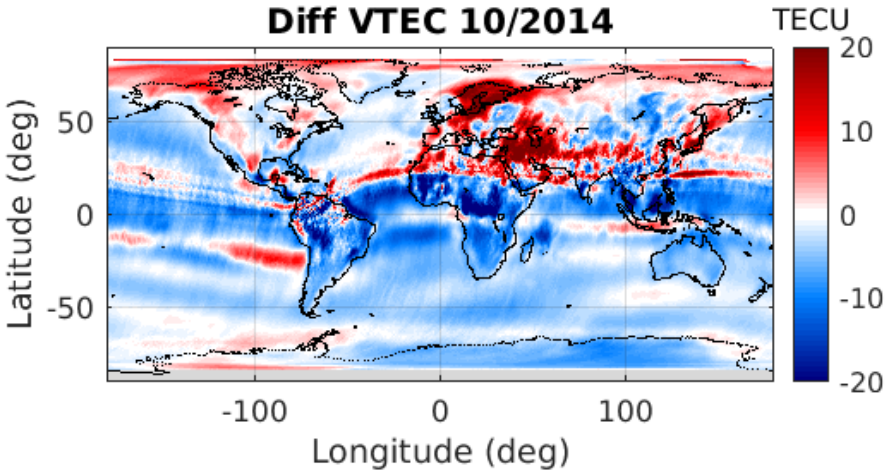

(c)

Figure A. 8. VTEC global maps of October 2014 (descending orbits): (a) L1 VTEC, (b) SMOS-derived VTEC, and (c) difference between the SMOS-derived VTEC and the L1 VTEC.

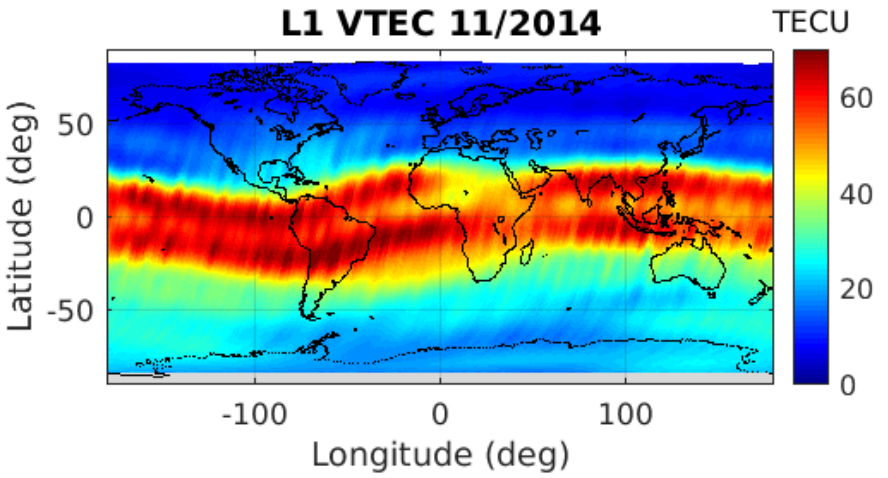

(a)

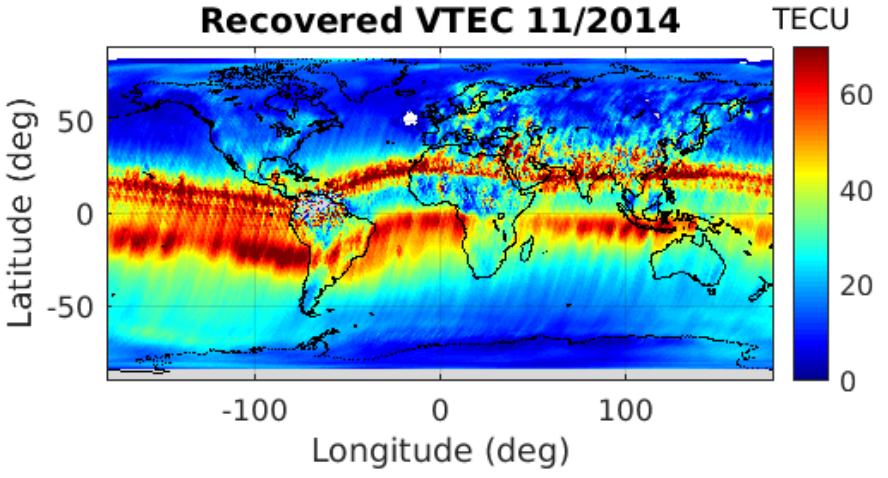

(b)

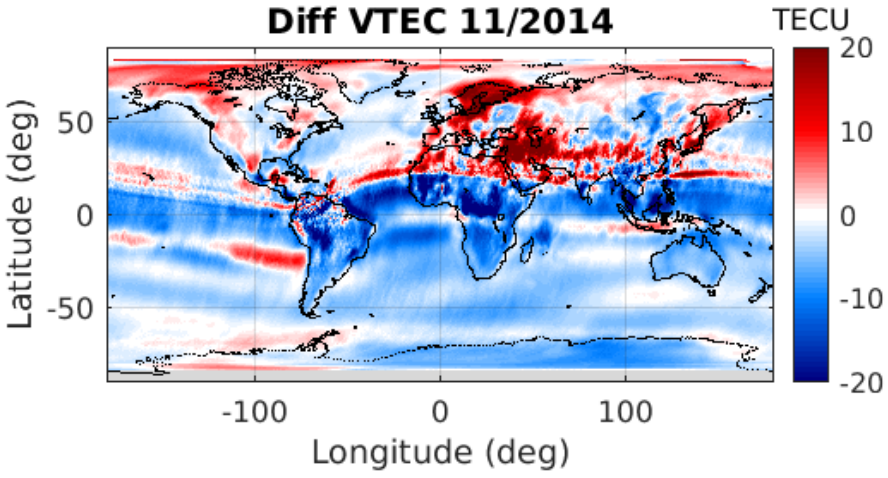

(c)

Figure A. 9. VTEC global maps of November 2014 (descending orbits): (a) L1 VTEC, (b) SMOS-derived VTEC, and (c) difference between the SMOS-derived VTEC and the L1 VTEC.

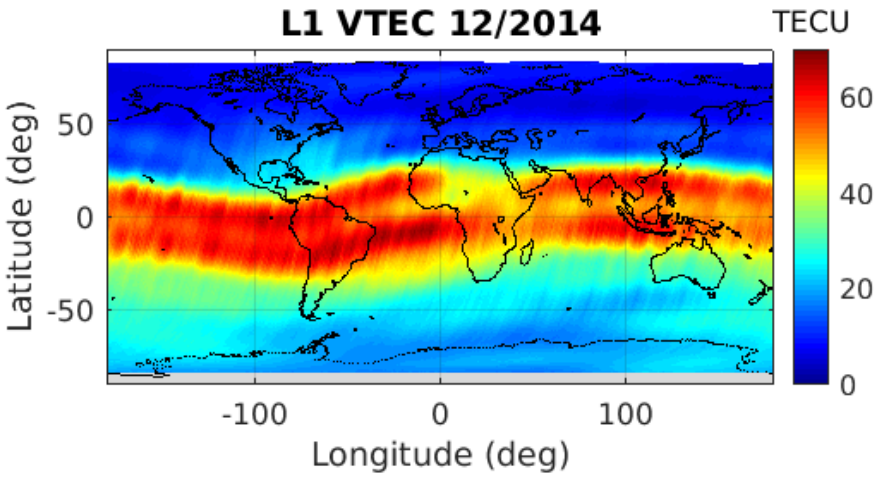

(a)

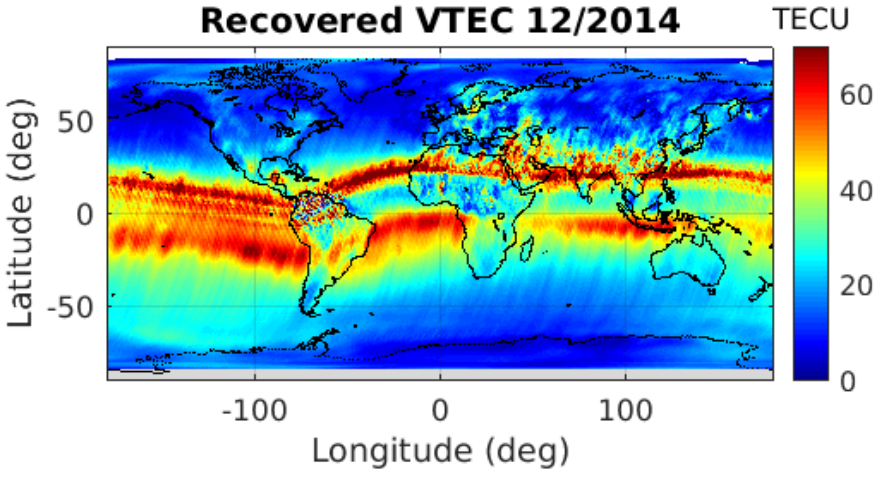

(b)

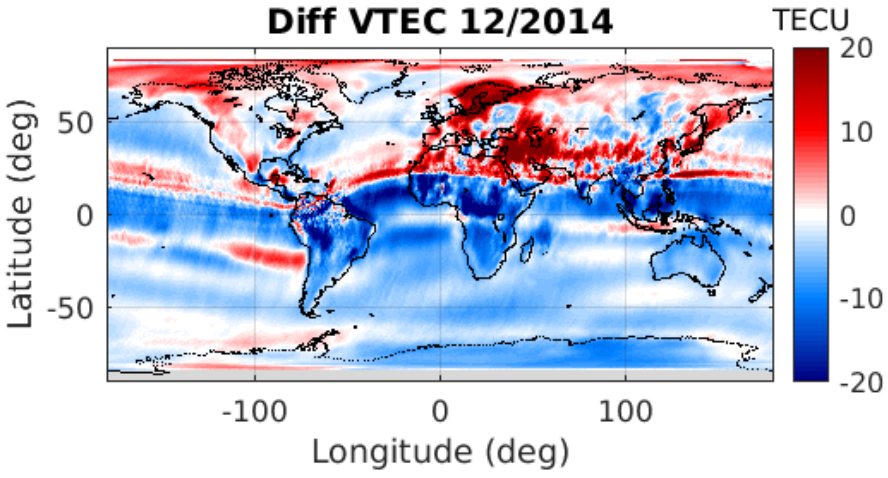

(c)

Figure A. 10. VTEC global maps of December 2014 (descending orbits): (a) L1 VTEC, (b) SMOS-derived VTEC, and (c) difference between the SMOS-derived VTEC and the L1 VTEC.

Appendix B

Monthly VTEC Global Maps of Ascending Orbits

This appendix is devoted to show the monthly SMOS-derived VTEC maps of the ascending orbits of the months that are not shown in section 6.2.

In the following images, the L1 VTEC is shown in subfigure (a); in the (b), the SMOS-derived VTEC map; and in the (c), the difference between the second one and the first one.

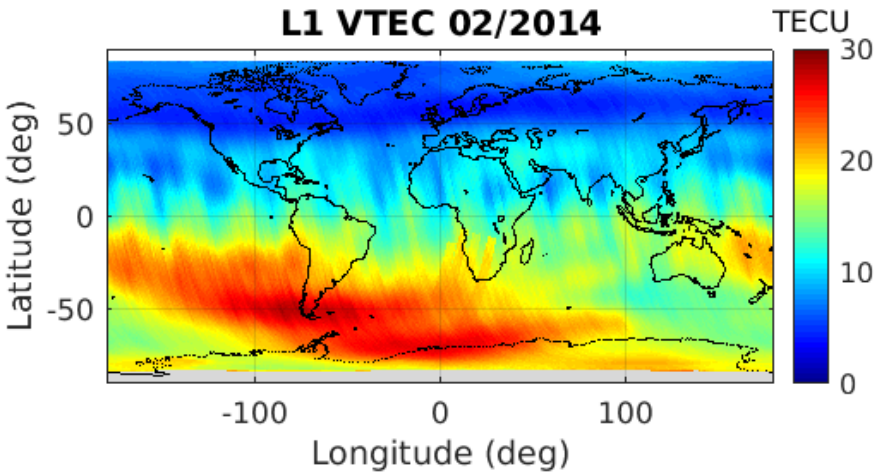

(a)

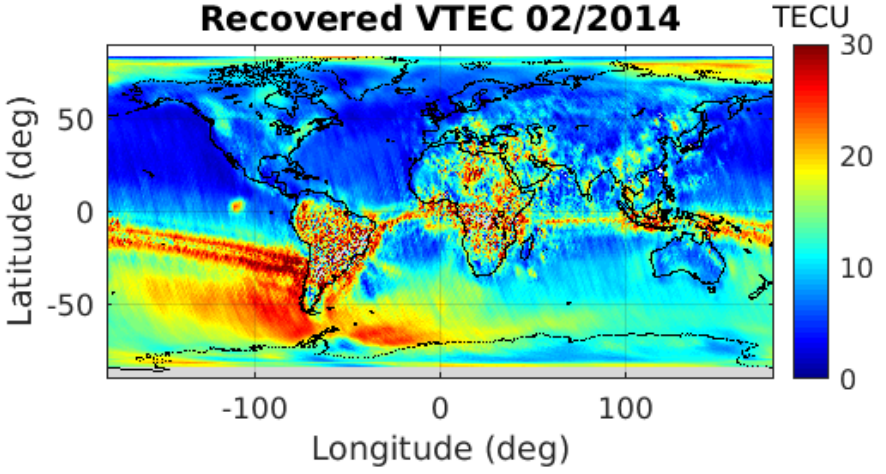

(b)

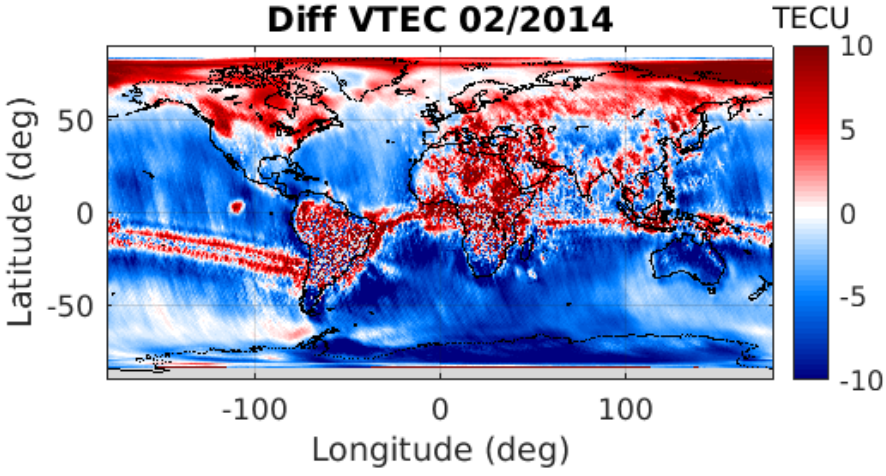

(c)

Figure B. 1. VTEC global maps of February of 2014 (ascending orbits): (a) L1 VTEC, (b) SMOS-derived VTEC, and (c) difference between the SMOS-derived VTEC and the L1 VTEC.

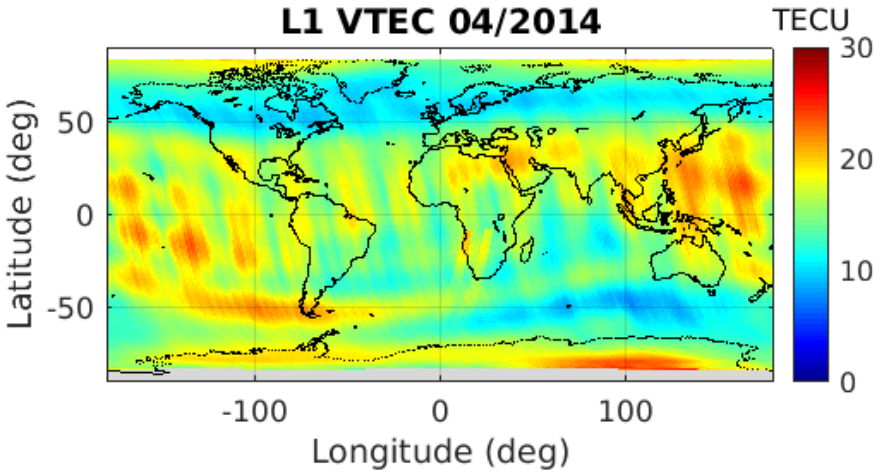

(a)

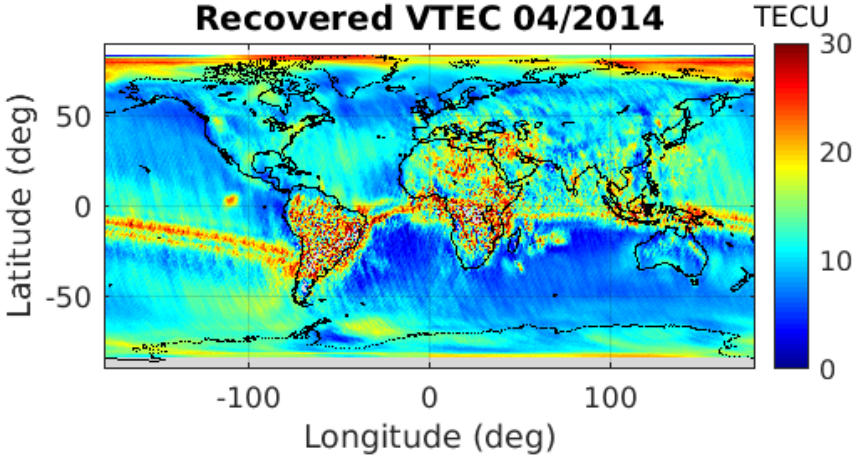

(b)

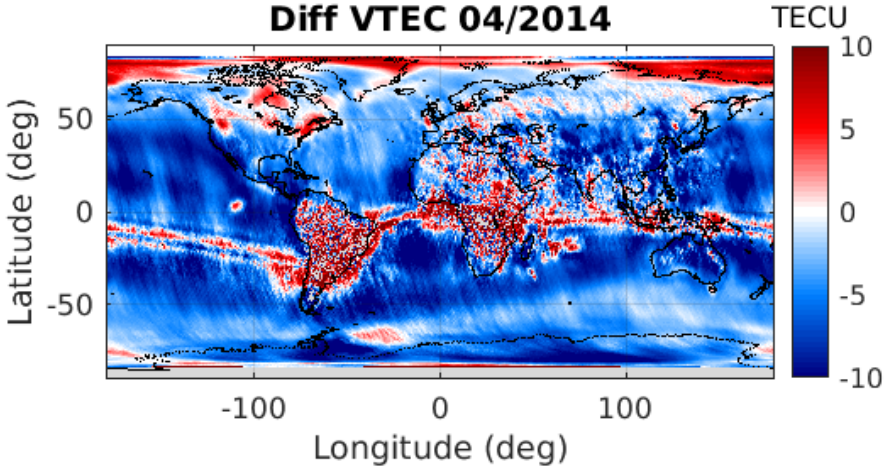

(c)

Figure B. 2. VTEC global maps of April 2014 (ascending orbits): (a) L1 VTEC, (b) SMOS-derived VTEC, and (c) difference between the SMOS-derived VTEC and the L1 VTEC.

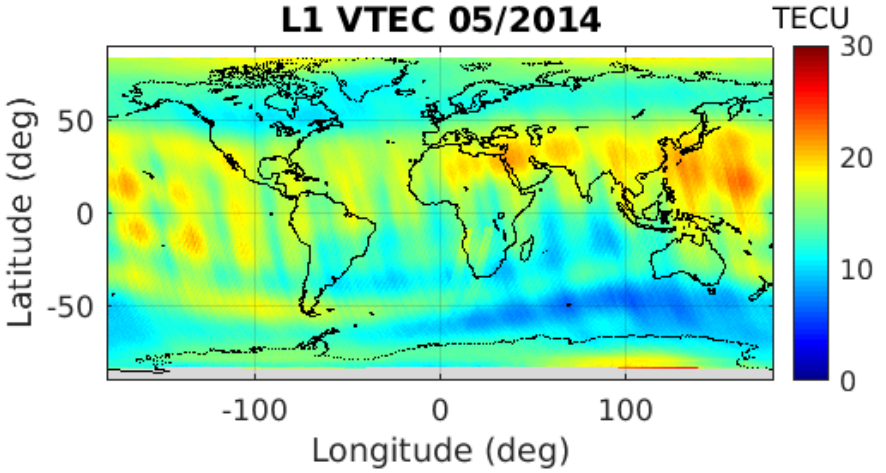

(a)

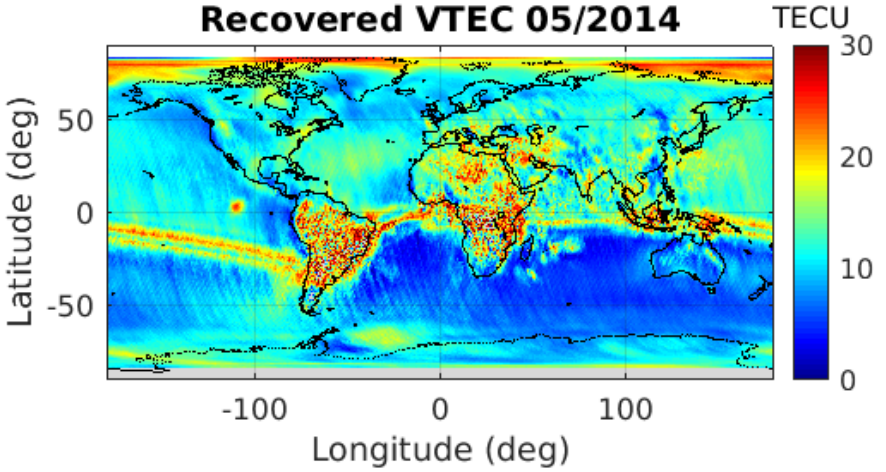

(b)

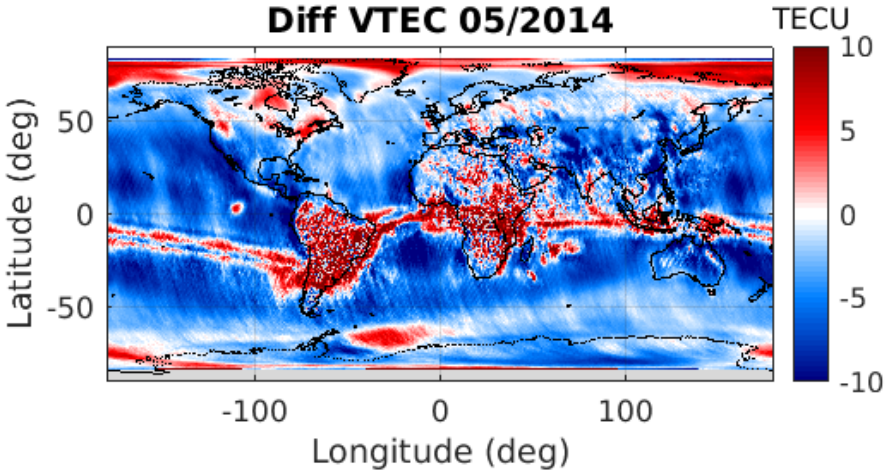

(c)

Figure B. 3. VTEC global maps of May 2014 (ascending orbits): (a) L1 VTEC, (b) SMOS-derived VTEC, and (c) difference between the SMOS-derived VTEC and the L1 VTEC.

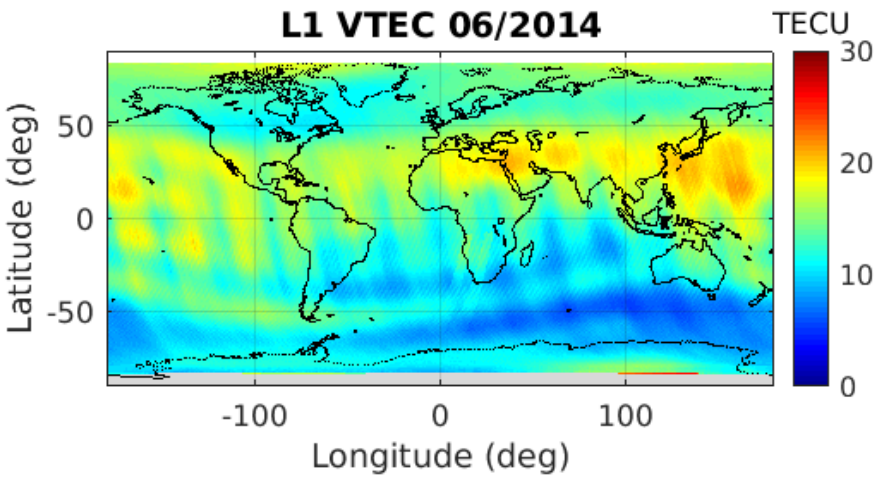

(a)

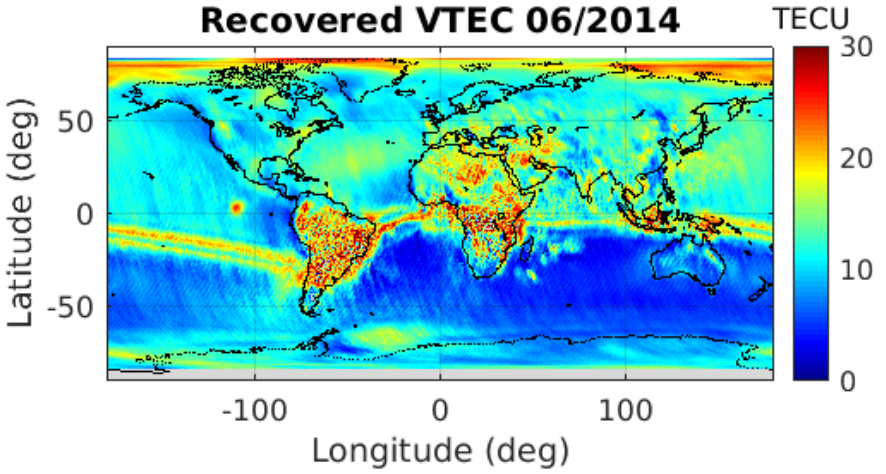

(b)

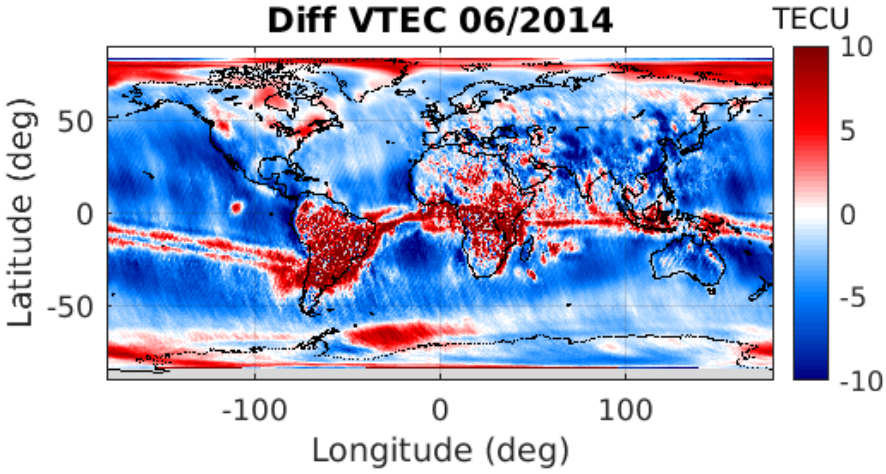

(c)

Figure B. 4. VTEC global maps of June 2014 (ascending orbits): (a) L1 VTEC, (b) SMOS-derived VTEC, and (c) difference between the SMOS-derived VTEC and the L1 VTEC.

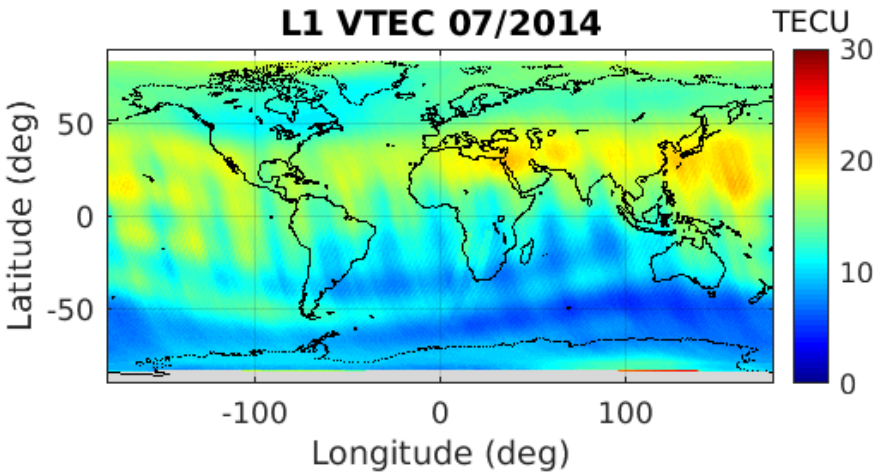

(a)

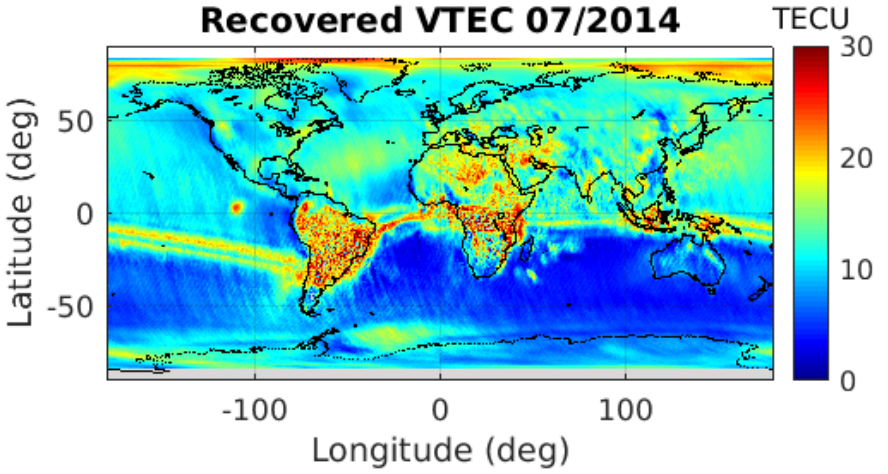

(b)

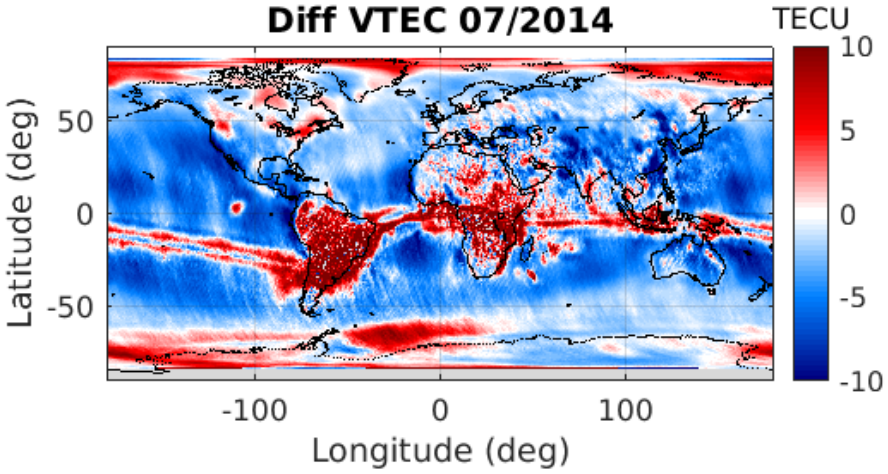

(c)

Figure B. 5. VTEC global maps of July 2014 (ascending orbits): (a) L1 VTEC, (b) SMOS-derived VTEC, and (c) difference between the SMOS-derived VTEC and the L1 VTEC.

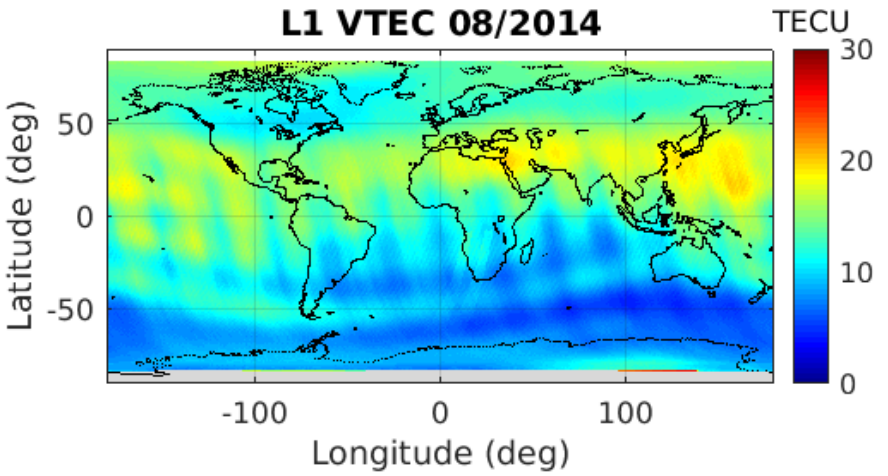

(a)

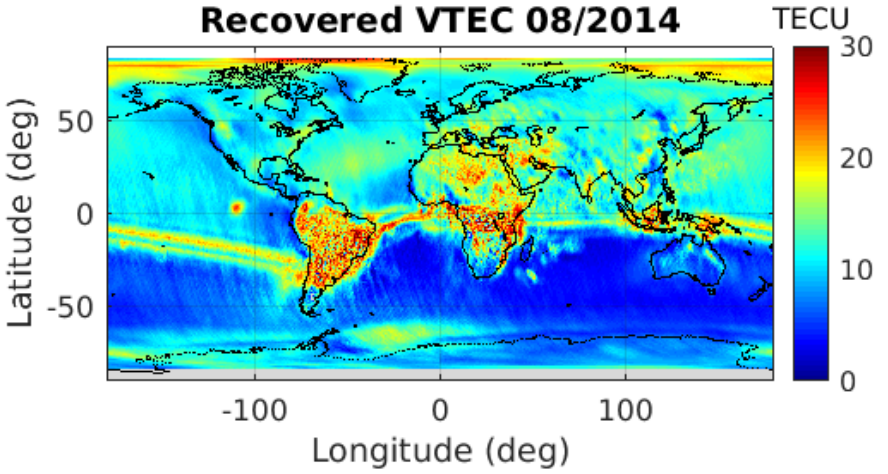

(b)

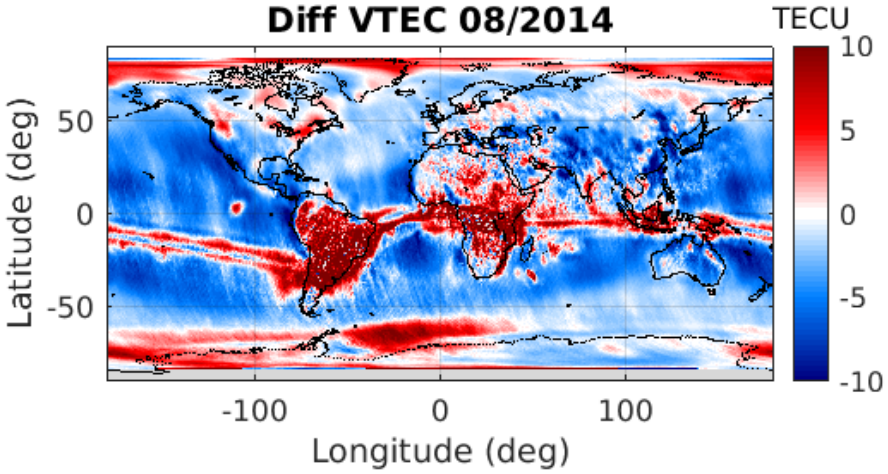

(c)

Figure B. 6. VTEC global maps of August 2014 (ascending orbits): (a) L1 VTEC, (b) SMOS-derived VTEC, and (c) difference between the SMOS-derived VTEC and the L1 VTEC.

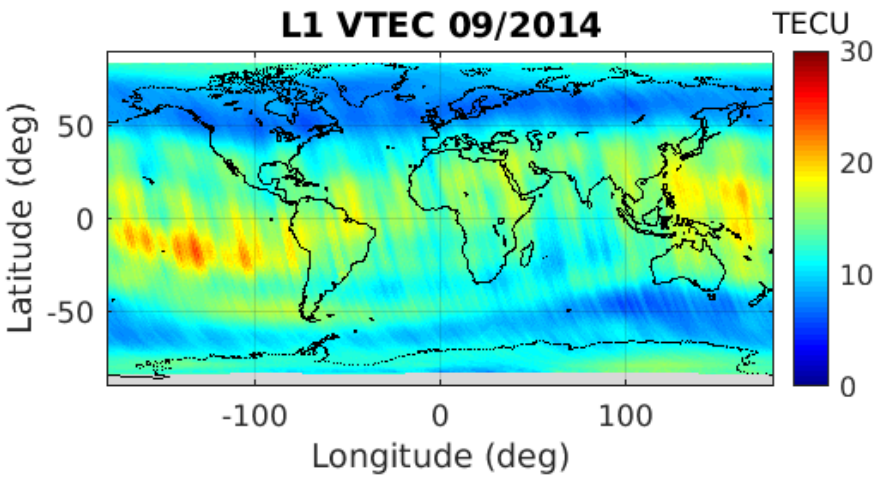

(a)

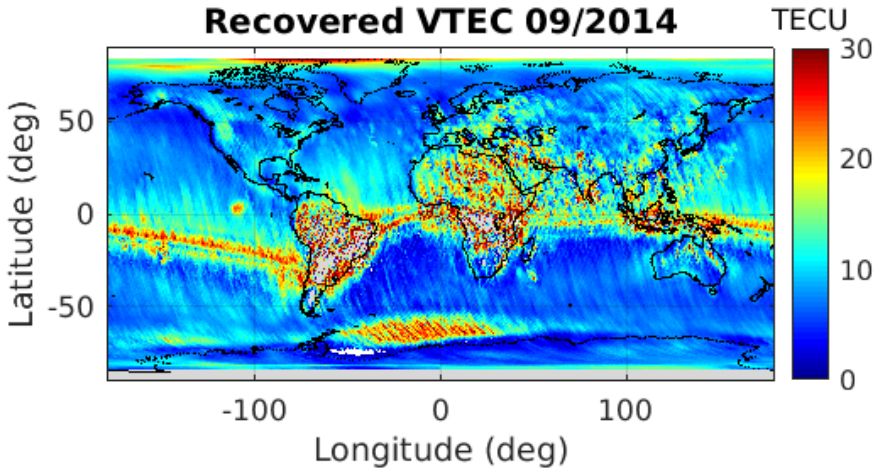

(b)

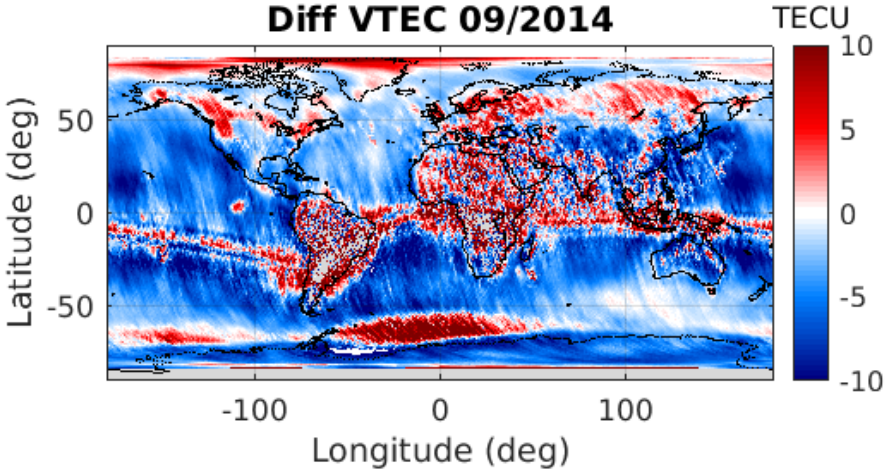

(c)

Figure B. 7. VTEC global maps of September 2014 (ascending orbits): (a) L1 VTEC, (b) SMOS-derived VTEC, and (c) difference between the SMOS-derived VTEC and the L1 VTEC.

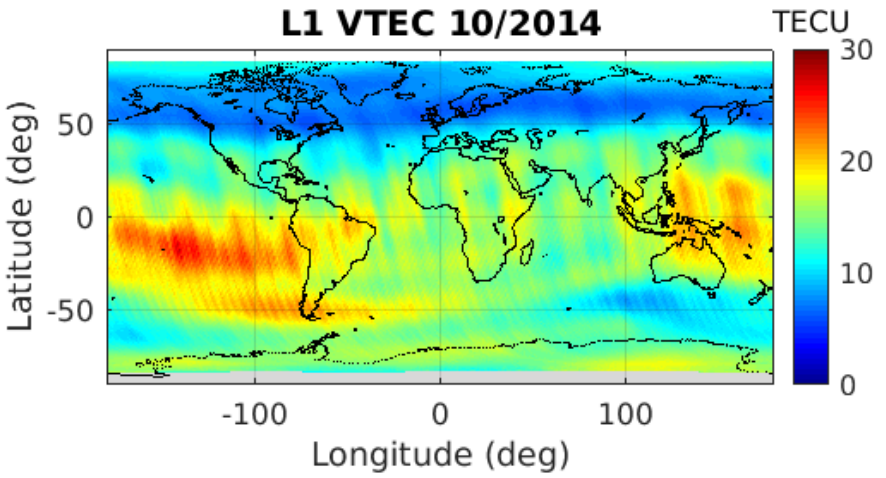

(a)

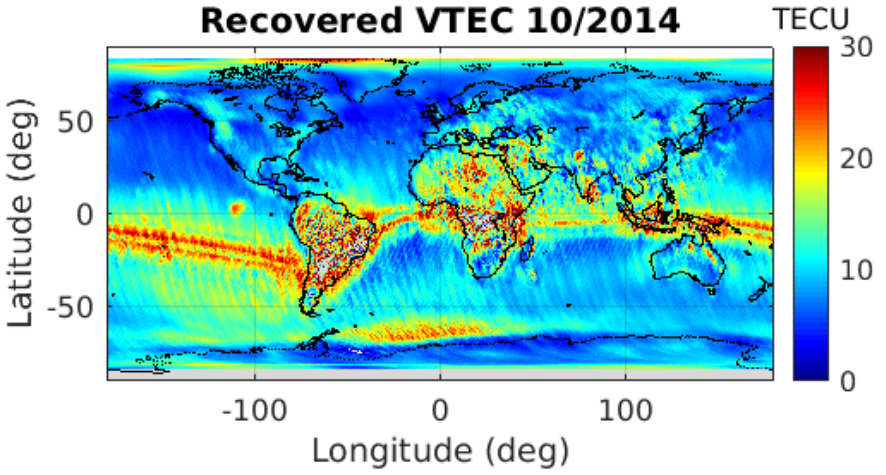

(b)

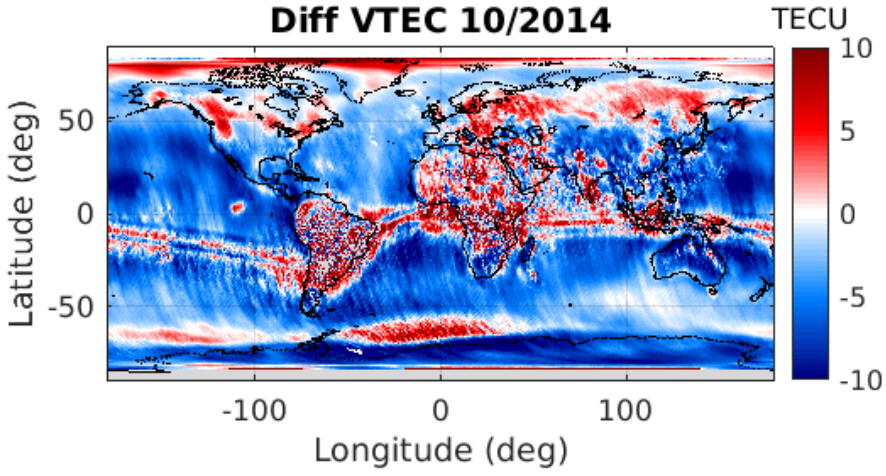

(c)

Figure B. 8. VTEC global maps of October 2014 (ascending orbits): (a) L1 VTEC, (b) SMOS-derived VTEC, and (c) difference between the SMOS-derived VTEC and the L1 VTEC.

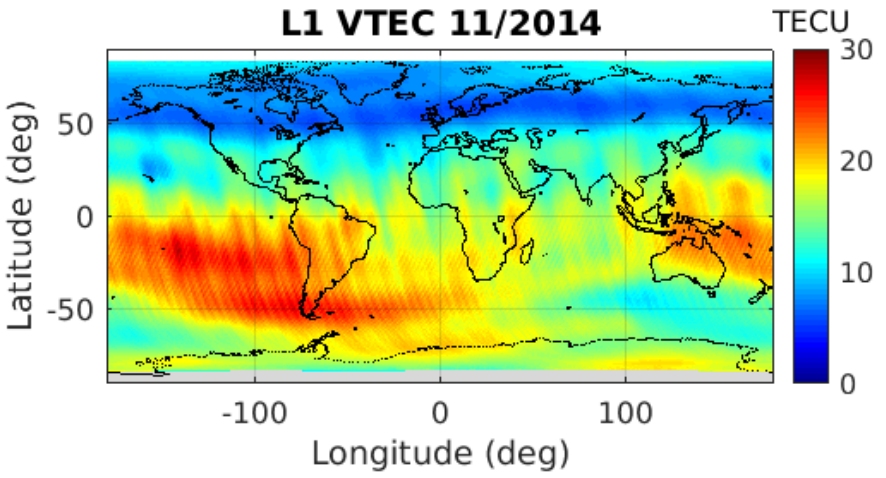

(a)

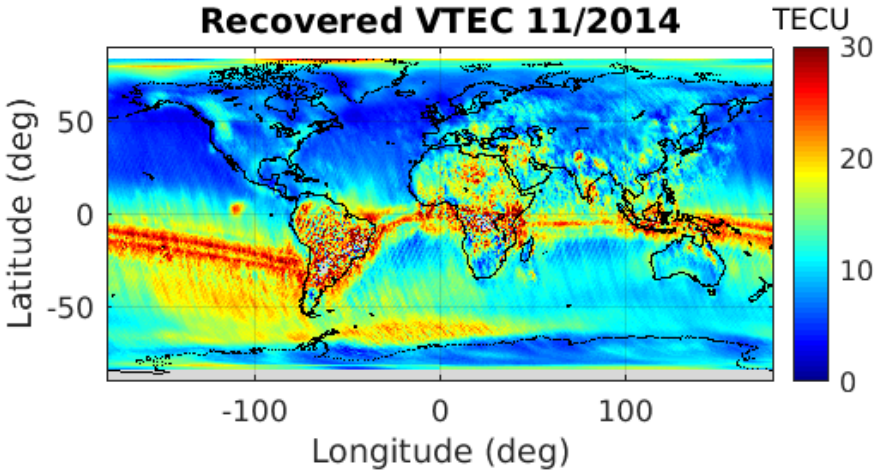

(b)

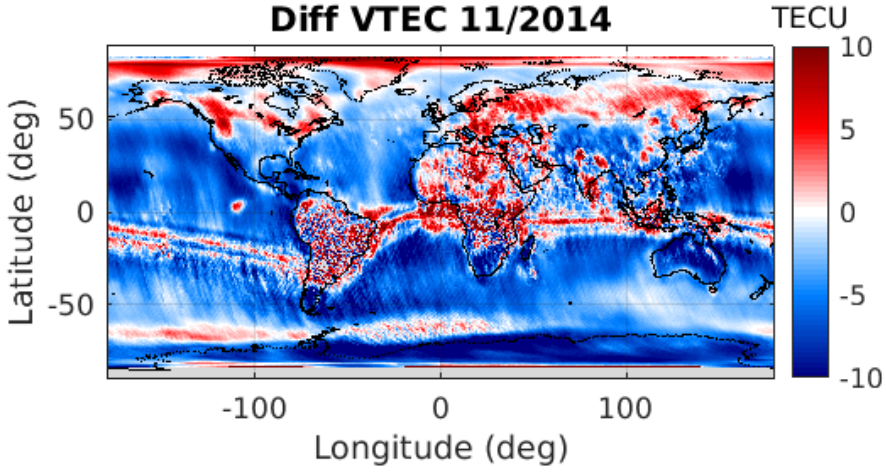

(c)

Figure B. 9. VTEC global maps of November 2014 (ascending orbits): (a) L1 VTEC, (b) SMOS-derived VTEC, and (c) difference between the SMOS-derived VTEC and the L1 VTEC.

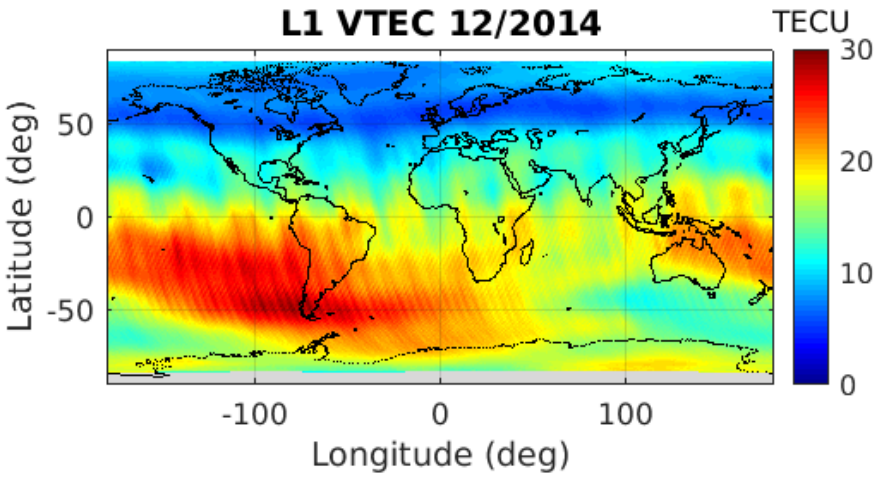

(a)

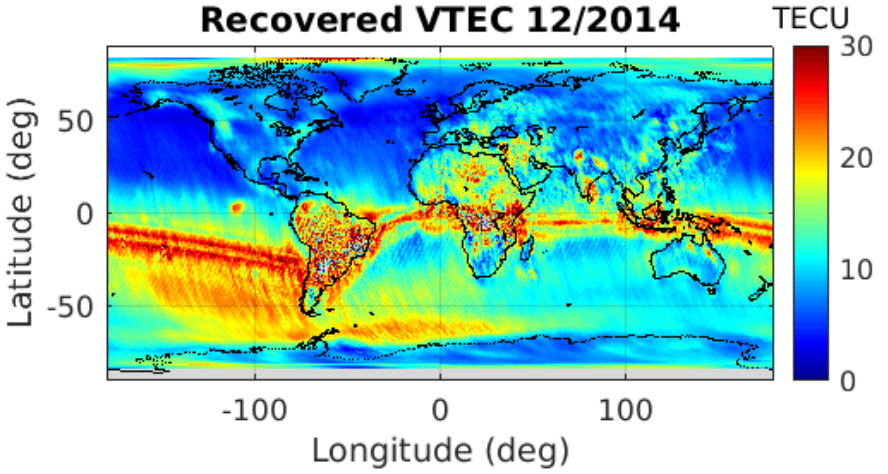

(b)

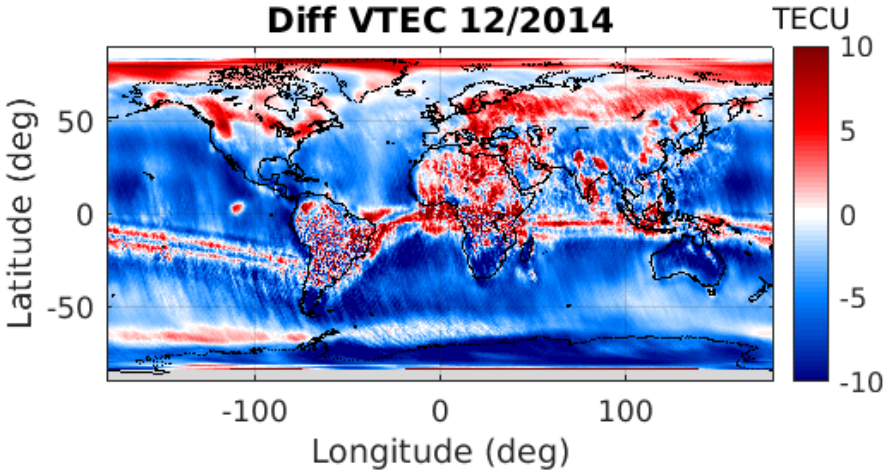

(c)

Figure B. 10. VTEC global maps of December 2014 (ascending orbits): (a) L1 VTEC, (b) SMOS-derived VTEC, and (c) difference between the SMOS-derived VTEC and the L1 VTEC.

References

Antonov, J. I., Seidoy, D., Boyer, T. P., Locarnini, R. A., Mishonov, A. V., Garcia, H. E., Baranova, O. K., Zweng, M. M., & Johnson, D. R. (2010). World Ocean Atlas 2009, Volume 2: Salinity. *S. Levitus, Ed. NOAA Atlas NESDIS 69, U.S. Government Office, Washington, D.C.*, 184 pp.

Barbosa, J. (2021). *SMOS Level 1 and Auxiliary Data Products Specifications* (SO-TN-IDR-GS-0005). Technical Report. Indra Sistemas. Available in https://earth.esa.int/eogateway/documents/20142/37627/SMOSL1-Aux-Data-Product-Specification.pdf

Barre, H. M. J. P., Duesmann, B., & Kerr, Y. H. (2008). SMOS: The Mission and the System. *IEEE Transactions on Geoscience and Remote Sensing*, *46*(3), 587–593. https://doi.org/10.1109/TGRS.2008.916264

Bengoa, B. (2020). *SMOS Level 2 and Auxiliary Data Products Specifications* (SO-TN-IDR-GS-0006). Technical Report. Indra Sistemas. Available in https://earth.esa.int/eogateway/documents/20142/0/SMOS-L2- Aux-Data-Product- Specification.pdf

Bilitza, D., Altadill, D., Truhlik, V., Shubin, V., Galkin, I., Reinisch, B., & Huang, X. (2017). International Reference Ionosphere 2016: From ionospheric climate to real-time weather predictions: IRI-2016. *Space Weather*, *15*(2), 418–429. https://doi.org/10.1002/2016SW001593

Brown, M. A., Torres, F., Corbella, I., & Colliander, A. (2008). SMOS Calibration. *IEEE Transactions on Geoscience and Remote Sensing*, *46*(3), 646–658. https://doi.org/10.1109/TGRS.2007.914810

Camps, A., Bara, J., Sanahuja, I. C., & Torres, F. (1997). The processing of hexagonally sampled signals with standard rectangular techniques: Application to 2-D large aperture synthesis interferometric radiometers. *IEEE Transactions on Geoscience and Remote Sensing*, *35*(1), 183–190. https://doi.org/10.1109/36.551946

Camps, A., Corbella, I., Bara, J., & Torres, F. (1998). Radiometric sensitivity computation in aperture synthesis interferometric radiometry. *IEEE Transactions on Geoscience and Remote Sensing*, *36*(2), 680–685. https://doi.org/10.1109/36.662749

Colliander, A., Ruokokoski, L., Suomela, J., Veijola, K., Kettunen, J., Kangas, V., Aalto, A., Levander, M., Greus, H., Hallikainen, M. T., & Lahtinen, J. (2007). Development and Calibration of SMOS Reference Radiometer. *IEEE Transactions on Geoscience and Remote Sensing*, *45*(7), 1967–1977. https://doi.org/10.1109/TGRS.2007.894055

Corbella, I., Torres, F., Camps, A., Bara, J., Duffo, N., & Vall-Ilossera, M. (2000). L-band aperture synthesis radiometry: Hardware requirements and system performance. *IGARSS 2000. IEEE 2000 International Geoscience and Remote Sensing Symposium. Taking the Pulse of the Planet: The Role of Remote Sensing in Managing the Environment. Proceedings (Cat. No.00CH37120)*, *7*, 2975–2977. https://doi.org/10.1109/IGARSS.2000.860307

Corbella, I., Duffo, N., Vall-llossera, M., Camps, A., & Torres, F. (2004). The visibility function in interferometric aperture synthesis radiometry. *IEEE Transactions on Geoscience and Remote Sensing*, *42*(8), 1677–1682. https://doi.org/10.1109/TGRS.2004.830641

Corbella, I., Torres, F., Duffo, N., González-Gambau, V., Camps, A., & Vall-llossera, M. (2008). Fast Processing Tool for SMOS Data. *IGARSS 2008 - 2008 IEEE International Geoscience and Remote Sensing Symposium*, II-1152-II–1155. https://doi.org/10.1109/IGARSS.2008.4779204

Corbella, I., Torres, F., Duffo, N., Martín-Neira, M., González-Gambau, V., Camps, A., & Vall-llossera, M. (2009). On-Ground Characterization of the SMOS Payload. *IEEE Transactions on Geoscience and Remote Sensing*, *47*(9), 3123–3133. https://doi.org/10.1109/TGRS.2009.2016333

Corbella, I., Torres, F., Duffo, N., González-Gambau, V., Pablos, M., Duran, I., & Martín-Neira, M. (2011). MIRAS Calibration and Performance: Results From the SMOS In-Orbit Commissioning Phase. *IEEE Transactions on Geoscience and Remote Sensing*, *49*(9), 3147–3155. https://doi.org/10.1109/TGRS.2010.2102769

Corbella, I., Torres, F., Wu, L., Duffo, N., Duran, I., & Martín-Neira, M. (2013). Spatial biases analysis and mitigation methods in SMOS images. *2013 IEEE International Geoscience and Remote Sensing Symposium - IGARSS*, 3415–3418. https://doi.org/10.1109/IGARSS.2013.6723562

Corbella, I., Lin, W., Torres, F., Duffo, N., & Martín-Neira, M. (2015). Faraday Rotation Retrieval Using SMOS Radiometric Data. *IEEE Geoscience and Remote Sensing Letters*, *12*(3), 458–461. https://doi.org/10.1109/LGRS.2014.2345845

Corbella, I., Torres, F., Duffo, N., Duran, I., González-Gambau, V., & Martín-Neira, M. (2019). Wide Field of View Microwave Interferometric Radiometer Imaging. *Remote Sensing*, *11*(6), 682. https://doi.org/10.3390/rs11060682

Crapolicchio, R. (2008). *VTEC usage for SMOS Level 1 Operational Processor*. XSMS-GSEG-EOPG-TN-06-0019 - issue 3.1.

Daganzo, E., Oliva, R., Kerr, Y., Nieto, S., Richaume, P., & Mecklenburg, S. (2012). SMOS radiometer in 1400-1427 MHz: Impact of the RFI environment and approach to its mitigation and cancellation. *2012 IEEE International Geoscience and Remote Sensing Symposium*, 3316–3319. https://doi.org/10.1109/IGARSS.2012.6350594

Daganzo, E., Oliva, R., Llorente, A., & Uranga, E. (2017, May 24). *Harmful Interference to Earth Observation Sensing Systems: The Case of SMOS Radiometer in the 1400-1427 passive band*. https://www.itu.int/en/ITU-R/space/workshops/2017

Daniell, R. E., Brown, L. D., Anderson, D. N., Fox, M. W., Doherty, P. H., Decker, D. T., Sojka, J. J., & Schunk, R. W. (1995). Parameterized ionospheric model: A global ionospheric parameterization based on first principle models. *Radio Science*, *30*(5), 1499–1510. https://doi.org/10.1029/95RS01826

Dinnat, E. P., Boutin, J., Yin, X., Le Vine, D. M., Waldteufel, P., & Vergely, J.-L. (2014). Comparison of SMOS and Aquarius Sea Surface Salinity and analysis of possible causes for the differences. *2014 XXXIth URSI General Assembly and Scientific Symposium (URSI GASS)*, 1–4. https://doi.org/10.1109/URSIGASS.2014.6929701

Donlon, C. (2020). *Copernicus Imaging Microwave Radiometer (CIMR)* (ESA-EOPSM-CIMR-MRD-3236-issue 4.0). Mission Requirements document. Earth and Mission Science Division. Available in https://esamultimedia.esa.int/docs/EarthObservation/CIMR-MRD-v4.0-20201006_Issued.pdf

Drinkwater, M., Kerr, Y., Font, J., & Berger, M. (2009). *Exploring the Water Cycle of the "Blue Planet"* (ESA Bulletin No. 137; pp. 6–15).

Emery, W., & Camps, A. (2017). Microwave Radiometry. In *Introduction to Satellite Remote Sensing: Atmosphere, Ocean, Cryosphere and Land Applications* (pp. 131–290). Elsevier. https://doi.org/10.1016/B978-0-12-809254-5.00004-X

Entekhabi, D., Njoku, E. G., O'Neill, P. E., Kellogg, K. H., Crow, W. T., Edelstein, W. N., Entin, J. K., Goodman, S. D., Jackson, T. J., Johnson, J., Kimball, J., Piepmeier, J. R., Koster, R. D., Martin, N., McDonald, K. C., Moghaddam, M., Moran, S., Reichle, R., Shi, J. C., Spencer, M. W., Thurman, S. W., Tsang, L., & Van Zyl, J. (2010). The Soil Moisture Active Passive (SMAP) Mission. *Proceedings of the IEEE*, *98*(5), 704–716. https://doi.org/10.1109/JPROC.2010.2043918

References

ESA. (2019, February 14). *Objectives—Earth Online—ESA*. https://earth.esa.int/web/guest/missions/esa-operational-eo-missions/smos/objectives

FAO. (2022, May 2). *Maps and figures | Global Forest Resources Assessments | Food and Agriculture Organization of the United Nations*. https://www.fao.org/forest-resources-assessment/past-assessments/fra-2005/maps-and-figures/en/

Floury, N. (2007). *Estimation of Faraday rotation from Auxiliary data*. smos_iono_tn_v2r3 - issue 3.2.

Gabarro, C., Gonzalez-Gambau, V., Corbella, I., Torres, F., Martinez, J., Portabella, M., & Font, J. (2013). Impact of the Local Oscillator Calibration Rate on the SMOS Measurements and Retrieved Salinities. *IEEE Transactions on Geoscience and Remote Sensing*, *51*(9), 4633–4642. https://doi.org/10.1109/TGRS.2012.2233744

Gallagher, D. L., Craven, P. D., & Comfort, R. H. (1988). An empirical model of the earth's plasmasphere. *Advances in Space Research*, *8*(8), 15–24. https://doi.org/10.1016/0273-1177(88)90258-X

Gonzalez-Gambau, V. (2012). *Contribution to the characterization of interferometric radiometers devoted to Earth observation: Application to the MIRAS/SMOS payload* [Ph.D. Thesis, University Polytechnic of Catalonia]. http://hdl.handle.net/10803/96760

González-Gambau, V., Olmedo, E., Turiel, A., Martínez, J., Ballabrera-Poy, J., Portabella, M., & Piles, M. (2016). Enhancing SMOS brightness temperatures over the ocean using the nodal sampling image reconstruction technique. *Remote Sensing of Environment*, *180*, 205–220. https://doi.org/10.1016/j.rse.2015.12.032

Hernández-Pajares, M., Juan, J. M., Sanz, J., Orus, R., Garcia-Rigo, A., Feltens, J., Komjathy, A., Schaer, S. C., & Krankowski, A. (2009). The IGS VTEC maps: A reliable source of ionospheric information since 1998. *Journal of Geodesy*, *83*(3–4), 263–275. https://doi.org/10.1007/s00190-008-0266-1

Hochegger, G., Nava, B., Radicella, S., & Leitinger, R. (2000). A family of ionospheric models for different uses. *Physics and Chemistry of the Earth, Part C: Solar, Terrestrial & Planetary Science*, *25*(4), 307–310. https://doi.org/10.1016/S1464-1917(00)00022-2

Kakoti, G., Bhuyan, P. K., & Hazarika, R. (2017). Seasonal and solar cycle effects on TEC at 95°E in the ascending half (2009–2014) of the subdued solar cycle 24: Consistent underestimation by IRI 2012. *Advances in Space Research*, *60*(2), 257–275. https://doi.org/10.1016/j.asr.2016.09.002

Kerr, Y., Reul, N., Martín-Neira, M., Drusch, M., Alvera-Azcarate, A., Wigneron, J.-P., & Mecklenburg, S. (2016). ESA's Soil Moisture and Ocean Salinity Mission – Achievements and applications after more than 6 years in orbit. *Remote Sensing of Environment*, *180*, 1–2. https://doi.org/10.1016/j.rse.2016.03.020

Kerr, Y. H., Waldteufel, P., Wigneron, J.-P., Delwart, S., Cabot, F., Boutin, J., Escorihuela, M.-J., Font, J., Reul, N., Gruhier, C., Juglea, S. E., Drinkwater, M. R., Hahne, A., Martín-Neira, M., & Mecklenburg, S. (2010). The SMOS Mission: New Tool for Monitoring Key Elements ofthe Global Water Cycle. *Proceedings of the IEEE*, *98*(5), 666–687. https://doi.org/10.1109/JPROC.2010.2043032

Lagerloef, G., Colomb, F. R., Le Vine, D., Wentz, F., Yueh, S., Ruf, C., Lilly, J., Gunn, J., Chao, Y., deCharon, A., Feldman, G., & Swift, C. (2008). The Aquarius/SAC-D Mission: Designed to Meet the Salinity Remote-Sensing Challenge. *Oceanography*, *21*(1), 68–81. https://doi.org/10.5670/oceanog.2008.68

Le Vine, D. M., & Abraham, S. (2002). The effect of the ionosphere on remote sensing of sea surface salinity from space: Absorption and emission at L band. *IEEE Transactions on Geoscience and Remote Sensing*, *40*(4), 771–782. https://doi.org/10.1109/TGRS.2002.1006342

Le Vine, D. M., Abraham, S., Utku, C., & Dinnat, E. P. (2013). Aquarius Third Stokes Parameter Measurements: Initial Results. *IEEE Geoscience and Remote Sensing Letters*, *10*(3), 520–524. https://doi.org/10.1109/LGRS.2012.2211994

Le Vine, D. M., Dinnat, E. P., Lagerloef, G. S. E., de Matthaeis, P., Abraham, S., Utku, C., & Kao, H. (2014). Aquarius: Status and recent results. *Radio Science*, *49*(9), 709–720. https://doi.org/10.1002/2014RS005505

Le Vine, D. M., & Abraham, S. (2016a). Faraday rotation and the SMAP radiometer. *2016 14th Specialist Meeting on Microwave Radiometry and Remote Sensing of the Environment (MicroRad)*, 25–26. https://doi.org/10.1109/MICRORAD.2016.7530497

Le Vine, D. M., & Abraham, S. (2016b). Faraday rotation measurement with the SMAP radiometer. *2016 IEEE International Geoscience and Remote Sensing Symposium (IGARSS)*, 288–290. https://doi.org/10.1109/IGARSS.2016.7729066

Lin, W. (2014). *Contribution to spatial bias mitigation in interferometric radiometers devoted to Earth observation: Application to the SMOS mission* [Ph.D. Thesis, University Polytechnic of Catalonia]. http://hdl.handle.net/2117/95304

Ludwig, A. (1973). The definition of cross polarization. *IEEE Transactions on Antennas and Propagation*, *21*(1), 116–119. https://doi.org/10.1109/TAP.1973.1140406

Martin-Neira, M., Ribo, S., & Martin-Polegre, A. J. (2002). Polarimetric mode of MIRAS. *IEEE Transactions on Geoscience and Remote Sensing*, *40*(8), 1755–1768. https://doi.org/10.1109/TGRS.2002.802489

Martín-Neira, M., Oliva, R., Corbella, I., Torres, F., Duffo, N., Durán, I., Kainulainen, J., Closa, J., Zurita, A., Cabot, F., Khazaal, A., Anterrieu, E., Barbosa, J., Lopes, G., Tenerelli, J., Díez-García, R., Fauste, J., Martín-Porqueras, F., González-Gambau, V., Turiel, A., Delwart, S., Crapolicchio, R., & Suess, M. (2016). SMOS instrument performance and calibration after six years in orbit. *Remote Sensing of Environment*, *180*, 19–39. https://doi.org/10.1016/j.rse.2016.02.036

McMullan, K. D., Brown, M. A., Martin-Neira, M., Rits, W., Ekholm, S., Marti, J., & Lemanczyk, J. (2008). SMOS: The Payload. *IEEE Transactions on Geoscience and Remote Sensing*, *46*(3), 594–605. https://doi.org/10.1109/TGRS.2007.914809

Mecklenburg, S., Drusch, M., Kaleschke, L., Rodriguez-Fernandez, N., Reul, N., Kerr, Y., Font, J., Martin-Neira, M., Oliva, R., Daganzo-Eusebio, E., Grant, J. P., Sabia, R., Macelloni, G., Rautiainen, K., Fauste, J., de Rosnay, P., Munoz-Sabater, J., Verhoest, N., Lievens, H., Delwart, S., Crapolicchio, R., de la Fuente, A., & Kornberg, M. (2016). ESA's Soil Moisture and Ocean Salinity mission: From science to operational applications. *Remote Sensing of Environment*, *180*, 3–18. https://doi.org/10.1016/j.rse.2015.12.025

Nava, B., Coïsson, P., & Radicella, S. M. (2008). A new version of the NeQuick ionosphere electron density model. *Journal of Atmospheric and Solar-Terrestrial Physics*, *70*(15), 1856–1862. https://doi.org/10.1016/j.jastp.2008.01.015

Oliva, R., & ESA team. (2015). *Definition of a metric to assess SMOS L1 Data Quality* (SM-TN-AURO-L1OP-0003; Issue 1.1). Technical Report. ESA.

Oliva, R., Daganzo, E., Richaume, P., Kerr, Y., Cabot, F., Soldo, Y., Anterrieu, E., Reul, N., Gutierrez, A., Barbosa, J., & Lopes, G. (2016). Status of Radio Frequency Interference (RFI) in the 1400–1427 MHz passive band based on six years of SMOS mission. *Remote Sensing of Environment*, *180*, 64–75. https://doi.org/10.1016/j.rse.2016.01.013

Oliva, R. (2018). Mitigation of SMOS RFI Contamination Based on BT Frequency Extrapolation. *IGARSS 2018 - 2018 IEEE International Geoscience and Remote Sensing Symposium*, 309–312. https://doi.org/10.1109/IGARSS.2018.8518532

Oliva, R., Gonzalez-Gambau, V., & Turiel, A. (2019). Assessment of SMOS RFI Mitigation by means of a Triple collocation technique. *IGARSS 2019 - 2019 IEEE International Geoscience and Remote Sensing Symposium*, 4543–4546. https://doi.org/10.1109/IGARSS.2019.8898639

Oliva, R. (2020). *SMOS ESLs 2020+ Technical Note on the T3 latitudinal gradient across-task T3* (issue 1.1). Zenithal Blue Technologies; SMOS-ZBT-Xtask-T3.

Piepmeier, J. R., Johnson, J. T., Mohammed, P. N., Bradley, D., Ruf, C., Aksoy, M., Garcia, R., Hudson, D., Miles, L., & Wong, M. (2014). Radio-Frequency Interference Mitigation for the Soil Moisture Active Passive Microwave Radiometer. *IEEE Transactions on Geoscience and Remote Sensing*, *52*(1), 761–775. https://doi.org/10.1109/TGRS.2013.2281266

Planck, M. (1901). Ueber das Gesetz der Energieverteilung im Normalspectrum. *Annalen der Physik*, *309*(3), 553–563. https://doi.org/10.1002/andp.19013090310

Radicella, S. M. (2009, March 23). *Ionospheric Modelling*. https://indico.ictp.it/event/a08148/session/91/contribution/57/material/0/0.pdf

Randa, J., Lahtinen, J., Camps, A., Gasiewski, A. J., Hallikainen, M. T., Le Vine, D. M., Martin-Neira, M., Piepmeier, J., Rosenkranz, P. W., Ruf, C. S., Shiue, J., & Skou, N. (2008). *Recommended terminology for microwave radiometry* (NBS TN 1551; 0 ed., p. NBS TN 1551). National Bureau of Standards. https://doi.org/10.6028/NIST.TN.1551

Roma-Dollase, D., Hernández-Pajares, M., Krankowski, A., Kotulak, K., Ghoddousi-Fard, R., Yuan, Y., Li, Z., Zhang, H., Shi, C., Wang, C., Feltens, J., Vergados, P., Komjathy, A., Schaer, S., García-Rigo, A., & Gómez-Cama, J. M. (2018). Consistency of seven different GNSS global ionospheric mapping techniques during one solar cycle. *Journal of Geodesy*, *92*(6), 691–706. https://doi.org/10.1007/s00190-017-1088-9

Rubino, R., Torres, F., Duffo, N., González-Gambau, V., Corbella, I., & Martin-Neira, M. (2017). Direct Faraday rotation angle retrieval in SMOS field of view. *2017 IEEE International Geoscience and Remote Sensing Symposium (IGARSS)*, 697–698. https://doi.org/10.1109/IGARSS.2017.8127047

Rubino, R., Duffo, N., González-Gambau, V., Torres, F., Corbella, I., & Martin-Neira, M. (2018). New Methodology for the Faraday Rotation Angle Retrieval in the SMOS Field of View. *IGARSS 2018 - 2018 IEEE International Geoscience and Remote Sensing Symposium*, 3089–3092. https://doi.org/10.1109/IGARSS.2018.8517502

Rubino, R., Duffo, N., González-Gambau, V., Corbella, I., Torres, F., Durán, I., & Martín-Neira, M. (2019a). New Methodology to Retrieve the Faraday Rotation Angle Using SMOS Data. *LPS19 -Living Planet 2019*. LPS19 -Living Planet 2019, Milan.

Rubino, R., Duffo, N., González-Gambau, V., Corbella, I., Torres, F., Durán, I., & Martín-Neira, M. (2019b). Refining the Methodology to Correct the Faraday Rotation Angle from

SMOS Measurements. *IGARSS 2019 - 2019 IEEE International Geoscience and Remote Sensing Symposium*. https://doi.org/10.1109/IGARSS.2019.8897755

Rubino, R., Duffo, N., González-Gambau, V., Corbella, I., Torres, F., & Martin-Neira, M. (2020). Characterizing Systematic Errors in the Faraday Rotation Retrieval from SMOS Measurements. *IGARSS 2020 - 2020 IEEE International Geoscience and Remote Sensing Symposium*, 6431–6433. https://doi.org/10.1109/IGARSS39084.2020.9323288

Rubino, R., Duffo, N., González-Gambau, V., Corbella, I., Torres, F., Oliva, R., & Martín-Neira, M. (2022). Correcting the FRA Systematic Error in VTEC Maps from SMOS Radiometric Data. *IEEE Transactions on Geoscience and Remote Sensing*, *in revision*.

Shi, J., Dong, X., Zhao, T., Du, Y., Liu, H., Wang, Z., Zhu, D., Ji, D., Xiong, C., & Jiang, L. (2016). The water cycle observation mission (WCOM): Overview. *2016 IEEE International Geoscience and Remote Sensing Symposium (IGARSS)*, 3430–3433. https://doi.org/10.1109/IGARSS.2016.7729886

Silvestrin, P., Berger, M., Kerr, Y. H., & Font, J. (2001). ESA's Second Earth Explorer Opportunity Mission: The Soil Moisture and Ocean Salinity Mission – SMOS. *IEEE Geosci. Remote Sens. Lett.*, *118*, 5. https://doi.org/10.1016/j.rse.2015.12.025

Tenerelli, J., & Reul, N. (2010). *Analysis of L1PP calibration approach impacts in SMOS TB and 3-days SSS retrievals over the Pacific using an alternative Ocean Target Transformation applied to L1OP data* (IFREMER/CL, Tech. Rep.).

Thébault, E., Finlay, C. C., Beggan, C. D., Alken, P., Aubert, J., Barrois, O., Bertrand, F., Bondar, T., Boness, A., Brocco, L., Canet, E., Chambodut, A., Chulliat, A., Coïsson, P., Civet, F., Du, A., Fournier, A., Fratter, I., Gillet, N., Hamilton, B., Hamoudi, M., Hulot, G., Jager, T., Korte, M., Kuang, W., Lalanne, X., Langlais, B., Léger, J.-M., et al. (2015). International Geomagnetic Reference Field: The 12th generation. *Earth, Planets and Space*, *67*(1). https://doi.org/10.1186/s40623-015-0228-9

Ulaby, F. T., Moore, R. K., & Fung, A. K. (1981). Microwave remote sensing: Active and passive. In *Microwave remote sensing fundamentals and radiometry: Vol. I*. Addison-Wesley.

Vergely, J.-L., Waldteufel, P., Boutin, J., Yin, X., Spurgeon, P., & Delwart, S. (2014). New total electron content retrieval improves SMOS sea surface salinity. *Journal of Geophysical Research: Oceans*, *119*(10), 7295–7307. https://doi.org/10.1002/2014JC010150

Yin, X., Boutin, J., & Spurgeon, P. (2013). Biases Between Measured and Simulated SMOS Brightness Temperatures Over Ocean: Influence of Sun. *IEEE Journal of Selected Topics in*

Applied Earth Observations and Remote Sensing, *6*(3), 1341–1350. https://doi.org/10.1109/JSTARS.2013.2252602

Yueh, S. H. (2000). Estimates of Faraday rotation with passive microwave polarimetry for microwave remote sensing of Earth surfaces. *IEEE Transactions on Geoscience and Remote Sensing*, *38*(5), 2434–2438. https://doi.org/10.1109/36.868900

Zine, S., Boutin, J., Font, J., Reul, N., Waldteufel, P., Gabarro, C., Tenerelli, J., Petitcolin, F., Vergely, J.-L., Talone, M., & Delwart, S. (2008). Overview of the SMOS Sea Surface Salinity Prototype Processor. *IEEE Transactions on Geoscience and Remote Sensing*, *46*(3), 621–645. https://doi.org/10.1109/TGRS.2008.915543